From Oxidation to Deposition: Novel Tools for Measuring Atmospheric Per- and Polyfluoroalkyl Substances

Alessia Alessandra Colussi

A dissertation submitted to the Faculty of Graduate Studies in partial fulfillment of the requirements for the degree of Doctor of Philosophy

Graduate Program in Chemistry
York University
Toronto, Ontario

April 2026

Dedication

To my nonni, Lidia and Mino, and my abuelita, Elsa – your love was steady, generous, and never in short supply. So much of who I am (and how I work) comes from you. I hope this would have made you proud.

To my sweet Aria – my first writing buddy and unofficial productivity supervisor. Your tail wags, sleepy sighs, and gentle presence carried me through the early chapters of this work. Your love lives in these pages – even if your edits were mostly paw-shaped.



You are missed, always.

This is for you.

Abstract

Per- and polyfluoroalkyl substances (PFAS) are a group of persistent, bioaccumulative, and toxic compounds characterized by strong carbon-fluorine bonds and their resulting environmental stability. Volatile and semi-volatile neutral PFAS and their precursors can undergo gas-phase oxidation to form perfluoroalkyl acids (PFAAs), including perfluorocarboxylic acids (PFCAs), which are widely detected in environmental matrices. Although long-chain PFAS have been phased out over the past two decades, increased production and degradation of precursor compounds have led to growing concern over the persistence, mobility, and expanding global distribution of ultrashort- and short-chain PFAAs. Chapter 2 investigates the hydroxyl (OH)-initiated oxidation of 4:2 fluorotelomer alcohol, a PFCA precursor, under low-NO_x conditions at atmospherically relevant relative humidities (22%, 44%, and 60%). Using an oxidation flow reactor coupled to proton transfer reaction time-of-flight mass spectrometry, we detected the 4:2 fluorotelomer aldehyde and carboxylic acid, confirming proposed mechanisms and providing initial constraints on humidity-dependent OH kinetics. This technique provides an alternative to traditional dry smog chamber experiments with improved representation of ambient atmospheric conditions. Chapter 3 presents an open-source, modular, and affordable automatic wet deposition sampler capable of off-grid operation. The system was deployed across the Newfoundland and Labrador Boreal Ecosystem Latitudinal Transect and operated continuously using solar-assisted battery power. Performance was evaluated under summer and winter conditions, and proof-of-concept validation included routine rainwater chemistry measurements. Chapter 4 describes the development and validation of an artifact-minimized denuder sampling method to measure gas-phase perfluoropropionic acid (PFPrA), achieving 99.83 ± 0.03% capture efficiency. Additionally, year-long deposition and denuder sampling in regions home to endangered Canadian whale

populations, at Tadoussac, Québec and Saturna Island, British Columbia, showed trifluoroacetic acid (TFA) and PFPrA as dominant PFCAs and demonstrated site-specific differences in wet versus dry deposition. A concurrent intercomparison with passive air samplers showed consistent seasonal trends for TFA, supporting the consistency of the denuder sampling. These measurements establish baseline levels in the two whale habitats and show that atmospheric deposition is an important source of ultrashort-chain PFCAs there. Together, these results present novel tools and foundational data to better understand atmospheric PFAS oxidation, transport, and deposition, while developing monitoring capabilities in remote and sensitive environments.

Acknowledgements

The completion of this work was made possible through the continued support and collaboration of many people. First and foremost, I would like to thank my supervisors, Dr. Cora Young and Dr. Trevor VandenBoer, for their guidance, patience, and deep commitment to the craft of research. Your advice and belief in my work meant a great deal to me and I am thankful for the time you invested in both me and this project. I am also grateful to my supervisory committee members, Dr. John Liggio and Dr. Robert McLaren, for their constructive feedback and support throughout this process. Your encouragement and expertise have been instrumental in shaping both this dissertation and my growth as a researcher. Thank you as well to Dr. Roxana Sühring and Dr. Satinder Kaur Brar for serving on my defense committee and for your time and insight.

My sincere thanks, once again, to Dr. John Liggio as well as to Amy Leithead, Dr. Jeremy Wentzell, Dr. Chuba Shunthirasingham, and Dr. Chao Peng for their support during my time at Environment and Climate Change Canada. I am grateful for the opportunity to have used their laboratory facilities and resources and for their scientific insights and guidance during my time there. I also thank Geri Crooks, Raeanne House, Darryl Davie, Sandrine Vigneron, François Gagnon, Charlie Wentholt, and Louis-Georges Esquilat for their help with sampling-site access and setup, off-season storage of deployed instrumentation, and sample collection during the Whales Initiative. This work would not have been possible without your contributions.

To all past and present lab mates in the CJY and VDB research groups – thank you for the shared knowledge, the laughs, and the many conversations that made my time in graduate school both productive and memorable. A special thank you to the best officemates: Lisa (my day-one lab partner-in-crime) and Andrea, and to Teles (the best peer mentor around), Leyla, Melodie, Leigh, Daniel, and Stephen for the brainstorming sessions and support over the years.

To my wonderful family and friends outside of the Petrie Science and Chemistry Buildings – thank you for your encouragement and for reminding me that there is life beyond the lab and research deadlines. I am especially grateful to my parents, Claudia and Elio. Your patience, unconditional love, and steady support made this achievement possible. I would not be here without you. Thank you for everything. To my brother, Andrea; my cousins, Daniela, Marina (my favourite PSE 207 PhD), Misia, Olivia, and Dante; and my best friend, Christina – thank you for keeping me grounded (with welcome distractions) throughout this process. Your care and encouragement have meant a great deal. Finally, Azzurra, who sat beside me through many long writing sessions – occasionally contributing a well-timed bark or a paw on the keyboard. Your quiet companionship brought comfort during moments of doubt and stress. Your contributions, though unpublishable, were invaluable and have earned you an honourary dog-torate.

Table of Contents

List of Tables

List of Figures

List of Symbols, Nomenclature, and Abbreviations

°C	degrees Celsius
%	percent
σ	standard deviation (sigma)
µ	mean (mu)
µg	microgram
µL	microlitre
µm	micrometre (micron)
µS	microsiemens
^{19}F-NMR	Fluorine-19 Nuclear Magnetic Resonance spectroscopy
A	Ampere
AAS	Active Air Sampler
ADS	Annular Denuder System
AGM	Absorbent Glass Mat
Ah	Amp-hour
ARIA	Air Regulating Instrument for Atmospheric sampling
C	Carbon
CEPA	Canadian Environmental Protection Act
CAPMoN	Canadian Air and Precipitation Monitoring Network
CD	Conductivity Detection
CFC	Chlorofluorocarbon

Cl	Chlorine
cm	centimetre
cm^3	cubic centimetre
CO	Carbon monoxide
CO_2	Carbon dioxide
DD	Dry Deposition
DIW	Deionized Water
DOC	Dissolved Organic Carbon
E	Electric field strength
ECCC	Environment and Climate Change Canada
ER	Eagle River
ESI	Electrospray Ionization
FTAL	Fluorotelomer Aldehyde
FTCA	Fluorotelomer Carboxylic Acid
FTIR	Fourier Transform Infrared spectroscopy
FTOH	Fluorotelomer alcohol
g	gram
GC	Gas Chromatography
GC-MS	Gas Chromatography Mass Spectrometry
GC-MS/MS	Gas Chromatography tandem Mass Spectrometry
GCo	Grand Codroy

GFF	Glass Fiber Filter
H_2O_2	Hydrogen peroxide
H_2SO_4	Sulfuric acid
H_3O^+	Hydronium ion
HCFC	Hydrochlorofluorocarbon
HCl	Hydrochloric acid
HDPE	High-Density Polyethylene
HFC	Hydrofluorocarbon
HFO	Hydrofluoroolefin
HFO-1234yf	2,3,3,3-tetrafluoropropene
$HgCl_2$	Mercuric chloride
HNO_3	Nitric acid
HPLC	High-Performance Liquid Chromatography
hr	hour
HR	Humber River Camp 10
HO_2	Hydroperoxyl (radical)
I-CIMS	Iodide-adduct Chemical Ionization Mass Spectrometry
IC	Ion Chromatography
IC-CD	Ion Chromatography with Conductivity Detection
IC-MS	Ion Chromatography Mass Spectrometry
IS	Internal Standard

K	Potassium
kcal	kilocalorie
kg	kilogram
KHP	Potassium Hydrogen Phthalate
kJ	kilojoule
km	kilometre
k_{obs}	observed rate constant (4:2 FTOH + OH)
L	Litre
LC	Liquid Chromatography
LC-MS	Liquid Chromatography Mass Spectrometry
LC-MS/MS	Liquid Chromatography tandem Mass Spectrometry
LOD	Limit of Detection
LOQ	Limit of Quantification
m	metre
M	molar concentration (mol L^{-1})
MΩ	megohm
m^2	square metre
m^3	cubic metre
mA	milliampere
MAT	Mean Annual Temperature
mg	milligram

Milli-Q water	deionized water (18.2 MΩ·cm)
min	minute
mL	millilitre
mm	millimetre
MS	Mass Spectrometry
MVS	Medium Volume Sampler
m/z	mass-to-charge ratio
N	buffer gas density
N_2	Nitrogen gas
NADP	National Atmospheric Deposition Program
Na_2CO_3	Sodium carbonate
ncps	normalized counts per second
ng	nanogram
NL-BELT	Newfoundland and Labrador Boreal Ecosystem Latitudinal Transect
nm	nanometre
NO_x	nitrogen oxides ($NO + NO_2$)
OECD	Organization for Economic Cooperation and Development
OF	Open Fall precipitation
OFR	Oxidation Flow Reactor
OH	Hydroxyl (radical)
O_3	Ozone

ORNL	Oak Ridge National Laboratory
P/N	Part Number
Pa	Pascal
PA	Proton Affinity
PAS	Passive Air Sampler
PB	Pynn's Brook
PBDE	Polybrominated Diphenyl Ether
PBL	Planetary Boundary Layer
PCB	Polychlorinated Biphenyl
PD	Permeation Device
PES	Polyethersulfone
PFA	Perfluoroalkoxy
PFAA	Perfluoroalkyl Acid
PFAS	Per- and Polyfluoroalkyl Substances
PFBA	Perfluorobutanoic Acid (C4 PFCA)
PFCA	Perfluorocarboxylic Acid
PFHxA	Perfluorohexanoic Acid (C6 PFCA)
PFOA	Perfluorooctanoic Acid (C8 PFCA)
PFOS	Perfluorooctane Sulfonic Acid (C8 PFSA)
PFPeA	Perfluoropentanoic Acid (C5 PFCA)
PFPrA	Perfluoropropionic Acid (C3 PFCA)

PFSA	Perfluorosulfonic Acid
pg	picogram
PM_{10}	coarse mode particulate matter (2.5 to 10 μm)
$PM_{2.5}$	fine mode particulate matter (≤ 2.5 μm)
POP	Persistent Organic Pollutant
ppbv	parts-per-billion-by-volume (10^{-9} mol mol^{-1})
ppm	parts-per-million
ppmv	parts-per-million-by-volume (10^{-6} mol mol^{-1})
pptv	parts-per-trillion-by-volume (10^{-12} mol mol^{-1})
ppqv	parts-per-quadrillion-by-volume (10^{-15} mol mol^{-1})
PTR	Proton Transfer Reaction
PTR-ToF-MS	Proton Transfer Reaction Time-of-Flight Mass Spectrometry
PUF	Polyurethane Foam
QFF	Quartz Fiber Filter
RH	Relative Humidity
ROC	Reactive Organic Carbon
RO_2	alkylperoxy radicals
RSD	Relative Standard Deviation
s	second
SF	Stem Flow
SKU	Stock Keeping Unit

SLEB	St. Lawrence Estuary beluga
SO_2	Sulfur dioxide
SR	Salmon River
SRKW	Southern Resident killer whale
TD	Total Deposition
TF	Throughfall precipitation
TFA	Trifluoroacetic Acid (C2 PFCA)
Tg	teragram
ToF	Time-of-Flight
U.S. EPA	United States Environmental Protection Agency
UV	Ultraviolet
V	Volt
VAC	Volts of Alternating Current
VDC	Volts of Direct Current
VOC	Volatile Organic Compound
W	Watt
WD	Wet Deposition
XAD	Polystyrene-divinylbenzene resin

Preface

This thesis consists of a collection of manuscripts, either published or prepared for submission to peer-reviewed scientific journals. As a result, some repetition of introductory and experimental details was unavoidable. All manuscripts were authored by Alessia A. Colussi, with critical feedback provided by Cora J. Young and Trevor C. VandenBoer. The research and manuscript preparation were conducted under the supervision of Cora J. Young and Trevor C. VandenBoer. The specific contributions of co-authors are outlined below:

Chapter 1: Introduction

Contributions – Prepared by Alessia A. Colussi with editorial comments by Cora J. Young and Trevor C. VandenBoer.

Chapter 2: Atmospheric Fate of 4:2 Fluorotelomer Alcohol using an Oxidation Flow Reactor and Proton Transfer Reaction Time-of-Flight Mass Spectrometry.

Environmental Science: Processes & Impacts. 2026, *in press,* doi: 10.1039/d5em00943j.

Alessia A. Colussi[1], Trevor C. VandenBoer[1], Cora J. Young[1], and John Liggio[2]

[1] Department of Chemistry, York University, Toronto, ON, Canada
[2] Air Quality Research Division, Environment and Climate Change Canada, Toronto, ON, Canada

Contributions: Alessia A. Colussi performed the chamber experiments and data analysis. Alessia A. Colussi wrote the manuscript with contributions from all authors. All authors were involved in examining and reviewing the results. All authors were involved in editing the manuscript.

Chapter 3: Cost Effective Off-Grid Automatic Precipitation Samplers for Pollutant and Biogeochemical Atmospheric Deposition.

Atmospheric Measurement Techniques. 2024, *17*(12), pp. 3697-3718

Alessia A. Colussi[1,⁺], *Daniel Persaud*[1,⁺], *Melodie Lao*[1], *Bryan K. Place*[2,‡], *Rachel F. Hems*[2,§], *Susan E. Ziegler*[3], *Kate A. Edwards*[4,ǂ], *Cora J. Young*[1,2], and *Trevor C. VandenBoer*[1,3]

[1] Department of Chemistry, York University, Toronto, ON
[2] Department of Chemistry, Memorial University, St. John's, NL
[3] Department of Earth Science, Memorial University, St. John's, NL

[4] Canadian Forest Service, Natural Resources Canada, Corner Brook, NL
[⁘] These authors contributed equally to this work.

[‡] Now at: SciGlob Instruments & Services LLC, Columbia, MD, USA
[§] Now at: Department of Chemistry and Biochemistry, Oberlin College and Conservatory, OH, USA
[ǂ] Now at: Climate Change Impacts and Adaptation Division, Lands and Minerals Sector, Natural Resources Canada, Ottawa, ON

Contributions: Alessia A. Colussi, Daniel Persaud, and Melodie Lao performed the data analysis. Alessia A. Colussi and Daniel Persaud wrote the manuscript with contributions from all authors. Sampler design and construction were led by Trevor C. VandenBoer, with assistance from Bryan K. Place and Rachel F. Hems for the initial prototypes, Daniel Persaud and Melodie Lao for the revised iteration, and Alessia A. Colussi for the final modular control boards. Sample collection and associated characterization measurements were performed by Bryan K. Place and Trevor C. VandenBoer. The sampling experiments were conceptualized and conducted by Trevor C. VandenBoer, Cora J. Young, Kate A. Edwards, and Susan E. Ziegler. All authors were involved in examining and reviewing the results. All authors were involved in editing the paper.

Chapter 4: Quantifying Ultrashort- and Short-chain Perfluorocarboxylic Acids in Endangered Canadian Whale Habitats (*in preparation*)

Alessia A. Colussi[1], Dylan J. Indos[1], Eric Vanhauwaert[1], Chubashini Shunthirasingham[2], Nick Alexandrou[2], Hayley Hung[2], Trevor C. VandenBoer[1], and Cora J. Young[1]

[1] Department of Chemistry, York University, Toronto, ON, Canada

[2] Air Quality Processes Research Section, Environment and Climate Change Canada, Toronto, ON, Canada

Contributions: Alessia A. Colussi led the field sampling coordination and logistics, which were implemented with contributions from Hayley Hung, Chubashini Shunthirasingham, and Nick Alexandrou. Alessia A. Colussi performed the field sample data analysis. Dylan J. Indos led the denuder sample efficiency experiments using the IC-CD system, and Eric Vanhauwaert led the IC-CD analysis of those samples. Alessia A. Colussi led the writing of the manuscript, with contributions from Dylan J. Indos, Trevor C. VandenBoer, and Cora J. Young. Alessia A. Colussi, Dylan J. Indos, Trevor C. VandenBoer, and Cora J. Young were involved in examining and reviewing the results. All authors were involved in editing the manuscript

Chapter 5: Conclusions and Future Directions

Contributions – Prepared by Alessia A. Colussi with editorial comments by Cora J. Young and Trevor C. VandenBoer.

Chapter 1

Introduction

1.1 Principles of Pollutant Transport and Fate in the Atmosphere

The atmosphere plays a central role in the global distribution of pollutants, influencing how chemicals emitted at local and regional levels are transported, transformed, and ultimately deposited across terrestrial and aquatic environments. Pollutants emitted from upwind sources, such as smokestacks, fires, tailpipes, and vegetation, can be carried downwind (horizontally) by wind advection and spread via turbulent mixing in all directions, including vertically, throughout atmospheric layers.[1-4] These mixing and advection processes govern the spatial distribution of airborne species and, in combination with chemical reactions and removal pathways, helps determine how long chemicals remain in the atmosphere and where they deposit. The troposphere, the lowest atmospheric layer where almost all weather occurs, extends from Earth's surface up to the tropopause; its height varies from ~7 to 8 km near the poles to as high as ~18 to 20 km at the equator (typical global average ~10 to 13 km) and contains the majority of the atmosphere's mass and water vapour.[5] Within the lower troposphere, the planetary boundary layer (PBL) is directly influenced by the Earth's surface and characterized by strong turbulence and vertical mixing that redistribute pollutants soon after emission.[6] Pollutants that rise above the PBL into the upper (free) troposphere can be transported over much longer distances because vertical mixing and deposition processes are relatively weaker there.[7] Temperature inversions – stable layers where warmer air overlies cooler surface air – can suppress vertical mixing and trap pollutants near the surface under stable conditions, contributing to pollutant accumulation near the ground.[8]

Once in the atmosphere, airborne substances are subject to a range of chemical and physical processes that govern their fate: they may remain airborne, become chemically transformed into other compounds, or be removed to the surface.[9] Chemical transformation occurs through reaction with hydroxyl (OH) radicals, ozone (O_3), and other reactive species, as well as through photolysis,

hydrolysis, and acid-base reactions, leading to the formation of secondary compounds.[2] Pollutants are removed from the atmosphere by deposition processes that transfer gases and particles to aquatic and terrestrial surfaces. Dry deposition refers to the direct transfer of airborne gases and particulates onto surfaces in the absence of precipitation. This is done via mechanisms such as gravitational settling, absorption, and impaction onto vegetation, soil, or water – a key sink for airborne material between rain events.[10] In contrast, wet deposition occurs when atmospheric pollutants are scavenged by precipitation (e.g., rain, snow, sleet, hail, or fog) either within clouds or as droplets fall through the air, incorporating dissolved gases and particles and delivering them to the surface with the precipitation.[11] Both wet and dry deposition are primary removal pathways which results in contaminants being deposited to the Earth's surface, influencing biogeochemical cycles and environmental health.[9]

A pollutant's behaviour in the atmosphere also depends on whether it exists predominantly in the gas-phase or is associated with airborne particles (aerosols), as gas-particle partitioning affects both transport and removal processes.[12] Atmospheric aerosols are tiny particles suspended in the air, consisting of a mixture of chemical components such as inorganic species (e.g., salts), carbonaceous material, mineral dust, as well as water-soluble and water-insoluble organic matter.[13] Gaseous species are generally removed from the atmosphere through chemical transformation as well as by deposition, whereas those in the particle phase are primarily removed by wet and dry deposition.[14] Together, these processes, along with advection and turbulent mixing, determine a pollutant's atmospheric lifetime – the average time a compound remains in the atmosphere before removal by chemical or physical processes – and thus influences how far and over what timescale the pollutant can be transported and deposited.[15] Short-lived species tend to impact local and

regional environments while long-lived species can be transported over continental to global scale before removal.[16]

At a mechanistic level, atmospheric lifetime is governed by chemical and physical loss processes that depend on a compound's physicochemical properties. Chemical removal is controlled by reaction rate constants with atmospheric oxidants (e.g., OH radicals and O_3) and their ambient concentrations, which together determine overall reaction rates. Physical removal processes, including wet and dry deposition, are influenced by properties such as water solubility (or Henry's law constant, K_{AW}), volatility, and gas-particle partitioning behaviour, which affect both atmospheric residence time and deposition efficiency.[17] Additional molecular properties, such as polarizability, can further influence intermolecular interactions and partitioning behaviour, indirectly affecting atmospheric persistence.[18] Understanding these interconnected processes is essential for interpreting how airborne contaminants travel, transform, and exit the atmosphere, and for predicting where and how they will interact with terrestrial and aquatic environments.

1.2 Per- and Polyfluoroalkyl Substances: A Non-stick Nightmare

The mechanisms that govern the atmospheric transport and fate of traditional pollutants, such as polychlorinated biphenyls (PCBs) and polycyclic aromatic hydrocarbons (PAHs), also shape how emerging contaminants disperse and cycle through the environment. Among these, per- and polyfluoroalkyl substances (PFAS) are a class of amphiphilic, organofluorine compounds where *per*fluoroalkyl substances are fully fluorinated (all hydrogen substituents have been replaced by fluorine atoms) and *poly*fluoroalkyl substances are partially fluorinated (having at least one carbon with hydrogen atoms bound to it).[19] This group of chemicals contain hydrophilic functional groups and hydrophobic alkyl chains and can be either linear or branched, with chain-

lengths of two to twenty carbons.[19] Long-chain PFAS characteristically contain seven to twenty carbons in their backbone whereas short-chain PFAS have four to six, and ultrashort-chain compounds contain two or three carbons only. These fluorinated compounds highlight the interconnection between a chemical's persistence and atmospheric processes. Despite the generally low volatility of many long-chain ionic PFAS, some neutral and volatile PFAS (e.g., fluorotelomer alcohols, FTOHs, and other precursors) can exist in the gas-phase, where they are primarily removed through gas-phase oxidation, enabling long-range atmospheric transport prior to transformation. In contrast, ionic and highly water-soluble PFAS – such as a subclass of PFAS known as perfluorocarboxylic acids (PFCAs) – are more efficiently removed from the atmosphere via wet deposition processes.[20]

In 2018, the Organization for Economic Cooperation and Development (OECD) included over 4700 unique CAS numbers for PFAS available in the global market[21]; however, in 2021 they revised their definition of PFAS to include any chemical containing at least one saturated -CF_2 or -CF_3 moiety. This resulted in one of the largest open chemical collections, PubChem, listing over seven million PFAS under this revised definition.[22] It must also be noted that organofluorine chemistry is largely anthropogenic, as naturally occurring fluorinated compounds are extremely rare. Those that do exist typically contain only a single fluorine atom and lack multiple perfluorinated carbon atoms; thus, they do not fall under previous definitions of PFAS and are not classified as such.[23] Having first been recognized as "contaminants of emerging concern" in the late 1990s, PFAS have since then been widely detected in precipitation, oceans, surface waters, surface soils, biota (including humans), and the atmosphere following decades of commercial and consumer use.[24-30] As understanding of their persistence, toxicity, and widespread environmental

occurrence has increased, PFAS have become the focus of growing international regulatory attention.[31-34]

1.2.1 Physiochemical Properties

The carbon-fluorine bond present within perfluoroalkyl moieties, $-C_nF_{2n}-$ or $-C_nF_{2n+1}$, is one of the strongest single bonds in chemistry and has an average bond dissociation energy of 480 kJ mol^{-1}.[35] This bond exhibits strong polarity due to the small size and high electronegativity of the fluorine atom (fluorine = 4.0 compared to carbon = 2.5).[36] In combination, the strength of the carbon-fluorine bond, the effective shielding of the carbon atom by fluorine atoms, and the presence of three pairs of nonbonding electrons around each fluorine atom contribute to the well-known stability of PFAS.[37] The strength of the carbon-fluorine bond increases as more fluorine atoms are substituted onto a carbon atom.[35] When all hydrogens atoms within a carbon chain are replaced with fluorine, a highly stable perfluoralkyl chain remains. This complete substitution is achievable due to less space being needed for the formation of carbon-fluorine bonds when compared to the larger halogens.[23] Fluorine's low polarizability and high ionization potential also results in weak intra- and intermolecular interactions. While the inclusion of a perfluoroalkyl moiety decreases water solubility – due to carbon-fluorine bonds being poor hydrogen bond acceptors[38], the addition of a hydrophilic headgroup (e.g., carboxylic acid or sulfonic acid), increases PFAS water solubility and gives rise to the extremely low surface tension of PFAS. These compounds are also non-flammable and are highly resistant to degradation via abiotic (e.g., hydrolysis and photolysis) and biotic (e.g., decomposition of organic matter) mechanisms.[39-41]

1.2.2 Manufacturing, Applications, and Environmental Fate

In looking at the manufacturing of perfluorinated compounds over the last several decades, two key processes must be noted: telomerization and electrochemical fluorination.[42,43] Telomerization is a chemical reaction between tetrafluoroethylene ($F_2C=CF_2$) oligomers and pentafluoroiodoethane (C_2F_5I) to produce straight, even chained perfluoroalkyl iodides ($C_nF_{2n+1}I$). With telomerization producing nearly 100% pure linear isomers[19,44,45], the resulting fluorotelomer aldehydes have historically been used to make various fluorotelomer products such as FTOHs (Section 1.3.1). Consequently, telomerization has become the dominant method for manufacturing PFCAs while electrochemical fluorination is relied on specifically for the large-scale production of perfluorooctanoic acid (PFOA) and perfluorooctane sulfonic acid (PFOS) – two of the most common and widely detected long-chain PFAS.[46] The latter manufacturing process, in the presence of an electric current, involves the replacement of all hydrogen atoms in a hydrocarbon with fluorine atoms.[47,48] Rearrangement and fragmentation of the hydrocarbon can occur and subsequently results in fluorinated compounds of varying chain-lengths and a mixture of branched, linear, and cyclic isomers.[49]

With its earliest manufacturing dating back to the 1930s[50,51], PFAS have been utilized in a variety of applications across a wide range of industries. This class of fluorinated compounds have been found in aqueous film forming foams, oil-resistant coatings for food packaging, pesticides, floor polishes, and stain-, water-, and soil-resistant coatings for textiles and leather.[52-54] As a result, PFAS can be released into the environment via landfill leachate[55,56], wastewater treatment plant effluent[57,58], chemical production facilities[59], etc. The widespread nature of PFAS within the environment stems from their ability to undergo long-range atmospheric[60,61] and aquatic[62] transport, and they have therefore often been described in the literature as "ubiquitous." They have

been detected across a wide range of environmental compartments globally, including precipitation, surface waters, soils, and biota, reflecting their extensive environmental distribution and persistence.[63] Their presence is largely associated with systems that have been directly or indirectly influenced by atmospheric transport since the onset of large-scale production in the mid-20th century (when the initial widespread production, use, and atmospheric release of PFAS began), or with environments impacted by long-range transport away from point sources, including sites where aqueous film-forming foams have been applied.[63] Accordingly, while PFAS are often described as ubiquitous in contemporary environmental systems, this terminology depends on the spatial and temporal context considered.[63] For example, PFAS are not expected to be present in environmental reservoirs that have remained isolated from atmospheric exchange since before the 1950s, such as old glacial ice layers, deeper geological formations, or groundwater systems last replenished prior to the development of PFAS.[63] In this sense, PFAS are more precisely described as "widespread" or "commonly detected" across actively cycling surface environments rather than universally present across all environmental reservoirs.[63]

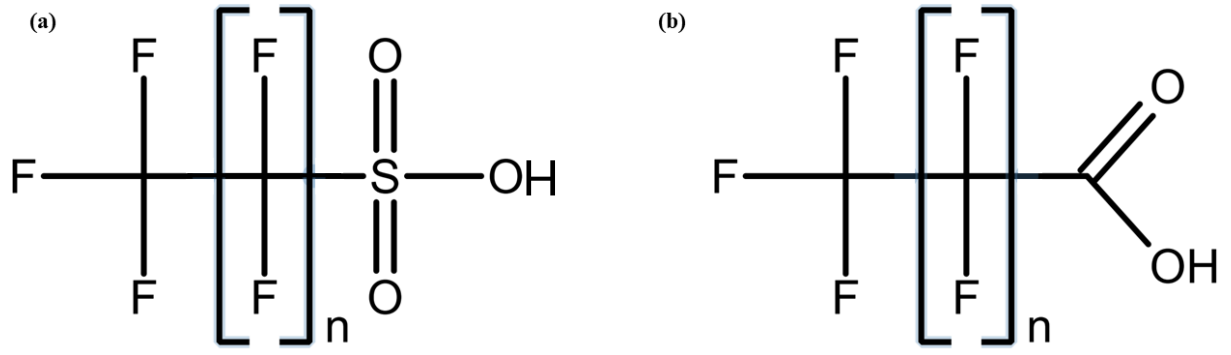

Figure 1-1. Generalized chemical structure of **(a)** perfluorosulfonic acids (PFSAs) and **(b)** perfluorocarboxylic acids (PFCAs) with varying chain length.

An important subclass of PFAS known as perfluoroalkyl acids (PFAAs) consist of perfluorosulfonic acids (PFSAs) and the aforementioned PFCAs (Figure 1-1). Persistent PFAS can be formed via exclusively anthropogenic PFAA precursors that are manufactured predominantly for i) the fluoropolymer and surfactant industries and ii) as chlorofluorocarbon (CFC) replacements.[64] Previous studies have shown the potential for PFSAs to form through atmospheric oxidation of precursor compounds (e.g., potassium perfluorohexane sulfonate and perfluorohexane sulfonyl fluoride)[65,66] whereas PFCAs have been shown to form in the atmosphere via the oxidation of precursor compounds and the hydrolysis of acyl halides from hydrochlorofluorocarbons (HCFCs) and hydrofluorocarbons (HFCs). For example, the unsaturated hydrofluoroolefin 2,3,3,3-tetrafluoropropene (HFO-1234yf) – used to replace an older generation of HFC refrigerants – degrades in the atmosphere to form trifluoroacetic acid (TFA, C2 PFCA).[67,68] Due to their low pK_a values, PFCAs are typically ionized across a wide range of environmentally relevant pH levels. Consequently, TFA is a well-known PFCA owing to its direct release into the environment either through its use or its loss via industrial emissions.[69] This compound can dissociate into trifluoroacetate ions (pK_a = 0.23) and become highly mobile in surface water, ground water, etc.[70] Acting as strong electron-withdrawing groups, fully fluorinated carbons pull electron density away from the negatively charged carboxylate group within the conjugate base. This electron-withdrawing effect destabilizes the parent acid while stabilizing the conjugate base, making PFCAs more prone to releasing a proton; thus, resulting in a lower pK_a and increased acidity.[71]

1.2.3 Long-chain PFAS: Regulatory Action and Proposed Alternatives

Increasing scientific evidence of PFAS persistence and toxicity has driven a series of international regulatory actions. In a 2002 hazard assessment performed by the OECD, PFOS was found to be persistent, bioaccumulative, and toxic within mammals and the environment.[72] Since then, exposure to PFAS has been linked to adverse effects such as kidney, ovarian, and testicular cancer in humans[73,74] and immunotoxicity and hormonal disruption in animals.[75.76] Upon entering ecosystems, long-chain PFAAs have been found to move up food chains and accumulate within human and animal tissues such as those of the liver, kidney, and lung.[77,78] In 2000, a key global manufacturer of PFOS, 3M, phased it out of production and use[79] while the United States Environmental Protection Agency (U.S. EPA) – alongside other global producers of PFOA – developed a stewardship program which successfully eliminated PFOA (and other ≥C7 PFAS) emissions and product content by 2015.[80] However, exposures within the USA continue after phaseouts with over 90% of pregnant women still being exposed to PFOS and PFOA.[81] Consequently, the 3M phase-out introduced perfluorobutyl-based chemistries and substituted eight carbon-based chemistries for that of four carbon-based chemistries.[82]

Additionally, PFAS regulation is embedded within a range of international and regional chemical management frameworks. For example, PFOS, its salts, and related compounds are listed under the Stockholm Convention on Persistent Organic Pollutants, reflecting global recognition of their persistence, bioaccumulation potential, long-range transport, and toxicity.[31,32] In the European Union, PFAS are increasingly regulated under the REACH framework, with a growing emphasis on grouping approaches and class-based restrictions rather than individual substance-by-substance assessment.[33] Within Canada, a similar PFOA initiative was created between Health Canada, Environment and Climate Change Canada (ECCC), and global producers.[83] Canada has

also published a state of the science report for screening health assessments as well as a risk management strategy for PFOS.[84] Subsequently, PFOA, PFOS, and other PFAS were included in the Prohibition of Certain Toxic Chemical regulations in 2012.[85] More recently, Canada has announced a move toward treating PFAS – excluding fluoropolymers – as a class under the Canadian Environmental Protection Act (CEPA), enabling coordinated prioritization and risk assessment of the broader PFAS family rather than individual compounds, reflecting increasing international consensus that their structural diversity and widespread use require class-based regulatory approaches.[34]

Beyond PFAA-specific regulations, broader environmental treaties have also shaped the atmospheric fate of fluorinated compounds. The Montreal Protocol (1989) was established to phase out O_3-depleting substances, including CFCs, as defined by the United Nations Environment Programme. These compounds were largely replaced by HCFCs and HFCs which have been shown to produce short-chain PFCAs following atmospheric oxidation.[64,86-88] Specifically, ultrashort- (C2 and C3) and short-chain (C4 to C6) PFCAs such as TFA, perfluoropropionic acid (PFPrA, C3 PFCA), and perfluorobutanoic acid (PFBA, C4 PFCA) can be formed from the atmospheric degradation of these replacements. While their toxicity is not well known, short-chain PFCAs have been found to accumulate in different plant tissues.[89-91] Subsequent amendments, i.e., the Kigali Amendment (2019), further targeted HFCs by implementing lower global warming potential alternatives such as t HFOs.[92]

Commonly used as refrigerants, these HFO replacement compounds were chosen due to their lower global warming potentials as well as their shorter atmospheric lifetimes compared to the replacement compounds mentioned previously.[92] However, the degradation of HFOs – e.g., HFO-1234yf, is assumed to yield 100% TFA.[93] Due to the strength of the carbon–fluorine bond,

the trifluoromethyl group is resistant to degradation in the environment and TFA is released as a terminal residue following the degradation of parent compounds.[69] Although it was initially thought unlikely to bioaccumulate within food chains, up to 3800 mg kg^{-1} (dry weight) of TFA has been measured in plants within the vicinity of a fluorochemical industrial site with an average field bioaccumulation factor of 13,000.[94] Additionally, TFA has been found in maize[94,95] and conifer needles[94,96], as well as in plant-based foods[97] and beverages such tea[98] and juice.[99] A recent study also showed the potential accumulation of TFA in (predominantly) herbivorous species, whereas PFOS, and to a lesser extent long-chain PFCAs (>C7) dominated in carnivores.[100] These findings ultimately suggests that the ingestion of plant-based foods and beverages could be a significant path for PFAS exposure in mammals. While previous studies have focused on the toxicity and bioaccumulation potential of long-chain PFAAs, industrial PFAS manufacturers maintained that ultrashort- and short-chain PFAAs were not of great concern; thus, they sought out to replace long-chain PFAAs with their short-chain homologues.[101] As a result, human and environmental short-chain PFAA exposure is projected to increase over time due to increasing global production and use. With their mobility and persistence, as well as the inability of water treatment plants to inhibit their spread in the environment, some researchers are calling for short-chain PFAAs to be recognized with equivalent concern to long-chain PFAAs.[102]

1.3 Atmospheric Oxidation of Volatile and Semi-volatile PFAS

Volatile and semi-volatile neutral PFAS (e.g., FTOHs) can undergo oxidation in the gas-phase to form PFAAs (i.e., PFCAs; Figure 1-2).[64] The long-range atmospheric transport of PFCAs can occur through a combination of direct and indirect transport. They can be directly transported as PFCAs via oceanic currents, as well as through the particle- or gas-phase, and they can also be

indirectly transported as precursor compounds prior to atmospheric oxidation. Previous studies have shown that oxidation of precursor compounds has led to the observance of PFCAs in both remote mountainous and polar regions.[103,104] Thus, the persistence and lengthy lifetimes of these precursors demonstrate the adverse long-term risks that PFAS exposure poses to human and environmental health.

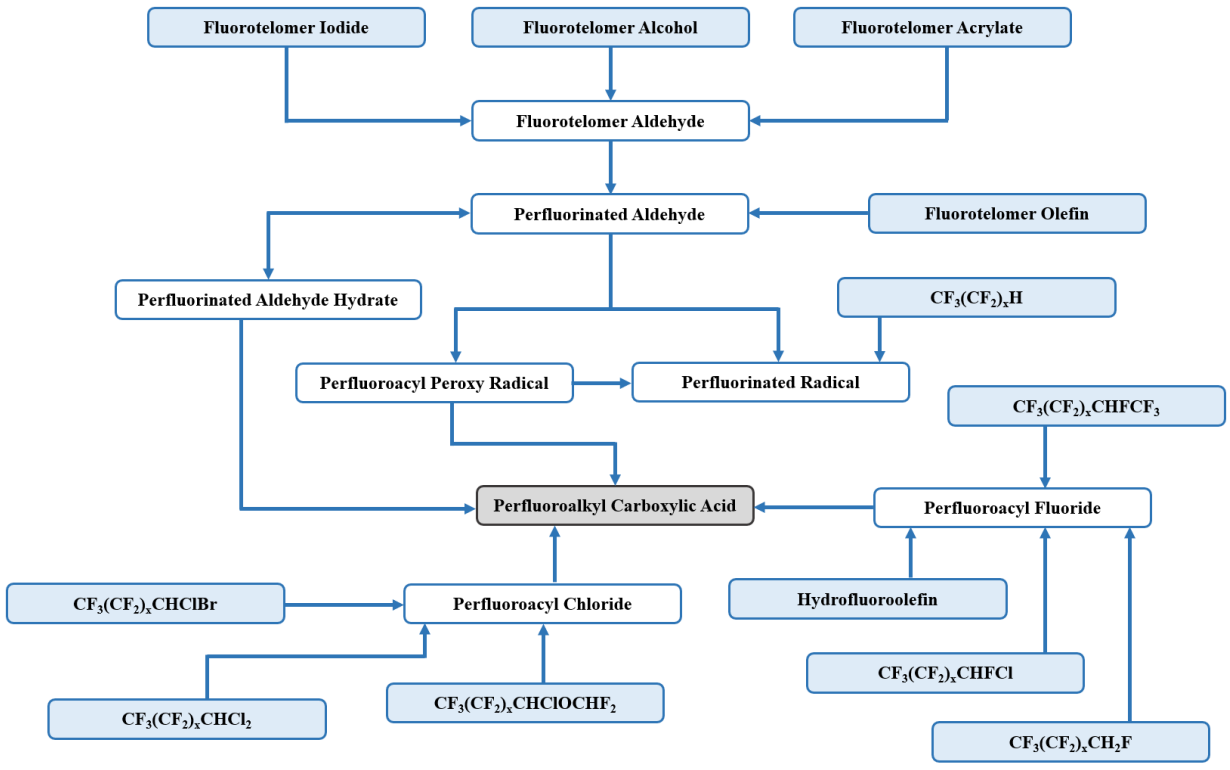

Figure 1-2. Transformation pathways of PFCA precursors, adapted from Young and Mabury.[64] Blue-shaded compounds are commercially produced.

1.3.1 Fluorotelomer Alcohols (FTOHs)

As previously mentioned, characteristic precursors of perfluorinated materials can be synthesized via telomerization of fluoroalkenes or electrochemical fluorination (Figure 1-3). In particular, FTOHs are synthesized by radical telomerization of fluoroalkenes such as

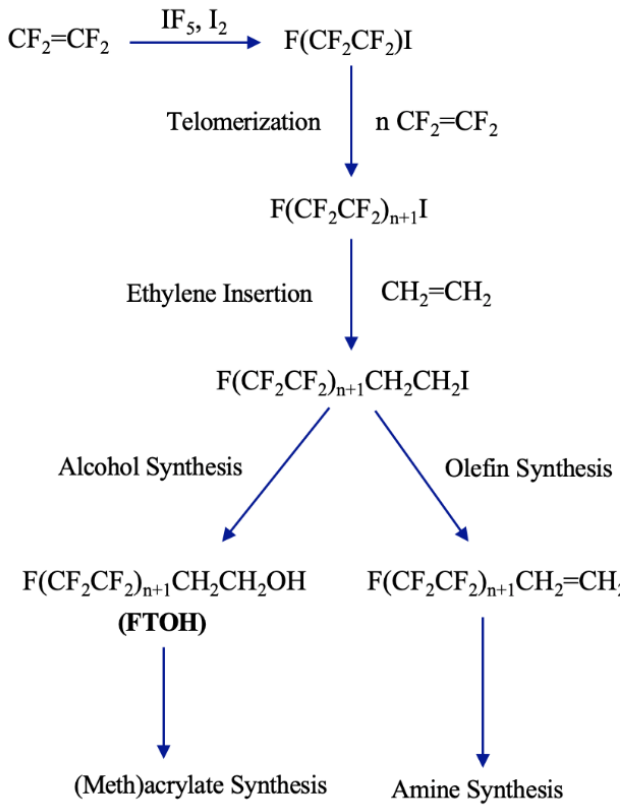

Figure 1-3. Pathway depicting the industrial synthesis of FTOHs utilizing the telomerization of tetrafluoroethylene with pentafluoroethyl iodide, adapted from Lehmler.[106]

tetrafluoroethylene, hexafluoropropene, trifluoroethylene, etc.[105] Telomerization is defined by the reaction of a telogen, such as pentafluoroethyl iodide, with one or more unsaturated molecules known as taxogens, such as the aforementioned tetrafluoroethylene.[106] The resulting linear, fluorotelomer compounds have a molecular formula of $CF_3(CF_2)_xCH_2CH_2OH$ and are named according to the number of fluorinated and hydrogenated carbons present within the structure. For example, the ratio of the FTOH to be discussed in Chapter 2, the 4:2 FTOH, describes the presence of four fluorinated carbon atoms and two hydrogenated carbon atoms. Widely used for industrial and commercial applications, FTOHs have been detected in a variety of products such as adhesives, polishes, paints, and electronic materials.[107] In some uses, such as for firefighting foams and stain-repellant coatings for paper, carpets, leather, and textiles, FTOHs are released directly

into the environment.[106] The global production of FTOHs was projected to be around 11 to 14 $\times 10^6$ kg year^{-1} prior to phase-outs[108,109] and is now estimated to be between 5 and 6.5 $\times$ 10^6 kg year^{-1}, with 40% of that production occurring in North America.[110] In addition, even after they are no longer produced, FTOHs are released through consumer product usage and their eventual disposal (e.g., landfills).[111-114] Previous studies have reported on the global distribution of gas-phase FTOHs in ambient air, with concentrations ranging from 51.4 to 1210 pg m^{-3} in Asia[115], 181 to 288 pg m^{-3} in Europe[116,117], and 11 to 165 pg m^{-3} in North America.[118] Moreover, this group of compounds have an estimated half-life in the atmosphere of ~20 days and are believed to live long enough to achieve sufficient widespread hemispheric distribution.[119] Thus, FTOHs have been deemed plausible sources of PFCAs in remote locations such as Northern Europe and the Arctic.[104,120]

1.3.2 Measuring FTOHs

1.3.2.1 Smog Chamber Studies

Over the past two decades, several studies have sought to provide insight into the oxidation mechanisms, products, and kinetics of FTOH atmospheric degradation. With high vapour pressures and low water solubilities, FTOHs are expected to be observed in the gas-phase following release into the environment.[119] While the rate constants for the reaction of OH radicals with primary alcohols are well-established, further investigation into their reactivity with FTOHs is needed to better understand the environmental fate of these PFCA precursors. Previously, smog chamber experiments utilizing offline Fourier transform infrared spectroscopy (FTIR) and fluorine-19 nuclear magnetic resonance spectroscopy (^{19}F-NMR) have been applied to study the degradation and reactivity of FTOHs. These smog chamber systems are controlled environmental

reaction chambers used to simulate atmospheric chemical processes under defined conditions of temperature, light, and oxidant concentrations.[121] They have been widely used to study secondary organic aerosol formation, reaction kinetics, atmospheric aging of primary pollutants, and near-ground O_3 formation.[122] However, these systems can be limited by wall losses[123] and by the influence of water vapour.[124] Offline analysis techniques such as liquid chromatography tandem mass spectrometry (LC-MS/MS) and gas chromatography mass spectrometry (GC-MS) have also been applied to the experimental and environmental analysis of PFAS.[108,118,125,126] Although chamber studies have provided foundational insight into FTOH oxidation pathways, there remains a critical need for experimental approaches that enable real-time, gas-phase detection of PFAS and their oxidation products.

1.3.2.2 Oxidation Flow Reactors (OFRs)

Oxidation flow reactors (OFRs) provide a complementary approach for investigating rapid oxidation chemistry under controlled conditions. Characteristically, OFRs have been widely used to study heterogeneous reactions of volatile organic compounds (VOCs) with gas-phase oxidants such as O_3 and OH radicals. These reactors utilize oxidants at considerably higher concentrations than what is present in the atmosphere to accelerate the ensuing oxidation chemistry.[127] Within minutes it is possible to attain exposures equivalent to multiple days or weeks of atmospheric oxidation. These higher-than-ambient concentrations can be generated via the photolysis of a chosen oxidant using low-pressure ultraviolet (UV) lamps. Consequently, this necessitates shorter sample residence times and reduced wall effects.[128,129] The photolysis of O_3 is commonly employed to generate OH radicals and represents a well-established approach for achieving controlled and quantifiable oxidation conditions in OFR studies[127,130-133], as utilized in this work

(Chapter 2). As a result of their increased use and popularity, OFRs have been applied in numerous studies to, for example, infer the transition between functionalization (i.e., oxygen addition) and fragmentation, the presence of gas-phase fragmentation reactions (i.e., carbon-carbon bond cleavage), and the subsequent impact of these processes on secondary organic aerosol formation yields.[134] Importantly, OFRs can be readily coupled to real-time gas-phase measurement techniques, such as proton-transfer-reaction time-of-flight mass spectrometry (PTR-ToF-MS) and iodide-adduct chemical ionization mass spectrometry (I-CIMS), allowing oxidation chemistry to be observed with high temporal resolution and under well-controlled conditions.

1.3.2.3 Real-time Gas-phase PFAS Detection

Chemical ionization mass spectrometry is an adaptable soft ionization technique for the detection of gaseous species with high sensitivity.[135] With appropriate selection of ion-molecule reaction chemistry, CIMS is capable of selectively detecting target compounds while largely preserving molecular information. Integrating selective ionization chemistry at atmospheric pressure with high-resolution MS has successfully addressed the needs for lower instrument detection limits[136], enabling direct online detection of trace concentrations of gas-phase species.[137] The utilization of CIMS has become increasingly important for the real-time detection of several atmospherically relevant inorganic and organic compounds[138] and, more recently, it has been applied for the real-time, online characterization of PFAS.[139-141] Specifically, Riedel et al. has demonstrated that the I-CIMS can detect the 4:2, 6:2, 8:2, and 10:2 FTOHs amongst other PFAS.[139] While I-CIMS has been demonstrated as an effective tool for detecting FTOHs and other PFAS, it has never been used in FTOH oxidation experiments. These experiments have typically been conducted in smog chambers using ^{19}F-NMR and FTIR techniques. Water acts as an interferent in

these methods[142,143], as well as in I-CIMS[144-148], so previous FTOH oxidation studies were performed under dry conditions and are thus not entirely reflective of ambient conditions. When coupled to OFRs, online techniques such as I-CIMS allow for oxidation chemistry to be observed with high temporal resolution, enabling direct measurement of precursor decay and product formation.

Proton transfer reaction time-of-flight mass spectrometry is a widely used form of CIMS for the real-time detection of trace concentration VOCs such as acetone, toluene, and methanol.[149] The principal ion chemistry within this method is the use of the hydronium ion (H_3O^+) as the primary reactant and is shown in EQ 1.

$$H_3O^+ + X \rightarrow X{\bullet}H^+ + H_2O \qquad \textbf{(EQ 1)}$$

Protonated water ions are produced in the ion source prior to being introduced into the drift reaction chamber. Within the drift chamber, H_3O^+ undergo collisions with sample gas molecules (X) and a proton is transferred – resulting in a protonated VOC ($X{\bullet}H^+$) and neutral water. Advantages of a PTR include: i) its selectivity for VOCs (only compounds with a proton affinity > neutral water, 165 kcal mol^{-1}, will be ionized), ii) the sample gas can be introduced directly (foregoing pre-treatment), and iii) individually controlled and spatially separated processes of generating H_3O^+ and ionizing VOCs ensures absolute quantification.[150] Coupled with the PTR ionization technique in this work is ToF-MS, an approach known for its high sensitivity with an almost unlimited mass range.[151] The modern availability of high-speed digitizers and computer interfacing highlights some of the benefits of utilizing ToF as a mass analyzer.[152] The PTR-ToF-MS utilized in Chapter 2 is that of the Ionicon Analytik PTR-ToF 8000 and the overall setup is comprised of four stages:

a PTR-ion source, a drift tube reaction chamber, a transfer lens system, and an orthogonal acceleration ToF-MS (Figure 1-4).

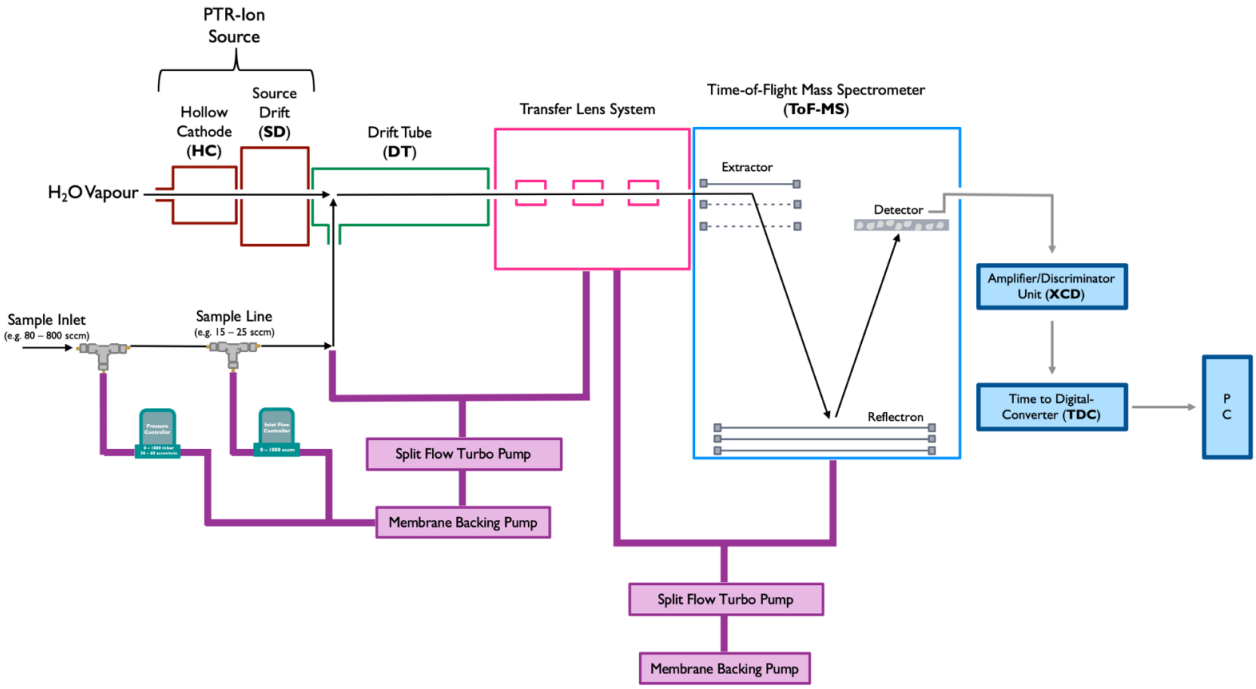

Figure 1-4. Simplified schematic of a Proton Transfer Reaction Time-of-Flight Mass Spectrometer (PTR-ToF-MS), adapted from Jordan et al.[153]

The PTR-ion source stage can be subdivided into two substages: a hollow cathode discharge and a source drift. Water vapour reacts with electrons in the hollow cathode and the resulting ions enter the source drift (along with the water vapour) to produce H_3O^+.[153] An electric field is applied to transport H_3O^+ into the drift tube where the proton transfer occurs. Here, a drift pressure is provided to ensure sufficient reactive collisions between the analyte and the proton donor ions. An electric field applied to this chamber continuously pulls the protonated analyte towards the next stage where, once in the transfer line system, they are guided to the final stage. Within the ToF-MS, ions are focused into a short source region under the influence of an electric

field. This field then accelerates the ions into a longer, field-free drift region where, ideally, all ions possess the same kinetic energy. However, their velocities – and thus their time of flight – differ based on their individual masses.[154] After passing through this region, ions are pulsed and extracted from the incoming ion beam and then directed downward toward the reflectron, which reverses their trajectory and refocuses them toward the detector plate.[155] To obtain timing information, pulsers are used to determine the time of ion extraction.[152] Weak signals are then amplified through the amplifier/discriminator unit prior to signals being digitized in the time-to-digital converter and output onto a computer. As a result, PTR-ToF-MS instruments have been further developed for the real-time measurements of VOCs in air – including oxygenated (aldehyde, ketone, alcohol), unsaturated (alkene, diene), and aromatic hydrocarbons.[156] While PTR-ToF-MS has traditionally been applied to non-halogenated VOCs, its ability to provide quantitative real-time measurements makes it a valuable complementary technique to other CIMS approaches used for PFAS detection. In this work (Chapter 2), we coupled an OFR with PTR-ToF-MS to make novel 4:2 FTOH measurements under humified conditions.[157]

1.4 Measuring Atmospheric PFAS Deposition

1.4.1 Protecting Canada's Endangered Whales: The Whales Initiative

With PFOS and PFOA, amongst other long-chain PFAAs, also appearing on CEPA's Toxic Substance List as banned chemicals, the 2018 Canadian federal budget provided funding for a five-year Whales Initiative with the purpose of protecting and supporting the recovery of endangered Canadian whale populations.[158] These efforts reflect broader international and national initiatives to regulate and reduce emissions of persistent organic pollutants (POPs), including PFAS, in order to protect vulnerable ecosystems and species.[159] This initiative focused on three key populations:

i) the St. Lawrence Estuary belugas (SLEBs), ii) the Southern Resident killer whales (SRKWs), and iii) the North Atlantic right whale. The primary objective of this project was to identify key sources of atmospheric contaminants impacting the abovementioned species, with the aim of implementing strategies to decrease contaminant inputs and minimize overall exposure. Contaminants within these habitats emerge from local, regional, and global sources (Figure 1-5). Local sources near the specified endangered whale habitats include direct discharges into waterbodies from a variety of point and non-point sources such as coastal landfills, harbours, and tributary inflows. Regional and global sources reach these habitats via long-range atmospheric transport mechanisms including ocean currents, the migration of contaminated prey, and airflows. Among these transport pathways, atmospheric deposition is a key mechanism linking contaminant emissions to remote marine ecosystems.

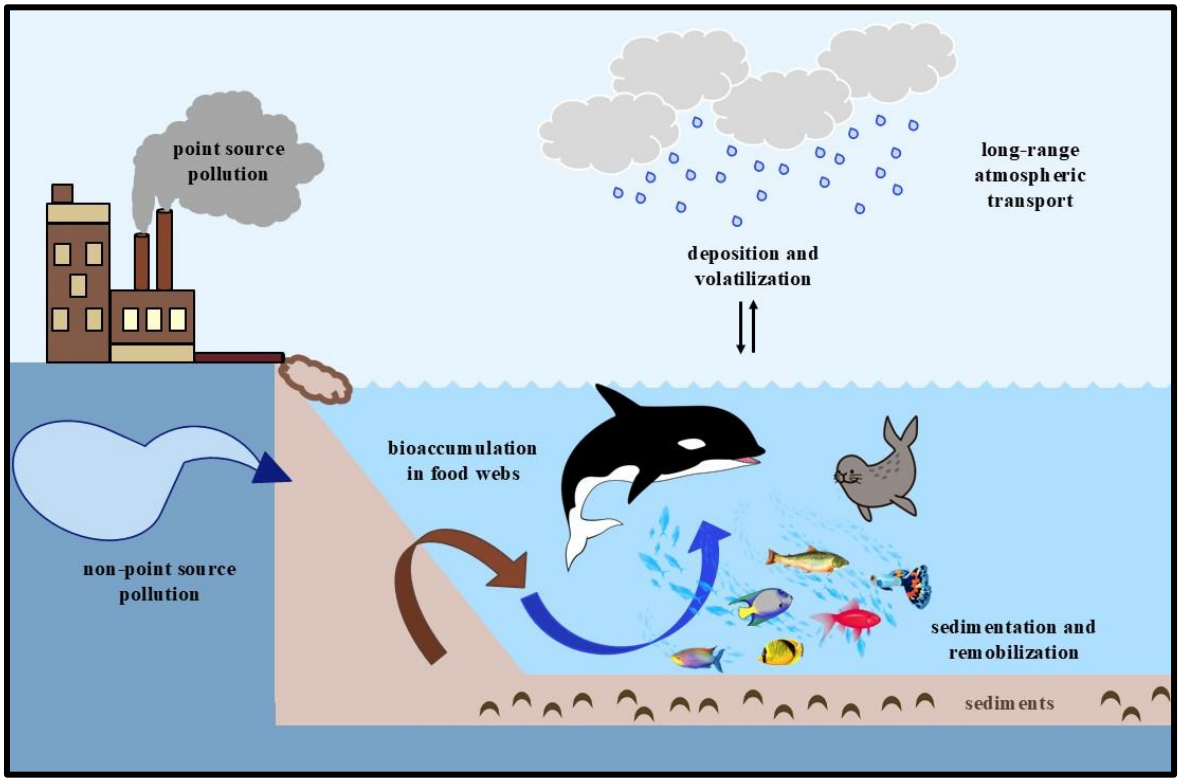

Figure 1-5. Depiction of pollutants entering the marine environment and affecting the habitat and health of the killer whale, adapted from Alava et al.[160]

Whales are model ecological indicators for the presence of POPs, like PFAS, within marine environments as they are particularly vulnerable to contaminant accumulation via dietary and environmental exposure.[161,162] A variety of POPs including PCBs, polybrominated diphenyl ethers (PBDEs), and some organochlorine pesticides have been previously quantified in SRKW and SLEB biopsy samples[163,164] as well as environmental samples taken in the regions home to the these whale populations.[165-168] Within the SLE (Québec, Canada), approximately 900 beluga whales (*Delphinapterus leucas*) are expected to reside[169]; however, a recent study utilizing high-resolution instrumentation estimates that the population falls between 1530 to 2190 belugas instead.[170] Listed in 2014 as an endangered species within Canada, the SLEBs decline in population – with no apparent recovery – has been linked to multiple possible stressors including underwater vessel noise[171-174], overfishing[175], modified trophodynamics[176], and exposure to POPs.[164,177]

Similarly in the northeastern Pacific Ocean, three ecotypes of killer whales (*Orcinus orca*) inhabit the area; however, for the purposes of this study, only the endangered SRKWs will be discussed. With only 73 remaining and facing a population extinction probability of 26%[178], the three main threats to these mammals are: acoustic and physical disturbance, environmental contaminants, and reduced prey availability.[179-182] Recent research on POP exposure in SRKW habitats detail effects on reproductive hormones and lipid-remobilization, pregnancy failure, etc.[183-185] and due to their larger amount of fat storage, killer whales are at higher risk of pollutant accumulation leading to adverse health effects and continuing population decline.[163,186,187] Specific to this research, long-chain PFAAs like PFOS have also been shown to bioaccumulate and biomagnify in aquatic food webs putting apex predators such as seals, polar bears, and whales at risk.[188,189] Recent studies have identified a suite of 54 PFAS within the livers of endangered

SLEBs[190] and within the skeletal muscle and liver of SRKWs.[191] These findings demonstrate the presence of PFAS in marine mammal tissues and highlight the importance of understanding environmental transport pathways that contribute to exposure.

1.4.2 Measuring Ambient PFAAs

Given the significance of atmospheric deposition as a pathway for PFAS to enter vulnerable marine environments, it is necessary to understand the techniques available for quantifying atmospheric PFAS. Currently, atmospheric measurements of ultrashort-PFCAs are limited. Most existing studies have focused on PFCAs with chain-lengths of C4 and above using either direct (i.e., gas- and particle-phase collection)[192,193] or indirect (i.e., deposition sampling) approaches.[194,195] Passive and active air sampling are two established methods for the direct measurement of the gas and particle phases. Passive air samplers collect airborne contaminants onto a sorbent material, in the absence of a pump, via diffusion. A medium of either polystyrene-divinylbenzene resins (i.e., XAD), polyethylene, or polyurethane foam (PUF) – placed in an open housing made of plastic, glass, or stainless steel – have been used for the collection of trace atmospheric acids.[196] Unlike passive air sampling, active air sampling can facilitate the simultaneous, yet separate, collection of the gas- and particle-phase. In this method, a pump actively draws air through the sampling media and the collected volume of air can then be accurately measured using a calibrated flow meter.[197]

By comparison, deposition samplers are classified as an indirect measurement technique for atmospheric pollutants and are further differentiated by the deposition in which they collect. Total “bulk” deposition samplers are used to collect a combined sample of both wet and dry deposition, with dry deposition referring to the direct settling of gaseous and particulate matter to

the Earth's surface.[10] Wet-only collectors, which use precipitation-triggered lids, are designed to isolate wet deposition – which encompasses gases and particles either as they are intercepted by falling precipitation below the cloud or scavenged and dissolved in cloud droplets (i.e., rain, snow, and hail).[11] With the atmosphere serving as a transport pathway for both natural and anthropogenic chemicals, much of the previous PFAS research has focused on their wet and dry deposition into soil, water, and organisms. Due to their potential for adverse effects on human and environmental health, their presence and movement in the air have also become an increasing concern.[197]

1.4.2.1 Deposition Samplers

Wet deposition is widely regarded as a major removal pathway for PFAAs from the atmosphere and a useful indicator of their atmospheric concentrations.[198-200] Levels of PFAAs in precipitation can influence, and be influenced by, contamination in soil[201], surface water[202], and groundwater.[203] These concentrations are shaped by several factors, including deposition frequency and intensity, the physicochemical properties of individual PFAS (e.g., chain length), and the proximity to emission sources.[204,205] Bulk samplers capture both wet and dry deposition, providing an overall measure of atmospheric inputs, whereas wet-only collectors isolate precipitation events to more directly quantify contaminants removed via precipitation. Despite their utility, truly selective wet deposition measurements are technically challenging. Many existing approaches rely on total deposition collection and modelling work to estimate the wet and dry fractions. For example, a recent study combined total deposition measurements and modelling to quantify and attribute TFA sources in Switzerland, assuming TFA behaves like nitric acid (HNO_3) – with nearly all TFA present in the liquid-phase and efficiently removed via precipitation.[30] Such simplified parametrizations strongly influence modelled wet deposition rates

and ultimately introduce uncertainty if they do not reflect real atmospheric behaviour. As a result, most previous wet-only datasets are not direct measurements, leaving reliable, high-resolution data on wet deposition limited.

Both wet-only[206,207] and total deposition sampling methods have been previously applied for POPs, including PCBs, PBDEs, and PAHs.[192,198,208] For example, PAHs have been commonly collected via glass funnel-bottle bulk collectors with sampling periods lasting from one week to one month. In rural areas, stainless steel buckets have also been used to collect bulk PAH deposition.[209,210] Although bulk deposition collection is a straightforward and cost-effective method, it is prone to contamination from non-atmospheric sources such as plant debris, insects, and bird droppings. This can lead to an overestimation of total deposition and an underestimation of wet deposition, as documented in several studies.[211-213] In contrast, a notable advantage of isolated wet deposition measurements is that they only require a precipitation collection container and the ability to time its deployment and retrieval to correspond with specific precipitation events. While total deposition captures overall atmospheric input and long-term accumulation trends, wet deposition is particularly valuable for assessing spatial and temporal variability.

Wet deposition sampling provides targeted insight into the atmospheric transfer of PFAS to environmental compartments and is essential for understanding spatial and temporal patterns in PFCA distribution and contamination. To date, only a few deposition studies have specifically reported measurements of TFA and PFPrA.[192,193,214] The limited availability of robust, selective wet deposition samplers motivates the development of new tools for atmospheric PFAS research. To address this limitation, a novel automated system for selective wet deposition sampling has been developed (Chapter 3).[215] This system enables event-based wet deposition sampling by opening only during conductive precipitation events. This limits exposure to dry atmospheric

deposition and reduces environmental contamination between sampling events, which are common sources of uncertainty in bulk deposition measurements. Rainwater conductivity arises primarily from dissolved ionic species present in precipitation, including sulfate, nitrate, ammonium, and chloride, which originate from both natural sources (e.g., marine aerosols and soil dust) and anthropogenic emissions (e.g., combustion and agricultural activities).[216] As a result, conductivity, as a proxy for total dissolved ionic content, is used to detect precipitation events and initiate automated sample collection. By addressing key limitations of existing deposition sampling approaches, this automated system provides a more reliable framework for quantifying wet deposition of PFAS and improving constraints on atmospheric transport and deposition pathways to sensitive aquatic environments.

1.4.2.2 Active Air Sampling

While deposition measurements provide important insights into contaminant removal from the atmosphere, air sampling is a complementary technique. These measurements enable the simultaneous, phase-specific collection of gas- and particle-bound species, offering higher temporal resolution and additional information on atmospheric transport processes. Within the literature, passive air sampling has proven effective for spatial mapping of hydrophobic chemicals in the atmosphere[217], including PFCAs, and offers practical advantages as it does not require electricity or costly sampling materials – making it well-suited for remote or resource-limited sampling locations. Although active air sampling requires access to power, an advantage of this method, in relation to passive air sampling, is its ability to sample large volumes of air in shorter periods of time; thus, resulting in higher resolution temporal data and better detection limits.[197] In focusing solely on active air sampling, this technique has previously utilized a wide range of

sorbents and filters, including PUF, XAD-2, PUF/XAD combinations, quartz fiber filters (QFFs), glass fiber filters (GFFs), etc., to collect a variety of compounds with differing physiochemical properties (i.e., polarity and volatility).[218] However, observed positive sampling artifacts have been reported when applying this technique.[219] The presence of these positive "blow-on" sampling artifacts result in an overestimation of the particle-phase concentration, as, for example, PFCAs can adsorb to particulate matter already collected on the filter or to the QFFs or GFFs themselves.[111,204]

Active air samplers have also been observed to experience negative "blow-off" sampling artifacts where particle-phase concentrations are underestimated due to the volatilization of chemicals adsorbed onto particulate matter following collection on filters.[219] To avoid these sampling artifacts – which can occur simultaneously, the annular (diffusion) denuder was developed where the gas-phase is collected first followed by the particle-phase.[220] Applied in conjunction with high- or medium-volume active air samplers, the multi-channel annular denuder design is composed of two inner concentric glass tubes situated around a solid center glass rod.[221] These glass surfaces are etched to provide greater surface area for the application of a coating solution to remove gaseous target analytes. Following the removal of these analytes from the gas-phase via diffusion chemistry, particulate analytes can then be separately collected on a filter housed downwind of the denuder.[111.204]

1.4.2.2.1 Annular Denuder System

Building on active air sampling, the annular denuder system (ADS) provides a means to minimize artifacts and collect phase-specific pollutants.[221] As described by the U.S. EPA, this research utilized a method analogous to those used for other strong atmospheric acids (e.g.,

gaseous HNO_3) and involves the use of an ADS.[221] According to the U.S. EPA Compendium Method IO-4.2, this system includes: (i) an inlet with a cyclone, (ii) annular denuders, and (iii) filter packs.[221] A medium volume sampler (MVS) – our inlet with a cyclone – actively collects both fine ($PM_{2.5}$, ≤2.5 μm) and coarse (PM_{10}, between 2.5 μm and 10 μm) mode particulate matter on sampling filters. Fine mode particles are of particular interest as they can make their way deep into the respiratory tract. Studies find that exposure to $PM_{2.5}$ can cause short-term health effects such as eye, throat, and lung irritation whereas long-term exposure may be linked to more severe symptoms of respiratory tract diseases, weakened lung function, and increased morbidity and mortality of cardiopulmonary diseases.[222] In an annular denuder, an alkaline coating solution is applied to remove acidic gaseous pollutants via diffusion chemistry. Building on the method development described in Chapter 3, Chapter 4 applies the PFPrA validated denuders – alongside the automated deposition samplers – to quantify ultrashort- and short-chain PFCAs within the regions home to SLEBs and SRKWs. Gas-phase PFCAs were collected using a MVS containing sodium carbonate-coated annular denuders while particulate PFAAs were collected on QFFs but will not be discussed in this work.

Briefly, using a pump, a MVS draws in ambient air where a sampling cyclone fractionates the airborne particles to the specified cut-off diameter of the cyclone. For example, the $PM_{2.5}$ sampling inlet includes a cyclone which is used to filter larger particles from ambient air by the specified 2.5 μm cut-off diameter. The tangential inlet generates a swirling motion which forces particles larger than this cut-off diameter towards the outer wall. The vacuum pump pulls the flowing spiral downwards and these particles are collected in a dustbin at the bottom of the sampler. Responsible for this particle separation is the natural phenomenon of Brownian motion – the random motion of particles suspended in a gas (or liquid) resulting from their collision with

fast moving molecules in a gas (or liquid).[223] As a result, particles larger than 2.5 μm have a high inertia and remain in the dustbin whilst the smaller particles entrained within the filtered airflow are redirected and travel upwards towards a centrally located exit. Swirl and turbulence are the two competing phenomena in the separation process. The swirling motion produces a centrifugal force on all suspended matter and the specific terminal velocity for the larger particles is the driving force behind the separation. Turbulence disperses the solid particles and increases the likelihood that particles get caught in the exit stream.[224] Following the passing of ambient air through the cyclone, the filtered airstream passes next through a coated annular denuder. The air containing the desired particle fraction then passes through a filter where the particles are collected and made available for offline analysis. The use of an ADS minimizes sampling artifacts, increasing confidence in phase-specific measurements and providing more reliable data for interpreting atmospheric loading and deposition pathways relevant to environmental exposure within the endangered whale habitats.

1.5 Analytical Methods for Quantifying PFAAs

Over the past few decades, a variety of chromatographic techniques have been developed utilizing GC and LC. Gas chromatography mass spectrometry systems are often applied to simultaneously perform the separation and detection of neutral, semi-volatile, and volatile PFAS in matrices such as air. While this instrumentation is commonly used due to its widespread availability, PFAAs, for example, are non-volatile and must therefore be derivatized. There are many different derivatization methods used when analyzing PFCAs, including pentafluorophenyl diazoethane[225,226], 2,4-difluoroaniline[195,227], benzyl bromide[228], and dimethyl sulfate.[229-231] However, derivatization methods can be expensive, time-consuming, and can often require

extensive sample preparation and the use of hazardous chemicals.[232] Liquid chromatography has become a popular choice for the analysis of PFAAs due to its ability to detect said compounds in a variety of matrices such as blood[233], animal tissue[234], river water[235], drinking water[236], and ice cores.[104] In particular, liquid chromatography electrospray ionization tandem mass spectrometry (LC-ESI-MS/MS) has been applied to PFAS research since PFCAs are water soluble, have surfactant properties, and are susceptible to ESI.[237] However, LC systems are expensive and contain Teflon parts which act as a source of contamination within the analysis.[119] It is also difficult to retain ultrashort- and short-chain PFCAs on reversed-phase columns due to their higher water-solubility and polarity compared to long-chain PFAAs.[238] This method has also been shown to present challenges in the form of ion suppression during the analysis of trace PFAAs and fluorotelomer-based precursors.[239,240] Ion chromatography (IC) has previously been used for the separation and analysis of ultrashort-chain PFCAs such as TFA.[241] More recently, IC has been coupled with MS (IC-MS) to analyze haloacetic acids[242,243] and ultrashort- and short-chain PFCAs.[244] Given that PFAS are typically ionic under most environmental conditions and pHs[245], IC-MS presents a promising approach for PFCA analysis and offers high selectivity and sensitivity.[244,246,247]

1.5.1 Ion Chromatography Mass Spectrometry (IC-MS)

Ion chromatography is a separation technique that utilizes electrostatic interactions between ions and an oppositely charged stationary phase.[248] The separation process involves loading a liquid sample containing ions onto a column packed with ion-exchange resin – anion exchange resins for negatively charged ions and cation exchange resins for positively charged ions. This allows for ions with opposite charges to bind to the separation (analytical) column, with ions

that are uncharged or are weakly bound to the resin eluting first while those that are strongly bound are eluted by altering the mobile phase (e.g., by increasing solvent concentration). Characteristically, a pump is used to force an aqueous solution (eluent) through the system at a fixed rate (mL min^{-1}). In the load position of a six-port valve, a sample loop becomes filled with the analytical sample and held there until injection. Simultaneously, the eluent is pumped through the rest of the system and bypasses the sample loop.[249] In the inject position, a valve is turned so that the eluent passes the sample from within the sample loop into the analytical column. For the work discussed in Chapter 4, the sample containing eluent passes first through a guard column and then into the separation column. The eluent/analyte mixture then makes its way through a suppressor which enhances the conductivity of the sample ions and reduces that of the eluent; thus, increasing analyte detection sensitivity. The suppressor contains three channels: a central eluent channel and two side channels containing electrodes. Briefly, a direct current voltage is applied across the electrodes and water is electrolytically split to form electrolysis ions which are used for suppression reactions as shown in EQs 2 and 3.[250]

$$\text{At the anode: } H_2O \rightarrow 2H^+ + 1/2O_2 + 2e^- \quad \textbf{(EQ 2)}$$

$$\text{At the cathode: } H_2O + 2e^- \rightarrow 2OH^- + H_2 \quad \textbf{(EQ 3)}$$

From the suppressor, the eluent/analyte mixture flows into a conductivity cell for detection. Inside the detector, the eluent/analyte mixture passes through a cell equipped with electrodes – where an alternating current is applied. The resulting rise in current corresponds to an increase in conductivity, which is directly proportional to the ion concentration.[250] Once the target ions are eluted, a change in electric current is detected as a constant voltage is maintained across the electrodes. The separated ions are then directed towards a mass spectrometer and undergo a soft

ionization technique – ESI. Once in the ion source of the MS, this technique applies a high voltage to the liquid sample to produce gas-phase ions.[251] These ions are then introduced into a mass analyzer; for example, a single quadrupole mass analyzer consists of four parallel rods in which a combination of radio frequency and direct current voltages are applied.[252] Only ions with a specific mass-to-charge ratio will follow a stable trajectory through the quadrupole and reach the detector, while those with unstable paths collide with the rods and do not reach the detector.[252] To analyze the collected field samples described later in this work, an IC-MS system composed of a Thermo Scientific™ Dionex™ ICS-6000 (outfitted with dual pump and dual column and detector compartments) and a single quadrupole ISQ™ EC MS analyzer was used. Method parameters are described in Chapter 4. Overall, IC has become an indispensable tool in modern analytical work, allowing complex anionic and cationic mixtures to be separated and quantitatively measured in relatively short periods of time[249], making it particularly well-suited for studies of environmentally relevant compounds such as PFAS.

1.6 Goals and Objectives

Atmospheric PFAS research remains limited by significant knowledge gaps in the understanding of i) the chemical transformation pathways of PFAS precursors under atmospherically relevant conditions, ii) the lack of robust, event-based wet deposition measurements that can reliably distinguish atmospheric input from background contamination, and iii) the lack of high-resolution measurements of ultrashort- and short-chain PFCAs in remote and ecologically sensitive environments. These limitations constrain our ability to accurately quantify atmospheric sources, transport pathways, and deposition fluxes of PFAS, particularly for compounds that are highly mobile, persistent, and environmentally relevant. Building on these

gaps, this research applies a suite of novel laboratory and field-based approaches to investigate the sources, atmospheric behaviour, and environmental fate of PFAS. By combining mechanistic insights, method development, and field measurements, this work advances our current understanding of atmospheric PFAS transformation and provides innovative techniques for their measurement in various environments. The overarching goal of this dissertation – studying the sources, atmospheric behaviour, and environmental fate of PFAS – is achieved through a series of objectives, each emphasizing the development and application of a novel method: (A) employing OFR coupled to PTR-ToF-MS to study the degradation of a known PFAS precursor; (B) validating the design of a custom-built automated array of precipitation samplers that can be operated both on- and off-grid for wet deposition collection; and (C) quantifying ultrashort- and short-chain PFCAs in regions home to endangered Canadian whale populations. These objectives will be accomplished through individual works discussed in Chapter 2 (Objective A), Chapter 3 (Objective B), and Chapter 4 (Objective C).

Chapter 2 details laboratory experiments (ECCC; Toronto, ON, Canada) focusing on the oxidation of a known PFAS precursor – the 4:2 FTOH. Here, a new approach to studying PFAS is applied by coupling an OFR to PTR-ToF-MS for real-time measurement of gas-phase PFAS and identification of resulting degradation products under varying relative humidities, thereby providing insights into precursor oxidation kinetics. Chapter 3 describes an open-source, modular, and affordable instrument that can selectively collect wet deposition samples. We demonstrated that these platforms are capable of continuous operation off-grid, with a solar top-up of battery packs, for monthly collections performed across the Newfoundland and Labrador Boreal Ecosystem Latitudinal Transect during snow-free conditions from 2014 through 2016. The proof-of-concept systems were validated with basic measurements of rainwater chemistry including pH,

conductivity, and dissolved organic carbon. Chapter 4 describes the field deployment of a validated active air sampling (denuder) method alongside wet and total deposition samplers to quantify ultrashort- and short-chain PFCAs. Measurements were made at rural and remote field sites within the habitats of the SLEBs (Tadoussac, Québec) and SRKWs (Saturna Island, British Columbia), respectively. An inter-method comparison was also performed to compare the active air sampling findings with those of concurrently collected passive air samples. Together, these objectives provide a comprehensive approach to characterizing the sources, chemical transformation, and deposition of PFAS to the environment, offering reliable measurements to support future atmospheric modelling, monitoring efforts, and conservation-focused research.

1.7 References

1. Sharan, M.; Yadav, A. K.; Singh, M. P.; Agarwal, P; Nigam, S. A mathematical model for the dispersion of air pollutants in low wind conditions. *Atmos. Environ*. **1996**, *30(8)*, 1209–20.

2. Seinfeld, J. H.; Pandis, S. N. Atmospheric chemistry and physics: from air pollution to climate change. John Wiley & Sons, **2016**.

3. Ge, B.; Wang, Z.; Lin, W.; Xu, X.; Li, J.; Ji, D.; Ma, Z. Air pollution over the North China Plain and its implication of regional transport: A new sight from the observed evidences. *Environ. Pollut.* **2018**, *234*, 29–38.

4. Shen, L.; Zhao, T.; Liu, J.; Wang, H.; Bai, Y.; Kong, S.; Shu, Z. Regional transport patterns for heavy PM2.5 pollution driven by strong cold airflows in Twain-Hu Basin, Central China. *Atmos. Environ*. **2022**. *269*, 118847.

5. National Oceanic and Atmospheric Administration. Layers of the Atmosphere, **2024**. Retrieved from https://www.noaa.gov/jetstream/atmosphere/layers-of-atmosphere.

6. Hanrahan, G. Key concepts in environmental chemistry. *Academic Press*, **2012**.

7. Donnell, E. A.; Fish, D. J.; Dicks, E. M.; Thorpe, A. J. Mechanisms for pollutant transport between the boundary layer and the free troposphere. *J. Geophys. Res. Atmos.* **2001**, *106*(D8), 7847–7856.

8. Kiyani, V.; Esmaili, A.; Alijani, F.; Samani, S.; Vasić, L. Investigation of drainage structures in the karst aquifer system through turbidity anomaly, hydrological, geochemical and stable isotope analysis (Kiyan springs, western Iran). *Environ. Earth Sci.* **2022**, *81*(22), 517.

9. United States Environmental Protection Agency. Community Multiscale Air Quality Modeling System (CMAQ). **2016**. Retrieved from: www.epa.gov/cmaq/chemical-process-overview.

10. Lovett, G.M.; Kinsman, J.D. Atmospheric pollutant deposition to high-elevation ecosystems. *Atmos. Environ. Part A. General Topics*. **1990**, *24*(11), 2767–2786.

11. Pekey, B.; Karakaş, D.; Ayberk, S. Atmospheric deposition of polycyclic aromatic hydrocarbons to Izmit Bay, Turkey. *Chemosphere*. **2007**, *67*(3), 537–547.

12. Manavi, S. E.; Aktypis, A.; Siouti, E.; Skyllakou, K.; Myriokefalitakis, S.; Kanakidou, M.; Pandis, S. N. Atmospheric aerosol spatial variability: Impacts on air quality and climate change. *One Earth*, **2025.** *8*(3).

13. Seinfeld, J. H. Tropospheric chemistry and composition–Aerosols/Particles. *Encyclopedia of Atmospheric Sciences*. **2003**, *54*, 2349–2354

14. Trinh, M. M.; Chang, M. B. Review on occurrence and behavior of PCDD/Fs and dl-PCBs in atmosphere of East Asia. *Atmos Environ*. **2018**, *180*, 23–36.

15. Geddes, J.A.; Murphy, J.G. The science of smog: a chemical understanding of ground level ozone and fine particulate matter. In *Metropolitan Sustainability*, Woodhead Publishing, **2012**, 205–230.

16. Duce, R. A.; Galloway, J. N.; Liss, P. S. The impacts of atmospheric deposition to the ocean on marine ecosystems and climate. *World Meteorological Organization (WMO) Bulletin*, **2009**, *58*(1), 61.

17. Knote, C.; Hodzic, A.; Jimenez, J. L. The effect of dry and wet deposition of condensable vapors on secondary organic aerosols concentrations over the continental US. *Atmos. Chem.Phys.* **2015**, *15*(1), 1–18.

18. Staikova, M.; Wania, F.; Donaldson, D. J. Molecular polarizability as a single-parameter predictor of vapour pressures and octanol–air partitioning coefficients of non-polar compounds: a priori approach and results. *Atmos. Environ.* **2004**, *38*(2), 213–225.

19. Buck, R. C.; Franklin, J.; Berger, U.; Conder, J. M.; Cousins, I. T.; De Voogt, P.; Jensen, A. A.; Kannan, K.; Mabury, S. A.; van Leeuwen, S. P. Perfluoroalkyl and polyfluoroalkyl substances in the environment: terminology, classification, and origins. *Integr. Environ. Assess. Manag.* **2011**, *7*(4), 513–541.

20. Faust, J. A. PFAS on atmospheric aerosol particles: a review. *Environ. Sci.: Process. Impacts.* **2023**, *25*(2), 133–150.

21. Organization for Economic Cooperation and Development. Toward a New Comprehensive Global Database of Per and Polyfluoroalkyl Substances (PFASs): Summary Report on Updating the OECD 2007 List of per- and Polyfluorinated Substances (PFASs). *OECD Report*, **2018**, ENV/JM/MONO20187, 24.

22. Schymanski, E. L.; Zhang, J.; Thiessen, P. A.; Chirsir, P.; Kondic, T.; Bolton, E. E. Per-and polyfluoroalkyl substances (PFAS) in PubChem: 7 million and growing. *Environ. Sci. Technol.* **2023**, *57*(44), 16918–16928.

23. Banks, R. E.; Tatlow, J. C. Organofluorine chemistry: nomenclature and historical landmarks. In *Organofluorine chemistry: principles and commercial applications*, Boston, MA: Springer US, **1994**, 1–24.

24. Yamashita, N.; Kannan, K.; Taniyasu, S.; Horii, Y.; Petrick, G.; Gamo, T. A global survey of perfluorinated acids in oceans. *Mar. Pollut. Bull.* **2005**, *51*(8-12), 658–668.

25. Sunderland, E. M.; Hu, X. C.; Dassuncao, C.; Tokranov, A. K.; Wagner, C. C.; Allen, J. G. A review of the pathways of human exposure to poly-and perfluoroalkyl substances (PFASs) and present understanding of health effects. *J. Expo. Sci. Environ. Epidemiol.* **2019**, *29*(2), 131–147.

26. De Silva, A. O.; Armitage, J. M.; Bruton, T. A.; Dassuncao, C.; Heiger-Bernays, W.; Hu, X. C.; Kärrman, A.; Kelly, B.; Ng, C.; Robuck, A.; Sun, M. PFAS exposure pathways for humans and wildlife: a synthesis of current knowledge and key gaps in understanding. *Environ. Toxicol. Chem.* **2021**, *40*(3), 631–657.

27. Kurwadkar, S.; Dane, J.; Kanel, S. R.; Nadagouda, M. N.; Cawdrey, R. W.; Ambade, B.; Struckhoff, G. C.; Wilkin, R.; Per-and polyfluoroalkyl substances in water and wastewater: A critical review of their global occurrence and distribution. *Sci. Total Environ.* **2022**, *809*, 151003.

28. Salvatore, D.; Mok, K.; Garrett, K. K.; Poudrier, G.; Brown, P.; Birnbaum, L. S.; Goldenman, G.; Miller, M. F.; Patton, S.; Poehlein, M; Varshavsky, J. Presumptive contamination: a new approach to PFAS contamination based on likely sources. *Environ. Sci. Technol. Lett.* **2022**, *9*(11), 983–990.

29. Li, X., Wang, Y., Cui, J., Shi, Y. and Cai, Y., 2024. Occurrence and fate of per-and polyfluoroalkyl substances (PFAS) in atmosphere: size-dependent gas-particle partitioning, precipitation scavenging, and amplification. *Environ. Sci. Technol.* **2024**, *58*(21), 9283–9291.

30. Henne, S.; Storck, F. R.; Wöhrnschimmel, H.; Leuenberger, M.; Vollmer, M. K.; Reimann, S. Trifluoroacetate (TFA) in precipitation and surface waters in Switzerland: trends, source attribution, and budget. *Atmos. Chem. Phys.* **2025**, *25*(23), 18157–18186.

31. United Nations Environment Programme. Decision SC-4/17: Listing of Perfluorooctane Sulfonic Acid, its Salts and Perfluorooctane Sulfonyl Fluoride. UNEP-POPS-COP.4-SC-4-17. *Conference of the Parties to the Stockholm Convention on Persistent Organic Pollutants*, Geneva, Switzerland. **2009**. Retrieved from: http://chm.pops.int/TheConvention/ConferenceoftheParties/ReportsandDecisions/tabid/208/Default.aspx.

32. United Nations Environment Programme. Decision SC-9/12: Listing of Perfluorooctanoic Acid (PFOA), its Salts and PFOA-Related Compounds. UNEP-POPS-COP.9-SC-9-12. *Conference of the Parties to the Stockholm Convention on Persistent Organic Pollutants*, Geneva, Switzerland. **2019**. Retrieved from: http://chm.pops.int/TheConvention/ConferenceoftheParties/Meetings/COP9/tabid/7521/ItemId/7235/Default.aspx.

33. Weber, R.; Girones, L. PFAS and Planetary Boundaries: Global Challenges for Waste Management and Policy Solutions. *Environ. Sci. Technol*. **2026**, *60*(5), 3707–3715.

34. Environment and Climate Change Canada & Health Canada. Risk management approach for per- and polyfluoroalkyl substances (PFAS), excluding fluoropolymers. **2025**. Retrieved from: https://www.canada.ca/en/environment-climate-change/services/evaluating-existing-substances/risk-management-approach-per-polyfluoroalkyl-substances.html

35. Kissa, E. Fluorinated Surfactants: Synthesis, Properties, Applications. Surfactant Science Series 50, 1st ed.; Marcel Dekker, **1994**.

36. Key, B. D.; Howell, R. D.; Criddle, C. S. Fluorinated organic in the biosphere. *Environ. Sci. Technol.* **1997**, *31*, 2445–2454.

37. Ding, G.; Peijnenburg, W. J. Physicochemical properties and aquatic toxicity of poly-and perfluorinated compounds. *Critical reviews in Environ. Sci. Technol.* **2013**, *43*(6), 598–678.

38. Dunitz, J. D.; Taylor, R. Organic Fluorine Hardly Ever Accepts Hydrogen Bonds. *Chen. Eur. J.* **1997**, *3*(1), 89–98.

39. Giesy, J. P.; Mabury, S. A.; Martin, J. W.; Kannan, K.; Jones, P. D.; Newsted, J. L.; Coady, K. Perfluorinated compounds in the Great Lakes. In *Persistent organic pollutants in the Great Lakes*, Berlin, Heidelberg: Springer Berlin Heidelberg, **2006**, 391–438.

40. Panieri, E.; Baralic, K.; Djukic-Cosic, D.; Buha Djordjevic, A; Saso, L. PFAS molecules: a major concern for the human health and the environment. *Toxics*, **2022**, *10*(2), 44.

41. Tshangana, C. S.; Nhlengethwa, S. T.; Glass, S.; Denison, S.; Kuvarega, A. T.; Nkambule, T. T. I.; Mamba, B. B.; Alvarez, P. J.; Muleja, A. A. Technology status to treat PFAS-contaminated water and limiting factors for their effective full-scale application. *npj Clean Water*, **2025**, *8*(1), 41.

42. Kissa, E. Fluorinated surfactants and repellants (2nd ed.). New York: Marcel Decker, **2001**.

43. Schultz, M.; Barofsky, D.; Field, J. Fluorinated alkyl surfactants. *Environ. Eng. Sci.* **2003**, *20*, 487–501.

44. Schulz, K.; Silva, M. R.; Klaper, R. Distribution and effects of branched versus linear isomers of PFOA, PFOS, and PFHxS: A review of recent literature. *Sci. Total Environ.* **2020**, *733*, 139186.

45. Mu, H.; Wang, J.; Chen, L.; Hu, H.; Wang, J.; Gu, C.; Ren, H; Wu, B. Identification and characterization of diverse isomers of per-and polyfluoroalkyl substances in Chinese municipal wastewater. *Water Res.* **2023**, *230*, 119580.

46. United States Environmental Protection Agency. Multi-industry Per- and Polyfluoroalkyl Substances (PFAS) Study - 2021 Preliminary Report, **2021**. Retrieved from https://www.epa.gov/system/files/documents/2021-09/multi-industry-pfas-study_preliminary-2021-report_508_2021.09.08.pdf

47. Jansen, A.; Lyche, J. L.; Polder, A.; Aaseth, J.; Skaug, M. A. Increased blood levels of persistent organic pollutants (POP) in obese individuals after weight loss - A review. *J. Toxicol. Environ. Health B Crit. Rev*. **2017**, *20*(1), 22–37.

48. Prabhu, R. N.; Lakshmipraba, J.; Persistent Organic Pollutants (Part II): The New POPs–Sources and Adverse Effects. In *Organic Pollutants: Toxicity and Solutions*, Cham: Springer International Publishing, **2021**, 29–57.

49. Gebbink, W. A.; Letcher, R. J. Linear and branched perfluorooctane sulfonate isomer patterns in herring gull eggs from colonial sites across the Laurentian Great Lakes. *Environ. Sci. Technol.* **2010**, *44*(10), 3739–3745.

50. Wilkens D, Alexander Y. Kinetic Chemicals, assignee. Preparation of fluorine compounds. Patent US 2,005,710. **1935**.

51. Banks, R. E.; Tatlow, J. C. Synthesis of C-F bonds: the pioneering years, 1835–1940. *J. Fluor. Chem.* **1986**, *33*(1–4), 71–108.

52. Renner, R. Growing concern over perfluorinated chemicals. *Environ. Sci. Technol.* **2001**, *35*(7), 154A–60A.

53. Glüge, J.; Scheringer, M.; Cousins, I. T.; DeWitt, J.C.; Goldenman, G.; Herzke, D.; Lohmann, R.; Ng, C. A.; Trier, X.; Wang, Z. An overview of the uses of per-and polyfluoroalkyl substances (PFAS). *Environ. Sci.: Process. Impacts.* **2020**. *22*(12), 2345–2373.

54. Gaines, L. G. Historical and current usage of per-and polyfluoroalkyl substances (PFAS): A literature review. *Am. J. Ind. Med.* **2023**, *66*(5), 353–378.

55. Busch, J.; Ahrens, L.; Sturm, R.; Ebinghaus, R. Polyfluoroalkyl compounds in landfill leachates. *Environ. Pollut.* **2010**, 158, 1467–1471.

56. Benskin, J. P.; M. G. Ikonomou, M. B. Woudneh, and J. R. Cosgrove. Rapid characteriza tion of perfluoroalkyl carboxylate, sulfonate, and sulfonamide isomers by high-performance liquid chromatography-tandem mass spectrometry. *J. Chromatogr. A.* **2012**, *1247*, 165–170.

57. Ahrens, L.; Felizeter, S.; Sturm, R.; Xie, Z.; Ebinghaus, R. Polyfluorinated compounds in effluents of wastewater treatment plants and surface water along the River Elbe, Germany. *Mar. Pollut. Bull.* **2009**, *58*, 1326–1333.

58. Houtz, E. F.; Sutton, R.; Park, J. S.; Sedlak, M. Poly- and perfluoroalkyl substances in wastewater: Significance of unknown precursors, manufacturing shifts, and likely AFFF impacts. *Water Res.* **2016**, *95*, 142–149.

59. Hu, X. C.; Andrews, D. Q.; Lindstrom, A. B.; Bruton, T. A.; Schaider, L. A.; Grandjean, P.; Lohmann, R.; Carignan, C. C.; Blum, A.; Balan, S. A.; Higgins, C. P. Detection of poly- and perfluoroalkyl substances (PFASs) in US drinking water linked to industrial sites, military fire training areas, and wastewater treatment plants. *Environ. Sci. Tech. Lett.* **2016**, *3*(10), 344–350.

60. Shoeib, M.; Harner, T.; Vlahos, P. Perfluorinated Chemicals in the Arctic Atmosphere. *Environ. Sci. Technol.* **2006**, *40*(24), 7577−7583.

61. Wang, Z.; Xie, Z.; Mi, W.; Möller, A.; Wolschke, H.; Ebinghaus, R. Neutral Poly/Per-Fluoroalkyl Substances in Air from the Atlantic to the Southern Ocean and in Antarctic Snow. *Environ. Sci. Technol*. **2015**, *49*(13), 7770−7775.

62. Kim, S. K.; Kannan, K. Perfluorinated acids in air, rain, snow, surface runoff, and lakes: relative importance of pathways to contamination of urban lakes. *Environ. Sci. Technol*. **2007**, *41*(24), 8328−8334.

63. Tokranov, A. K.; Hopkins, Z. R.; Lindsey, B. D.; Jurgens, B. C. PFAS Are Widespread, Not Ubiquitous: Clarifying Misconceptions About the Prevalence of "Forever Chemicals". *Environ. Sci. Technol*. **2025**, 59(24), 11947–11949.

64. Young, C. J.; Mabury, S.A. *Atmospheric Perfluorinated Acid Precursors: Chemistry, Occurrence, and Impacts*. Edited by N. Whitacre, D. M. Springer New York, New York, **2010**. doi: 10.1007/978-1-4419-6880-7.

65. D'eon, J. C.; Hurley, M. D.; Wallington, T. J; Mabury, S. A. Atmospheric chemistry of N-methyl perfluorobutane sulfonamidoethanol, C4F9SO2N (CH3) CH2CH2OH: kinetics and mechanism of reaction with OH. *Environ. Sci. Tech.* **2006**, *40*(6), pp.1862–1868.

66. Martin, J. W.; Ellis, D. A.; Mabury, S. A.; Hurley, M. D; Wallington, T. J. Atmospheric chemistry of perfluoroalkanesulfonamides: kinetic and product studies of the OH radical and Cl atom initiated oxidation of N-ethyl perfluorobutanesulfonamide. *Environ. Sci. Technol.* **2006**, *40*(3), 864–872.

67. Im, J.; Walshe-Langford, G. E.; Moon, J. W.; Löffler, F. E. Environmental fate of the next generation refrigerant 2, 3, 3, 3-tetrafluoropropene (HFO-1234yf). *Environ. Sci. Technol.* **2014**, *48*(22), 13181–13187.

68. Sulbaek Andersen, M. S.; Wallington, T. J.; Burkholder, J. B.; Madronich, S.; Hanson, M. L.; Van Hoomissen, D.; Solomon, K. R. Yields of perfluorocarboxylic acids from the atmospheric oxidation of Montreal Protocol related gases. *Environmental Science: Atmospheres*. **2026**. doi: 10.1039/D5EA00179J.

69. Solomon, K. R.; Velders, G. J.; Wilson, S. R.; Madronich, S.; Longstreth, J.; Aucamp, P. J.; Bornman, J. F. Sources, fates, toxicity, and risks of trifluoroacetic acid and its salts: Relevance to substances regulated under the Montreal and Kyoto Protocols. *J. Toxicol. Environ. Health Part B*. **2016**, *19*(7), 289–304.

70. Sun, M.; Cui, J. N.; Guo, J.; Zhai, Z.; Zuo, P.; Zhang, J. Fluorochemicals biodegradation as a potential source of trifluoroacetic acid (TFA) to the environment. *Chemosphere*, **2020**, *254*, 126894.

71. Lemal, D. M. Perspective on Fluorocarbon Chemistry. *J. Org. Chem*. **2004**, *69*(1), 1–11.

72. Organization for Economic Cooperation and Development. Hazard assessment of perfluorooctane sulfonate (PFOS) and its salts. ENV/JM/RD(2002)17/FINAL. Joint Meeting of the Chemicals Committee and the Working Party on Chemicals, Pesticides, and Biotechnology, Environment Directorate, Organisation for Economic Co-operation and Development (Paris). **2002**. Retrieved from http://www.oecd.org/dataoecd/23/18/2382880.pdf.

73. Barry, V.; Winquist, A.; Steenland, K. Perfluorooctanoic acid (PFOA) exposures and incident cancers among adults living near a chemical plant. *Environ. Health Perspectives*, **2013**, *121*(11-12), 1313–1318.

74. Vieira, V. M.; Hoffman, K.; Shin, H. M.; Weinberg, J. M.; Webster, T. F.; Fletcher, T. Perfluorooctanoic acid exposure and cancer outcomes in a contaminated community: a geographic analysis. *Environ. Health Perspectives*, **2013**, *121*(3), 318–323.

75. Lau, C.; Anitole, K.; Hodes, C.; Lai, D.; Pfahles-Hutchens, A.; Seed, J. Perfluoroalkyl acids: a review of monitoring and toxicological findings. *Toxicol. Sci.* **2007**, *99*(2), 366–394. https://doi.org/10.1093/toxsci/kfm128.

76. Rand, A. A.; Mabury, S. A. Is there a human health risk associated with indirect exposure to perfluoroalkyl carboxylates (PFCAs)? *Toxicology*, **2017**, 375, 28–36. https:// doi.org/10.1016/j.tox.2016.11.011.

77. Pérez, F.; Nadal, M.; Navarro-Ortega, A.; Fàbrega, F.; Domingo, J. L.; Barceló, D.; Farré, M. Accumulation of perfluoroalkyl substances in human tissues. *Environ. Int.*, **2013**, *59*, 354–362.

78. Valdersnes, S.; Nilsen, B. M.; Breivik, J. F.; Borge, A.; Maage, A. Geographical trends of PFAS in cod livers along the Norwegian coast. *PloS one*, **2017**, *12*(5), e0177947.

79. Gaber, N.; Bero, L.; Woodruff, T. J. The devil they knew: chemical documents analysis of industry influence on PFAS science. *Ann.Glob. Health*, **2023**, *89*(1), 37.

80. United States Environmental Protection Agency. PFOA Stewardship Program. U.S. EPA Public Docket OPPT-2006-0621. **2006**.

81. Padula, A. M.; Ning, X.; Bakre, S.; Barrett, E. S.; Bastain, T.; Bennett, D. H.; Bloom, M. S.; Breton, C. V.; Dunlop, A. L.; Eick, S. M.; Ferrara, A. Birth outcomes in relation to prenatal exposure to per-and polyfluoroalkyl substances and stress in the environmental influences on child health outcomes (ECHO) program. *Environ. Health Perspect.* **2023**, *131*(3), 037006.

82. United States Environmental Protection Agency. Phase-out Plan for POSF-based Products. U.S. EPA Public Docket OPPT 2002-0043; 3M Specialty Materials Markets Group: St. Paul, MN. **2000**.

83. Environment and Climate Change Canada. Environmental Performance Agreement Respecting Perfluorinated Carboxylic Acids (PFCAs) and Their Precursors in Perfluorochemical Products Sold in Canada. **2010**.

84. Health Canada. ARCHIVED - State of the Science Report for a Screening Health Assessment: Perfluorooctane Sulfonate, Its Salts and Its Precursors that Contain the C8F17SO2 or C8F17SO3 Moiety - *Canada.ca*, **2006**. Retrieved from https://www.canada.ca/en/health-canada/services/environmental-workplace-health/reports-publications/environmental-contaminants/state-science-report-screening-health-assessment-perfluorooctane-sulfonate-salts-precursors-that-contain-c8f17so2-c8f17so3-moiety.html.

85. Environment and Climate Change Canada. Prohibition of Certain Toxic Substances Regulations, 2012: overview, **2014**. Retrieved from https://www.canada.ca/en/environment-climate-change/services/management-toxic-substances/prohibition-regulations.html.

86. United Nations Environment Programme. The Montreal Protocol on Substances That Deplete the Ozone Layer, as Either Adjusted and/or Amended in London 1990, Copenhagen 1992, Cienna 1995, Montreal 1997, Beijing 1999. In *Ozone Secretariat, United Nations Environment Programme*; **2000**.

87. United Nations Environment Programme. Report of the Twenty-Eighth Meeting of the Parties to the Montreal Protocol on Sustances That Deplete the Ozone Layer, Kigali. In *United Nations Environment Programme*, **2016**, *2*, 49–52.

88. United Nations Environment Programme. Handbook for the Montreal Protocol on Substances That Deplete the Ozone Layer. In *Ozone Secretariat, United Nations Environment Programme*, **2018**.

89. Felizeter, S.; McLachlan, M. S.; de Voogt, P. Uptake of Perfluorinated Alkyl Acids by Hydroponically Grown Lettuce (Lactuca Sativa). *Environ. Sci. Technol.* **2012**, 46 (21), 11735–11743.

90. Lu, Q.; He, Z. L.; Stoffella, P. J. Land Application of Biosolids in the USA: A Review. *Appl. Environ. Soil Sci*. **2012**, *2012*(1), 201462.

91. Lan, Z.; Zhou, M.; Yao, Y.; Sun, H. Plant Uptake and Translocation of Perfluoroalkyl Acids in a Wheat–Soil System. *Environ. Sci. Pollut. Res.* **2018**, *25*(31), 30907–30916.

92. Salierno, G. On the chemical pathways influencing the effective global warming potential of commercial hydrofluoroolefin gases. *ChemSusChem*, **2024**, *17*(17), e202400280.

93. Holland, R.; Khan, M. A. H.; Driscoll, I.; Chhantyal-Pun, R.; Derwent, R. G.; Taatjes, C. A.; Orr-Ewing, A. J.; Percival, C. J.; Shallcross, D. E. Investigation of the production of trifluoroacetic acid from two halocarbons, HFC-134a and HFO-1234yf and its fates using a global three-dimensional chemical transport model. *ACS Earth Space Chem.* **2021**, *5*(4), 849–857.

94. Chen, H.; Yao, Y.; Zhao, Z.; Wang, Y.; Wang, Q.; Ren, C.; Wang, B.; Sun, H.; Alder, A. C.; Kannan, K. Multimedia distribution and transfer of per-and polyfluoroalkyl substances (PFASs) surrounding two fluorochemical manufacturing facilities in Fuxin, China. *Environ. Sci. Technol.* **2018**, *52*(15), 8263–8271.

95. Lan, Z.; Yao, Y.; Xu, J.; Chen, H.; Ren, C.; Fang, X.; Zhang, K.; Jin, L.; Hua, X.; Alder, A. C.; Wu, F. Novel and legacy per-and polyfluoroalkyl substances (PFASs) in a farmland environment: Soil distribution and biomonitoring with plant leaves and locusts. *Environ. Pollut.* **2020**, *263*, 114487.

96. Scott, B. F.; Spencer, C.; Martin, J. W.; Barra, R.; Bootsma, H. A.; Jones, K. C.; Johnston, A. E.; Muir, D. C. G. Comparison of haloacetic acids in the environment of the northern and southern hemispheres. *Environ. Sci. Technol.* **2005**, *39*(22), 8664–8670.

97. EU Reference Laboratories for Residues of Pesticides. In *EURL SRM-Residue Findings Report.* **2017**, 1−10. Retrieved from https://www.eurl pesticides.eu/userfiles/file/eurlsrm/eurlsrm_residue-observation_tfa dfa.pdf.

98. Scheurer, M.; Nödler, K. Ultrashort-chain perfluoroalkyl substance trifluoroacetate (TFA) in beer and tea–An unintended aqueous extraction. *Food Chem.* **2021**, *351*, 129304.

99. van Hees, P.; Karlsson, P.; Bucuricova, L.; Olsman, H.; Yeung, L. Trifluoroacetic Acid (TFA) and Trifluoromethane Sulphonic Acid (TFMS) in Juice and Fruit/Vegetable Purees. In *Eurofins Scientific*. **2024**, 1−8. Retrieved from https:// cdnmedia.eurofins.com/european-east/media/uxcnaa2c/eurofins_ tfa_tfms_juice_24_final.pdf (accessed 2026−01−28).

100. Guckert, M.; Rupp, J.; Nürenberg, G.; Nödler, K.; Koschorreck, J.; Berger, U.; Drost, W.; Siebert, U.; Wibbelt, G.; Reemtsma, T. Differences in the internal PFAS patterns of herbivores, omnivores and carnivores-lessons learned from target screening and the total oxidizable precursor assay. *Sci. Tot. Environ.* **2023**, *875*, 162361.

101. Wang, Z.; Cousins, I. T.; Scheringer, M.; Hungerbühler, K. Fluorinated alternatives to long-chain perfluoroalkyl carboxylic acids (PFCAs), perfluoroalkane sulfonic acids (PFSAs) and their potential precursors. *Environ. Int.* **2013**, *60*, 242−248.

102. Brendel, S.; Fetter, É.; Staude, C.; Vierke, L.; Biegel-Engler, A. Short-chain perfluoroalkyl acids: environmental concerns and a regulatory strategy under REACH. *Environ. Sci. Eur.* **2018**, *30*(1), 9.

103. MacInnis, J. J.; French, K.; Muir, D. C. G.; Spencer, C.; Criscitiello, A.; De Silva, A. O.; Young, C. J. Emerging Investigator Series: A 14-Year Depositional Ice Record of Perfluoroalkyl Substances in the High Arctic. *Environ. Sci.: Process. Impacts.* **2017**, *19*(1), 22−30.

104. Pickard, H. M.; Criscitiello, A. S.; Spencer, C.; Sharp, M. J.; Muir, D. C. G.; De Silva, A. O.; Young, C. J. Continuous Non-Marine Inputs of per- and Polyfluoroalkyl Substances to the High Arctic: A Multi-Decadal Temporal Record. *Atmos. Chem. Phys*. **2018**, *18*(7), 5045−5058.

105. Ameduri, B.; Boutevin, B. Telomerization reactions of fluorinated alkenes. *Top. Curr. Chem.* **1997**, 192, 165−233.

106. Lehmler, H. J. Synthesis of environmentally relevant fluorinated surfactants—a review. *Chemosphere*, **2005**, *58*(11), 1471−1496.

107. Sulbaek Andersen, M. P.; Nielsen, O. J.; Hurley, M. D.; Ball, J. C.; Wallington, T. J.; Ellis, D. A.; Martin, J. W.; Mabury, S. A. Atmospheric chemistry of 4: 2 fluorotelomer alcohol (n-C4F9CH2CH2OH): Products and mechanism of Cl atom initiated oxidation in the presence of NO x. *J. Phys. Chem. A.* **2005**, *109*(9), 1849−1856.

108. Martin, J. W.; Muir, D. C. G.; Moody, C. A.; Ellis, D. A.; Kwan, W. C.; Solomon, K. R.; Mabury, S. A. Collection of Airborne Fluorinated Organics and Analysis by Gas Chromatography/Chemical Ionization Mass Spectrometry. *Anal. Chem*. **2002**, *74*(3), 584−590. https://doi.org/10.1021/ac015630d.

109. Dupont Global. PFOA Strategy Update: Presentation to USEPAOPPT, **2005**.

110. Barber, J. L.; Berger, U.; Chaemfa, C.; Huber, S.; Jahnke, A.; Temme, C.; Jones, K. C. Analysis of per-and polyfluorinated alkyl substances in air samples from Northwest Europe. *J. Environ. Monit.* **2007**, *9*(6), 530−541.

111. Ahrens, L.; Shoeib, M.; Harner, T.; Lee, S. C.; Guo, R.; Reiner, E. J. Wastewater treatment plant and landfills as sources of polyfluoroalkyl compounds to the atmosphere. *Environ. Sci. Technol.* **2011**, *45*(19), 8098−8105.

112. Weinberg, I.; Dreyer, A.; Ebinghaus, R. Landfills as sources of polyfluorinated compounds, polybrominated diphenyl ethers and musk fragrances to ambient air. *Atmos. Environ.* **2011**, *45*(4), 935−941.

113. Tian, Y.; Yao, Y.; Chang, S.; Zhao, Z.; Zhao, Y.; Yuan, X.; Wu, F.; Sun, H. Occurrence and phase distribution of neutral and ionizable per-and polyfluoroalkyl substances (PFASs) in the atmosphere and plant leaves around landfills: a case study in Tianjin, China. *Environ. Sci. Technol.* **2018**, *52*(3), 1301−1310.

114. Lin H.; Lao, J. Y.; Wang, Q.; Ruan, Y.; He, Y.; Lee, P. K.; Leung, K. M.; Lam, P. K. Per-and polyfluoroalkyl substances in the atmosphere of waste management infrastructures: Uncovering secondary fluorotelomer alcohols, particle size distribution, and human inhalation exposure. *Environ. Int.* **2022**, 167, 107434.

115. Li, J.; Del Vento, S.; Schuster, J.; Zhang, G.; Chakraborty, P.; Kobara, Y.; Jones, K. C. Perfluorinated Compounds in the Asian Atmosphere. *Environ. Sci. Technol.* **2011**, *45*(17), 7241–7248. https://doi.org/10.1021/es201739t.

116. Jahnke, A.; Ahrens, L.; Ebinghaus, R.; Temme, C. Urban versus Remote Air Concentrations of Fluorotelomer Alcohols and Other Polyfluorinated Alkyl Substances in Germany. *Environ. Sci. Technol.* **2007**, *41*(3), 745–752. https://doi.org/10.1021/es0619861.

117. Nilsson, H.; Kärrman, A.; Rotander, A.; van Bavel, B.; Lindström, G.; Westberg, H. Inhalation Exposure to Fluorotelomer Alcohols Yield Perfluorocarboxylates in Human Blood? *Environ. Sci. Technol.* **2010**, *44*(19), 7717–7722. https://doi.org/10.1021/es101951t.

118. Stock, N. L.; Lau, F. K.; Ellis, D. A.; Martin, J. W.; Muir, D. C. G.; Mabury, S. A. Polyfluorinated Telomer Alcohols and Sulfonamides in the North American Troposphere. *Environ. Sci. Technol.* **2004**, *38*(4), 991–996. https://doi.org/10.1021/es034644t.

119. Ellis, D. A.; Martin, J. W.; De Silva, A. O.; Mabury, S. A.; Hurley, M. D.; Sulbaek Andersen, M. P.; Wallington, T. J. Degradation of Fluorotelomer Alcohols: A Likely Atmospheric Source of Perfluorinated Carboxylic Acids. *Environ. Sci. Technol.* **2004**, *38*(12), 3316–3321. https://doi.org/10.1021/es049860w.

120. Wallington, T. J.; Hurley, M. D.; Xia, J.; Wuebbles, D. J.; Sillman, S.; Ito, A.; Penner, J. E.; Ellis, D. A.; Martin, J.; Mabury, S. A.; Nielsen, O. J.; Sulbaek Andersen, M. P. Formation of C7F15COOH (PFOA) and Other Perfluorocarboxylic Acids during the Atmospheric Oxidation of 8:2 Fluorotelomer Alcohol. *Environ. Sci. Technol.* **2006**, *40*(3), 924–930. https://doi.org/10.1021/es051858x.

121. Chu, B.; Chen, T.; Liu, Y.; Ma, Q.; Mu, Y.; Wang, Y.; Ma, J.; Zhang, P.; Liu, J.; Liu, C.; Gui, H. Application of smog chambers in atmospheric process studies. *Natl. Sci. Rev.* **2022**, *9*(2), nwab103. https://doi.org/10.1093/nsr/nwab103.

122. Yuan, Q.; Zhang, Z.; Wang, M.; Ho, K. F.; Wang, T.; Lee, S. Characterization of a smog chamber for studying formation of gas-phase products and secondary organic aerosol. *J. Environ. Sci.* **2024**, *136*, 570–582.

123. Trump, E. R.; Epstein, S. A.; Riipinen, I.; Donahue, N. M.; Wall effects in smog chamber experiments: A model study. *Aerosol Sci. Technol.* **2016**, *50*(11), 1180–1200.

124. Akimoto, H.; Hoshino, M.; Inoue, G.; Sakamaki, F.; Washida, N.; Okuda, M. Design and characterization of the evacuable and bakable photochemical smog chamber. *Environ. Sci. Technol.* 1979, *13*(4), 471–475.

125. Dinglasan, M. J. A.; Ye, Y.; Edwards, E. A.; Mabury, S. A. Fluorotelomer Alcohol Biodegradation Yields Poly- and Perfluorinated Acids. *Environ. Sci. Technol.* **2004**, *38*(10), 2857–2864. https://doi.org/10.1021/es0350177.

126. Taniyasu, S.; Kannan, K.; So, M. K.; Gulkowska, A.; Sinclair, E.; Okazawa, T.; Yamashita, N. Analysis of Fluorotelomer Alcohols, Fluorotelomer Acids, and Short- and Long-Chain Perfluorinated Acids in Water and Biota. *J. Chromatogr. A*. **2005**, *1093*(1), 89–97. https://doi.org/10.1016/j.chroma.2005.07.053.

127. Peng, Z.; Jimenez, J. L. Radical Chemistry in Oxidation Flow Reactors for Atmospheric Chemistry Research. *Chem. Soc. Rev.* **2020**, *49*(9), 2570–2616. https://doi.org/10.1039/C9CS00766K.

128. Palm, B. B.; Campuzano-Jost, P.; Ortega, A. M.; Day, D. A.; Kaser, L.; Jud, W.; Karl, T.; Hansel, A.; Hunter, J. F.; Cross, E. S.; Kroll, J. H.; Peng, Z.; Brune, W. H.; Jimenez, J. L. In Situ Secondary Organic Aerosol Formation from Ambient Pine Forest Air Using an Oxidation Flow Reactor. *Atmos. Chem. Phys.* **2016***, 16*(5), 2943–2970. https://doi.org/10.5194/acp-16-2943-2016.

129. Brune, W. H. The Chamber Wall Index for Gas–Wall Interactions in Atmospheric Environmental Enclosures. *Environ. Sci. Technol.* **2019**, *53*(7), 3645–3652. https://doi.org/10.1021/acs.est.8b06260.

130. George, I. J.; Vlasenko, A.; Slowik, J. G.; Broekhuizen, K.; Abbatt, J. P. Heterogeneous oxidation of saturated organic aerosols by hydroxyl radicals: uptake kinetics, condensed-phase products, and particle size change. *Atmos. Chem. Phys.* **2007**, *7*(16), 4187−4201.

131. Peng, Z.; Day, D. A.; Stark, H.; Li, R.; Lee-Taylor, J.; Palm, B. B.; Brune, W. H.; Jimenez, J. L. HOx radical chemistry in oxidation flow reactors with low-pressure mercury lamps systematically examined by modeling. *Atmos. Meas. Tech.* **2015**, *8*(11), 4863−90.

132. Rowe, J.P., Lambe, A.T. and Brune, W.H., 2020. Effect of varying the λ= 185 and 254 nm photon flux ratio on radical generation in oxidation flow reactors. *Atmos. Chem. Phys.* **2020**, *20*(21), 13417−13424.

133. Czech, H.; Yli-Pirilä, P.; Tiitta, P.; Ihalainen, M.; Hartikainen, A.; Schneider, E.; Martens, P.; Paul, A.; Hohaus, T.; Rüger, C. P.; Jokiniemi, J. The effect of aging conditions at equal OH exposure in an oxidation flow reactor on the composition of toluene-derived secondary organic aerosols. *Environ. Sci.: Atmos.* **2024**, *4*(7), 718−31.

134. Li, K.; Liggio, J.; Lee, P.; Han, C.; Liu, Q.; Li, S. M. Secondary Organic Aerosol Formation from \alpha -Pinene, Alkanes, and Oil-Sands-Related Precursors in a New Oxidation Flow Reactor. *Atmos. Chem. Phys.* **2019**, *19*(15), 9715–9731. https://doi.org/10.5194/acp-19-9715-2019.

135. Harrison, A. G. Chemical Ionization Mass Spectrometry, 2nd ed.; Routledge: New York, NY, **1992**.

136. Jokinen, T.; Sipilä, M.; Junninen, H.; Ehn, M.; Lönn, G.; Hakala, J.; Petäjä, T.; Mauldin Iii, R. L.; Kulmala, M.; Worsnop, D. R. Atmospheric sulphuric acid and neutral cluster measurements using CI-APi-TOF. *Atmos. Chem. Phys.* **2012**, *12*(9), 4117−4125.

137. Cai, R.; Mikkila, J.; Bengs, A.; Koirala, M.; Mikkila, J.; Holm, S.; Juuti, P.; Meder, M.; Partovi, F.; Shcherbinin, A.; Worsnop, D. Extending the range of detectable trace species with the fast polarity switching of chemical ionization orbitrap mass spectrometry. *Anal. Chem.* **2024**, *96*(21), 8604−8612.

138. Iyer, S.; Lopez-Hilfiker, F.; Lee, B. H.; Thornton, J. A.; Kurtén, T. Modeling the Detection of Organic and Inorganic Compounds Using Iodide-Based Chemical Ionization. *J. Phys. Chem. A.* **2016**, *120*(4), 576–587. https://doi.org/10.1021/acs.jpca.5b09837.

139. Riedel, T. P.; Lang, J. R.; Strynar, M. J.; Lindstrom, A. B.; Offenberg, J. H. Gas-Phase Detection of Fluorotelomer Alcohols and Other Oxygenated Per- and Polyfluoroalkyl Substances by Chemical Ionization Mass Spectrometry. *Environ. Sci. Technol. Lett.* **2019**, *6*(5), 289–293. https://doi.org/10.1021/acs.estlett.9b00196.

140. Bowers, B. B.; Thornton, J. A.; Sullivan, R. C. Evaluation of Iodide Chemical Ionization Mass Spectrometry for Gas and Aerosol-Phase per- and Polyfluoroalkyl Substances (PFAS) Analysis. *Environ. Sci.: Process. Impacts.* **2023**, *25*(2), 277–287. https://doi.org/10.1039/D2EM00275B.

141. Mattila, J. M.; Krug, J. D.; Roberson, W. R.; Burnette, R. P.; McDonald, S.; Virtaranta, L.; Offenberg, J. H.; Linak, W. P. Characterizing Volatile Emissions and Combustion Byproducts from Aqueous Film-Forming Foams Using Online Chemical

Ionization Mass Spectrometry. *Environ. Sci. Technol.* **2024**, *58*(8), 3942–3952. https://doi.org/10.1021/acs.est.3c09255.

142. Gerig, J. T. Fluorine nmr. Biophysics Textbook Online. **2001**, 1−35.

143. Zhang, X.; He, A.; Guo, R.; Zhao, Y.; Yang, L.; Morita, S.; Xu, Y.; Noda, I.; Ozaki, Y. A. New Approach to Removing Interference of Moisture from FTIR Spectrum. *Spectrochim. Acta A Mol. Biomol. Spectrosc.* **2022**, 265, 120373.

144. Huey, L. G.; Hanson, D. R.; Howard, C. J.; Reactions of SF6-and I-with Atmospheric Trace Gases. *J. Phys. Chem.* **1995**, *99*(14), 5001−5008.

145. Slusher, D. L.; Huey, L. G.; Tanner, D. J.; Flocke, F. M.; Roberts, J. M. A thermal dissociation–chemical ionization mass spectrometry (TD-CIMS) technique for the simultaneous measurement of peroxyacyl nitrates and dinitrogen pentoxide. *J. Geophys. Res. Atmos.* **2004**, *109*, D19315, doi:10.1029/2004JD004670.

146. Lee, B. H.; Lopez-Hilfiker, F. D.; Mohr, C.; Kurtén, T.; Worsnop, D. R.; Thornton, J. A. An iodide-adduct high-resolution time-of-flight chemical-ionization mass spectrometer: Application to atmospheric inorganic and organic compounds. *Environ. Sci. Technol.* **2014**, *48*(11), 6309–6317.

147. Brophy, P.; Farmer, D. K. A switchable reagent ion high resolution time-of-flight chemical ionization mass spectrometer for real-time measurement of gas phase oxidized species: characterization from the 2013 southern oxidant and aerosol study. *Atmos. Meas. Tech.* **2015**, *8*(7), 2945–2959.

148. Lopez-Hilfiker, F. D.; Iyer, S.; Mohr, C.; Lee, B. H.; D'Ambro, E. L.; Kurtén, T.; Thornton, J. A. Constraining the sensitivity of iodide adduct chemical ionization mass spectrometry to multifunctional organic molecules using the collision limit and thermodynamic stability of iodide ion adducts. *Atmos. Meas. Tech.* **2016**, *9*(4), 1505–1512.

149. Blake, R. S.; Monks, P. S.; Ellis, A. M. Proton-Transfer Reaction Mass Spectrometry. *Chem. Rev.* **2009**, *109*(3), 861–896. https://doi.org/10.1021/cr800364q.

150. Calamai, L.; Villanelli, F.; Bartolucci, G.; Pieraccini, G.; Moneti, G. 4.24 - Sample Preparation for Direct MS Analysis of Food. In *Comprehensive Sampling and Sample Preparation*; Pawliszyn, J., Ed.; Academic Press: Oxford, **2012**, 535–557. https://doi.org/10.1016/B978-0-12-381373-2.00148-4.

151. Brais, C. J.; Ibañez, J. O.; Schwartz, A. J.; Ray, S. J. Recent Advances in Instrumental Approaches to Time-of-Flight Mass Spectrometry. *Mass Spectrom. Rev.* **2021**, *40*(5), 647–669. https://doi.org/10.1002/mas.21650.

152. Cotter, R. J. Time-of-flight mass spectrometry for the structural analysis of biological molecules. *Anal. Chem.* **1992**, *64*(21), 1027A–1039A.

153. Jordan, A.; Haidacher, S. G. H. E. H.; Hanel, G.; Hartungen, E.; Märk, L.; Seehauser, H.; Schottkowsky, R.; Sulzer, P.; Märk, T. D. A high resolution and high sensitivity proton-transfer-reaction time-of-flight mass spectrometer (PTR-TOF-MS). *Int. J. Mass Spectrom.* **2009**, *286*(2-3), 122–128.

154. Weickhardt, C.; Moritz, F.; Grotemeyer, J. Time-of-flight mass spectrometry: State-of the-art in chemical analysis and molecular science. **1996**, *15*(3), 139–162.

155. Scherer, S.; Altwegg, K.; Balsiger, H.; Fischer, J.; Jäckel, A.; Korth, A.; Mildner, M.; Piazza, D.; Reme, H.; Wurz, P. A novel principle for an ion mirror design in time-of-flight mass spectrometry. *Int. J. Mass Spectrom.* **2006**, *251*(1), 73–81.

156. Tanimoto, H.; Aoki, N.; Inomata, S.; Hirokawa, J.; Sadanaga, Y. Development of a PTR-TOFMS Instrument for Real-Time Measurements of Volatile Organic Compounds in Air. *Int. J. Mass Spectrom.* **2007**, *263* (1), 1–11.

157. Colussi, A.A., Vandenboer, T.C., Young, C. and Liggio, J. Atmospheric Fate of 4: 2 Fluorotelomer Alcohol using an Oxidation Flow Reactor and Proton Transfer Reaction Time-of-Flight Mass Spectrometry. *Environ. Sci.: Process. Impacts*. **2026**, i*n press*, doi: 10.1039/D5EM00943J.

158. Transport Canada. Whales Initiative: Protecting The Southern Resident Killer Whale - Transport Canada. **2018.** Retrieved from https://www.tc.gc.ca/en/initiatives/oceans-protection-plan/whales-initiative-protecting-southern-resident-killer-whale.html.

159. Bilela, L. L.; Matijošytė, I.; Krutkevičius, J.; Alexandrino, D. A.; Safarik, I.; Burlakovs, J.; Gaudêncio, S. P.; Carvalho, M. F. Impact of per-and polyfluorinated alkyl substances (PFAS) on the marine environment: Raising awareness, challenges, legislation, and mitigation approaches under the One Health concept. *Mar. Pollut. Bull.* **2023**, *194*, 115309.

160. Alava, J. J.; Ross, P. S.; Lachmuth, C.; Ford, J. K.; Hickie, B. E.; Gobas, F. A. Habitat-based PCB environmental quality criteria for the protection of endangered killer whales (Orcinus orca). *Environ. Sci. Technol.* **2012**, *46*(22), 12655–12663.

161. Ross, P. S.; Ellis, G. M.; Ikonomou, M. G.; Barrett-Lennard, L. G.; Addison, R. F. High PCB concentrations in free-ranging Pacific killer whales, Orcinus orca: effects of age, sex and dietary preference. *Mar. Pollut. Bull.* **2000**, *40*(6), 504–515.

162. Houde, M.; Hoekstra, P. F.; Solomon, K. R.; Muir, D. C. G. Organohalogen Contaminants in Delphinoid Cetaceans. *Rev. Environ. Contam. Toxicol.* **2005**, 184, 1−57.

163. Krahn, M. M.; Hanson, M. B.; Baird, R. W.; Boyer, R. H.; Burrows, D. G.; Emmons, C. K.; Ford, J. K.; Jones, L. L.; Noren, D. P.; Ross, P. S.; Schorr, G. S.; Persistent organic pollutants and stable isotopes in biopsy samples (2004/2006) from Southern Resident killer whales. *Mar. Pollut. Bull.* **2007**, *54*(12), 1903–1911.

164. Lebeuf, M.; Measures, L.; Noel, M.; Raach, M.; Trottier, S. A Twenty-One Year Temporal Trend of Persistent Organic Pollutants in St. Lawrence Estuary Beluga, Canada. *Sci. Total Environ.* **2014**, 485, 377−386.

165. Quémerais, B.; Lemieux, C.; Lum, K. R. Concentrations and sources of PCBs and organochlorine pesticides in the St. Lawrence River (Canada) and its tributaries. *Chemosphere*. **1994**, *29*(3), 591−610.

166. Wright, C.; Johannessen, S. C.; Macdonald, R. W.; Burd, B. J.; Hill, P. R.; Van Roodselaar, A.; Bertold, S. The Strait of Georgia Ambient Monitoring Program: Phase I, 2002-2007: Sediment and Benthos. Canadian Data Report of Fisheries and Aquatic Sciences 1208. *Ocean Sciences Division, Fisheries and Ocean Canada, Institute of Ocean Sciences*, **2008**.

167. Ross, P. S.; Frouin, H.; Dangerfield, N. J.; Crewe, N. F.; Dubetz, C.; Fischer, M. B.; Fraser, T. L.; Ross, A. R. S. *Sediment concentrations of PCBs, PBDEs, PCDDs and PCDFs from disposal at sea sites at Brown Passage and Douglas Channel, British Columbia in 2011*. Fisheries and Oceans Canada, Institute of Oceans Sciences, Pacific Region, **2012**.

168. Arblaster, J.; Ikonomou, M. G.; Gobas, F. A. P. C. Toward ecosystem-based sediment quality guidelines for polychlorinated biphenyls (PCBs). *Integr. Environ. Assess. Manag.* **2015**, *11*(4), 689–700.

169. Mosnier, A.; Doniol-Valcroze, T.; Gosselin, J. F.; Lesage, V.; Measures, L. N.; Hammill, M. O. Insights into Processes of Population Decline Using an Integrated Population Model: The Case of the St. Lawrence Estuary Beluga (Delphinapterus leucas). *Ecol. Modell.* **2015**, 314, 15−31.

170. Lesage, V.; Wing, S.; Zuur, A. F.; Gosselin, J. F.; Mosnier, A.; St-Pierre, A. P.; Michaud, R.; Berteaux, D. Environmental factors and behaviour of St. Lawrence Estuary beluga generate heterogeneity in availability bias for photographic and visual aerial surveys. *Fisheries and Oceans Canada, Canadian Science Advisory Secretariat,* ***2*****024**.

171. Simard, Y.; Lepage, R.; Gervaise, C. Anthropogenic sound exposure of marine mammals from seaways: Estimates for Lower St. Lawrence Seaway, eastern Canada. *Appl. Acoust.* **2010**, 71, 1093–1098.

172. McQuinn, I. H.; Lesage, V.; Carrier, D.; Larrivée, G.; Samson, Y.; Chartrand, S.; Michaud, R.; Theriault, J. A threatened beluga (Delphinapterus leucas) population in the traffic lane: Vessel-generated noise characteristics of the Saguenay-St. Lawrence Marine Park, Canada. *J. Acoust. Soc. Am.* **2011**, 130, 3661–3673.

173. Gervaise, C.; Simard, Y.; Roy, N.; Kinda, B.; Menard, N. Shipping noise in whale habitat: Characteristics, sources, budget, and impact on belugas in Saguenay–St. Lawrence Marine Park hub. *J. Acoust. Soc. Am.* **2012**, 132, 76–89.

174. Chion, C.; Bonnell, T. R.; Lagrois, D.; Michaud, R.; Lesage, V.; Dupuch, A.; McQuinn, I. H.; Turgeon, S. Agent-based modelling reveals a disproportionate exposure of females and calves to a local increase in shipping and associated noise in an endangered beluga population. *Mar. Pollut. Bull.* **2021**, 173, 112977.

175. Savenkoff, C.; Castonguay, M.; Chabot, D.; Hammill, M. O.; Bourdages, H.; Morissette, L. Changes in the northern Gulf of St. Lawrence ecosystem estimated by inverse modelling: evidence of a fishery-induced regime shift? *Estuar. Coast. Shelf Sci.* **2007**, 73, 711–724.

176. Lesage, V.; Lair, S.; Turgeon, S.; Béland, P. Diet of St. Lawrence Estuary Beluga (Delphinapterus leucas) in a changing ecosystem. *Can. Field-Nat.* **2020**, *134*(1), 21–35.

177. Simond, A. E.; Houde, M.; Lesage, V.; Michaud, R.; Verreault, J. Metabolomic Profiles of the Endangered St. Lawrence Estuary Beluga Population and Associations with Organohalogen Contaminants. *Sci. Total Environ.* **2020**, 717.

178. Murray, C. C.; Hannah, L. C.; Doniol-Valcroze, T.; Wright, B.; Stredulinsky, E.; Locke, A.; Lacy, R. Cumulative Effects Assessment for Northern and Southern Resident Killer Whale (Orcinus orca) Populations in the Northeast Pacific. *DFO Canadian Science Advisory Research Document*. **2019**, *56*.

179. COSEWIC. COSEWIC assessment and update status report on the killer whale Orcinus orca, Southern Resident population, Northern Resident population, West Coast Transient population, Offshore population and Northwest Atlantic/Eastern Arctic population, in Canada. *Committee on the Status of Endangered Wildlife in Canada.* **2008**, viii + 65.

180. United States National Marine Fisheries Service, Northwest Region. Recovery Plan for Southern Resident Killer Whales (Orcinus orca). **2008**. Retrieved from: https://repository.library.noaa.gov/view/noaa/15975.

181. Ford, J. K.; Ellis, G. M.; Olesiuk, P. F.; Balcomb, K. C. Linking killer whale survival and prey abundance: food limitation in the oceans' apex predator? *Biol. Lett.* **2010**, *6*(1), 139–142.

182. Murray, C. C.; Hannah, L. C.; Doniol-Valcroze, T.; Wright, B. M.; Stredulinsky, E. H.; Nelson, J. C.; Locke, A.; Lacy, R. C. A cumulative effects model for population trajectories of resident killer whales in the Northeast Pacific. *Biol. Conserv.* **2021**, *257*, 109124.

183. Lundin, J. I.; Ylitalo, G. M.; Booth, R. K.; Anulacion, B.; Hempelmann, J. A.; Parsons, K. M.; Giles, D. A.; Seely, E. A.; Hanson, M. B.; Emmons, C. K.; Wasser, S. K. Modulation in Persistent Organic Pollutant Concentration and Profile by Prey Availability and Reproductive Status in Southern Resident Killer Whale Scat Samples. *Environ. Sci. Technol.* **2016**, *50*, 6506−6516.

184. Wasser, S. K.; Lundin, J. I.; Ayres, K.; Seely, E.; Giles, D.; Balcomb, K.; Hempelmann, J.; Parsons, K.; Booth, R. Population growth is limited by nutritional impacts on pregnancy success in endangered Southern Resident killer whales (Orcinus orca). *PLoS One*. **2017**, *12*(6), e0179824.

185. Alava, J. J. Legacy and emerging pollutants in marine mammals' habitat from British Columbia, Canada: Management perspectives for sensitive marine ecosystems. In *Stewarding the Sound*. CRC Press, **2019**, 87–114

186. Desforges, J. P.; Hall, A.; McConnell, B.; Rosing-Asvid, A.; Barber, J. L.; Brownlow, A.; De Guise, S.; Eulaers, I.; Jepson, P. D.; Letcher, R. J.; Levin, M. Predicting global killer whale population collapse from PCB pollution. *Science*, **2018**, *361*(6409), 1373–1376.

187. Andvik, C.; Jourdain, E.; Ruus, A.; Lyche, J. L.; Karoliussen, R.; Borgå, K. Preying on seals pushes killer whales from Norway above pollution effects thresholds. *Sci. Rep.* **2020**, *10*(1), 11888.

188. Tomy, G. T.; Budakowski, W.; Halldorson, T.; Helm, P. A.; Stern, G. A.; Friesen, K.; Pepper, K.; Tittlemier, S. A.; Fisk, A. T. Fluorinated organic compounds in an eastern Arctic marine food web. *Environ. Sci. Technol.* **2004**, *38*(24), 6475–6481.

189. Butt, C. M.; Berger, U.; Bossi, R.; Tomy, G. T.; Levels and trends of poly-and perfluorinated compounds in the arctic environment. *Sci. Total Environ.* **2010**, *408*(15), 2936–2965.

190. Barrett, H.; Du, X.; Houde, M.; Lair, S.; Verreault, J.; Peng, H. Suspect and nontarget screening revealed class-specific temporal trends (2000–2017) of poly-and perfluoroalkyl substances in St. Lawrence Beluga Whales. *Environ. Sci. Technol.* **2021**, *55*(3), 1659–1671.

191. Lee, K.; Alava, J. J.; Cottrell, P.; Cottrell, L.; Grace, R.; Zysk, I.; Raverty, S. Emerging contaminants and new POPs (PFAS and HBCDD) in endangered Southern Resident and Bigg's (Transient) killer whales (Orcinus orca): In utero maternal transfer and pollution management implications. *Environ. Sci. Technol.* **2022**, *57*(1), 360–374.

192. Scott, B.; Spencer, C.; Mabury, S. A.; Muir, D. C. Poly and perfluorinated carboxylates in North American precipitation. *Environ. Sci. Technol.* **2006***, 40*(23), 7167–7174. https://doi.org/10.1021/es061403n.

193. Pike, K. A.; Edmiston, P. L.; Morrison, J. J.; Faust, J. A.; Correlation analysis of perfluoroalkyl substances in regional US precipitation events. *Water Res.* **2021**, *190*, 116685.

194. Vierke, L.; Ahrens, L.; Shoeib, M.; Reiner, E. J.; Guo, R.; Palm, W.; Ebinghaus, R.; Harner, T. Air concentrations and particle–gas partitioning of polyfluoroalkyl compounds at a wastewater treatment plant. *Environ. Chem.* **2011**, *8*(4), 363. https://doi.org/10.1071/en10133.

195. Wu, J.; Martin, J. W.; Zhai, Z.; Lu, K.; Li, L.; Fang, X.; Jin, H.; Hu, J.; Zhang, J. Airborne trifluoroacetic acid and its fraction from the degradation of HFC-134a in Beijing, China. *Environ. Sci. Technol.* **2014**, *48*(7), 3675–3681.

196. Wania, F.; Shunthirasingham, C. Passive air sampling for semi-volatile organic chemicals. *Environ. Sci.: Processes Impacts*. **2020**, *22*, 1925–2002. 10.1039/d0em00194e.

197. Wallace, M. A. G.; Smeltz, M. G.; Mattila, J. M.; Liberatore, H. K.; Jackson, S. R.; Shields, E. P.; Xhani, X.; Li, E. Y.; Johansson, J. H. A review of sample collection and analytical methods for detecting per-and polyfluoroalkyl substances in indoor and outdoor air. *Chemosphere*. **2024**, *358*, 142129.

198. Kwok, K. Y.; Taniyasu, S.; Yeung, L. W. Y.; Murphy, M. B.; Lam, P. K. S.; Horii, Y.; Kannan, K.; Petrick, G.; Sinha, R. K.; Yamashita, N. Flux of perfluorinated phemicals through wet deposition in Japan, the United States, and several other countries. *Environ. Sci. Technol.* **2010**, *44*(18), 7043−7049.

199. D'Ambro, E. L.; Pye, H. O. T.; Bash, J. O.; Bowyer, J.; Allen, C.; Efstathiou, C.; Gilliam, R. C.; Reynolds, L.; Talgo, K.; Murphy, B. N. Characterizing the Air Emissions, Transport, and Deposition of Per and Polyfluoroalkyl Substances from a Fluoropolymer Manufacturing Facility. *Environ. Sci. Technol.* **2021**, *55*(2), 862−870.

200. Wang, S.; Lin, X.; Li, Q.; Li, Y.; Yamazaki, E.; Yamashita, N.; Wang, X. Particle size distribution, wet deposition and scavenging effect of per- and polyfluoroalkyl substances (PFASs) in the atmosphere from a subtropical city of China. *Sci. Total Environ.* **2022**, *823*, 153528.

201. Meng, J.; Wang, T.; Song, S.; Wang, P.; Li, Q.; Zhou, Y.; Lu, Y. Tracing perfluoroalkyl substances (PFASs) in soils along the urbanizing coastal area of Bohai and Yellow Seas, China. *Environ. Pollut.* **2018**, *238*, 404−412.

202. Sammut, G.; Sinagra, E.; Helmus, R.; de Voogt, P. Perfluoroalkyl substances in the Maltese environment − (I) surface water and rain water. *Sci. Total Environ.* **2017**, *589*, 182−190.

203. Wei, C.; Wang, Q.; Song, X.; Chen, X.; Fan, R.; Ding, D.; Liu, Y. Distribution, source identification and health risk assessment of PFASs and two PFOS alternatives in groundwater from non-industrial areas. *Ecotoxicol. Environ. Saf.* **2018**, *152*, 141−150.

204. Ahrens, L.; Harner, T.; Shoeib, M.; Lane, D. A.; Murphy, J. G. Improved characterization of gas–particle partitioning for per-and polyfluoroalkyl substances in the atmosphere using annular diffusion denuder samplers. *Environ. Sci. Technol.* **2012**, *46*(13), 7199−7206.

205. Taniyasu, S.; Yamashita, N.; Moon, H. B.; Kwok, K. Y.; Lam, P. K.; Horii, Y.; Petrick, G.; Kannan, K. Does wet precipitation represent local and regional atmospheric transportation by perfluorinated alkyl substances? *Environ. Int.* **2013**, *55*, 25−32.

206. Shimizu, M. S.; Mott, R.; Potter, A.; Zhou, J.; Baumann, K.; Surratt, J. D.; Turpin, B.; Avery, G. B.; Harfmann, J.; Kieber, R. J.; Mead, R. N. Atmospheric deposition and annual flux of legacy perfluoroalkyl substances and replacement perfluoroalkyl ether carboxylic acids in Wilmington, NC, USA. *Environ. Sci. Technol. Lett.* **2021**, *8*(5), 366−372.

207. Wang, F.; Wang, W.; Zhao, D.; Liu, J.; Lu, P.; Rose, N. L.; Zhang, G. Source apportionment and wet deposition of atmospheric poly-and per-fluoroalkyl substances in a metropolitan city centre of southwest China. *Atmos. Environ.* **2022**, *273*, 118983.

208. Amodio, M.; Catino, S.; Dambruoso, P. R.; De Gennaro, G.; Di Gilio, A.; Giungato, P.; Laiola, E.; Marzocca, A.; Mazzone, A.; Sardaro, A.; Tutino, M. Atmospheric Deposition: Sampling Procedures, Analytical Methods, and Main Recent Findings from the Scientific Literature. *Adv. Meteorol*. **2014**, *2014*(1), 161730.

209. Gambaro, A.; Radaelli, M.; Piazza, R.; Stortini, A. M.; Contini, D.; Belosi, F.; Zangrando, R.; Cescon, P. Organic Micropollutants in Wet and Dry Depositions in the Venice Lagoon. *Chemosphere*. **2009**, *76*(8), 1017–1022, doi:10.1016/j.chemosphere.2009.04.063.

210. Bergknut, M.; Laudon, H.; Jansson, S.; Larsson, A.; Gocht, T.; Wiberg, K. Atmospheric Deposition, Retention, and Stream Export of Dioxins and PCBs in a Pristine Boreal Catchment. *Environ. Pollut.* **2011***, 159*(6), 1592–1598.

211. Lindberg, S. E.; Lovett, G. M.; Richter, D. D.; Johnson, D. W. Atmospheric Deposition and Canopy Interactions of Major Ions in a Forest. *Science.* **1986**, *231*(4734), 141–145, doi:10.1126/science.231.4734.141.

212. Richter, D. D.; Lindberg, S. E. Wet Deposition Estimates from Long-Term Bulk and Event Wet-Only Samples of Incident Precipitation and Throughfall. *J. Environ. Qual.* **1988**, *17*(4), 619–622, doi: 10.2134/jeq1988.00472425001700040017x.

213. Stedman, J. R.; Heyes, C. J.; Irwin, J. G. A Comparison of Bulk and Wet-Only Precipitation Collectors at Rural Sites in the United Kingdom. *Water Air Soil Pollut.* **1990**, *52*(3), 377–395, doi: 10.1007/BF00229445.

214. Persaud, D.; Joudan, S.; VandenBoer, T. C.; Young, C. J. Atmospheric removal of trifluoroacetic acid by dry and wet deposition: a multiyear analysis in Toronto. *Environ. Sci. Technol. Lett*. **2026**, *13*(2), 261–267. doi: 10.1021/acs.estlett.5c01100.

215. Colussi, A. A.; Persaud, D.; Lao, M.; Place, B. K.; Hems, R. F.; Ziegler, S. E.; Edwards, K. A.; Young, C. J.; VandenBoer, T. C. Cost Effective Off-Grid Automatic Precipitation Samplers for Pollutant and Biogeochemical Atmospheric Deposition. *Atmos. Meas. Tech.* **2024**, *17,* 3697–3718.

216. Ramírez, O.; Ladino-Quintero, N.; Bernal, O. J.; de la Rosa, J. D. A comprehensive overview of the ionic composition of rainwater across Latin America. *Environ. Rev.* **2025**, *33*, 1–18.

217. Shoeib, M.; Harner, T.; Lee, S. C.; Lane, D. A.; Zhu, J. Sorbent-Impregnated polyurethane foam disk for passive air sampling of volatile fluorinated chemicals. *Anal. Chem.* **2008**, *80*(3), 675–682. https://doi.org/10.1021/ac701830s.

218. Forbes, P. Atmospheric Chemistry analysis: a review. *Anal. Chem.* **2019**, *92*(1), 455–472.

219. Galarneau, E.; Bidleman, T. F. Modelling the temperature-induced blow-off and blow-on artefacts in filter-sorbent measurements of semivolatile substances. *Atmos. Environ.* **2006**, *40*(23), 4258–4268.

220. Lane, D. A.; Johnson, N. D.; Barton, S. C.; Thomas, G. H. S.; Schroeder, W. H. Development and evaluation of a novel gas and particle sampler for semivolatile chlorinated organic compounds in ambient air. *Environ. Sci. Technol*. **1988**, 22, 941−947.

221. Winberry Jr., W. T.; Ellestad, T.; Stevens, B. Compendium of Methods for the Determination of Inorganic Compounds in Ambient Air: Method IO-4.2, Determination of Reactive Acidic and Basic Gases and Strong Acidity of Atmospheric Fine Particles (<2.5µm) in Ambient Air. Center for Environmental Research Information Office of Research and Development, United States Environmental Protection Agency. **1999**. Retrieved from: https://www.epa.gov/sites/default/files/2019-11/documents/mthd-4-2.pdf. Lane, D. A.; Johnson, N. D.; Barton, S. C.; Thomas, G. H. S.; Schroeder, W. H. Development and evaluation of a novel gas and particle sampler for semivolatile chlorinated organic compounds in ambient air. Environ. Sci. Technol. 1988, 22, 941−947.

222. Xing, Y. F.; Xu, Y. H.; Shi, M. H.; Lian, Y. X. The impact of PM2.5 on the human respiratory system. *J. Thorac. Dis.* **2016**, *8*(1), 69.

223. Brown, R. XXVII. A brief account of microscopical observations made in the months of June, July and August 1827, on the particles contained in the pollen of plants; and on the general existence of active molecules in organic and inorganic bodies. *Philos. Mag.* **1828**, *4*(21), 161–173.

224. Elsayed, K.; Lacor, C. The effect of cyclone inlet dimensions on the flow pattern and performance. *Appl. Math. Model.* **2011**, *35*(4), 1952–1968.

225. Frank, H.; Renschen, D.; Klein, A. Scholl, H. Trace Analysis of Airborne Haloacetates. *J. High Resolut. Chromatogr.* **1995**, *18*(2), 83–88.

226. Frank, H.; Christoph, E. H.; Holm-Hansen, O.; Bullister, J. L. Trifluoroacetate in ocean waters. *Environ. Sci. Technol.* **2002**, *36*(1), 12–15.

227. Scott, B. F.; Alaee, M. Determination of Haloacetic Acids from Aqueous Samples Collected from the Canadian Environment Using an in Situ Derivatization Technique. *Water Qual. Res. J. Canada.* **1998**, *33*(2), 279–293.

228. Fujii, Y.; Harada, K. H.; Koizumi, A. Analysis of Perfluoroalkyl Carboxylic Acids in Composite Dietary Samples by Gas Chromatography/Mass Spectrometry with Electron Capture Negative Ionization. *Environ. Sci. Technol.* **2012**, *46*(20), 11235–11242.

229. Zehavi, D.; Seiber, J. N. An Analytical Method for Trifluoroacetic Acid in Water and Air Samples Using Headspace Gas Chromatographic Determination of the Methyl Ester. *Anal. Chem.* **1996**, *68*(19), 3450–3459.

230. Wujcik, C. E.; Cahill, T. M.; Seiber, J. N. Extraction and Analysis of Trifluoroacetic Acid in Environmental Waters. *Anal. Chem.* **1998**, *70*(19), 4074–4080.

231. Cahill, T. M.; Benesch, J. A.; Gustin, M. S.; Zimmerman, E. J.; Seiber, J. N. Simplified Method for Trace Analysis of Trifluoroacetic Acid in Plant, Soil, and Water Samples Using Headspace Gas Chromatography. *Anal. Chem.* **1999**, *71*(20), 4465–4471.

232. Al Amin, M.; Sobhani, Z.; Liu, Y.; Dharmaraja, R.; Chadalavada, S.; Naidu, R.; Chalker, J. M.; Fang, C. Recent advances in the analysis of per-and polyfluoroalkyl substances (PFAS) – A review. *Environ. Technol. Innov.* **2020**, *19*, 100879.

233. Kannan, K.; Corsolini, S.; Falandysz, J.; Fillmann, G.; Kumar, K. S.; Loganathan, B. G.; Mohd, M. A.; Olivero, J.; Wouwe, N. V.; Yang, J. H.; Aldous, K. M. Perfluorooctanesulfonate and related fluorochemicals in human blood from several countries. *Environ. Sci. Technol.* **2004**, *38*(17), 4489–4495.

234. Berger, U.; Haukås, M. Validation of a screening method based on liquid chromatography coupled to high-resolution mass spectrometry for analysis of perfluoroalkylated substances in biota. *J. Chromatogr. A.* **2005**, *1081*(2), 210–217.

235. So, M. K.; Miyake, Y.; Yeung, W. Y.; Ho, Y. M.; Taniyasu, S.; Rostkowski, P.; Yamashita, N.; Zhou, B. S.; Shi, X. J.; Wang, J. X.; Giesy, J. P. Perfluorinated compounds in the Pearl river and Yangtze river of China. *Chemosphere*. **2007**, *68*(11), 2085–2095.

236. Post, G. B.; Louis, J. B.; Cooper, K. R.; Boros-Russo, B. J.; Lippincott, R. L. Occurrence and potential significance of perfluorooctanoic acid (PFOA) detected in New Jersey public drinking water systems. *Environ. Sci. Technol.* **2009**, *43*(12), 4547–4554.

237. Brase, R. A.; Spink, D. C. Enhanced Sensitivity for the analysis of perfluoroethercarboxylic acids using LC–ESI–MS/MS: Effects of probe position, mobile phase additive, and capillary voltage. *J. Am. Soc. Mass Spectrom.* **2020**, *31*(10), 2124–2132.

238. Wang, Y.; Liu, M.; Duy, S. V.; Munoz, G.; Sauvé, S.; Liu, J. Fast analysis of short-chain and ultra-short-chain fluorinated organics in water by on-line extraction coupled to HPLC-HRMS. *Sci. Total Environ.* **2024**, *943*, 173682.

239. Ayala-Cabrera, J. F.; Javier Santos, F.; Moyano, E. Negative-ion atmospheric pressure ionisation of semi-volatile fluorinated compounds for ultra-high-performance liquid chromatography tandem mass spectrometry analysis. *Anal. Bioanal. Chem.* **2018**, *410*(20), 4913–4924.

240. Stróżyńska, M.; Schuhen, K. Extraction and derivatization for perfluorocarboxylic acids in liquid and solid matrices: A review. *Anal. Sci. Adv.* **2021**, *2*(7–8), 343–353. doi: 10.1002/ansa.202000089.

241. Barron, L.; Paull, B. Simultaneous determination of trace oxyhalides and haloacetic acids using suppressed ion chromatography-electrospray mass spectrometry. *Talanta*, **2006**, *69*(3), 621–630.

242. Wu, S.; Anumol, T.; Gandhi, J.; Snyder, S. A. Analysis of haloacetic acids, bromate, and dalapon in natural waters by ion chromatography–tandem mass spectrometry. *J. Chromatogr. A.* **2017***,* 1487, 100 107. https://doi.org/10.1016/j.chroma.2017.01.006.

243. Zhang, X.; Saini, C.; Pohl, C. A.; Liu, Y. Fast determination of nine haloacetic acids, bromate and dalapon in drinking water samples using ion chromatography electrospray tandem mass spectrometry. *J. Chromatogr. A.* **2020**, *1621*, 461052. https://doi.org/10.1016/j.chroma.2020.461052.

244. Clouthier, J.; VandenBoer, T. C.; Young, C. J. Direct-inject suppressed ion chromatography-mass spectrometry method with online preconcentration for short- and ultrashort-chain perfluoroakyl carboxylic acids in fresh water. *Anal. Methods.* **2026**, doi: 10.1039/D5AY02105G.

245. Thackray, C. P.; Selin, N. E.; Young, C. J. A global atmospheric chemistry model for the fate and transport of PFCAs and their precursors. *Environ. Sci.: Process. Impacts*. **2020**, *22*(2), 285–293.

246. Idjaton, B. I.; Togola, A.; Ghestem, J. P.; Kastler, L.; Bristeau, S.; Ronteltap, M.; Colombano, S.; Devau, N.; Lions, J.; van Hulle-busch, E. D. Determination of Organic Fluorinated Compounds Content in Complex Samples Through Combustion Ion Chromatography Methods: A Way to Define a "Total Per- and Polyfluoroalkyl Substances (PFAS)" Parameter?. *Sci. Total Environ.* **2024**, *932,* 172589, doi: 10.1016/j.scitotenv.2024.172589.

247. Skedung, L.; Savvidou, E.; Schellenberger, S.; Reimann, A.; Cousins, I. T.; Benskin, J. P. Identification and Quantification of Fluorinated Polymers in Consumer Products by Combustion Ion Chromatography and Pyrolysis-Gas Chromatography-Mass Spectrometry. *Environ. Sci.: Process. Impacts.* **2024**, *26*(1), 82–93, doi: 10.1039/D3EM00438D.

248. Ngere, J. B.; Ebrahimi, K. H.; Williams, R.; Pires, E.; Walsby-Tickle, J.; McCullagh, J. S. Ion-exchange chromatography coupled to mass spectrometry in life science, environmental, and medical research. *Anal. Chem.* **2023**, *95*(1), 152–166.

249. Haddad, P.; Fritz, J. S; Gjerde, D. T. Ion Chromatography. *Anal. Bioanal. Chem.* **2010**, *396*(2), 549–550.

250. Thermo Fisher Scientific Inc, Manual, T.S.O.S., Dionex ICS-6000 Ion Chromatography System, **2018**. Retrieved from https://documents.thermofisher.com/TFS-Assets/CMD/manuals/man-22181-97002-ics-6000-man2218197002-en.pdf.

251. Bruins, A. P. Mechanistic aspects of electrospray ionization. *J. Chromatogr. A.* **1998**, *794*(1-2), 345–357.

252. Kaklamanos, G.; Aprea, E.; Theodoridis, G. Mass spectrometry: principles and instrumentation. In *Chemical analysis of food*, Academic Press, **2020**, 525–552.

Chapter 2

Atmospheric Fate of 4:2 Fluorotelomer Alcohol using an Oxidation Flow Reactor and Proton Transfer Reaction Time-of-Flight Mass Spectrometry

2.1 Abstract

Commonly used methodologies applied to studying the atmospheric degradation of per- and polyfluoroalkyl substances (PFAS) require analyses to be conducted offline and under dry conditions, potentially limiting the atmospheric relevance of the resulting mechanism and kinetics. We coupled an oxidation flow reactor (OFR) to a proton transfer reaction time-of-flight mass spectrometer (PTR-ToF-MS), focusing on the NO_x-free oxidation of a perfluorocarboxylic acid precursor – the 4:2 fluorotelomer alcohol (FTOH) – in the first application of this system to PFAS. The PTR-ToF-MS was calibrated under dry conditions (0 to 1% relative humidity, RH) and at RHs of 22%, 44%, and 60%. The oxidation of 4:2 FTOH by hydroxyl (OH) radicals was observed in real-time, as a function of RH, with PTR-ToF-MS detecting both primary and secondary 4:2 FTOH degradation products: the 4:2 fluorotelomer aldehyde and 4:2 fluorotelomer carboxylic acid, respectively. The resulting pseudo-first-order kinetics (k_{obs}) were determined and compared to previously reported FTOH values. The determined k_{obs} values were $(1.0 \pm 0.1) \times 10^{-12}$ (22% RH), $(7.4 \pm 0.8) \times 10^{-13}$ (44% RH), and $(7.2 \pm 0.8) \times 10^{-13}$ cm^3 $molecules^{-1}$ s^{-1} (60% RH), comparable to prior reports at 22% RH and lower as RH increased. This type of experiment demonstrates that the OFR-PTR-ToF-MS technique can be transferred to study other suspected, but uncharacterized, atmospheric PFAS transformations.

2.2 Introduction

For over seven decades, a diverse group of synthetic, fluorinated organic compounds known as per- and polyfluoroalkyl substances (PFAS) have been widely used for industrial and commercial applications. Due to the strength and stability of the carbon–fluorine bond, PFAS have ideal chemical properties, such as hydrophobicity and lipophobicity, and are utilized in

various applications (e.g., food packaging, textiles, electroplating of metals).[1] They can enter the atmosphere directly via emissions from manufacturing facilities, wastewater treatment plants, landfills, etc.,[1,2] and their terminal acid degradation products are very resistant to metabolic and environmental degradation.[3] Additionally, some PFAS are considered toxic and bioaccumulative; high levels of PFAS exposure have been associated with adverse health effects in humans[4-7] and wildlife.[8-12]

Volatile and semi-volatile atmospheric PFAS, such as fluorotelomer alcohols (FTOHs), are used in the fluoropolymer and surfactant industry and as chlorofluorocarbon replacements.[13] They are included in the formulations of a variety of products such as adhesives, polishes, paints, and electronic materials[14] and in some cases, FTOHs can be released directly into the environment from product use.[15] In 2006, the global production of FTOHs was estimated to be between 11 to 14×10^6 kg yr^{-1} with 40% of that production occurring in North America.[16,17] This group of compounds has an estimated atmospheric half-life of 10 to 20 days and are able to be widespread to achieve relatively uniform hemispheric distribution.[18] Several studies have reported gas-phase FTOHs at tens to hundreds of pg m^{-3} in samples from around the world.[19-22] Thus, their atmospheric degradation has been deemed as a plausible contributing source of perfluorocarboxylic acids (PFCAs) found in remote locations such as the Arctic.[23,24]

The atmospheric fate of gas-phase FTOHs has been the subject of several prior investigations, all of which used smog chambers and Fourier transform infrared spectroscopy (FTIR).[16,18,19] More recently, a chamber coupled with mass spectrometry enabled continuous measurements of the degradation products of hydrofluoroether alcohols, a subclass of PFAS, for the first time.[25] Collectively, these smog chamber studies – including the recent work on hydrofluoroether alcohols – were conducted under dry conditions, in part to minimize interference

from water vapour. Water is a well-known interferent in smog chamber studies employing methods such as fluorine-19 nuclear magnetic resonance spectroscopy (^{19}F NMR)[26], FTIR[27], and modern mass spectrometry techniques like iodide adduct chemical ionization mass spectrometry (I-CIMS).[28-32] As a result, although the effects of water vapour on the oxidation kinetics of non-fluorinated alcohols (20% to 95% relative humidity, RH)[33-38] have been explored to some extent, comparable data for fluorinated analogues such as FTOHs are lacking. Here we revisit the degradation of 4:2 FTOH under dry and humidified conditions to expand our mechanistic understanding of the atmospheric chemistry of this compound.

In this work, we apply proton transfer reaction time-of-flight mass spectrometry (PTR-ToF-MS) to the study of 4:2 FTOH oxidation by coupling it to an oxidation flow reactor (OFR). This new approach to measuring gas-phase PFAS allows us to examine its atmospheric degradation and formation of products, both facilitated by hydroxyl (OH) radicals. The use of OFR-PTR-ToF-MS can overcome the experimental limitations of performing oxidation chemistry under more atmospherically relevant RH conditions in the absence of NO_x ($NO + NO_2$). This work shows that: i) a PTR-ToF-MS can be used to measure gas-phase PFAS, ii) 4:2 FTOH degradation products can be identified in real-time using PTR-ToF-MS, and iii) OFR experiments can be used to study the degradation kinetics of 4:2 FTOH and, by extension, many other volatile PFAS.

2.3 Methodology

2.3.1 OFR Experiments

A custom-built OFR was used in these chamber experiments (Figure A-1) which has been described and characterized previously.[39-41] The current reactor is a fused quartz flow tube with a cone-shaped diffusion inlet and seven outlets. Six of the outlets act as exhaust to reduce gas-phase

wall losses and to maintain plug flow.[39] The flow rate through the 16 L OFR was approximately 2 L min^{-1}, resulting in a residence time of 8 mins. Using the density of air (1.293 kg m^{-3}) and dynamic viscosity of air (1.714×10^{-5} Pa s)[42], a Reynolds number of 16 was calculated to confirm laminar flow within the OFR during all experiments. These reactors utilize oxidants at concentrations considerably higher than the ambient atmosphere to accelerate oxidation chemistry.[43] Within minutes, exposures equivalent to multiple days or weeks of atmospheric oxidation are possible. These higher-than-ambient concentrations are generated by the photolysis of a chosen oxidant precursor using low-pressure ultraviolet (UV) lamps. Compared to traditional smog chambers, the rapid oxidation timeframes result in shorter sample residence times and reduced wall effects within an experiment.[44,45]

Oxidation flow reactors have been used to infer the transition between functionalization (i.e., oxygen addition)[46] and fragmentation (i.e., carbon-carbon bond cleavage)[47] for volatile organic compounds (VOCs), and the subsequent impact of these processes on secondary organic aerosol formation.[40,46,48] It has been noted that these experimental conditions may not fully reflect ambient reaction pathways under all conditions, and thus OFRs may have limitations on their atmospheric relevance, particularly with respect to oxidant formation and alkylperoxy radical (RO_2) chemistry.[43,49,50] The low-NO_x experiments described in this work follows the standard methodology consistent with OFR best practices; however, one limitation specific to this work is the elevated concentrations of hydroperoxyl (HO_2) radicals within the reactor relative to typical atmospheric levels. This increased HO_2 abundance can alter the radical chemistry by favouring RO_2 + HO_2 reactions over RO_2 + NO pathways, which can lead to differences in product distributions. Nonetheless, given that this study does not aim to quantitatively resolve product distributions, the influence of altered radical pathways is not expected to affect the main findings.

Approximately 750 parts-per-billion-by-volume (10^{-9} mol mol^{-1}, ppbv) of externally generated ozone (O_3, model TG-10; Ozone Solutions, San Antonio, TX, USA) was introduced into the OFR and was photolyzed using UV light at 254 nm provided by low-pressure mercury lamps (part number, P/N, 82-3309-9; Jelight Company Inc., Irvine, CA, USA). This produces $O(^1D)$, which reacts with water vapour to generate OH. This method is a well-established approach in OFR studies[43,51-54] and produces a steady-state OH concentration that can be quantitatively estimated using a carbon monoxide (CO) tracer. Radical production is influenced by O_3 and H_2O concentrations as well as UV lamp intensity, and this configuration is relatively resilient to OH suppression at O_3 levels reaching up to 70 parts-per-million (ppm) due to a higher OH concentration and enhanced HO_2 recycling, which helps maintain stable radical chemistry.[53] In the absence of light, we performed negative control experiments of 4:2 FTOH in the presence of residual O_3 to measure whether any loss took place on the timescales present in this system. The average temperature inside of the OFR was 23.0 ± 0.7°C and the RHs were controlled at 21.8 ± 0.7%, 44.0 ± 3.9%, and 59.6 ± 5.5% (model HMP60; Vaisala Oyj, Vantaa, Finland). The OH levels within the OFR were adjusted using the voltages applied to, and the number of, UV lamps. The OH exposure – the product of the average residence time in the reactor and OH concentration – was then estimated by measuring the rate of decay of CO[55] during offline calibrations (Figure A-2). Both CO and O_3 were measured using standard gas analyzers (CO by model 23r; ABB Inc – Los Gatos Research, San Jose, CA, USA and O_3 by model 202; 2B Technologies, Broomfield, CO, USA). The OH exposure values were determined using the second-order rate constant between CO and OH ($(1.54 \pm 0.14) \times 10^{-13}$ cm^3 $molecules^{-1}$ s^{-1})[56] and the resulting photochemical ages were calculated assuming a global average OH concentration (1.50×10^6 molecules cm^{-3})[57] (Section

A.1). The calculated OH exposure ranged from 1.94×10^{11} to 2.68×10^{12} molecules s cm^{-3}, and the corresponding photochemical ages at each RH are provided in Table A-1.

2.3.2 PTR-ToF-MS Measurements

A PTR-ToF-MS (Ionicon Analytik GmbH, Innsbruck, Austria) acquiring data at 0.5 Hz was used to measure the 4:2 FTOH as it reacted with OH radicals in real-time. The PTR-ToF-MS operating principles and its applications have been described in detail elsewhere.[58-62] Here, the PTR-ToF-MS drift tube pressure was maintained at 2.15 mbar and the electric field at a 600 V difference. The resulting electric field strength (E) and buffer gas density (N) ratio was 140 Townsend. The mass-to-charge ratio (m/z) of the ions are determined by the measured flight times, and an entire mass spectrum ($m/z \leq 480$) is produced with every pulse. Trichlorobenzene (housed in a permeation tube) was continuously added to the inlet to monitor m/z calibration of the instrument. The raw mass spectra were acquired using TofDaq (Tofwerk AG, Thun, Switzerland) and analyzed using Tofware (Tofwerk AG, Thun Switzerland). The instrument resolution was approximately 3500 $m/\Delta m$ for the 4:2 FTOH (exact m/z 265.027492) and high-resolution fitting provided analyte signal intensity based on their exact mass with 15 ± 1 ppm accuracy. Due to RH-dependent m/z shifts, observed masses for the reagent ion as well as 4:2 FTOH and its degradation products varied slightly across experiments. However, all values remained within the instrument's mass accuracy specification of 15 ± 1 ppm. Therefore, the exact protonated masses were used throughout for analyte identification and reporting.

Calibration was performed by delivering gas-phase 4:2 FTOH (2101-3-95; SynQuest Labs, Alachua, FL, USA) to the PTR-ToF-MS using a custom-made, temperature-controlled permeation device (PD).[63] Approximately 250 µL of 4:2 FTOH was added to a 60 mm perfluoroalkoxy tube

(3.2 mm inner diameter with 5 mm outer diameter, P/N 5733K73; McMaster-Carr, Aurora, OH, USA) and thermally sealed on both ends, allowing for a consistent mass of 4:2 FTOH gas to permeate at a constant temperature and pressure.[63,64] The PD was housed in an aluminum block that was temperature controlled using a cartridge heater and was regulated to 75.0 ± 0.1°C, while 10 mL min^{-1} of dry nitrogen gas flowed over the PD. The mass emission rate was quantified gravimetrically over 26 weeks as 254 ± 2 ng min^{-1} (Figure A-3). Calibrations covered 3 to 21 ppbv of 4:2 FTOH and were performed under RH conditions relevant to each experiment, which spanned 22%, 44%, and 60% RH (Section A.2, Figure A-4) using m/z 265.02749. This was required due to the potential for water vapour altering the instrument response. Calibrations were done through the OFR in the absence of light and O_3, with mixing ratios controlled by increasing the dilution flow. Zero air passed through a heated platinum catalyst held at 350°C and was used to acquire a background signal which was then subtracted from each calibration point and normalized to the isotope of the hydronium reagent ion ($H_3{}^{18}O^+$, m/z 21.022635) to generate instrument measurements with units of normalized counts per second (ncps).

2.3.3 Data Treatment: Rate Constant, k_{obs}

The rate constant (k_{obs}, cm^3 $molecule^{-1}$ s^{-1}) for the reaction of OH radicals with 4:2 FTOH was determined by measuring the decrease in FTOH signal as a function of OH exposure (Section A.3). Wall loss due to diffusion to the OFR surfaces can lead to lost analyte signal. Using the diffusion coefficient of 1-hexanol as a proxy[65], the estimated diffusion time across the reactor radius for 4:2 FTOH molecules was 417 s, slightly shorter than the experimental OFR gas residence time of 468 s. Given the similarity between these two values, the impact of surface effects was examined by fitting the system response times to single and double exponential

functions during the calibration (Table A-2) and k_{obs} determinations (Table A-3) at each RH (see Section 2.4.2).

2.4 Results and Discussion

2.4.1 PTR-ToF-MS: Technique for Measuring Gas-phase PFAS

There are few reports considering the applicability or limitations of using atmospheric mass spectrometry techniques for the detection of volatile PFAS in ambient air compared to controlled lab conditions. Here, the sensitivity and two-second limit of detection (LOD, assuming a signal-to-noise ratio of 3) for 4:2 FTOH under dry conditions were $(12.7 \pm 0.6) \times 10^{-3}$ ncps ppbv^{-1} and 63 parts-per-trillion by volume (10^{-12} mol mol^{-1}, pptv), respectively (Section A.4, Table A-4). The average sensitivity ($(70.4 \pm 2.3) \times 10^{-4}$ ncps ppbv^{-1}) and LOD (109 pptv) under humidified conditions was used for the corresponding experiments. Gaseous 4:2 FTOH has not been previously measured using PTR-ToF-MS and so the sensitivity and LOD values reported here cannot be directly compared to other studies. Rather, we directly compare against that of other common VOCs measured via PTR-ToF-MS. The sensitivity value reported here is much smaller than the sensitivity for common VOCs like acetone (30.9 ncps ppbv^{-1})[66] and ethanol (99.23 ncps ppbv^{-1}).[67] The lower sensitivity here is reasonable as we would expect FTOHs to have lower proton affinity (PA) than other VOCs due to the electron withdrawing properties from fluorination. While the PA for 4:2 FTOH has not been reported, that of 1:2 FTOH is 700 kJ mol^{-1}.[68] The length of the perfluorinated chain has little effect on FTOH properties[13]; hence, it is reasonable to assume the PA of the 4:2 FTOH is ~700 kJ mol^{-1}. This PA is similar to that of water (691 kJ mol^{-1})[69] but lower than those of commonly measured VOCs, such as n-propanol (786 to 791 kJ mol^{-1})[70] and acetone (812 kJ mol^{-1}).[71] Our 4:2 FTOH LOD was also found to be in a comparable range to that reported

for acetone using PTR-ToF-MS[66,72,73] (Table A-5), but higher than 4:2 FTOH measured by I-CIMS (7.9 pptv[74] and 2.9 pptv[75]). We note these LODs are orders of magnitude too high to detect ambient FTOHs because average measurements in North America (Table A-6), Europe, and Asia have not exceeded 220 ng m^{-3} (0.022 pptv).[1,16,22,76-78] The Vocus – a PTR-ToF-MS with the highest sensitivity and resolving power on the market – has reported LODs for common VOCs from 10 to 90 pptv[66,72,73] (Table A-5), which suggests even it would be unable to detect ambient FTOHs. Thus, a Vocus, a traditional PTR-ToF-MS, and an I-CIMS are not sufficiently sensitive for the detection of ambient FTOHs, but all are suitable for use in laboratory experiments.

2.4.2 PTR-ToF-MS: Real-time Detection of 4:2 FTOH Degradation Products

The experiments carried out in this work focused on the degradation of approximately 10 ppbv of 4:2 FTOH, in the absence of NO_x, at RHs of 22%, 44%, and 60%. Previous smog chamber studies have only investigated the reactivity of FTOHs, including the 4:2 FTOH, under dry conditions with OH radicals and chlorine (Cl) atoms, in both the presence and absence of NO_x.[18,79-83] The OH-initiated oxidation pathways of FTOHs were first proposed in 2004 (Figure 2-1) and based on smog chamber experiments initiated with Cl atoms, as they react in the same manner with FTOHs as OH radicals.[18] In this initial study, the in-situ FTIR analysis of FTOH oxidation products suggested the formation of PFCAs at yields below 10%. Due to the low yields and overlapping IR spectra of PFCAs, FTIR lacked the sensitivity and specificity needed for their definitive identification or quantification. Instead, an offline analysis using liquid chromatography tandem mass spectrometry revealed that each FTOH produced a corresponding PFCA retaining the full perfluorinated chain (i.e., 8:2 FTOH produced perfluorononanoic acid). These analyses also showed the formation of a homologous series of shorter-chain PFCAs; for example, the

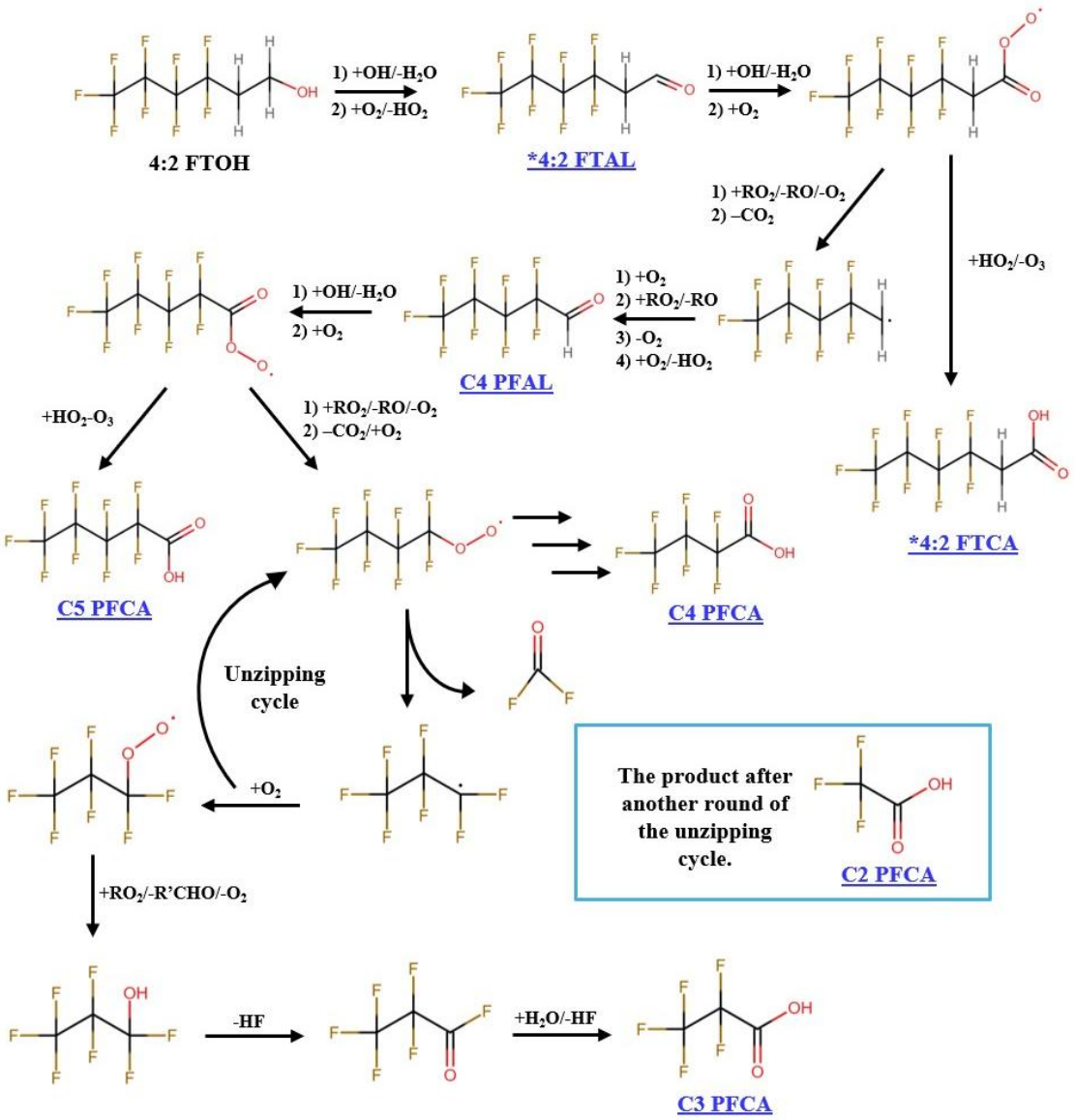

Figure 2-1. The proposed atmospheric degradation mechanism of the 4:2 FTOH + OH radicals in a NO_x-free environment.[18] The expected stable end products are underlined in blue, with the specific products observed in this work being asterisked (*). The compounds shown are as follows: 4:2 fluorotelomer aldehyde (4:2 FTAL); 4:2 fluorotelomer carboxylic acid (4:2 FTCA); perfluoropentanal (C4 PFAL); perfluoropentanoic acid (C5 PFCA); perfluorobutanoic acid (C4 PFCA); pentafluoropropionic acid (C3 PFCA); and trifluoroacetic acid (TFA, C2 PFCA).

oxidation of 8:2 FTOH resulted in PFCAs ranging from trifluoroacetic acid upward. Additionally, ^{19}F NMR detected perfluorinated acid fluorides, which can hydrolyze to their corresponding carboxylic acids, thereby providing further evidence for PFCA formation during FTOH

atmospheric oxidation. As a result, various studies have since concluded that, in a low NO_x or NO_x-free environment, the atmospheric oxidation of FTOHs results in the aldehyde product in a yield close to 100%.[18,23,79,80,84] Thus, the expected first generation oxidation product here was the 4:2 fluorotelomer aldehyde (4:2 FTAL; $CF_3(CF_2)_3CH_2CHO$). Further oxidation of 4:2 FTAL has been reported to yield the secondary products 4:2 fluorotelomer carboxylic acid (4:2 FTCA; $CF_3(CF_2)_3CH_2COOH$), 4:2 perfluorinated aldehyde (4:1 PFAL; $CF_3(CF_2)_3CHO$), and the corresponding peracid ($CF_3(CF_2)_3CH_2C(O)OOH$).[18,80]

During these experiments, the PTR-ToF-MS detected two degradation products – the primary 4:2 FTAL (m/z 263.011842) and the secondary 4:2 FTCA (m/z 279.006757). No subsequent oxidation products, such as PFCAs (e.g., TFA), were detected under the described experimental conditions. This likely results from limitations of the PTR-ToF-MS being hindered for compounds with strong surface interactions and unfavourable PAs. For example, TFA[69] has a reported PA of 711.7 kJ mol^{-1}, which is comparable to that of water[69] and 4:2 FTOH[68] but lower still than those of commonly measured VOCs.[70,71] Additionally, while a secondary product was observed here, further oxidation to PFCAs is expected based on previous chamber and modelling studies[18,23] but would almost certainly be present below the detection limits of the instrument and require an additional chemical ionization mass spectrometer.[85] Nevertheless, as this study focused on demonstrating the feasibility of real-time PFAS oxidation kinetics and early-stage product identification, Figure 2-2 clearly illustrates that as 4:2 FTOH degrades (blue trace), the 4:2 FTAL primary product signal (pink trace) initially increases before it starts to decrease upon reaction to form 4:2 FTCA (purple trace). This trend is also seen at RHs of 44% and 60% (Figure A-5). The 4:2 FTAL primary product can also react with OH and photolyze. Available light in the OFR is provided at shorter wavelengths than the most abundant actinic photons, which could also affect

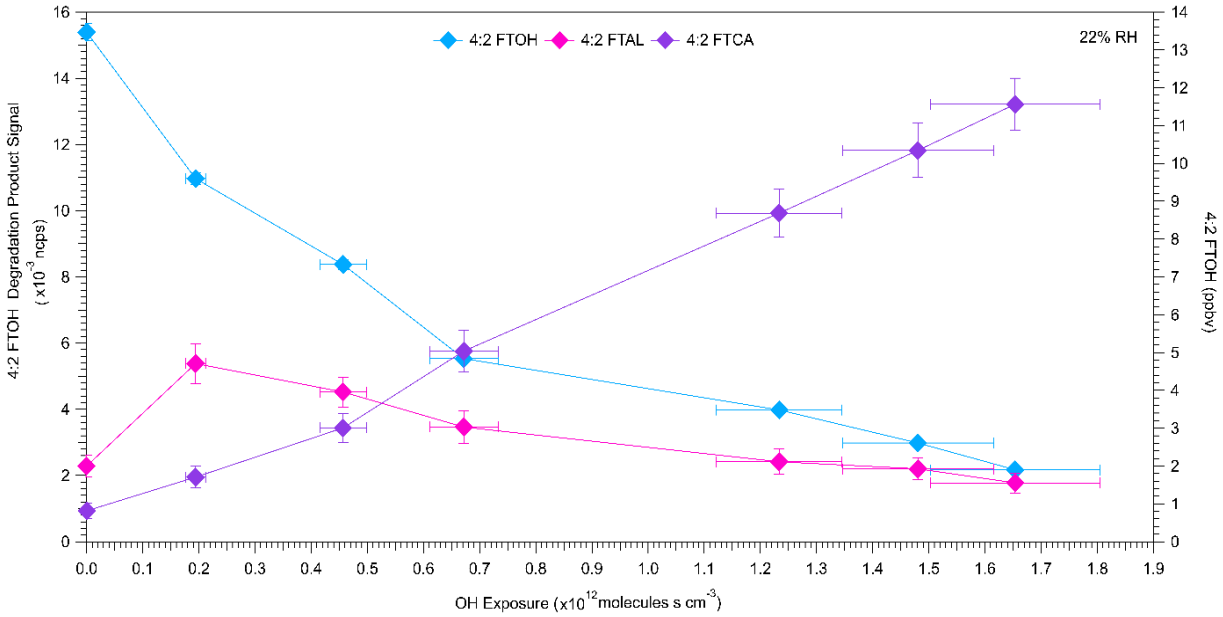

Figure 2-2. The change in 4:2 FTOH (ppbv; m/z 265.027492) and the detected degradation products (4:2 FTAL, m/z 2630.11842; 4:2 FTCA, m/z 279.006757; ncps) with increasing OH exposure (molecules s cm^{-3}) at 22% RH. The right y-axis depicts the decreasing mixing ratio of permeating 4:2 FTOH, and the propagated error at each point, as it reacts with OH radicals. On the left y-axis are the normalized average signals of the degradation products, with each point's corresponding standard deviation. The x-axis shows the OH exposure and the propagated error at each point.

the observed interconversion rates here. In comparing the cross-sections of the 1:2 and 6:2 FTALs at different wavelengths[84,86] (Table A-7), it is possible for photolysis of 4:2 FTAL to occur at 254 nm. However, secondary photolytic product yields within the OFR here are likely underestimated as less photolysis is likely to occur at shorter wavelengths.[84,86] Without calibration standards for the 4:2 FTAL and 4:2 FTCA, we cannot calculate product yields for comparison to previous studies.[87] A third peak of interest was also noted (m/z 260.996192; Figure A-5), which we suspect to be the dehydrated form of the 4:2 FTCA. Based on previously reported PTR-MS product-ion fragmentation of non-fluorinated organic acids, the dehydrated 4:2 FTCA may have been formed via the loss of water following protonation via hydronium.[87] Similar ionization has been previously observed for acetic acid[88] and is believed to result here in an elemental formula of

$CF_3(CF_2)_3CH_2C(O)^+$, with the positive charge on the carbonyl carbon.[87] As with our calibrations for the 4:2 FTOH, the PTR-MS sensitivity towards the detected products decreases with increasing RH.[87-89]

As shown by their widespread global distribution, including to remote regions, some PFAS can undergo long-range atmospheric transport (i.e., neutral, volatile PFAS like FTOHs) or transport via global ocean currents (i.e., ionic PFAS).[13,23] With the gas-phase oxidation of FTOHs to PFCAs expected to be more prevalent in remote locations where NO_x concentrations are low[18,23], this NO_x-free work should be more atmospherically representative of such environments. Previous NO_x-free experiments primarily investigated FTOH reaction mechanisms with Cl atoms. This was done for two main reasons: i) Cl atoms can be a reliable proxy for OH radicals and ii) Cl atoms can be more cleanly generated than OH radicals in a Pyrex smog chamber. Where Cl atoms were produced via the photolysis of Cl_2, OH radicals were generated by photolyzing methyl nitrite – generating NO as a byproduct.[90] Other techniques have been used in recent years to cleanly generate OH radicals, such as hydrogen peroxide (H_2O_2) in an Ingeniven FEP Teflon Gas Sampling Bag to observe hydrofluoroether oxidation.[25] Historically, the photolysis of H_2O_2 in Pyrex smog chambers fitted with FTIR has been avoided due to the presence of water vapour. These limitations demonstrate the advantages of the described OFR approach here. Since the mechanism of OH oxidation with 4:2 FTOH under NO_x-free conditions was previously inferred from Cl-initiated experiments, our results ultimately show that the mechanism under OH-initiated, NO_x-free conditions is consistent with those predictions.

2.4.3 Oxidation Kinetics: OH Initiated Reaction of 4:2 FTOH

The rate constant for the reactivity of OH radicals with the 4:2 FTOH was determined by measuring the decrease in signal as a function of OH exposure. From the blank-corrected and normalized data, the observed rate constant, k_{obs} (cm^3 $molecule^{-1}$ s^{-1}), for the oxidation of 4:2 FTOH was determined using EQ 1.[41]

$$\ln\left(\frac{[4{:}2\ \mathrm{FTOH}]}{[4{:}2\ \mathrm{FTOH}]_0}\right) = \ln\left(\frac{I}{I_0}\right) = -k_{obs}[OH]t \qquad \textbf{(EQ 1)}$$

Here $[4{:}2\ FTOH]_0$ is the initial 4:2 FTOH concentration (molecules cm^{-3}) and [4:2 FTOH] is the measured 4:2 FTOH concentration (molecules cm^{-3}) at a given OH exposure (molecules s cm^{-3}), which is the product of the OH concentration ([OH], molecules cm^{-3}) and the average residence time (t) in the OFR (s). The I_0 and I terms are the signal intensities (ncps) for the 4:2 FTOH in the absence and presence of OH radicals, respectively. The reaction is a bimolecular process following a pseudo-first-order reaction, with 4:2 FTOH in excess relative to OH. The value of k_{obs} was determined by plotting the natural logarithm of the intensity ratios against OH exposure (Figure 2-3). At the three different RHs explored here, the k_{obs} values (Figure 2-3a, Table A-3) were $(1.0 \pm 0.1) \times 10^{-12}$, $(6.5 \pm 0.4) \times 10^{-13}$, and $(6.3 \pm 0.1) \times 10^{-13}$ cm^3 $molecules^{-1}$ s^{-1} at 22%, 44%, and 60% RH, respectively. The linear regression coefficients indicate good linearity at all RHs, with $R^2 \geq 0.97$ (Table A-3). Statistical analyses (t-test) were performed and the rate constant at 22% RH was significantly different from those at both 44% and 60% RH ($p < 1 \times 10^{-6}$), whereas no statistically significant difference was observed between 44% and 60% RH ($p = 0.26$). This suggests that the reaction behaviour changes appreciably between 22% and 44% RH but remains relatively stable at higher humidity levels.

In the only study which reported the OH oxidation rate of 4:2 FTOH in the presence of NO_x and under dry conditions, the rate constant was (1.07 ± 0.22) x 10^{-12} cm^3 $molecules^{-1}$ s^{-1}.[79] The k_{obs} values measured here are the same order of magnitude. The results are also consistent when compared to kinetic data for the 1:2 and 6:2 FTOHs (Table 2-1), where chain-length has been found to not affect the kinetics of longer-chained FTOH reactions with OH.[13] It should also be noted that the 4:2 FTOH rate constants measured at 44% and 60% RH are 37% slower (Table A-3, Section A.3). Water may induce greater wall effects or altered PTR-MS sensitivity. The 4:2 FTOH could diffuse to the surface of the OFR (417 s) within the experimental residence time (468 s), leading to the potential for wall losses. The instrument response was also calculated at each RH by fitting to single and double exponential functions to account for any changes from surface effects in the OFR and of the PTR-ToF-MS sampling inlet. Previously, instrument and inlet surface effects for highly surface active gases (e.g., hydrochloric acid) have been characterized by fitting decay curves to a double exponential.[91-94] Since the 4:2 FTOH is much more volatile and unable to ionize, it is not surprising that system response times were marginally affected resulting in k_{obs} that were higher by ~25% at the two higher RHs when taking these into account with the double exponential approach.

The final average OH reaction rate constant values at 44% and 60% RH are (7.4 ± 0.8) × 10^{-13} and (7.2 ± 0.8) × 10^{-13} cm^3 $molecules^{-1}$ s^{-1}, respectively, when averaging the results obtained from all three calculation approaches (Table 2-1). Statistical analyses (t-test) were performed and the 'original' k_{obs} at 22% RH was found to be significantly different from both averaged k_{obs} at 44% and 60% RH ($p < 1 \times 10^{-4}$). However, no statistically significant difference was observed between the averaged rate constants at 44% and 60% RH ($p = 0.79$). Although a statistically significant decrease in the observed rate constants was found between 22% and ≥44% RH, the

described experimental setup does not allow us to distinguish between a water vapour dependence of the 4:2 FTOH oxidation and systematic effects associated with increased RH, including diffusion driven wall interactions. While diffusion timescale estimates and exponential fitting analyses suggest that such effects are unlikely to fully account for the observed difference, they cannot be completely ruled out. This suggests that the reaction behaviour differs notably between 22% and 44% RH and increasing it further to 60% RH does not result in statistically significant additional change. Thus, we cannot reliably say that the averaged 44% and 60% RH rate constants are different or that diffusion driven wall interactions are contributing to the slower rates.

Table 2-1. Summary of the 4:2 FTOH + OH rate constants found within this study at different RHs compared to the previously determined value under dry conditions, as well as those constants determined for the 1:2 and 6:2 FTOHs. The 4:2 FTOH k_{obs} at 22% RH is the 'original' rate constant while those at 44% and 60% RH are reported as an average of the three calculation approaches described in the main text.

Analyte	Rate constant (cm^3 $molecules^{-1}$ s^{-1})	RH (%)	Method	Reference
4:2 FTOH $CF_3(CF_2)_3CH_2CH_2OH$	$(1.0 \pm 0.1) \times 10^{-12}$	22	OFR coupled to PTR-ToF-MS	This work
	$(7.4 \pm 0.8) \times 10^{-13}$	44		
	$(7.2 \pm 0.8) \times 10^{-13}$	60		
	$(1.07 \pm 0.22) \times 10^{-12}$	0	Relative rate	Ellis et al.[79]
1:2 FTOH $CF_3CH_2CH_2OH$	$(8.9 \pm 0.3) \times 10^{-13}$		Pulsed laser photolysis-laser-induced fluorescence	Kelly et al.[82]
	$(1.08 \pm 0.05) \times 10^{-12}$		Relative rate	
	$(6.91 \pm 0.91) \times 10^{-13}$			Hurley et al.[81]
6:2 FTOH $CF_3(CF_2)_5CH_2CH_2OH$	$(7.9 \pm 0.8) \times 10^{-13}$			Kelly et al.[82]

Another advantage of using OFR-PTR-ToF-MS in this work is its ability to directly study the decay of 4:2 FTOH with OH radicals. Previously reported chamber experiments have investigated the degradation and reactivity of FTOHs with OH radicals[79,81,82] and Cl atoms[18,80-83]

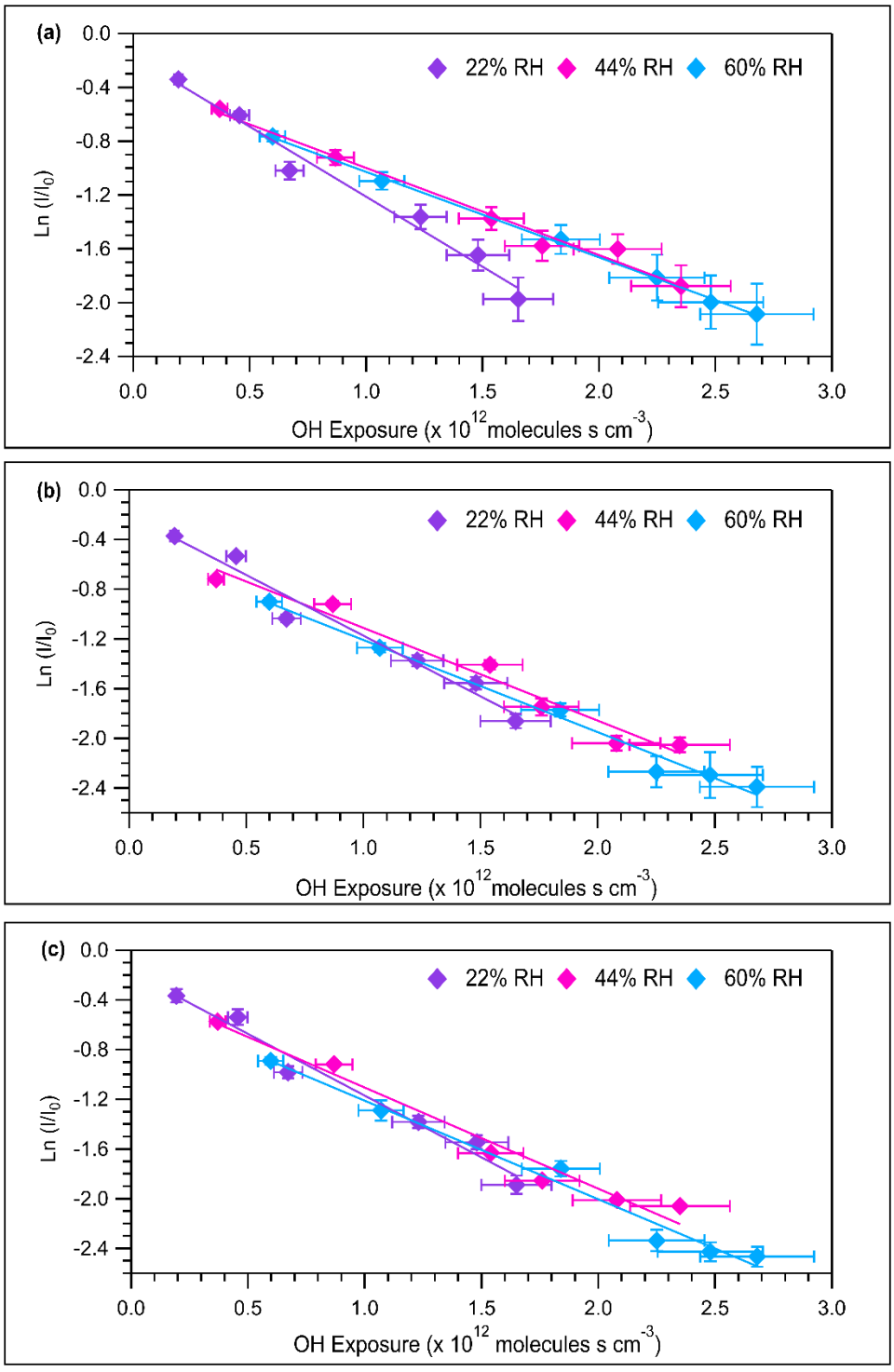

Figure 2-3. Loss of the 4:2 FTOH following reaction with OH radicals at different OH exposures and RHs. The response time of this method is shown here in the **(a)** original data as well as after being fitted to **(b)** single and **(c)** double exponential functions. The k_{obs} values were determined using a linear regression analysis weighted to the error in the y-axis. The k_{obs} values for the three different data sets can be found in Table A-3.

in both the presence and absence of NO_x; however, these experiments were done only under dry conditions. It should first be noted that saturated FTOHs, such as 4:2 FTOH and the structurally related 1:2 FTOH, do not react appreciably with O_3 under atmospheric conditions. Negative control experiments performed with O_3 did not detect any change in FTOH concentration at experimental timescales, consistent with previous findings that reported an atmospheric lifetime of approximately 5900 days for 1:2 FTOH with respect to reaction with O_3, assuming a background concentration of 40 ppb.[81] Together, these observations demonstrate that O_3 is not responsible for any measurable loss of 4:2 FTOH in our experiments; therefore, the decay of 4:2 FTOH in the OFR is dominated by reaction with OH radicals. Consequently, the atmospheric fate of FTOHs is likely limited by reaction with OH[13], as more than 90% of FTOHs oxidize via hydrogen abstraction at the carbon adjacent to the alcohol group.[79,83] Both OH radicals and Cl atoms are electrophilic with modest steric demands and both reactions are exothermic; thus, the abstraction behaviour of Cl atoms and OH radicals are expected to be similar.[95] While Cl atoms have shown to be a good surrogate for OH radicals, they are not perfect proxies due to differing regional selectivity.[96] This experimental setup allows the study of OH chemistry in the presence of water vapour instead of requiring Cl atoms. Consequently, the work described here contains the first measured rate constants made for the reaction between 4:2 FTOH and OH radicals at different RHs. The described OFR-PTR-ToF-MS technique is not limited by the presence of humidity, like FTIR, and can instead study chemistry under more atmospherically relevant conditions and make kinetic measurements on the timescale of seconds as opposed to minutes.[97] While previous research on PFCA precursors achieved good time resolution and observed similar degradation products, continuous high time resolution opens the door to study faster aspects of this gas-phase chemistry.[73,74,85,98,99] In an atmospheric context, humidity and light can vary on timescales of

minutes to hours while the abundance of radicals can change on timescales of seconds. To observe such chemistry requires fast, in-situ measurement techniques that capture rapidly shifting effects, which the PTR-ToF-MS is capable of.[85] In the context of chamber experiments, the high temporal resolution is beneficial to the observation of real-time reaction kinetics as well as the potential to detect transient intermediates. Ultimately, we suspect that while this greater time resolution may not be important for the study of all compounds, it could be beneficial for some and should be applied when possible.

2.5 Atmospheric Implications/Future Directions

For the first time, 4:2 FTOH degradation kinetics and products were measured at varying RHs relevant to the range found in the atmosphere. The potential effects of RH on the gas-phase kinetics of FTOHs, and PFAS in general, is not well understood within the literature and requires further investigation. Previous work has shown that RH can accelerate and decelerate the kinetics of non-fluorinated alcohols (20% to 95% RH).[33-38] Although the mechanism for a potential RH enhancement of 4:2 FTOH is not yet known, studies of similar molecules may provide insight into possible reaction pathways. Previous work on small alcohols (e.g., ethanol and n-propanol) suggest that water can enhance reaction rates by forming weak complexes with both the alcohol and OH.[34] These complexes can increase the effective collision probability as well as stabilize the transition state, making product formation more favourable. Further evidence is needed for 4:2 FTOH, as this water-assisted effect is reaction-specific and varies between systems[35], before a plausible mechanism for the water vapour dependence in our experiments can be proposed.

The PTR-ToF-MS detected the 4:2 FTAL and the 4:2 FTCA. In the future, if calibrations can be conducted, the identified degradation products can be further investigated as a function of

OH exposure or RH. Our observed rate coefficients at 22%, 44%, and 60% RH were similar in magnitude to the literature value reported at 0% RH[79], although lower rates were observed at higher RH. The latter cannot be conclusively attributed to a role for water vapour in the kinetics as experimental errors inherent to the OFR and PTR-ToF-MS cannot be ruled out. The primary objective of this work was to evaluate the feasibility of combining an OFR with PTR-ToF-MS to measure PFAS oxidation kinetics and to provide initial constraints on OH reaction kinetics for 4:2 FTOH under varying RH conditions. As the RH issues experienced here do not negate the kinetic findings, the results presented in this work highlight the need for continued investigation into the role of water vapour in the atmospheric oxidation of volatile PFAS and provides a foundation for improving mechanistic understanding of these processes in future studies.

While our experimental technique allows real-time study of 4:2 FTOH oxidation under atmospherically relevant RH, several limitations should be noted. High RH can influence instrument sensitivity and may contribute to systematic biases reflected in measured rate constants. The radical chemistry within the OFR may also differ from atmospheric conditions due to elevated HO_2 concentrations, which can alter product distributions. Additionally, this approach is most effective for volatile or semi-volatile species with favourable PAs, making detection of stable end products such as short-chain PFCAs challenging. Complementary analytical techniques may be required to observe full degradation to terminal oxidation products. Despite these limitations, this approach provides valuable real-time constraints on early-stage PFAS oxidation chemistry by detecting intermediates and highlights directions for future improvements. Ultimately, this work demonstrates the power of the OFR-PTR-ToF-MS as a useful real-time measurement technique to study gas-phase transformations of volatile PFAS within a laboratory setting. With an ability to study atmospherically realistic oxidative chemistry at different RHs, the described instrumental

setup has the potential to study suspected, but uncharacterized, mechanisms of atmospheric PFAS formation and degradation.

2.6 References

1. Ahrens, L.; Shoeib, M.; Harner, T.; Lee, S. C.; Guo, R.; Reiner, E. J. Wastewater treatment plant and landfills as sources of polyfluoroalkyl compounds to the atmosphere. *Environ. Sci. Technol.* **2011**, *45*(19), 8098−8105.

2. Tian, Y.; Yao, Y.; Chang, S.; Zhao, Z.; Zhao, Y.; Yuan, X.; Wu, F.; Sun, H. Occurrence and phase distribution of neutral and ionizable per-and polyfluoroalkyl substances (PFASs) in the atmosphere and plant leaves around landfills: a case study in Tianjin, China. *Environ. Sci. Technol.* ***2018****, 52*(3), 1301−1310.

3. Cousins, I. T.; DeWitt, J. C.; Glüge, J.; Goldenman, G.; Herzke, D.; Lohmann, R.; Ng, C. A.; Scheringer, M.; Wang, Z. The high persistence of PFAS is sufficient for their management as a chemical class. *Environ. Sci.: Process. Impacts.* **2020**, *22*(12), 2307–12.

4. Pérez, F.; Nadal, M.; Navarro-Ortega, A.; Fàbrega, F.; Domingo, J. L.; Barceló, D.; Farré, M. Accumulation of perfluoroalkyl substances in human tissues. *Environ. Int.*, **2013**, *59*, 354–362.

5. Vieira, V. M.; Hoffman, K.; Shin, H. M.; Weinberg, J. M.; Webster, T. F.; Fletcher, T. Perfluorooctanoic acid exposure and cancer outcomes in a contaminated community: a geographic analysis. *Environ. Health Perspectives*, **2013**, *121*(3), 318–323.

6. Sun, P.; Nie, X.; Chen, X.; Yin, L.; Luo, J.; Sun, L.; Wan, C.; Jiang, S. Nrf2 signaling elicits a neuroprotective role against PFOS-mediated oxidative damage and apoptosis. *Neurochem. Res.* **2018**, *43*(12), 2446–2459.

7. Fenton, S. E.; Ducatman, A.; Boobis, A.; DeWitt, J. C.; Lau, C.; Ng, C.; Smith, J. S.; Roberts, S. M. Per-and polyfluoroalkyl substance toxicity and human health review: Current state of knowledge and strategies for informing future research. *Environ. Toxicol. Chem.* **2021**, *40*(3), 606–630.

8. Giesy, J. P.; Kannan, K. Global distribution of perfluorooctane sulfonate in wildlife. *Environ. Sci. Technol.* **2001**, *35*(7), 1339–1342.

9. Tomy, G. T.; Budakowski, W.; Halldorson, T.; Helm, P. A.; Stern, G. A.; Friesen, K.; Pepper, K.; Tittlemier, S. A.; Fisk, A. T. Fluorinated organic compounds in an eastern Arctic marine food web. *Environ. Sci. Technol.* **2004**, *38*(24), 6475–6481.

10. Valdersnes, S.; Nilsen, B. M.; Breivik, J. F.; Borge, A.; Maage, A. Geographical trends of PFAS in cod livers along the Norwegian coast. *PloS one*, **2017**, *12*(5), e0177947.

11. Muir, D.; Bossi, R.; Carlsson, P.; Evans, M.; De Silva, A.; Halsall, C.; Rauert.; Herzke, D.; Hung, H.; Letcher, R.; Rigét, F. Levels and trends of poly-and perfluoroalkyl substances in the Arctic environment – An update. *Emerg. Contam.* **2019**, *5*, 240–271.

12. Roos, A. M.; Gamberg, M.; Muir, D.; Kärrman, A.; Carlsson, P.; Cuyler, C.; Lind, Y.; Bossi, R.; Rigét, F. Perfluoroalkyl substances in circum-Arctic Rangifer: caribou and reindeer. *Environ. Sci. Pollut. Res.* **2022**, *29*(16), 23721–23735.

13. Young, C. J.; Mabury, S. A. *Atmospheric Perfluorinated Acid Precursors: Chemistry, Occurrence, and Impacts*. Edited by N. Whitacre, D. M.; Springer New York, New York, **2010**. doi: 10.1007/978-1-4419-6880-6887.

14. Sulbaek Andersen, M. P.; Nielsen, O. J.; Hurley, M. D.; Ball, J. C.; Wallington, T. J.; Ellis, D. A.; Martin, J. W.; Mabury, S. A. Atmospheric chemistry of 4: 2 fluorotelomer alcohol (n-C4F9CH2CH2OH): Products and mechanism of Cl atom initiated oxidation in the presence of NO x. *J. Phys. Chem. A.* **2005**, *109*(9), 1849−1856.

15. Lehmler, H. J. Synthesis of environmentally relevant fluorinated surfactants—a review. *Chemosphere*. **2005**, *58*(11), 1471−1496.

16. Martin, J. W.; Muir, D. C. G.; Moody, C. A.; Ellis, D. A.; Kwan, W. C.; Solomon, K. R.; Mabury, S. A. Collection of Airborne Fluorinated Organics and Analysis by Gas Chromatography/Chemical Ionization Mass Spectrometry. *Anal. Chem*. **2002**, *74*(3), 584–590. https://doi.org/10.1021/ac015630d.

17. Dupont Global PF. Strategy Update: Presentation to USEPAOPPT, January 31, 2005. US Public Docket AR. 1914;226.

18. Ellis, D. A.; Martin, J. W.; De Silva, A. O.; Mabury, S. A.; Hurley, M. D.; Sulbaek Andersen, M. P.; Wallington, T. J. Degradation of Fluorotelomer Alcohols: A Likely Atmospheric Source of Perfluorinated Carboxylic Acids. *Environ. Sci. Technol.* **2004**, *38*(12), 3316–3321. https://doi.org/10.1021/es049860w.

19. Nilsson, H.; Kärrman, A.; Rotander, A.; van Bavel, B.; Lindström, G.; Westberg, H. Inhalation exposure to fluorotelomer alcohols yield perfluorocarboxylates in human blood? *Environ. Sci. Technol.* **2010**, *19*, 7717–7722.

20. Stock, N. L.; Lau, F. K.; Ellis, D. A.; Martin, J. W.; Muir, D. C. G.; Mabury, S. A. Polyfluorinated Telomer Alcohols and Sulfonamides in the North American Troposphere. *Environ. Sci. Technol.* **2004**, *38*(4), 991–996. https://doi.org/10.1021/es034644t.

21. Jahnke, A.; Ahrens, L.; Ebinghaus, R.; Temme, C. Urban versus Remote Air Concentrations of Fluorotelomer Alcohols and Other Polyfluorinated Alkyl Substances in Germany. *Environ. Sci. Technol.* **2007**, *41*(3), 745–752. https://doi.org/10.1021/es0619861.

22. Li, J.; Del Vento, S.; Schuster, J.; Zhang, G.; Chakraborty, P.; Kobara, Y.; Jones, K. C. Perfluorinated Compounds in the Asian Atmosphere. *Environ. Sci. Technol.* **2011**, *45*(17), 7241–7248. https://doi.org/10.1021/es201739t.

23. Wallington, T. J.; Hurley, M. D.; Xia, J.; Wuebbles, D. J.; Sillman, S.; Ito, A.; Penner, J. E.; Ellis, D. A.; Martin, J.; Mabury, S. A.; Nielsen, O. J.; Sulbaek Andersen, M. P. Formation of C7F15COOH (PFOA) and Other Perfluorocarboxylic Acids during the Atmospheric Oxidation of 8:2 Fluorotelomer Alcohol. *Environ. Sci. Technol.* **2006**, *40*(3), 924–930. https://doi.org/10.1021/es051858x.

24. Pickard, H. M.; Criscitiello, A. S.; Spencer, C.; Sharp, M. J.; Muir, D. C. G.; De Silva, A. O.; Young, C. J. Continuous Non-Marine Inputs of Per- and Polyfluoroalkyl Substances to the High Arctic: A Multi-Decadal Temporal Record. *Atmos. Chem. Phys*. **2018**, *18*(7), 5045–5058.

25. Folkerson, A. P.; Schneider, S. R.; Abbatt, J. P.; Mabury, S. A. Avoiding regrettable replacements: can the introduction of novel functional groups move PFAS from recalcitrant to reactive?. *Environ. Sci. Technol.* **2023**, *57*(44), 17032–17041.

26. Gerig, J. T. Fluorine nmr. Biophysics Textbook Online. **2001**, 1−35.

27. Zhang, X.; He, A.; Guo, R.; Zhao, Y.; Yang, L.; Morita, S.; Xu, Y.; Noda, I.; Ozaki, Y. A. New Approach to Removing Interference of Moisture from FTIR Spectrum. *Spectrochim. Acta A Mol. Biomol. Spectrosc.* **2022**, *265*, 120373.

28. Huey, L. G.; Hanson, D. R.; Howard, C. J.; Reactions of SF6-and I-with Atmospheric Trace Gases. *J. Phys. Chem.* **1995**, *99*(14), 5001−5008.

29. Slusher, D. L.; Huey, L. G.; Tanner, D. J.; Flocke, F. M.; Roberts, J. M. A thermal dissociation–chemical ionization mass spectrometry (TD-CIMS) technique for the simultaneous measurement of peroxyacyl nitrates and dinitrogen pentoxide. *J. Geophys. Res. Atmos.* **2004**, *109*, D19315, doi:10.1029/2004JD004670.

30. Lee, B. H.; Lopez-Hilfiker, F. D.; Mohr, C.; Kurtén, T.; Worsnop, D. R.; Thornton, J. A. An iodide-adduct high-resolution time-of-flight chemical-ionization mass spectrometer: Application to atmospheric inorganic and organic compounds. *Environ. Sci. Technol.* **2014**, *48*(11), 6309–6317.

31. Brophy, P.; Farmer, D. K. A switchable reagent ion high resolution time-of-flight chemical ionization mass spectrometer for real-time measurement of gas phase oxidized species: characterization from the 2013 southern oxidant and aerosol study. *Atmos. Meas. Tech.* **2015**, *8*(7), 2945–2959.

32. Lopez-Hilfiker, F. D.; Iyer, S.; Mohr, C.; Lee, B. H.; D'Ambro, E. L.; Kurtén, T.; Thornton, J. A. Constraining the sensitivity of iodide adduct chemical ionization mass spectrometry to multifunctional organic molecules using the collision limit and thermodynamic stability of iodide ion adducts. *Atmos. Meas. Tech.* **2016**, *9*(4), 1505–1512.

33. Jara-Toro, R. A.; Hernández, F. J.; Taccone, R. A.; Lane, S. I.; Pino, G. A. Water Catalysis of the Reaction between Methanol and OH at 294 K and the Atmospheric Implications. *Angew. Chem. Int. Ed.* **2017**, *56*(8), 2166–2170.

34. Jara-Toro, R. A.; Hernández, F. J.; Garavagno, M. D.; Taccone, R. A.; Pino, G. A. Water catalysis of the reaction between hydroxyl radicals and linear saturated alcohols (ethanol and n-propanol) at 294 K. *Phys. Chem. Chem. Phys.* **2018**, *20*(44), 27885–27896.

35. Chao, W.; Jr-Min Lin, J.; Takahashi, K.; Tomas, A.; Yu, L.; Kajii, Y.; Batut, S.; Schoemaecker, C.; Fittschen, C. Water vapor does not catalyze the reaction between methanol and OH radicals. *Angew. Chem. Int. Ed.* **2019**, *58*(15), 5013–5017.

36. Xu, L.; Tsona, N. T.; Tang, S.; Li, J.; Du, L. Role of (H2O) n (n= 1–2) in the gas-phase reaction of ethanol with hydroxyl radical: mechanism, kinetics, and products. *ACS Omega*. **2019**, *4*(3), 5805–5817.

37. Weber, I.; Bouzidi, H.; Krumm, B.; Schoemaecker, C.; Tomas, A.; Fittschen, C. Water does not catalyze the reaction of OH radicals with ethanol. *Phys. Chem. Chem. Phys.* **2020**, *22*(14), 7165–7168.

38. Neeman, E. M.; González, D.; Blázquez, S.; Ballesteros, B.; Canosa, A.; Antiñolo, M.; Vereecken, L. Albaladejo, J.; Jiménez, E. The impact of water vapor on the OH reactivity toward CH3CHO at ultra-low temperatures (21.7–135.0 K): Experiments and theory. *J. Chem. Phys.* **2021**, *155*(3), 034306.

39. Li, K.; Liggio, J.; Han, C.; Liu, Q.; Moussa, S. G.; Lee, P.; Li, S. M. Understanding the impact of high-NOx conditions on the formation of secondary organic aerosol in the photooxidation of oil sand-related precursors. *Environ. Sci. Technol.* **2019**, *53*(24), 14420–14429.

40. Li, K.; Liggio, J.; Lee, P.; Han, C.; Liu, Q.; Li, S. M. Secondary Organic Aerosol Formation from \alpha -Pinene, Alkanes, and Oil-Sands-Related Precursors in a New Oxidation Flow Reactor. *Atmos. Chem. Phys.* **2019**, *19*(15), 9715–9731. https://doi.org/10.5194/acp-19-9715-2019.

41. Liu, Q.; Liggio, J.; Li, K.; Lee, P.; Li, S. M. Understanding the impact of relative humidity and coexisting soluble iron on the OH-initiated heterogeneous oxidation of organophosphate flame retardants. *Environ. Sci. Technol.* **2019**, *53*(12), 6794−6803.

42. Massman, W. J. Molecular diffusivities of Hg vapor in air, O2 and N2 near STP and the kinematic viscosity and thermal diffusivity of air near STP. Atmos. Environ. **1999**, *33*(3), 453–457.

43. Peng, Z.; Jimenez, J. L. Radical Chemistry in Oxidation Flow Reactors for Atmospheric Chemistry Research. *Chem. Soc. Rev.* **2020**, *49*(9), 2570–2616. https://doi.org/10.1039/C9CS00766K.

44. Palm, B. B.; Campuzano-Jost, P.; Ortega, A. M.; Day, D. A.; Kaser, L.; Jud, W.; Karl, T.; Hansel, A.; Hunter, J. F.; Cross, E. S.; Kroll, J. H.; Peng, Z.; Brune, W. H.; Jimenez, J. L. In Situ Secondary Organic Aerosol Formation from Ambient Pine Forest Air Using an Oxidation Flow Reactor. *Atmos. Chem. Phys.* **2016**, *16*(5), 2943–2970. https://doi.org/10.5194/acp-16-2943-2016.

45. Brune, W. H. The Chamber Wall Index for Gas–Wall Interactions in Atmospheric Environmental Enclosures. *Environ. Sci. Technol.* **2019**, *53*(7), 3645–3652. https://doi.org/10.1021/acs.est.8b06260.

46. Lambe, A. T.; Onasch, T. B.; Croasdale, D. R.; Wright, J. P.; Martin, A. T.; Franklin J. P.; Massoli, P.; Kroll, J. H.; Canagaratna, M. R.; Brune, W. H.; Worsnop, D. R. Transitions from functionalization to fragmentation reactions of laboratory secondary organic aerosol (SOA) generated from the OH oxidation of alkane precursors. *Environ. Sci. Technol.* **2012**, *46*(10), 5430–5437.

47. Jimenez, J. L.; Canagaratna, M. R.; Donahue, N. M.; Prevot., A. S.; Zhang, Q.; Kroll, J. H.; DeCarlo, P. F.; Allan, J. D.; Coe, H.; Ng, N. L.; Aiken, A. C. Evolution of organic aerosols in the atmosphere. *Science*. **2009**, *326*(5959), 1525–1529.

48. Tkacik, D. S.; Lambe, A. T.; Jathar, S.; Li, X. Presto, A. A.; Zhao, Y.; Blake D.; Meinardi, S.; Jayne, J. T.; Croteau, P. L.; Robinson, A. L. Secondary organic aerosol formation from in-use motor vehicle emissions using a potential aerosol mass reactor. *Environ. Sci. Technol.* **2014**, *48*(19), 11235−11242.

49. Peng, Z.; Jimenez, J. L. Modeling of the chemistry in oxidation flow reactors with high initial NO. *Atmos. Chem. Phys.* 2017, *17*(19), 11991−12010.

50. Ma, X.; Li, K.; Zhang, S.; Yang, Z.; Xu, L.; Tsona Tchinda, N.; Du, L. Oxidation Flow Reactor and Its Application in Secondary Organic Aerosol Formation in Laboratory Studies. *Environ. Sci. Technol. Air.* **2025**, *2*(8), 1394−1410.

51. George, I. J.; Vlasenko, A.; Slowik, J. G.; Broekhuizen, K.; Abbatt, J. P. Heterogeneous oxidation of saturated organic aerosols by hydroxyl radicals: uptake kinetics, condensed-phase products, and particle size change. *Atmos. Chem. Phys.* **2007**, *7*(16), 4187−4201.

52. Peng, Z.; Day, D. A.; Stark, H.; Li, R.; Lee-Taylor, J.; Palm, B. B.; Brune, W. H.; Jimenez, J. L. HOx radical chemistry in oxidation flow reactors with low-pressure mercury lamps systematically examined by modeling. *Atmos. Meas. Tech.* **2015**, *8*(11), 4863−4890.

53. Rowe, J.P., Lambe, A.T. and Brune, W.H., 2020. Effect of varying the λ= 185 and 254 nm photon flux ratio on radical generation in oxidation flow reactors. *Atmos. Chem. Phys.* **2020**, *20*(21), 13417−13424.

54. Czech, H.; Yli-Pirilä, P.; Tiitta, P.; Ihalainen, M.; Hartikainen, A.; Schneider, E.; Martens, P.; Paul, A.; Hohaus, T.; Rüger, C. P.; Jokiniemi, J. The effect of aging conditions at equal

OH exposure in an oxidation flow reactor on the composition of toluene-derived secondary organic aerosols. *Environ. Sci.: Atmos.* **2024**, *4*(7), 718−731.

55. Liu, Q.; Liggio, J.; Wu, D.; Saini, A.; Halappanavar, S.; Wentzell, J. J.; Harner, T.; Li, K.; Lee, P.; Li, S. M. Experimental study of OH-initiated heterogeneous oxidation of organophosphate flame retardants: Kinetics, mechanism, and toxicity. *Environ. Sci. Technol.* **2019**, *53*(24), 14398−14408.

56. Liu, Y.; Sander, S. P. Rate Constant for the OH + CO Reaction at Low Temperatures. *J. Phys. Chem. A.* **2015**, *119*(39), 10060−10066. https://doi.org/10.1021/acs.jpca.5b07220

57. Mao, J.; Ren, X.; Brune, W. H.; Olson, J. R.; Crawford, J. H.; Fried, A.; Huey, L. G.; Cohen, R. C.; Heikes, B.; Singh, H. B.; Blake, D. R. Airborne measurement of OH reactivity during INTEX-B. *Atmos. Chem. Phys*. **2009**, *9*(1), 163−173.

55. Blake, R. S.; Monks, P. S.; Ellis, A. M. Proton-Transfer Reaction Mass Spectrometry. *Chem. Rev.* **2009**, *109*(3), 861–896. https://doi.org/10.1021/cr800364q.

59. de Gouw, J.; Warneke, C. Measurements of volatile organic compounds in the earth's atmosphere using proton-transfer-reaction mass spectrometry. *Mass Spectrom. Rev.* **2007**, *26*(2), 223−257.

60. Jordan, A.; Haidacher, S. G. H. E. H.; Hanel, G.; Hartungen, E.; Märk, L.; Seehauser, H.; Schottkowsky, R.; Sulzer, P.; Märk, T. D. A high resolution and high sensitivity proton-transfer-reaction time-of-flight mass spectrometer (PTR-TOF-MS). *Int. J. Mass Spectrom.* **2009**, *286*(2-3), 122–128.

61. Li, S. M.; Leithead, A.; Moussa, S. G.; Liggio, J.; Moran, M. D.; Wang, D.; Hayden, K.; Darlington, A.; Gordon, M.; Staebler, R.; Makar, P. A. Differences between measured and reported volatile organic compound emissions from oil sands facilities in Alberta, Canada. *Proc. Natl. Acad. Sci.* **2017**, *114*(19), E3756−E3765.

62. Wren, S. N.; Liggio, J.; Han, Y.; Hayden, K.; Lu, G.; Mihele, C. M.; Mittermeier, R. L.; Stroud, C.; Wentzell, J. J.; Brook, J. R. Elucidating real-world vehicle emission factors from mobile measurements over a large metropolitan region: a focus on isocyanic acid, hydrogen cyanide, and black carbon. *Atmos. Chem. Phys*. **2018**, *18*(23), 16979−7001.

63. Lao, M.; Crilley, L. R.; Salehpoor, L.; Furlani, T. C.; Bourgeois, I.; Neuman, J. A.; Rollins, A. W.; Veres, P. R.; Washenfelder, R. A.; Womack, C. C.; Young, C. J. A portable, robust, stable and tunable calibration source for gas-phase nitrous acid (HONO). *Atmos. Meas. Tech.* **2020**, *13*(11), 5873−5890.

64. Furlani, T. C.; Ye, R.; Stewart, J.; Crilley, L. R.; Edwards, P. M.; Kahan, T. F.; Young, C. J. Development and validation of a new in situ technique to measure total gaseous chlorine in air. *Atmos. Meas. Tech.* **2023**, *6*(1), 181−193.

65. Tang, M. J.; Shiraiwa, M.; Pöschl, U.; Cox, R. A.; Kalberer, M. Compilation and evaluation of gas phase diffusion coefficients of reactive trace gases in the atmosphere: Volume 2. Diffusivities of organic compounds, pressure-normalised mean free paths, and average Knudsen numbers for gas uptake calculations. *Atmos. Chem. Phys*. **2015**, 5585−5598.

66. Lee, A. K.; Abbatt, J. P.; Leaitch, W. R.; Li, S. M.; Sjostedt, S. J.; Wentzell., J. J.; Liggio, J.; Macdonald, A. M. Substantial secondary organic aerosol formation in a coniferous forest: observations of both day-and nighttime chemistry. *Atmos. Chem. Phys*. **2016**, *16*(11), 6721−6733.

67. Wu, C.; Wang, C.; Wang, S.; Wang, W.; Yuan, B.; Qi, J.; Wang, B.; Wang, H.; Wang, C.; Song, W.; Wang, X. Measurement report: Important contributions of oxygenated compounds to emissions and chemistry of volatile organic compounds in urban air. *Atmos. Chem. Phys*. **2020**, *20*(23), 14769−14785.

68. Delatour, T.; Menin, L.; Eriksen, B.; Gasilova, N.; Mujahid, C.; Theurillat, X. Dielectric barrier discharge ionization procures characteristic adducts of polyfluoroalkyl substances (PFAS) amenable by gas chromatography-mass spectrometry. *Microchem. J*. **2024**, *204*, 111012.

69. Hunter, E. P.; Lias, S. G. Evaluated gas phase basicities and proton affinities of molecules: an update. *J. Phys. Chem. Ref. Data.* **1998**, *27*(3), 413−656.

70. Long, J.; Munson, B. Proton affinities of some oxygenated compounds. J. Am. Chem. Soc. **1973**, *95*(8), 2427−2432.

71. Bouchoux, G.; Buisson, D. A.; Bourcier, S.; Sablier, M. Application of the kinetic method to bifunctional bases: ESI tandem quadrupole experiments. *Int. J. Mass Spectrom.* **2003**, *228*(2−3), 1035−1054.

72. Krechmer, J.; Lopez-Hilfiker, F.; Koss, A.; Hutterli, M.; Stoermer, C.; Deming, B.; Kimmel, J.; Warneke, C.; Holzinger, R.; Jayne, J.; Worsnop, D. Evaluation of a new reagent-ion source and focusing ion–molecule reactor for use in proton-transfer-reaction mass spectrometry. *Anal. Chem.* **2018**, *90*(20), 12011−12018.

73. Jensen, A. R.; Koss, A. R.; Hales, R. B.; de Gouw, J. A. Measurements of volatile organic compounds in ambient air by gas-chromatography and real-time Vocus PTR-TOF-MS: calibrations, instrument background corrections, and introducing a PTR Data Toolkit. *Atmos. Meas. Tech.* **2023**, *16*(21), 5261−5285.

74. Riedel, T. P.; Lang, J. R.; Strynar, M. J.; Lindstrom, A. B.; Offenberg, J. H. Gas-Phase Detection of Fluorotelomer Alcohols and Other Oxygenated Per- and Polyfluoroalkyl Substances by Chemical Ionization Mass Spectrometry. *Environ. Sci. Technol. Lett.* **2019**, *6*(5), 289–293. https://doi.org/10.1021/acs.estlett.9b00196.

75. Mattila, J. M.; Offenberg, J. H. Measuring Short-Chain per- and Polyfluoroalkyl Substances in Central New Jersey Air Using Chemical Ionization Mass Spectrometry. *J. Air Waste Manag. Assoc.* **2024**, *74*(8), 531–539. https://doi.org/10.1080/10962247.2024.2366491.

76. Shoeib, M.; Harner, T.; Vlahos, P. Perfluorinated Chemicals in the Arctic Atmosphere. *Environ. Sci. Technol.* **2006**, *40*(24), 7577−7583.

77. Barber, J. L.; Berger, U.; Chaemfa, C.; Huber, S.; Jahnke, A.; Temme, C.; Jones, K. C. Analysis of per-and polyfluorinated alkyl substances in air samples from Northwest Europe. *J. Environ. Monit.* ***2007****, 9*(6), 530−541.

78. Lin, A. M.; Thompson, J. T.; Koelmel, J. P.; Liu, Y.; Bowden, J. A.; Townsend, T. G. Landfill gas: a major pathway for neutral per-and polyfluoroalkyl substance (PFAS) release. *Environ. Sci. Technol. Lett.* **2024**, *11*(7), 730−737.

79. Ellis, D. A.; Martin, J. W.; Mabury, S. A.; Hurley, M. D.; Sulbaek Andersen, M. P.; Wallington, T. J. Atmospheric lifetime of fluorotelomer alcohols. *Environ. Sci. Technol.* **2003**, *37*(17), 3816−3820.

80. Hurley, M. D.; Ball, J. C.; Wallington, T. J.; Sulbaek Andersen, M. P.; Ellis, D. A.; Martin, J. W.; Mabury, S. A. Atmospheric chemistry of 4: 2 fluorotelomer alcohol (CF3 (CF2) 3CH2CH2OH): Products and mechanism of Cl atom initiated oxidation. *J. Phys. Chem. A.* **2004**, *108*(26), 5635−5642.

81. Hurley, M. D.; Misner, J. A.; Ball, J. C.; Wallington, T. J.; Ellis, D. A.; Martin, J. W.; Mabury, S. A.; Sulbaek Andersen, M. P. Atmospheric Chemistry of CF3CH2CH2OH: Kinetics, Mechanisms and Products of Cl Atom and OH Radical Initiated Oxidation in the Presence and Absence of NOX. *J. Phys. Chem. A*. **2005**, *109*(43), 9816−9826.

82. Kelly, T.; Bossoutrot, V.; Magneron, I.; Wirtz, K.; Treacy, J.; Mellouki, A.; Sidebottom, H.; Le Bras, G. A kinetic and mechanistic study of the reactions of OH radicals and Cl atoms with 3, 3, 3-trifluoropropanol under atmospheric conditions. *J. Phys. Chem. A.* **2005**, *109*(2), 347−355.

83. Papadimitriou, V. C.; Papanastasiou, D. K.; Stefanopoulos, V. G.; Zaras, A. M.; Lazarou, Y. G.; Papagiannakopoulos, P. Kinetic study of the reactions of Cl atoms with CF3CH2CH2OH, CF3CF2CH2OH, CHF2CF2CH2OH, and CF3CHFCF2CH2OH. *J. Phys. Chem. A.* **2007**, *111*(45), 11608−11617.

84. Chiappero, M. S.; Malanca, F. E.; Argüello, G. A.; Wooldridge, S. T.; Hurley, M. D.; Ball, J. C.; Wallington, T. J.; Waterland, R. L.; Buck, R. C. Atmospheric chemistry of perfluoroaldehydes (CxF2x+1CHO) and fluorotelomer aldehydes (CxF2x+ 1CH2CHO): quantification of the important role of photolysis. *J. Phys. Chem. A.* **2006**, *110*(43), 11944−11953.

85. Young, C. J.; Joudan, S.; Tao, Y.; Wentzell, J. J.; Liggio, J. High time resolution ambient observations of gas-phase perfluoroalkyl carboxylic acids: implications for atmospheric sources. *Environ. Sci. Technol. Lett.* **2024**, *11*(12), 1348−1354.

86. Sellevåg, S. R.; Kelly, T.; Sidebottom, H.; Nielsen, C. J. A study of the IR and UV-Vis absorption cross-sections, photolysis and OH-initiated oxidation of CF3CHO and CF3CH2CHO. *Phys. Chem. Chem. Phys.* **2004**, *6*(6), 1243−1252.

87. Pagonis, D.; Sekimoto, K.; de Gouw, J. A library of proton-transfer reactions of H3O+ ions used for trace gas detection. *J. Am. Soc. Mass Spectrom.* **2019**, *30*(7), 1330−1335.

88. Baasandorj, M.; Millet, D. B.; Hu, L.; Mitroo, D.; Williams, B. J. Measuring acetic and formic acid by proton-transfer-reaction mass spectrometry: sensitivity, humidity dependence, and quantifying interferences. *Atmos. Meas. Tech.* **2015**, *8*(3), 1303−1321.

89. Ernle, L.; Wang, N.; Bekö, G.; Morrison, G.; Wargocki, P.; Weschler, C. J.; Williams, J. Assessment of aldehyde contributions to PTR-MS m/z 69.07 in indoor air measurements. *Environ. Sci.: Atmos.* **2023**, *3*(9), 1286−1295.

90. Butt, C. M.; Young, C. J.; Mabury, S. A.; Hurley, M. D.; Wallington, T. J. Atmospheric Chemistry of 4: 2 Fluorotelomer Acrylate [C4F9CH2CH2OC(O)CH=CH2]: Kinetics, Mechanisms, and Products of Chlorine-Atom-and OH-Radical-Initiated Oxidation. *J. Phys. Chem. A*. **2009**, *113*(13), 3155−3161.

91. Zahniser, M. S.; Nelson, D. D.; McManus, B.; Kebabian, P. L.; Lloyd, D. Measurement of trace gas fluxes using tunable diode laser spectroscopy. Philos. Trans. R. Soc. A. **1995,** *351*(1696), 371−382.

92. Ellis, R. A.; Murphy, J. G.; Pattey, E.; Van, Haarlem, R.; O'Brien, J. M.; Herndon, S. C. Characterizing a quantum cascade tunable infrared laser differential absorption spectrometer (QC-TILDAS) for measurements of atmospheric ammonia. *Atmos. Meas. Tech.* **2010**, *3*(2), 397−406.

93. Moravek, A.; Singh, S.; Pattey, E.; Pelletier, L.; Murphy, J. G. Measurements and quality control of ammonia eddy covariance fluxes: a new strategy for high-frequency attenuation correction. *Atmos. Meas. Tech.* **2019**, *12*(11), 6059−78.

94. Furlani, T. C.; Veres, P. R.; Dawe, K. E.; Neuman, J. A.; Brown, S. S.; VandenBoer, T. C.; Young, C. J. Validation of a new cavity ring-down spectrometer for measuring tropospheric gaseous hydrogen chloride. *Atmos. Meas. Tech.* **2021**, *14*(8), 5859−5871.

95. Poutsma, M. L. Evolution of structure–reactivity correlations for the hydrogen abstraction reaction by chlorine atom. *J. Phys. Chem. A*. **2013**, *117*(4), 687−703.

96. Poutsma, M. L. Evolution of structure–reactivity correlations for the hydrogen abstraction reaction by hydroxyl radical and comparison with that by chlorine atom. *J. Phys. Chem. A*. 2013, *117*(30), 6433−49.

97. Young, C. J.; Hurley, M. D.; Wallington, T. J.; Mabury, S. A. Atmospheric chemistry of 4: 2 fluorotelomer iodide (n-C4F9CH2CH2I): Kinetics and products of photolysis and reaction with OH radicals and Cl atoms. *J. Phys. Chem. A*. **2008**, *112*(51), 13542−13548.

98. Veres, P.; Roberts, J. M.; Warneke, C.; Welsh-Bon, D.; Zahniser, M.; Herndon, S.; Fall, R.; de Gouw, J. Development of negative-ion proton-transfer chemical-ionization mass spectrometry (NI-PT-CIMS) for the measurement of gas-phase organic acids in the atmosphere. *Int. J. Mass Spectrom.* **2008**, *274*(1−3), 48−55.

99. Bowers, B. B.; Thornton, J. A.; Sullivan, R. C. Evaluation of Iodide Chemical Ionization Mass Spectrometry for Gas and Aerosol-Phase per- and Polyfluoroalkyl Substances (PFAS) Analysis. *Environ. Sci.: Process. Impacts.* **2023**, *25*(2), 277–287. https://doi.org/10.1039/D2EM00275B.

Appendix A: Supporting Information for Chapter 2

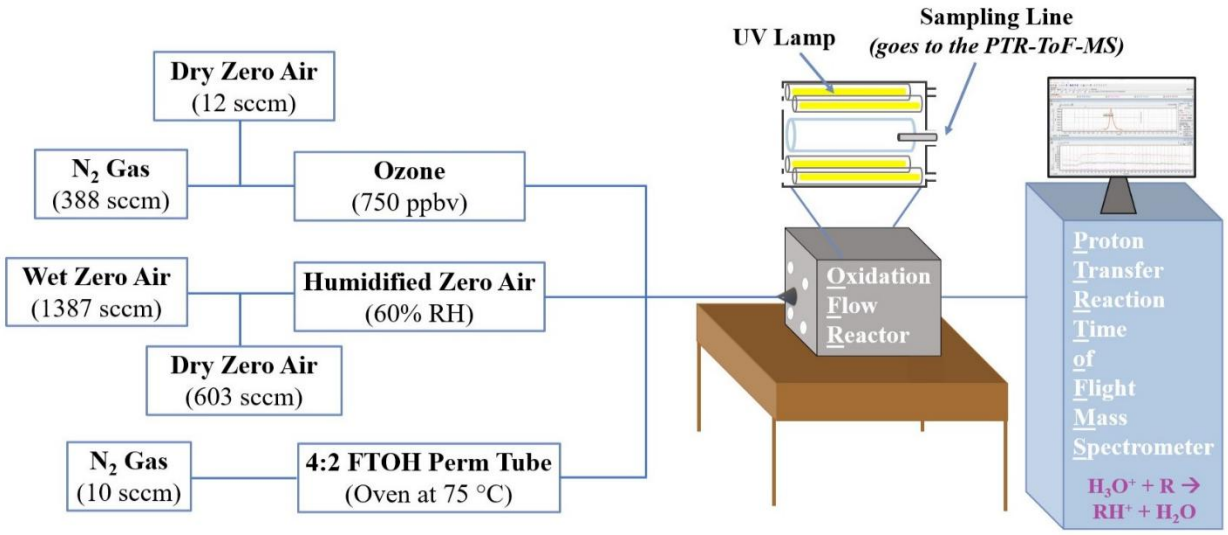

Figure A-1. Simplified schematic of the experimental setup, e.g., at 60% RH, utilized in the described chamber experiments. Specific to the proposed research, UV light at 254 nm is provided by low-pressure mercury lamps to photolyze externally generated O_3. This photolysis produces $O(^1D)$ which then reacts with water vapour in the reactor (grey-outlined cylinder) to generate the necessary OH radicals. Approximately 10 mL min^{-1} of nitrogen gas (N_2) is constantly flowing over a permeation device housing the liquid 4:2 FTOH. The N_2 flow containing permeated 4:2 FTOH then meets a flow of humified zero air before combining with the O_3 flow. This total flow (O_3 + humified zero air + 4:2 FTOH) then enters a conical diffusion inlet leading into the OFR prior to passing into the PTR-ToF-MS.

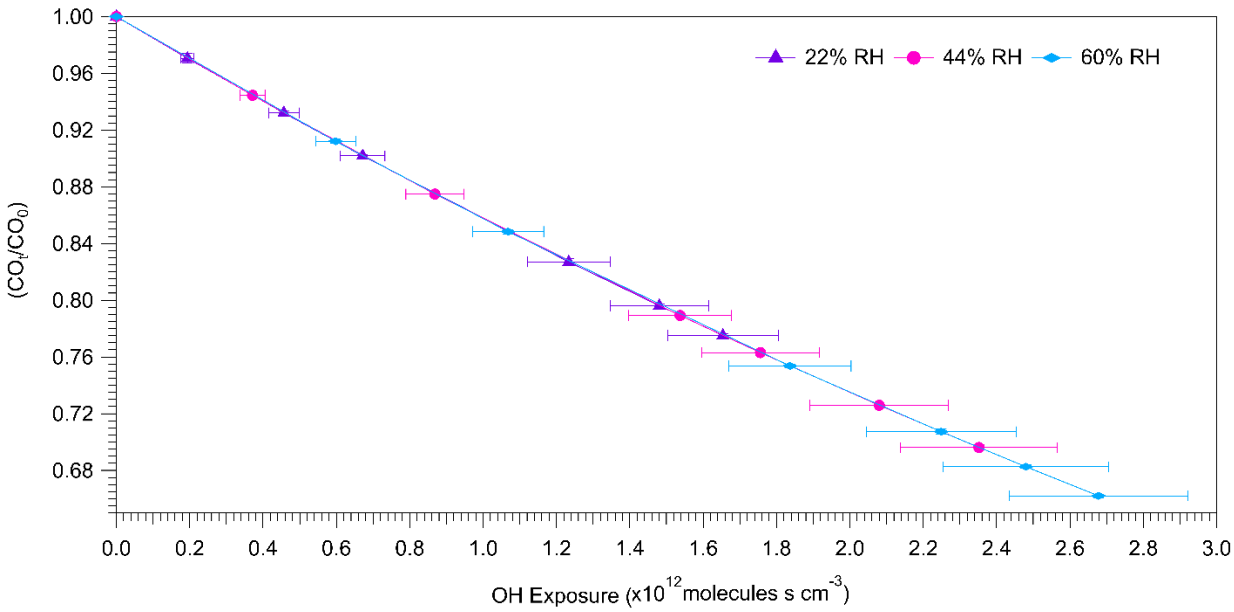

Figure A-2. Offline calibrations were performed to measure the decay of CO with increasing OH exposure (molecules s cm^{-3}). Plotted against OH exposure is the ratio of $[CO]_0$, the initial CO concentration (parts-per-million-by-volume; 10^{-6} mol mol^{-1}, ppmv) without O_3 photolysis to generate OH (i.e., UV lamps were off; ~1.07 to 1.08 ppmv), and $[CO]_t$, the CO concentration in the presence of constant OH from O_3 (i.e., UV lamps were turned on).

A.1 Determining OH Exposures at Different Relative Humidities

The OH exposure (molecules s cm^{-3}), which is the product of OH concentration (molecules cm^{-3}) and residence time (s) in the OFR, was determined by measuring the loss of CO as a function of time with respect to OH concentration (Figure A-2, EQ A1).

$$\text{OH exposure} = -\left(\frac{1}{k_{CO}}\right) \ln \frac{[CO]_t}{[CO]_0} \qquad \textbf{(EQ A1)}$$

Here k_{CO} is the second-order rate constant at 298 K ((1.54 ± 0.14) × 10^{-13} cm^3 $molecules^{-1}$ s^{-1})[1], $[CO]_0$ is the CO concentration without O_3 photolysis (i.e., UV lamps were off) to generate OH, and $[CO]_t$ is the CO concentration in the presence of constant OH from O_3 photolysis controlled by voltages applied when the UV lamps were turned on.[2] The reaction between CO and OH is bimolecular and corresponds to a second-order rate law:

$$\frac{\Delta[CO]}{\Delta t} = -k_{CO}[CO][OH] \qquad \textbf{(EQ A2)}$$

Within the OFR, OH is continuously being produced via the photolysis of externally generated O_3 and is assumed to be constant over the residence time. Thus, under this condition, the reaction follows pseudo-first-order kinetics with respect to CO. Therefore, EQ A2 can be rewritten as:

$$\frac{\Delta[CO]}{\Delta t} = -k'[CO] \qquad \textbf{(EQ A3)}$$

Then with respect to the conduct of an experiment over a given observation time for CO as:

$$\frac{\Delta[CO]_t}{[CO]_0} = -k'\Delta t \qquad \textbf{(EQ A4)}$$

Here, the OH exposure is defined as the time integrated OH concentration:

$$\text{OH exposure} = [\text{OH}]\Delta t \qquad \textbf{(EQ A5)}$$

Substituting EQ A5 into EQ A4 and rearranging to obtain an expression for OH exposure yields EQ A1.

The errors of the $\ln\left(\frac{[\text{CO}]_t}{[\text{CO}]_0}\right)$ term (EQ A6) and of the OH exposure (EQ A7) were determined to assess the precision of the kinetic method.

$$\frac{\text{Sy}}{\text{y}} = \sqrt{\left(\frac{[CO]_0\, error}{[CO]_0}\right)^2 + \left(\frac{[CO]_t}{[CO]_t}\right)^2} \qquad \textbf{(EQ A6)}$$

$$\frac{\text{Sy}}{\text{y}} = \sqrt{\left(\frac{k_{CO}\, error}{k_{CO}}\right)^2 + \left(\frac{ln\left(\frac{[CO]_t}{[CO]_0}\right) error}{ln\left(\frac{[CO]_t}{[CO]_0}\right)}\right)^2} \qquad \textbf{(EQ A7)}$$

Table A-1. The OH exposure ranges and corresponding atmospheric photochemical ages when assuming a global average tropospheric OH concentration of 1.50×10^6 molecules cm^{-3}.[3]

Relative Humidity	**OH Exposure Ranges (molecules s cm^{-3})**	**Photochemical Age Range (days)**
22%	1.94×10^{11} to 1.65×10^{12}	1.50 to 12.76
44%	3.71×10^{11} to 2.35×10^{12}	2.86 to 18.15
60%	5.98×10^{11} to 2.68×10^{12}	4.61 to 20.66

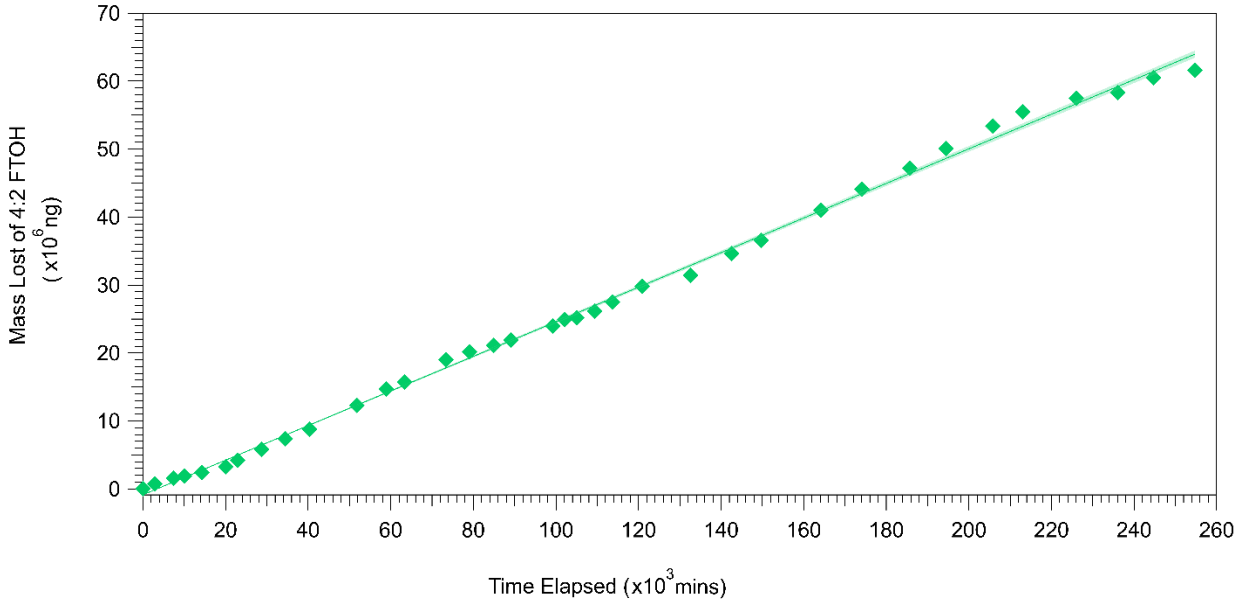

Figure A-3. Gas-phase 4:2 FTOH was generated using a temperature-controlled (75°C), custom-made permeation device. Plotted here is the mass of 4:2 FTOH lost (ng) over a 26-week period. The permeation device's emission rate was determined as 254 ± 2 ng min^{-1} with a R^2 value of 0.9977 and a relative standard deviation, indicated by the green shading over each marker, of ± 0.8291%.

A.2 Calibrating the PTR-ToF-MS for 4:2 FTOH

Assuming standard temperature and pressure, the following equations were used to calculate the 4:2 FTOH mixing ratios (EQ A8; ppbv), and their respective errors (EQ A9), on the calibration curves:

$$[4{:}\,2\ \mathrm{FTOH}] = y = (E_{4:2\ \mathrm{FTOH}})(Q_{4:2\ \mathrm{FTOH}})(MW_{4:2\ \mathrm{FTOH}})(V_m)(1 \times 10^9 \mathrm{ppbv}) \qquad \textbf{(EQ A8)}$$

$$\frac{Sy}{y} = \sqrt{\left(\frac{E_{4:2\ \mathrm{FTOH}}\ \mathrm{error}}{E_{4:2\ \mathrm{FTOH}}}\right)^2 + \left(\frac{\sqrt{(Q_{N_2}\ \mathrm{error})^2 + (\ Q_{ZA}\ \mathrm{error})^2}}{(Q_{N_2}\mathrm{error} + Q_{ZA})}\right)^2} \qquad \textbf{(EQ A9)}$$

In EQ A8, $E_{4:2\ FTOH}$ is the emission rate (ng min^{-1}) of the gaseous 4:2 FTOH generated using a custom-made permeation device, $Q_{4:2\ FTOH}$ is the volumetric flow rate within the OFR (L min^{-1}) during each experiment, $MW_{4:2\ FTOH}$ is the molecular weight of the 4:2 FTOH (g mol^{-1}), and V_m is the molar volume of air (~22.4 L mol^{-1}). In EQ A9, Q_{N_2} and N_{ZA} are the volumetric flow rates of nitrogen gas and zero air maintained by their respective mass flow controllers (mL min^{-1}).

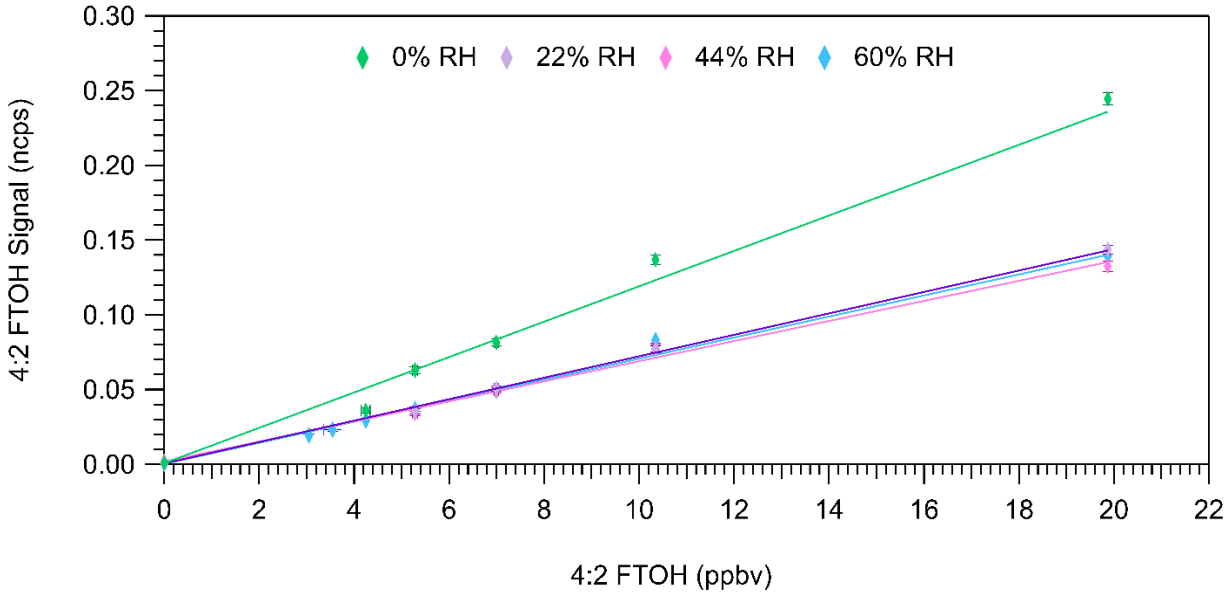

Figure A-4. Calibration curves for the 4:2 FTOH at 0%, 22%, 44%, and 60% RH. Prior to starting the calibration, a dilution flow of zero air – containing no 4:2 FTOH – flowed through the system. Each RH had a R^2 greater than 0.99 and a minimum of three non-zero points. The y-axis depicts the blank corrected and normalized average signal of the 4:2 FTOH (ncps) and each calibration point's corresponding standard deviation. The x-axis shows the mixing ratio of 4:2 FTOH permeating off the permeation device (ppbv) and the propagated error at each calibration point.

A.3 OFR: Assessing the Role of System Artifacts

To assess the impact of RH on the 4:2 FTOH + OH rate constants, three approaches were taken to determine the role of system artifacts. First, we ensured the flow within the OFR was laminar and calculated a Reynolds (Re; EQ A10 to A13) number of 16 indicative of this (i.e., Re < 2000) for an OFR residence time (τ) of 468 s and an OFR volume (V) of 0.016 m^3.

$$Re = \frac{\rho u D}{\mu} \quad \textbf{(EQ A10)}$$

$$u = \frac{Q}{A} \quad \textbf{(EQ A11)}$$

$$A = \pi\left(\frac{D}{2}\right)^2 \quad \textbf{(EQ A12)}$$

$$Q = \frac{V}{\tau} \quad \textbf{(EQ A13)}$$

In EQs A10 to A13, ρ is the density of air assuming standard temperature and pressure (1.293 kg m^{-3}), μ is the dynamic viscosity of air (1.714 x 10^{-5} Pa s)[4], u is the flow velocity (1.06 x 10^{-3} m s^{-1}), D is the OFR diameter (I.D., 0.203 m), Q is the volumetric flow rate (m^3 s^{-1}), and A is the cross-sectional area (m^2). With laminar flow present in these experiments, the competition of diffusion driven wall losses relative to loss of OH was calculated using Fick's second law of diffusion (EQ A14). Here we provide a simplified estimate of the time (t) a molecule takes to diffuse (d) the length of the radius of the OFR (r). The 6.8 x 10^{-2} cm^2 s^{-1} diffusion coefficient of 1-hexanol[5] was used as a proxy for that of 4:2 FTOH.

$$t = \frac{r^2}{4d} \quad \textbf{(EQ A14)}$$

Since the diffusion coefficient of 1-hexanol is an upper limit for the diffusivity of 4:2 FTOH, it can take up to 417 s for 4:2 FTOH molecules to reach the OFR surface under our

experimental conditions. Therefore, the loss of the 4:2 FTOH in our experiments may not result exclusively from reaction with OH and when the wall effects are assumed to be inconsequential the resulting first 'original' rate constants are obtained (Table A-2). System effects, including those of the inlet and reactor surfaces, were then assessed by applying single and double exponential fitting functions to the calibration and 4:2 FTOH decay curves from OH oxidation using Igor Pro (WaveMetrics®; Portland, OR, USA). Using each exponential fit, the plateaus at the conclusion of each OH exposure/decay period were compared to the originally determined rates.

This was done for both the calibration curves (Table A-2) and 4:2 FTOH + OH experiments (Table A-3) at each RH to compare and quantify the potential for system artifacts impacting our experimental observations. Within the calibrations, we found no evidence of surface effects, as the determined slopes were the same within error at each RH for each of the three fitting methods. Between the different RHs, changes in instrument response were observed – where the response was lower at 44% and 60% RH relative to 22% RH, yet within 10% of one another. All three responses were substantially lower than that determined under dry conditions.

For the oxidation experiments, the three different k_{obs} values for each RH are within the same order of magnitude and within 5 to 25% of one another. The single and double exponential fits result in different rate determinations in the oxidation experiments (Table A-3), compared to the original assumption that no wall effects exist in the system. We believe that system artifacts may play a role in the slower k_{obs} at higher RH, and that RH does alter the PTR-ToF-MS sensitivity and likely affects the rate of reaction between 4:2 FTOH and OH radicals. Further study into the effects of RH on FTOH reaction rates with OH is necessary on systems with potential surface and instrumentation effects minimized.

Table A-2. Comparing the original humified calibration curve data (Figure S4) to the data after being fit to single and double exponential functions.

22% RH			
	Original	**Single Exponential Fit**	**Double Exponential Fit**
R^2	0.9989	0.9992	0.9992
a (intercept)	$(-3.21 \pm 14.8) \times 10^{-4}$	$(-5.86 \pm 12.5) \times 10^{-4}$	$(-5.92 \pm 12.6) \times 10^{-4}$
b (slope)	$(7.27 \pm 0.14) \times 10^{-3}$	$(7.25 \pm 0.12) \times 10^{-3}$	$(7.26 \pm 0.12) \times 10^{-3}$
44% RH			
	Original	**Single Exponential Fit**	**Double Exponential Fit**
R^2	0.9941	0.9961	0.9964
a (intercept)	$(2.39 \pm 3.20) \times 10^{-3}$	$(1.91 \pm 2.59) \times 10^{-3}$	$(1.83 \pm 2.49) \times 10^{-3}$
b (slope)	$(6.66 \pm 0.30) \times 10^{-3}$	$(6.65 \pm 0.24) \times 10^{-3}$	$(6.65 \pm 0.23) \times 10^{-3}$
60% RH			
	Original	**Single Exponential Fit**	**Double Exponential Fit**
R^2	0.9922	0.9990	0.9993
a (intercept)	$(-4.21 \pm 2.29) \times 10^{-4}$	$(-5.71 \pm 9.20) \times 10^{-4}$	$(-6.72 \pm 7.95) \times 10^{-4}$
b (slope)	$(7.20 \pm 0.26) \times 10^{-3}$	$(7.07 \pm 0.10) \times 10^{-3}$	$(7.06 \pm 0.08) \times 10^{-3}$

Table A-3. Comparing the original humified k_{obs} (Figure 3-1) to the data after being fit to single and double exponential functions.

22% Relative Humidity			
	Original	**Single Exponential Fit**	**Double Exponential Fit**
R^2	0.9772	0.9673	0.9756
a (intercept)	$(-1.71 \pm 0.87) \times 10^{-1}$	$(-1.97 \pm 0.98) \times 10^{-1}$	$(-1.77 \pm 0.86) \times 10^{-1}$
-b (-slope)	$(1.0 \pm 0.1) \times 10^{-12}$	$(9.8 \pm 0.9) \times 10^{-13}$	$(9.9 \pm 0.8) \times 10^{-13}$
44% Relative Humidity			
	Original	**Single Exponential Fit**	**Double Exponential Fit**
R^2	0.9843	0.9690	0.9720
a (intercept)	$(-3.50 \pm 0.67) \times 10^{-1}$	$(-3.65 \pm 1.10) \times 10^{-1}$	$(-2.91 \pm 1.14) \times 10^{-1}$
-b (-slope)	$(6.5 \pm 0.4) \times 10^{-13}$	$(7.5 \pm 0.7) \times 10^{-13}$	$(8.1 \pm 0.7) \times 10^{-13}$
60% Relative Humidity			
	Original	**Single Exponential Fit**	**Double Exponential Fit**
R^2	0.9982	0.9866	0.9816
a (intercept)	$(-3.93 \pm 0.27) \times 10^{-1}$	$(-4.69 \pm 0.85) \times 10^{-1}$	$(-4.18 \pm 1.07) \times 10^{-1}$
-b (-slope)	$(6.3 \pm 0.1) \times 10^{-13}$	$(7.4 \pm 0.4) \times 10^{-13}$	$(7.9 \pm 0.5) \times 10^{-13}$

A.4 Comparing Gas-phase FTOH Measurements

While I-CIMS has been previously used for the identification of volatile PFAS in a laboratory setting[6-8], PTR-MS has many advantages over the conventional CIMS technique. For example, the generation of reagent ions within the PTR and the subsequent ionization of VOCs are spatially separated and individually controlled processes. While CIMS allows for more user control, the fixed PTR-MS conditions result in constant and well-defined settings in the drift tube and thus, makes the determination of absolute concentrations easier. Additionally, in the case of I-CIMS, water vapour plays an important role in the ionization efficiency of the iodide-adduct which ultimately influences instrument sensitivity.[9-12] The ionization of organic acids using I-CIMS has been shown to exhibit a strong dependence on RH.[13] Careful calibration of an I-CIMS as a function of the ion-molecule reactor water vapour pressure is necessary to map the instrument sensitivity for a given analyte to its quantity. In this work, the PTR sensitivity for the 4:2 FTOH appeared to decrease with increasing RH (Table A-4). This was expected as PTR-MS sensitivities are known to be sample RH-dependent for some VOCs.[14] If the drift tube electric field is kept low to reduce fragmentation of analyte ions, a fraction of H_3O^+ can be converted to $H_3O^+(H_2O)$ and instrument sensitivity decreases with increasing humidity.

Table A-4. Comparing the 4:2 FTOH sensitivities and two-second LODs determined for this work against measurements made by an I-CIMS.

	This Study			I-CIMS			
RH (%)	**R^2**	**Sensitivity (ncps $ppbv^{-1}$)**	**LOD (2 s, pptv)**	**Sensitivity (ncps $ppbv^{-1}$)[6]**	**LOD (3 s, pptv)[6]**	**Sensitivity (ncps $ppbv^{-1}$) [8]**	**LOD (3.33 s, pptv)[8]**
0	0.9913	$(12.7 \pm 0.6) \times 10^{-3}$	63	$(3.0 \pm 0.7) \times 10^{-3}$	7.9	2.0 ± 0.2	2.9
22	0.9989	$(7.3 \pm 0.1) \times 10^{-3}$	74				
44	0.9941	$(6.7 \pm 0.3) \times 10^{-3}$	200				
60	0.9922	$(7.2 \pm 0.3) \times 10^{-3}$	54				

Table A-5. Comparing the sensitivity and two-second LOD determined for this work against those associated with VOC measurements made by a Vocus PTR-ToF-MS and a traditional PTR-ToF-MS. The one-second pptv LODs were calculated as (reported LOD) × [(1/(sqrt(1 s/reported time in s))].

	Vocus PTR-ToF-MS			**PTR-ToF-MS**		
Analyte	**Sensitivity (ncps ppbv^{-1})**	**Reported LOD (pptv, time)**	**LOD (pptv, 1 s)**	**Sensitivity (ncps ppbv^{-1})**	**Reported LOD (pptv, time)**	**LOD (pptv, 1 s)**
4:2 FTOH (this study)				$(12.7 \pm 0.6) \times 10^{-3}$	63 (2 s)	89
Acetone	5000 ± 700[15] 18400 ± 700[16]	14 (5 s)[15] 10 (1 s)[16]	31.3 10	30.9[17]	18 (60 s) [17]	139.4
Ethanol	80 ± 60[15]	90 (5 s)[15]	201.2	99.23[18]	-[18]	-

Table A-6. Average urban air concentration (pg m^{-3}) of FTOHs in North America reported in the literature (∑gaseous and particulate phase) as parts-per-quadrillion by volume (10^{-15} mol mol^{-1}, ppqv).

	Martin et al., 2002 (~ 21.1 °C)[19]		**Shoeib et al., 2006** (~ 1.0 °C)[20]		**Ahrens et al., 2011** – ref. site 12 (~ 22.0 °C)[21]	
Analyte	pg m^{-3}	ppqv	pg m^{-3}	ppqv	pg m^{-3}	ppqv
6:2 FTOH	87	5.77	18	1.11	90	5.99
8:2 FTOH	55	2.86	41	1.99	144	7.51
10:2 FTOH	29	1.24	22	0.88	70	3.01

Table A-7. Absorption cross-sections in the 230 to 350 nm region at 297 K[22] and 298 K.[23] In comparing the cross sections of the 1:2 and 6:2 FTALs at different wavelengths, we can infer that – due to the smaller absorption cross sections – less photolysis is occurring at the shorter wavelength. This suggests that the photolysis of 4:2 FTAL is just as likely to occur at 254 nm in the same manner as it would in the environment (loss of -COH to form a polyfluorinated radical) but would result in decreased 4:2 FTCA yields within the OFR.

	Absorption Cross-section (x 10^{-20} cm^2 $molecule^{-1}$)		
	298 K	297 K	
UV Wavelength (nm)	**1:2 FTAL (CF_3CH_2CHO)**	**1:2 FTAL (CF_3CH_2CHO)**	**6:2 FTAL ($C_6F_{13}CH_2CHO$)**
230	0.272	0.250	0.683
240	0.377	0.320	0.418
250	0.728	0.640	1.662
254	0.963	0.840	2.305
260	1.403	1.280	4.050
270	2.223	2.070	7.327
280	3.071	2.950	10.562
290	3.685	3.540	13.121
300	3.753	3.540	13.555
310	3.133	2.960	11.739
320	1.916	1.780	8.234
330	0.757	0.670	4.077
340	0.277	0.230	1.973
350	0.067	0.017	1.175

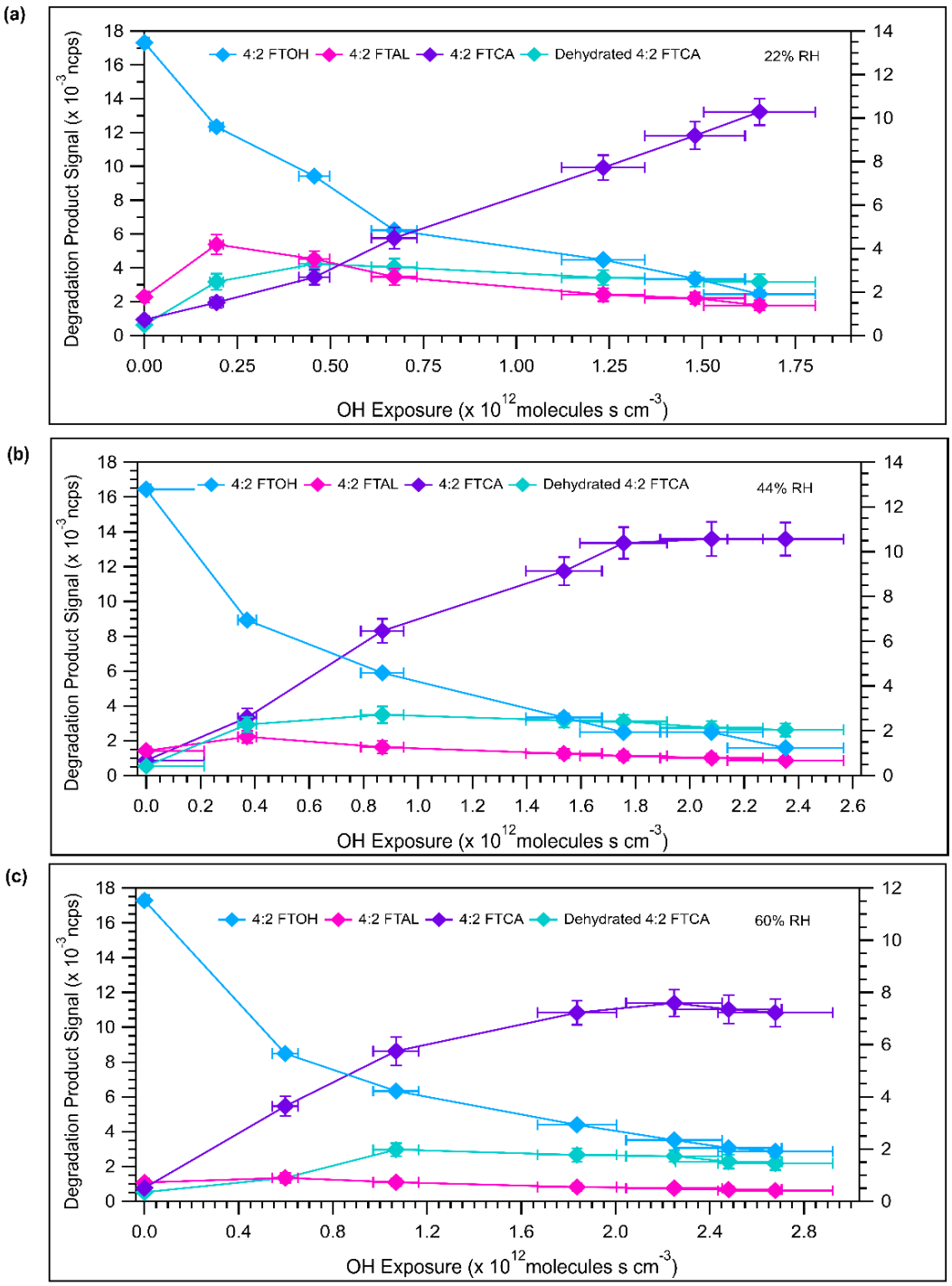

Figure A-5. The change in 4:2 FTOH (m/z 265.027492), the detected degradation products (4:2 FTAL, m/z 263.011842; 4:2 FTCA, m/z 279.006757), and the suspected dehydrated 4:2 FTCA (m/z 260.996192) with increasing OH at **(a)** 22%, **(b)** 44%, and **(c)** 60% RH. The right y-axis depicts the 4:2 FTOH mixing ratio of permeating 4:2 FTOH (ppbv), and the propagated error at each point, as it reacts with OH radicals. On the left y-axis are the normalized average signals of the degradation products (ncps), with each point's corresponding standard deviation. The x-axis shows the OH exposure (molecules s cm^{-3}) and the propagated error at each point.

A.5 References

1. Liu, Y.; Sander, S. P. Rate Constant for the OH + CO Reaction at Low Temperatures. *J. Phys. Chem. A.* **2015**, *119*(39), 10060−10066. https://doi.org/10.1021/acs.jpca.5b07220

2. Liu, Q.; Liggio, J.; Wentzell, J.; Lee, P.; Li, K.; Li, S. M. Atmospheric OH oxidation chemistry of particulate liquid crystal monomers: an emerging persistent organic pollutant in air. *Environ. Sci. Technol. Lett*. **2020**, *7*(9), 646−652.

3. Mao, J.; Ren, X.; Brune, W. H.; Olson, J. R.; Crawford, J. H.; Fried, A.; Huey, L. G.; Cohe n, R. C.; Heikes, B.; Singh, H. B.; Blake, D. R. Airborne measurement of OH reactivity during INTEX-B. *Atmos. Chem. Phys*. **2009**, *9*(1), 163−173.

4. Massman, W. J. Molecular diffusivities of Hg vapor in air, O2 and N2 near STP and the kinematic viscosity and thermal diffusivity of air near STP. Atmos. Environ. **1999**, *33*(3), 453–457.

5. Tang, M. J.; Shiraiwa, M.; Pöschl, U.; Cox, R. A.; Kalberer, M. Compilation and evaluation of gas phase diffusion coefficients of reactive trace gases in the atmosphere: Volume 2. Diffusivities of organic compounds, pressure-normalised mean free paths, and average Knudsen numbers for gas uptake calculations. *Atmos. Chem. Phys*. **2015**, 5585−5598.

6. Riedel, T. P.; Lang, J. R.; Strynar, M. J.; Lindstrom, A. B.; Offenberg, J. H. Gas-Phase Detection of Fluorotelomer Alcohols and Other Oxygenated Per- and Polyfluoroalkyl Substances by Chemical Ionization Mass Spectrometry. *Environ. Sci. Technol. Lett.* **2019**, *6*(5), 289–293. https://doi.org/10.1021/acs.estlett.9b00196.

7. Bowers, B. B.; Thornton, J. A.; Sullivan, R. C. Evaluation of Iodide Chemical Ionization Mass Spectrometry for Gas and Aerosol-Phase per- and Polyfluoroalkyl Substances (PFAS) Analysis. *Environ. Sci.: Process. Impacts.* **2023**, *25*(2), 277–287. https://doi.org/10.1039/D2EM00275B.

8. Mattila, J. M.; Offenberg, J. H. Measuring Short-Chain per- and Polyfluoroalkyl Substances in Central New Jersey Air Using Chemical Ionization Mass Spectrometry. *J. Air Waste Manag. Assoc.* **2024**, *74*(8), 531–539. https://doi.org/10.1080/10962247.2024.2366491.

9. Huey, L. G.; Hanson, D. R.; Howard, C. J.; Reactions of SF6-and I-with Atmospheric Trace Gases. *J. Phys. Chem.* **1995**, *99*(14), 5001−5008.

10. Slusher, D. L.; Huey, L. G.; Tanner, D. J.; Flocke, F. M.; Roberts, J. M. A thermal dissociation–chemical ionization mass spectrometry (TD-CIMS) technique for the simultaneous measurement of peroxyacyl nitrates and dinitrogen pentoxide. *J. Geophys. Res. Atmos.* **2004**, *109*, D19315, doi:10.1029/2004JD004670.

11. Lee, B. H.; Lopez-Hilfiker, F. D.; Mohr, C.; Kurtén, T.; Worsnop, D. R.; Thornton, J. A. An iodide-adduct high-resolution time-of-flight chemical-ionization mass spectrometer:

Application to atmospheric inorganic and organic compounds. *Environ. Sci. Technol.* **2014**, *48*(11), 6309–6317.

12. Lopez-Hilfiker, F. D.; Iyer, S.; Mohr, C.; Lee, B. H.; D'Ambro, E. L.; Kurtén, T.; Thornton, J. A. Constraining the sensitivity of iodide adduct chemical ionization mass spectrometry to multifunctional organic molecules using the collision limit and thermodynamic stability of iodide ion adducts. *Atmos. Meas. Tech.* **2016**, *9*(4), 1505–1512.

13. Brophy, P.; Farmer, D. K. A switchable reagent ion high resolution time-of-flight chemical ionization mass spectrometer for real-time measurement of gas phase oxidized species: characterization from the 2013 southern oxidant and aerosol study. *Atmos. Meas. Tech.* **2015**, *8*(7), 2945–2959.

14. Ernle, L.; Wang, N.; Bekö, G.; Morrison, G.; Wargocki, P.; Weschler, C. J.; Williams, J. Assessment of aldehyde contributions to PTR-MS m/z 69.07 in indoor air measurements. *Environ. Sci.: Atmos.* **2023**, *3*(9), 1286−1295.

15. Jensen, A. R.; Koss, A. R.; Hales, R. B.; de Gouw, J. A. Measurements of volatile organic compounds in ambient air by gas-chromatography and real-time Vocus PTR-TOF-MS: calibrations, instrument background corrections, and introducing a PTR Data Toolkit. *Atmos. Meas. Tech.* **2023**, *16*(21), 5261−5285.

16. Krechmer, J.; Lopez-Hilfiker, F.; Koss, A.; Hutterli, M.; Stoermer, C.; Deming, B.; Kimmel, J.; Warneke, C.; Holzinger, R.; Jayne, J.; Worsnop, D. Evaluation of a new reagent-ion source and focusing ion–molecule reactor for use in proton-transfer-reaction mass spectrometry. Anal. Chem. 2018, 90(20), 12011−12018.

17. Lee, A. K.; Abbatt, J. P.; Leaitch, W. R.; Li, S. M.; Sjostedt, S. J.; Wentzell., J. J.; Liggio, J. ; Macdonald, A. M. Substantial secondary organic aerosol formation in a coniferous forest: observations of both day-and nighttime chemistry. *Atmos. Chem. Phys*. **2016**, *16*(11), 6721−6733.

18. Wu, C.; Wang, C.; Wang, S.; Wang, W.; Yuan, B.; Qi, J.; Wang, B.; Wang, H.; Wang, C.; So ng, W.; Wang, X. Measurement report: Important contributions of oxygenated compounds to emissions and chemistry of volatile organic compounds in urban air. *Atmos. Chem. Phys*. **2020**, *20*(23), 14769−14785.

19. Martin, J. W.; Muir, D. C. G.; Moody, C. A.; Ellis, D. A.; Kwan, W. C.; Solomon, K. R.; Mabury, S. A. Collection of Airborne Fluorinated Organics and Analysis by Gas Chromatography/Chemical Ionization Mass Spectrometry. *Anal. Chem*. **2002**, *74*(3), 584–590. https://doi.org/10.1021/ac015630d.

20. Shoeib, M.; Harner, T.; Vlahos, P. Perfluorinated Chemicals in the Arctic Atmosphere. *Environ. Sci. Technol.* **2006**, *40*(24), 7577−7583.

21. Ahrens, L.; Shoeib, M.; Harner, T.; Lee, S. C.; Guo, R.; Reiner, E. J. Wastewater treatment plant and landfills as sources of polyfluoroalkyl compounds to the atmosphere. *Environ. Sci. Technol.* **2011**, *45*(19), 8098−8105.

22. Chiappero, M. S.; Malanca, F. E.; Argüello, G. A.; Wooldridge, S. T.; Hurley, M. D.; Ball, J . C.; Wallington, T. J.; Waterland, R. L.; Buck, R. C. Atmospheric chemistry of perfluoroaldehydes (CxF2x+1CHO) and fluorotelomer aldehydes (CxF2x+ 1CH2CHO): quantification of the important role of photolysis. *J. Phys. Chem. A.* **2006**, *110*(43), 11944−11953.

23. Sellevåg, S. R.; Kelly, T.; Sidebottom, H.; Nielsen, C. J. A study of the IR and UV-Vis absorption cross-sections, photolysis and OH-initiated oxidation of CF3CHO and CF3CH2CHO. *Phys. Chem. Chem. Phys.* **2004**, *6*(6), 1243−1252.

Chapter 3

Cost Effective Off-Grid Automatic Precipitation Samplers for Pollutant and Biogeochemical Atmospheric Deposition

3.1 Abstract

An important transport process for particles and gases from the atmosphere to aquatic and terrestrial environments is through dry and wet deposition. An open-source, modular, off-grid, and affordable instrument that can automatically collect wet deposition samples allows for more extensive deployment of deposition samplers in fieldwork and would enable more comprehensive monitoring of remote locations. Precipitation events selectively sampled using a conductivity sensor powered by a battery-based supply are central to off-grid capabilities. The prevalence of conductive precipitation – that which initially contains high solute levels and progresses through trace-level concentrations to ultrapure water in full atmospheric washout – depends on the sampling location but is ubiquitous. This property is exploited here to trigger an electric motor (via limit switches) to open and close a lid resting over a funnel opening. The motors are operated via a custom-built and modular digital logic control board, which has a low energy demand. All components, their design and rationale, and their assembly are provided for community use. The modularity of the control board allows the operation of up to six independent wet deposition units, such that replicate measurements (e.g., canopy throughfall) or different collection materials for various targeted pollutants can be implemented as necessary.

We demonstrate that these platforms are capable of continuous operation off-grid for integrated monthly and bimonthly collections performed across the Newfoundland and Labrador Boreal Ecosystem Latitudinal Transect (47 to 53°N) during the growing seasons of 2015 and 2016. System performance was assessed through the measured power consumption from 115 V of alternating current (grid power) or 12 V of direct current from battery supplies during operation under both standby (40 or 230 mA, respectively) and in-use (78 or 300 mA, respectively) conditions. In the field, one set of triplicate samplers was deployed in the open to collect incident

precipitation (open fall), while another set was deployed under the experimental forest canopy (throughfall). The proof-of-concept systems were validated with basic measurements of rainwater chemistry, which found: i) pH values ranging from 4.14 to 5.71 in incident open fall rainwater; ii) conductivities ranging from 21 to 166 μS cm^{-1}; and iii) dissolved organic carbon concentrations in open fall and canopy throughfall of 16 ± 10 and 22 ± 12 mg L^{-1}, respectively, with incident fluxes spanning 600 to 4200 mg C m^{-2} $year^{-1}$ across the transect. Ultimately, this demonstrates that the customized precipitation sampling design of this new platform enables more universal accessibility of deposition samples for the atmospheric observation community – for example, those who have made community calls for targeting biogeochemical budgets and/or contaminants of emerging concern in sensitive and remote regions.

3.2 Introduction

Atmospheric deposition is the central loss process for particles and gases to terrestrial and aquatic surfaces.[1] Particles and gases can be deposited by both dry and wet deposition processes. Dry deposition is facilitated by the direct interaction of gases and particles with boundary layer surfaces such as water, vegetation, and/or soil, while wet deposition involves in-cloud scavenging and below-cloud interception of gases and aerosols by, e.g., rain droplets and snow crystals.[2,3] Dry and wet deposition are global processes coupled to regional synoptic-scale conditions, but their relative importance depends on local sources and the global transport of atmospheric analytes of interest. Dry deposition consists of a variety of mechanisms for particles and gases, with fine mode particles and their chemical constituents being more likely (compared to ultrafine- and coarse-mode particles) to undergo atmospheric long-range transport prior to being deposited.[4] Wet deposition occurs when such long-lived atmospheric particles and gases are included and/or

scavenged into cloud water and transported to the surface of the Earth in precipitation (e.g., snow and rain). With the size and number of droplets in the atmosphere largely controlling the rate, wet deposition depends on a variety of meteorological factors affecting precipitation, such as the size distribution and concentration of ice- and droplet nucleating particles, as well as the solubility, concentration, and reactivity of gases.[5] Ultimately, deposition plays an important role in pollutant distribution and the biogeochemical cycling of long-studied major nutrients (e.g., nitrogen and sulfur in acid rain) and those that are increasingly being recognized for their importance, such as dissolved organic carbon (DOC).[6-9]

Recognizing the significance of atmospheric trace chemical deposition has led to the establishment of monitoring networks. For example, long-term wet deposition monitoring networks, like the Canadian Air and Precipitation Monitoring Network (CAPMoN) and the National Atmospheric Deposition Program (NADP), aim to provide critical data on the spatial and temporal patterns of wet and dry deposition. As a result, this has allowed for the estimation of regional and continental deposition rates of species regulated by national or international policies.[5] Data from these networks have been critical to understanding the efficacy of policy to reduce environmental issues like acid rain.[10] In particular, the Oslo and Geneva protocols have achieved an 80% decrease in both North American and European sulfur dioxide (SO_2) emissions since 1980.[11] Despite these successes, the reduction in acid deposition in ecosystems has been unexpectedly slow, leaving them sensitized and necessitating continued deposition monitoring.[12,13]

Over the past 60 years, the precipitation chemistry community has made advancements in deposition collectors to better understand atmospheric processes.[14] While bulk deposition collection (i.e., a collection bucket or jug fitted with a funnel open at all times[15]) is both a simple and economically feasible sampling method utilized by monitoring networks, it is subject to bias

through the collection of inputs other than atmospheric deposition (e.g., bird droppings, insects, plant debris). As a result, bulk collectors can overestimate total deposition and underestimate wet deposition in a variety of locations.[16-18] Sequential precipitation collection methods include manually segmenting samplers (requiring only a shelter, clean surface, and an operator) and linked collection vessels (sample containers that are filled in sequence via gravitational flow), amongst others, and have been developed to analyze rainwater composition and measure parameters such as pH and conductivity.[19-22] Sequential sampler designs have also been adapted to collect precipitation in remote field sites.[23,24] Although it is a more costly and time-intensive method when compared to bulk deposition collection, the major appeal of measuring isolated wet deposition is the ability to isolate this individual atmospheric process. Further innovation, such as the use of sensors to automate the isolation of collected precipitation or the addition of polymeric mesh barriers to reduce debris input in windy environments[5], can reduce bias and improve the preservation of samples, but commercial solutions often come at a substantial expense.

When targeting biogeochemically relevant species in deposition collectors, additional standard practices have been developed to improve the representativeness of sample composition. First, an appropriate monitoring site must be selected. Three categories of siting criteria, established by organizations such as CAPMoN and the NADP, are of particular importance: i) site representativeness and physical characteristics, ii) the distance from potential pollution sources, and iii) operational requirements.[25,26] This means that each site must be a location that receives precipitation representative of the hydrologic area; is ideally not within 500 m of local pollution sources, such as wood-burning stoves, garbage dumps, and vehicle parking lots; and is accessible for daily collections and maintenance and can be serviced by a reliable 115 V of alternating current (VAC) electrical power.[25,26] Despite these guidelines, there are many reasonable scenarios in which

these siting conditions cannot be met. As an example, remote sample collections are often required for global assessments on persistent contaminants or nutrients of biogeochemical importance. At remote locations, however, the sampling site may have no power provision, sample collection may be infrequent, and/or the infrastructure-bearing location itself may be a source of the targeted pollutants. As a result, innovation in collection strategies (such as time-integrated off-grid sampling, with modularity in the deployment of replicates) and materials for the quantitative collection of environmental targets is still needed to expand and/or modify networks to meet current and future monitoring and policy needs.

In biogeochemical cycles, for example, the improvement of constraints in atmospheric carbon linkages to terrestrial and aquatic processes is necessary. This would play a critical role in correctly assessing climate feedbacks and reducing uncertainty in Earth system models. The measurement of atmospheric DOC transport to surfaces has been limited, which has stopped the landscape-scale carbon balance from being obtained.[27] The pool of compounds from which DOC is derived in the atmosphere has also been limited and has only recently seen an increase in research intensity. Reactive organic carbon (ROC) is defined as the sum of nonmethane organic gases and primary and secondary organic aerosols.[8] The major removal mechanism of water-soluble organic compounds produced through oxidation from the atmosphere is the dry deposition of particle-bound pollutants and scavenging by rainfall.[28,29] When ROC is scavenged into rainfall, it becomes DOC and enters terrestrial and aquatic systems. Deposition measurements of ROC compounds are needed since they play a crucial role in the formation of secondary species such as ozone, particulate matter, and carbon dioxide (CO_2).[8,30]

There are several evolving drivers for studying atmospheric ROC; for example, light-absorbing organic carbon that can affect the global radiative balance and undergo photochemical

transformations in the condensed phase.[31-34] Reactive organic carbon can also influence cloud formation and contribute to precipitation acidity.[35,36] Measurements of speciated ROC are difficult due to the chemical complexity of emitted compounds and oxidation products.[37] To circumvent this, DOC can be monitored and quantified and then used as a proxy to estimate the total ROC in precipitation. However, quantitative measurements of DOC in precipitation samples are sparse due to its relatively low concentration of 0.1 to 10 mg C L^{-1}.[8,38] Recently, calls for carbon closure in the atmospheric processing of ROC have made this measurement increasingly important.[39-41] Similarly, to obtain the net landscape or watershed carbon exchange, studies require effective methods for capturing and preserving atmospheric DOC deposition to constrain biogeochemical linkages at global interfaces, as outlined above.

In this work, we present the design of a custom-built automated array of precipitation samplers that can be operated both on- and off-grid for wet deposition collection. The purpose of these samplers is to enable the cost-effective collection of integrated, water-soluble, conductive atmospheric constituents deposited in remote environments without grid power or routine access. A sensor interfaces with a custom-built motor control board capable of operating up to six independent wet deposition units such that canopy throughfall (TF) and incident precipitation (open fall, OF) measurements can be collected in replicate. The materials used can be easily changed in order to optimize the collection and preservation of a wide array of target analytes, such as DOC, when using high-density polyethylene (HDPE) and mercuric chloride ($HgCl_2$). We demonstrate that these platforms are capable of continuous operation off-grid for the monthly wet deposition collection of precipitation across the Newfoundland and Labrador Boreal Ecosystem Latitudinal Transect (NL-BELT) during snow-free periods in 2015 and 2016. Extremes in system performance were evaluated by testing the power consumption of a sampling array from spring

through fall when paired with a solar top-up system and during snow-free winter conditions using only a battery. The two years of field samples were collected using an array of six collection units, with triplicate collection of both incident precipitation and throughfall from rain passing through a forest canopy. Samples were analyzed to determine deposition volumes relative to total bulk volumes, the reproducibility of replicate samples, and the fraction of conductive rainfall within the total volume of precipitation at these remote sites. The captured fraction compared to the total volume deposited is used to gain insight into how these samplers can limit analyte dilution effects and improve method detection limits, such as by rejecting 50% of the total volume delivered as ultrapure precipitation, leading to a factor of two improvement. Chemical parameters – pH, conductivity, and DOC fluxes – collected according to established preservation protocols were then compared to prior measurements to validate this proof-of-concept system. Measurement methods for the pH and conductivity of rainwater are very well-established in the literature and serve as a baseline reference to ensure that the samples collected by the new devices presented in this work are consistent with what is expected in samples from a remote coastal environment, given the selective sampling strategy. We then move away from these well-established parameters to quantify DOC fluxes using established biogeochemical preservation techniques for fresh water and groundwater to demonstrate the potential of these samplers when they are applied to the automated collection of analytes of emerging importance and interest in the remote locations of our latitudinal transect.

3.3 Methodology

3.3.1 Precipitation Sampling Array Components

Each automated precipitation sampling setup can be operated as an array; here, they are

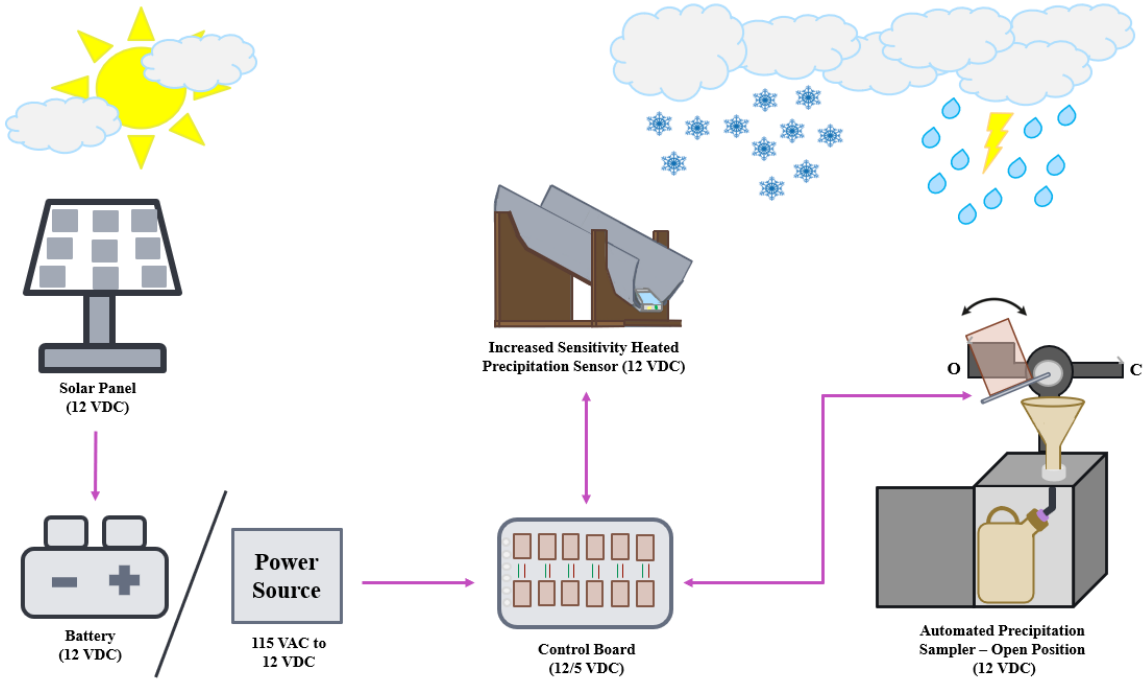

Figure 3-1. Schematic of custom-built automated precipitation sampling array components for off-grid wet deposition collection. The pink arrows denote the directions of the electrical signal and the power exchanged between components. The curved black arrow indicates the rotation of a motorized lid to obtain open (O) and closed (C) sampler configurations.

used in groups of up to six collection units (Figure 3-1). A collection unit is a simple opaque doored box. The box protects the sample containers against exposure to direct sunlight and provides a mounting location for the funnel and lid while also facilitating the easy exchange of sample containers. The collection units can be fitted with stabilizing legs that allow them to be bolted to concrete or pinned by retaining rods when on soil. In both cases, this prevents sample tipping and loss during high winds or wildlife-sampler interactions (e.g., Figures 3-2 and B-1). The collection of precipitation is facilitated by a funnel mounted through the top of the sampling unit. The funnel tip extends into the opening of the sample collection container placed inside. The connection can be sealed to better preserve volatile analytes with tubing that passes through a sealed grommet (part number, P/N, 9280K34; McMaster-Carr, Aurora, OH, USA) to enter the sample collection

container and minimize evaporative losses. Precipitation events are sampled selectively by modulating the position of a lid over the funnel with an electric motor. The collection unit motors are operated by a digital control board, which interfaces with a precipitation sensor and requires 12 V of direct current (VDC) power to be supplied to this system. Switches detecting the lid position ensure complete opening or closure of the funnel mouth for each collection unit.

3.3.1.1 Collection Units

The collection unit materials used to date have been 0.95 cm plywood and black polyacrylate sheeting. These materials have demonstrated high durability (on the order of four years) under field conditions (Figures B-1 and B-2). Opaque materials were explicitly selected to minimize photochemical reactions and the growth of photosynthetic microorganisms within the sample. The dimensions of the collection unit are detailed in Figure 3-2. Each can accommodate sample containers up to 20 L in volume for collection in locations with large monthly wet deposition volumes, such as in Newfoundland and Labrador (Table 3-1).

The box panels can be joined using hardware inserts (P/Ns 1556A54 and 1088A31; McMaster-Carr, Aurora, OH, USA), 3D printed corners (Figure B-4), or along the box edges with screws if using wood. The door is attached with two hinges (P/N 1549A57, McMaster-Carr, Aurora, OH, USA) and held closed with a magnetic contact (P/N 1674A61; McMaster-Carr, Aurora, OH, USA) or hooked latch. The electric motor controlling the lid is enclosed in a standard polyvinylchloride electrical junction box, which is attached to a short paddle mounted on one side of the collection unit. Here we used an electric worm-gear motor (12 VDC, two revolutions per minute; TS-32GZ370-1650; Tsiny Motor Industrial Co., Dong Guan, China) mounted inside the enclosure with matching hex bolts (P/N 91251A146; McMaster-Carr, Aurora, OH, USA) that pass through the weather-tight cover, while the drive shaft protrudes through a 3/8-inch (0.95 cm) hole

drilled in the cover. The drive shaft has a flat edge to affix the lid rod using a short set screw (Figure B-5) that is cemented semi-permanently in place with thread-locking compound (P/N 91458A112; Loctite Threadlocker Blue 242; McMaster-Carr, Aurora, OH, USA). The lid rod is 3/8-inch (0.95 cm) aluminum, which is machined on one end to allow connection to the motor drive shaft (Figure B-5) and has four threaded holes along its length to affix the lid (Figure B-3). The lid rod passes through a second mounting paddle on the box that keeps the lid level and capable of isolating the funnel from the atmosphere in the absence of precipitation. The lids used here were made of 1/8-inch (0.318 cm) Lexan polycarbonate sheet.

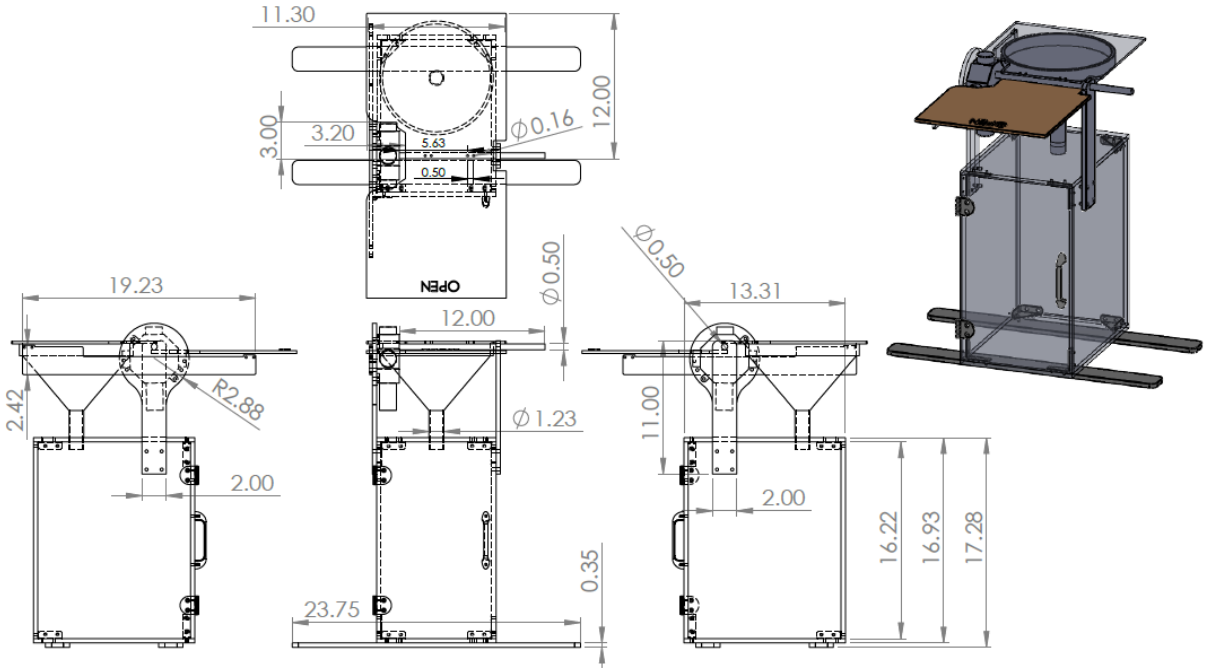

Figure 3-2. Detailed collection unit schematic, with all dimensions provided in inches (1 inch = 2.54 cm). Further specifications for the lid dimensions can be found in Figure B-3. The shaded 3D rendering depicts both open and closed states for the lid, the positioning of legs to secure it to surfaces, the placement of corner brackets, and the door handle and hinges.

Selective precipitation sampling is performed using a logic-based assessment of sensor and switch states (defined in Figure B-6) by the control board quadNOR gate chip (P/N DM74LS02, Fairchild Semiconductor), which activates the H-bridge motor driver chipset (Figure B-7). A 12 VDC signal drives the clockwise or counterclockwise rotation of the motor (installed in a suitable port of the junction box) via a cable from the control board, which passes through a weather tight compression fitting (e.g., Home Depot stock keeping unit number, SKU#, 1000116446). The motor rotation signal is interrupted when the lid makes contact with one of two weather-tight limit switches (P/N SW1257-ND; Omron, Digi-Key Electronics, Thief River Falls, MN, USA) mounted on opposite ends of a horizontal armature connected to the vertical motor mounting paddle (Figure 3-2). The switches controlling the lid location ensure that the funnel is completely open or covered as necessary for precipitation collection. The funnels used in this work are 20 cm in diameter and made from HDPE (Dynalon, P/N 71070-020, VWR International, Mississauga, ON, Canada). An 18 x 13 cm piece of filtration mesh (P/N 9265T49; McMaster-Carr, Aurora, OH, USA) that was tied together as a fitted cone insert with Nylon thread (e.g., fishing line) was used to prevent large debris from entering the sampler containers, for example, in the collection of TF precipitation under a forest canopy when accompanying litterfall is also expected. The exit of the funnel directs the collected precipitation into the narrow-mouth opening of the container inside the collection unit, such as a 20 L HDPE jug or 10 L HDPE jerrican (Bel-Art Products, P/N 11215-314; VWR International, Mississauga, ON, Canada)

3.3.1.2 Heated Precipitation Sensor

The detection of rain modulates the opening and closing of the collection units by an interdigitated resistive sensor (M152, Kemo Electronic GmbH, Geestland, Germany; Figures B-6

to B-8). This approach is consistent with established precipitation detection techniques used by government monitoring programs (e.g., CAPMoN).[25] The rain sensor detects conductive deposition by monitoring for the completion of a conductive circuit when electrolytes bridge the connection between the interdigitated gold electrodes. The sensor is supplied with 12 VDC from the power system to trigger a relay when a precipitation conductance above 1 MΩ·cm conductivity is detected (determined experimentally; see Section B.1). This is equivalent to approximately 8 μM sodium chloride. The sensor detection limit reflects an upper limit of precipitation ion loading because the design of the rain chute leads to an increase of more than a factor of 25 in the surface area on which solutes can accumulate to enhance the ionic content of the deposited water. An output of 12 VDC is sent to the digital control board by the relay when rain is sensed, or 0 VDC is sent in its absence, for signal processing and motor control (Figure B-7). When rain is sensed, the lids of the samplers in the array are simultaneously opened in <5 s (this is dependent on the rotational rate of the lid motor). To increase the sensitivity of this sensor and to extend the sampling duration when conductive atmospheric constituents are completely washed out of the atmosphere, a sloped tin chute (e.g., Home Depot SKU# 1001110514) was added to extend the surface of the rain sensor. The sensor was placed at the end of the chute and sealed in place with caulking to allow water droplets to move easily from the chute onto the sensor.

The angle of the chute can be adjusted to control the momenta of collected droplets so that they collect on the sensor surface and only flow off it when the rate of precipitation exceeds the sensor's evaporation capability. When soil is available, two bent rods can be used to hold the chute at the optimized angle of 10° (Figure B-2). They are inserted into the soil, and the chute is affixed to the tops of the rods with zip ties passed through small holes drilled in the sides of the chute, which are subsequently sealed with caulking. When soil is unavailable, for example in urban

environments, we have created a mounting frame to hold the chute at the optimized angle of 10° (Figure B-8). When precipitation is detected, the sensor surface draws a current of up to 1.0 ampere (A) into a heater to actively evaporate water from its surface so that it accurately detects the active periods of rain events. The heated sensor has undergone preliminary field tests and is also capable of detecting ice and snow, provided they contain electrolytes.

3.3.1.3 Power Supply Systems

The power for this system can be supplied from a battery at 12 VDC or using a 115 VAC to 12 VDC transformer power supply (P/N 285-1818-ND; TDK-Lambda Americas, Digi-Key Electronics, Thief River Falls, MN, USA). Depending on the duration of sampling and the time of year, the battery capacity can be changed to suit the power needs (Section 3.4.2.2). To provide sufficient power density over the one- to two-month-long collection periods in this study, the battery capacity was carefully matched, with top-up options implemented when prolonged or high frequency precipitation was expected. Absorbent glass mat (AGM) marine deep-cycle batteries can withstand discharge events down to less than 60% capacity and are robust under nearly all environmentally relevant temperatures (20 to 40°C). Additionally, these batteries interface easily with solar charging options as they are able to accept a high current input. Monthly collections in Newfoundland were powered with 76 amp-hour (Ah) AGM batteries (Motomaster Nautilus; Ultra XD group 24 high-performance AGM deep-cycle battery, 12 VDC) topped up by a 40 W solar panel interfaced with a charge controller to prevent overcharging (Coleman; model: 51840, max current of 8 A at 14 VDC).

For collections made every second month in Labrador, a 120 Ah battery with the same solar top-up strategy was used to ensure continuous operation. For either remote field deployment,

batteries and charge controllers were housed in a Pelican™ case (model 1440; Ocean Case Co. Ltd., Enfield, NS, Canada) fitted with weather-tight bulkhead cord grips (P/N 7529K655; McMaster-Carr, Aurora, OH, USA) through which charging and power cables were passed (Belden, Coleman, P/Ns 7004608, 70875227; Allied Electronics, Inc., Ottawa, ON, Canada). Humidity in all weatherproof cases was minimized by exchanging reusable desiccant packs (Ocean Case Co. Ltd., Enfield, NS, Canada) when depleted batteries were exchanged for fully charged replacements. Solar panels were repositioned monthly to optimize their orientation for solar-power provision. Using either power source, the control board converts and distributes the 12 VDC to the other components in the precipitation sampling array.

3.3.1.4 Custom Control Borad

A custom control board to operate a six-collection unit array was designed based on prior digital logic circuits for standalone collectors.[42] The 12 VDC battery or transformer output is supplied directly to the rain sensor and relay as well as to the motor drivers for lid opening (Figure B-9). Each collection unit is controlled independently to ensure the lids are fully opened or closed, thereby requiring six replicate motor driver control circuits that respond to their independent switch signals. The remainder of the signalling and digital logic operates on 5 VDC, which is produced by on-board voltage regulators (Micro Commercial Co., P/N MC7805CT-BP; Digi-Key Electronics, Thief River Falls, MN, USA). The lid switches are provided with 0 and 5 VDC to indicate a collection unit's open or closed status (Omron Electronics; P/N D2FW-G271M(D); Digi-Key Electronics, Thief River Falls, MN, USA). The signals from the sensor and switches connect to the board through four conductor cables (Belden, P/N 70003678; Allied Electronics Inc., Ottawa, ON, Canada) passed through weather-tight bulkhead cord grips and secured to screw

terminals (Figure B-9). The sensor and switch signal inputs interface with a quad-NOR-gate chipset (Texas Instruments, P/N 296-33594-5-ND; Digi-Key Electronics, Thief River Falls, MN, USA) to trigger the motor driver (STMicroelectronics, P/N 497-1395 5-ND; Digi-Key Electronics, Thief River Falls, MN, USA) such that it rotates or remains stationary. The additional resistors, capacitors, and diodes are necessary to maintain stable signalling throughout the printed circuit board (Figure B-9, Table B-1).

The custom control board was housed in a Pelican™ case (1400 NF; Pelican Zone, Mississauga, ON, Canada) fitted with cut to-use foam inserts and a reusable desiccant pack that was also exchanged alongside those for the battery cases. All collection units, sensors, and power supply cables were passed through eight weather-tight bulkhead cord grips and fixed to screw terminals on the board. The opposing ends of the cables were fitted with weather-tight Bulgin Buccaneer 400 or 4000 series circular cable connectors (Table B-2; Allied Electronics, Inc., Ottawa, ON, Canada) to allow easy field installation with mated connectors on the cables originating from each of the previously mentioned array components. Connected cables could then be buried in shallow soil trenches to reduce the attention of gnawing animals as well as potential entanglement hazards with other wildlife. Precipitation events were logged from the control boards using a HOBO four-channel analogue data logger (UX120-006M; Onset®, Bourne, MA, USA) that records the sensor, switch, and motor voltages. The fourth channel is reserved to monitor battery or power supply voltages over time (Section 3.4.2).

3.3.2 Power Demand and Management Tests

Power demand was calculated based on the cumulative component requirements prior to the selection of batteries. This was to ensure adequate capacity to collect samples over one- to two-

month-long field deployments and to cope with an assumed worst-case scenario of one week of constant rain without solar power charge restoration. Solar-panel power production capacity was determined based on the calculated energy required to recharge the battery. As a result, we selected a 40 W panel, which could complete the charging at 14 VDC with a week of direct sunlight at 8 hrs per day. The power demand for a six-sampler array was measured in standby and during operation with a digital power meter (Nashone PM90, Dalang Town, China) in real time when supplying 12 VDC with a transformer. Contrasting power demand tests were performed under different environmental conditions and power management configurations. The first was performed using the 76 Ah AGM battery with a solar top-up in an urban environment from July through August 2018, while the other was performed using a 103 Ah AGM battery alone from January through February 2019. The dataset can be found in Colussi et al.[43]

3.3.3 Continuous Monthly Collection of Remote Samples at NL-BELT

One array of six automated collection units (three for OF and three for TF) was deployed within one forested experimental field site located in each of the four watershed regions of the NL-BELT (24 samplers in total) between 2015 and 2016. Additionally, between one and three total deposition samplers were located at each of the four field sites (Table 3-1, Figure B-10). The watersheds span 5.5° latitude from the southernmost site, Grand Codroy (GCo), through the collocated Pynn's Brook (PB) and Humber River Camp 10 (HR) sites to Salmon River (SR), the highest-latitude site on the island of Newfoundland. The northernmost forested watershed, Eagle River (ER), is located in southern Labrador, and extensive details characterizing each of the four sites can be found in Ziegler et al.[44] All sampling locations are far from anthropogenic pollutant point sources, except for the ubiquitous presence of marine sea spray from the nearby marine

Table 3-1. NL-BELT sampling site details (locations and identifiers) alongside data from long-term weather stations operated by Environment and Climate Change Canada (ECCC). Soil pH was determined from samples collected at the same time as precipitation. Mean annual temperature (MAT) was derived from ECCC climate normals. Annual total-deposition precipitation volumes were either measured for the 2015-2016 period (ECCC, this work) or calculated by the Oak Ridge National Lab (ORNL) DAYMET archive.

						Precipitation Volumes		
Sampling Site	**Sampling Site Location**	**Station (Climate ID)**	**Station Location**	**Soil pH[a]**	**MAT (°C)[b]**	**ECCC (L)[b]**	**ORNL (L)[c]**	**This Work (L)**
Grand Codroy (GCo)	47°50'43.1"N 59°16'16.0"W	Doyles (8401EK4)	47°51'00" N, 59°15'00" W	3 to 4	5.2[1]	60.2[2]	122.1	85.3
Pynn's Brook (PB)	49° 05' 13.20"N, 57° 32' 27.60" W	South Brook Pasadena (8403693)	49°01'00" N, 57°37'00" W	3 to 4	4.6[1]	38.0[2]	54.3[d]	24.6[d]
Salmon River (SR)	51°15'21.6"N 56°08'16.8"W	Main Brook (40KE88)	51°11'00" N, 56°01'00" W	3 to 4	2.0[1]	48.9[2]	111.1	81.3
Eagle River (ER)	53°33'00.0"N 56°59'13.2"W	Cartwright (8501100)	53°42'30" N, 57°02'06" W	3 to 4	0[3]	42.9[3]	131.8	54.1

[a]Soil pH for the organic and mineral soil horizons determined by addition of 400 μL of aqueous 0.5 M calcium chloride to a 50:50 w/w slurry of dried soil in 18.2 MΩ·cm deionized water.
[b]Environment Canada: Canadian Climate Normals, 1981 to 2010, https://climate.weather.gc.ca/climate_normals/ (last accessed: 14 July 2023). [45]
[1]At least 20 years of measurements/data.
[2]At least 15 years of measurements/data.
[3]The World Meteorological Organization's "3 and 5 rule" (i.e., no more than 3 consecutive and no more than 5 total missing for either temperature or precipitation).
[c]Estimated deposition rates converted to volume using the ORNL DAYMET using sampling site pixels for corresponding sample collection periods in 2015 and 2016.[46]
[d]Volumes merged for 2015 and 2016 at PB and HR, with DAYMET estimated for HR only.

coastlines. The total deposition samplers were identical to the automatic collection units except that they were not fitted with a motor arm and lid, so they did not require a source of power. Three of the six automated samplers were deployed in the open at a distance from the forest stand equal to or greater than the height of the trees, in line with CAPMoN and NADP guidelines. The other three automated samplers were placed under the canopy to collect TF precipitation within the forest

sites. These samplers actively collected wet deposition into integrated monthly (Newfoundland) or two-month (Labrador) samples during snow-free periods (approximately June through November). The arrays were collected and stored during the winter months, while the total deposition samplers remained in field locations year-round. It is also important to note that during the growing season, sample collections were made at the same time – that is, OF and TF deposition were collected on a single day at each sampling site and within a few days of each other across the transect. Collected sample volumes were compared between the automated samplers and total deposition collectors for each collection interval as a check on proper function (i.e., less than or equal volumes in automated samples). During each site visit, the slope of the sensor was confirmed to be correct, sample containers were collected and replaced with clean units, the battery and desiccant packs were replaced with fully recharged devices, and the entire array was confirmed as being operational.

3.3.3.1 Sample Preservation

Four of the six sample containers (two each for OF and TF) were biologically sterilized using 1 mL of a saturated aqueous solution of $HgCl_2$ to preserve against biological growth and the loss of bioavailable nutrients over the collection periods. Unsterilized sample containers (without $HgCl_2$) were used for measurements of recalcitrant species and to assess any matrix effects exerted on target analyte quantitation. The use of $HgCl_2$ as a sample preservation technique is long-studied and well established[47,48]; thus, additional tests to verify the preservation of collected chemical species over time were not performed. The analysis of deposition collected in unsterilized and sterilized containers, however, serves as a method for internal sample validation – as does our evaluation of measurement outcomes in comparison to those reported within the literature.

Collected sample volumes were measured with a 1000 ± 10 mL graduated cylinder, and aliquots were collected for chemical analysis via transfer to precleaned 500 or 1000 mL HDPE containers (Nalgene; VWR International, Mississauga, ON, Canada). Samples were stored at 4°C before returning to the laboratory, where they were filtered with a 1000 mL Nalgene vacuum filtration system (P/N ZA-06730-53, ThermoFisher Scientific, Waltham, MA, USA), fitted with 0.45 µm polyethersulfone (PES) filters (P/N HPWP 04700; EMD Millipore Corporation, Billerica, MA, USA), to remove suspended solids. Filtered samples were transferred to new clean HDPE containers and stored for up to two months at 4°C in a cold room until analysis. The target analytes in this work are non-volatile and the described sample collection methods consider this property of the analytes as well as their interactions with container materials. The versatility of the system design allows for the use of different collection materials, keeper solvents for volatile organics, etc., so that the experimental design can be analyte specific, depending on the end-user needs. Sample preservation approaches should thus be identified by users of this new platform based on their scientific objectives and a review of the literature.[49-52] In addition to the internal validation approach described here, we aim to demonstrate that the precipitation samplers in this work are suitable for measuring conductive deposition on- and off-grid. Below, we highlight autonomous off-grid operations, determine the fraction of conductive rainfall collected from the total volume of precipitation, and validate our measurements through comparison to the literature.

3.3.4 Cleaning and Preparation of Sample Containers

All sample collection and storage containers for the quantitative analysis of target analytes, as well as all sample handling apparatuses, were made of HDPE or polypropylene. Prior to use in handling samples, these were all acid washed in 10% v/v hydrochloric acid (P/N BDH7417-1;

VWR International, Mississauga, ON, Canada), followed by six sequential rinses with distilled water and 10 rinses with 18.2 MΩ·cm deionized water (Milli-Q water; EMD Millipore Corporation, Billerica, MA, USA). Containers were dried by inversion on a clean benchtop protector overnight or with protection from dust using lint-free lab wipes over container openings when necessary. Field and method blanks were collected through the addition of Milli-Q water to cleaned containers, and/or sample handling devices, in order to quantify appropriate method detection limits and to identify any sources of systematic or random contamination. Blank subtraction was applied to measurements where appropriate.

3.3.5 Measurements of pH and Conductivity

The pH and conductivity of each sample were determined using a Thermo Scientific™ Orion Versa Star meter (ORIVSTAR52) interfaced with a pH electrode (model: 8157BNUMD, Ultra pH/ATC triode, ROSS) and a four-electrode conductivity cell (model: 013005MD, DuraProbe, ROSS). Prior to use, the probes were calibrated daily with standard solutions specific for these probes (Thermo Scientific™ Orion™ conductivity standard 1413 and pH 4, 7, and 10 buffers) and then stored between analyses according to the manufacturer's directions. Aliquots of 15 mL of precipitation from archived samples were subsampled into 40 mL polypropylene Falcon tubes. This was followed by the immersion of a cleaned electrode for the conductivity measurement. Next, a pH probe measurement was performed to prevent conductivity bias due to potassium chloride migration across the glass frit of the pH probe. Readings were recorded once the signals had stabilized. The datasets can be found in Colussi et al.[43]

3.3.6 Measurements of Dissolved Organic Carbon (DOC)

Measurements of DOC were performed by catalytic combustion of samples in a platinum-bead-packed quartz furnace at 720°C to quantitatively produce CO_2, followed by non-dispersive infrared absorption spectrophotometry using a Shimadzu total organic carbon (model: TOC-V) analyzer and an autosampler (model: ASI-V). The cleaning of materials prior to DOC determination followed the same procedure as for the sample containers. Precipitation aliquots of at least 12 mL were transferred to clean and combusted (500°C, 5 hrs) 40 mL borosilicate glass vials and then capped and stored at 4°C until analysis. Prior to analysis, the vial caps were re placed with cleaned polytetrafluoroethylene-lined septa. In organic dissolved carbon (e.g., carbonic acid) was purged from samples by acidification to pH 2 with high-performance liquid chromatography-grade phosphoric acid (20% v/v) and bubbling with an inert carrier gas. Samples were analyzed in triplicate and quantified using calibrations spanning from 0.1 to 10 or from 10 to 100 ppm (mg C L^{-1}) with potassium hydrogen phthalate (KHP), depending on the relative sample concentration range. Accuracy and precision were assessed using 1 and 10 ppm KHP check standards analyzed every 10 injections, respectively. Calibrations were performed at the beginning of every analysis day. The dataset can be found in Colussi et al.[43]

3.4. Results and Discussion

In addition to the general design advantages, in the section that follows, we present the results for various physical and chemical parameters to validate this new open-source custom-built modular system. The power consumption and snow-free performance testing are used to demonstrate the off-grid capabilities of these samplers, as are the two-year datasets. The lower power requirements are compared to existing commercial samplers and paired with solar top up to

prolong the use of the batteries and reduce the need to replace them on timescales shorter than the planned sampling duration (i.e., less than one month). We then evaluate the automated wet deposition volumes (the dilution of which during atmospheric washout events is prevented by the samplers) in comparison to the total volumes collected from collocated samplers to depict the fractionation by volume as a function of time. We also investigate the advantages of replicates collected across the four watersheds using deployments of triplicate samplers under field conditions. The ratio of collected TF to OF replicates highlights the ability of these samplers to capture the dynamic nature of precipitation interacting with forest canopies. Simple pH and conductivity measurements are then used as benchmarks to situate the NL-BELT data within the established literature to emphasize the robust operation of the samplers and the impact of the selective sampling. Fluxes of DOC are also integrated across all four sampling sites as we demonstrate the potential of these samplers to make measurements of more complex analyte pools that are of current interest to the atmospheric measurement community.

3.4.1 General Design Advantages

While several precipitation collectors have been similarly developed to address specific scientific objectives – e.g., the quantitation of dust in wet and dry deposition[53,54] and the determination of ions and DOC in a tropical rainforest[23] and urban environments[55] – we present a more general design for modular adaptability here. When compared to other precipitation collection apparatuses, the automated precipitation sampler developed in this work has several advantages. Most notable is the ability to collect integrated samples at remote locations by exploiting its off-grid capabilities. Our approach also maximizes the sensitivity of the rain sensor as long as electrolytes remain in the water reaching it. The chute ensures that even if the

precipitation contains ultra trace analyte quantities, it is still collected and quantified for an extended period when high-purity water may be deposited during an atmospheric washout event. The chute does this by accumulating, between rain events, water-soluble materials that require time to be completely washed off and through the release of ions from the material itself, which ages under environmental conditions. As the conductivity of the precipitation falls below the sensor threshold – conductive precipitation being that which initially contains high solute levels that progress through trace-level concentrations – the added ions from the chute prolong the collection of rain past this time point. In rainfall events where extended atmospheric washout occurs, i.e., where precipitation becomes ultrapure water, the sampler lids will eventually close, preventing the dilution of the sample while maintaining the collection of analytes of interest. A recent study has found that rainfall events could exhibit variability and that the lower atmosphere can be supplied with aerosols due to specific sources, atmospheric dynamics, and meteorological conditions.[55] If this occurs, the automated lid will reopen to sample the polluted air masses. In application to trace pollutants, this also reduces the methodological sample preparation time, as it decreases the extent to which additional handling steps, like solid-phase extraction, are required prior to analytical determinations.

The six replicate measurements used in each array provide a means of assessing sampling reproducibility (e.g., canopy TF has expected heterogeneity) and allows for multiple analyte classes to be targeted. Various analytes with different chemical properties and/or contamination considerations can be targeted by changing the materials used for the components that encounter the sample (i.e., lids, funnels, and sample holding containers). Replicate collection can also allow for selective sample preservation when quantifying deposited chemical species that may be reactive, volatile, or biologically transformed. The modularity of the overall system design also

allows the collection units to be dismantled entirely and easily reassembled on-site, minimizing logistical issues and costs for transport to remote regions. Lastly, these collection units are cost-effective. We were able to produce four arrays, each consisting of six collection units, at a fraction of the cost of a single equivalent commercial off-grid automated precipitation sampling unit.

With the majority of commercial precipitation samplers requiring a source of electricity, on-grid sample collection necessitates high infrastructure costs and/or the positioning of samplers closer than desired to point sources of anthropogenic pollution. As a result, especially in remote locations, site selection becomes heavily restricted and expensive when factoring in all the standard criteria, particularly with respect to the need for an easily accessible power source. Thus, the off-grid capabilities of our samplers lend dexterity to these systems, enabling deposition sampling that follows standard siting guidelines, like those of CAPMoN or NADP, without requiring grid power, and making them more accessible to the global atmospheric research community.[7] To further highlight and validate their capabilities, a series of fundamental performance parameters were collected and are discussed in detail in the sections that follow.

3.4.2 Power Consumption and Performance Testing

3.4.2.1 Power Consumption of the Instrumental Setup

The simplicity of the automated precipitation samplers allows for low power consumption during operation, which is particularly important for off-grid operation. The motors operating and rain sensor heating during active precipitation are the most energy-intensive elements of the system (Table 3-2). The integrated contribution of the motor over a month-long sampling period is, however, negligible compared to other components since it is operational for short periods of 5 to 10 s, with a current usage of only 38 mA. The continuous need to provide 5 VDC to the digital

logic via a step-down from 12 VDC is actually the component of the setup that consumes the most power in the absence of rain. When the samplers are in the closed position, under rain-free conditions, the power consumption of the entire array is 4.66 watts (W) and 2.86 W for transformed 115 VAC and battery 12 VDC supplies, respectively. The provision of 12 VDC to the board with a transformer for the 115 VAC application results in greater total power requirements. These values increase to 10.00 and 5.04 W with the detection of a conductive liquid on the precipitation sensor, as the sensor surface is heated to capture the active period of the event. Based on the measured power consumption, a fully charged 103 Ah AGM battery would provide at most 447 hrs (or 18 days) in standby mode under rain-free conditions and 294 hrs (or 12 days) if the heated surface of the sensor is in continuous use (Table 3-2). The lower range limit is unlikely since the sensor only operates for the duration of a rain event, after which the battery is available for solar top-up again. In the fieldwork conducted here, battery life was extended through the addition of 40W solar panels to the systems. The entire array was confirmed to be operational at the end of monthly (SR, PB, and GCo) and two-month (ER) integrated sampling periods on an ongoing basis, prior to exchange with a new fully charged battery, for two years.

In comparison to two commercial samplers used by national monitoring networks, the power requirements of our new samplers are substantially lower. The first commercial sampler we reviewed draws a maximum of 2 A, with a ceramic heater housed within the sampler case that draws 0.8 A constantly, resulting in an upper-limit power demand of 230 W (at 115 VAC) and a lower limit of 92 W. The commercial sampler can be upgraded to utilize a thermostated space heater for winter operation, drawing an additional 4.2 A (480 W) and resulting in a maximum power demand of about 800 W when using a 115 VAC power supply. The second commercial precipitation sampler we reviewed is used by national monitoring networks and draws

approximately 5 A, resulting in a power requirement of 575 W at 115 VAC. The commercial and standard precipitation samplers for deposition monitoring programs have much higher power requirements compared to those presented in this work. The commercial samplers utilize 80 to 100 times more power. With their lower power requirements, the new automated samplers prove to be advantageous in both on- and off-grid sampling yet are disadvantaged in being unable to collect snow in the winter.

3.4.2.2 Precipitation Sampler Performance Tests and Data Logging

In addition to low power consumption during precipitation sampling, a supplied battery can obtain constant power renewal when outfitted with a solar top-up that is kept exposed to sunlight by proper orientation. At the NL-BELT, adjustments were made for this during sample collection at each site visit. During the solar top-up tests discussed below, the voltages of the sensor and batteries were consistently monitored. Over a test period of 22 days, no appreciable decline in battery performance of a 76 Ah unit was observed despite the detection of more than 10 rain events during that period (Figure 3-3a).

In comparison, winter sampling with these devices is not recommended without substantial investment in a sufficient power density provided by high-performance cold-weather batteries. The lack of sunlight during winter at higher latitudes also negates the use of an effective small-scale solar top-up. Our tests show that when the samplers were deployed without a solar backup under snow-free winter conditions (temperatures ranging from -17.8 to 7°C), with a 103 Ah battery, the off-grid system only lasted for 17 days. At this point, the larger-capacity battery was fully depleted by frequent snow and rainfall – probably due to the heated precipitation sensor requiring additional energy to phase-change snow and ice to water and then to evaporate that water. This depletion

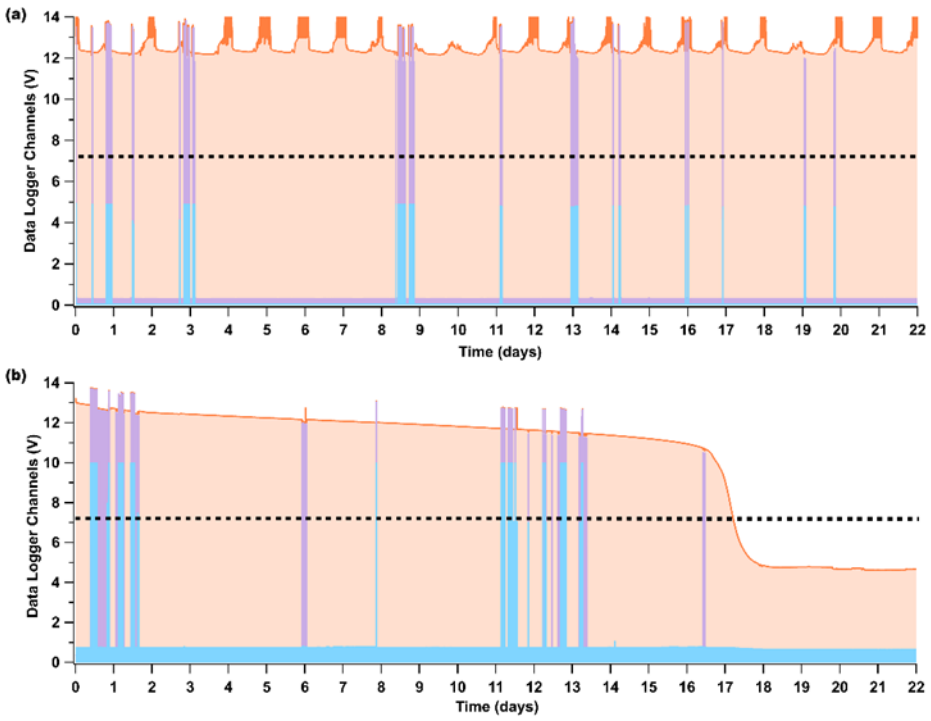

Figure 3-3. Performance of off-grid precipitation samplers during sample collections **(a)** from July 13 to August 7, 2018 (when using a 76 Ah battery and a solar-panel top-up) and **(b)** from January 22 to February 13, 2019 (when using a 103 Ah battery and no solar panel). Battery voltage (shaded orange) is elevated above 12 VDC when charging, or it decreases over time when no solar panel is used and precipitation is sensed and collected. The 12 VDC rain sensor relay signal (purple) and the open sampling-lid switch voltage (blue) indicate active periods of detected precipitation. The dashed black line indicates the 60% efficiency cutoff, 7.2 V, at which the battery should be recharged.

occurred despite the battery being housed in an insulated enclosure during the test. In addition, on days 6 and 16, the precipitation sensor relay was activated but the lid did not rotate to the open position (Figure 3-3b, blue trace). This could have been because the precipitation event was not intense enough for the lid to open fully and trigger the 5 V lid open switch or because of snow and ice buildup around the lids, resulting in them being unable to physically open. Overall, it may be possible to deploy these samplers during the winter if line power can be supplied. Such a deployment would further necessitate that the sampling funnel be heated (in addition to the sensor chute) to prevent snow and ice accumulation and render a liquid sample for collection in the jugs.

A heated funnel would also prevent snow or ice accumulation on top of the automated lids. Together, such power-hungry requirements for winter operation exceed simple off-grid use with a battery package that is easily transported into and out of remote field sites.

Table 3-2. Measured voltage, current, and power consumption of the rain sensor and circuitry in both the idle and maximally operational states when connected to a 12 VDC battery or transformed 115 VAC. Total power demand was measured for wet and dry sensor scenarios.

							Total			
			AC Outlet		DC Battery		AC Outlet		DC Battery	
Parameters	**Rain Sensor Idle**	**Rain Sensor Active**	**Idle Board**	**Motors In-Use**	**Idle Board**	**Motors In-Use**	**Dry**	**Wet**	**Dry**	**Wet**
Voltage (V)	12 DC	12 DC	114 AC	110 AC	12 DC	12 DC	-	-	-	-
Current (A)	0.008	0.120	0.040	0.078	0.230	0.300	-	-	-	-
Power (W)	0.10	1.44	4.56	8.58	2.76	3.60	4.66	10.0	2.86	5.04

3.4.3 Comparison of Sample Collection Volumes

The automated samplers were collocated with total deposition samplers and deployed across the experimental forests of four NL-BELT regions during the 2015 and 2016 growing seasons to observe deposition trends. In addition, we compare these observations to the long-term climate normals reported by ECCC and the estimated deposition at 1km x 1km resolution from the DAYMET reanalysis model (Table 3-1, Section B.2). Three automated samplers were deployed in the open to collect incident precipitation (OF), and another three were deployed under the experimental forest site canopy (TF). The mean OF volumes of triplicate measurements from south to north were 1.42, 1.38, 1.31, and 0.79 L, whereas the corresponding TF volumes were generally similar in magnitude at 0.96, 0.98, 1.02, and 1.13 L, for the 2015-16 sampling period (Figure 3-4).

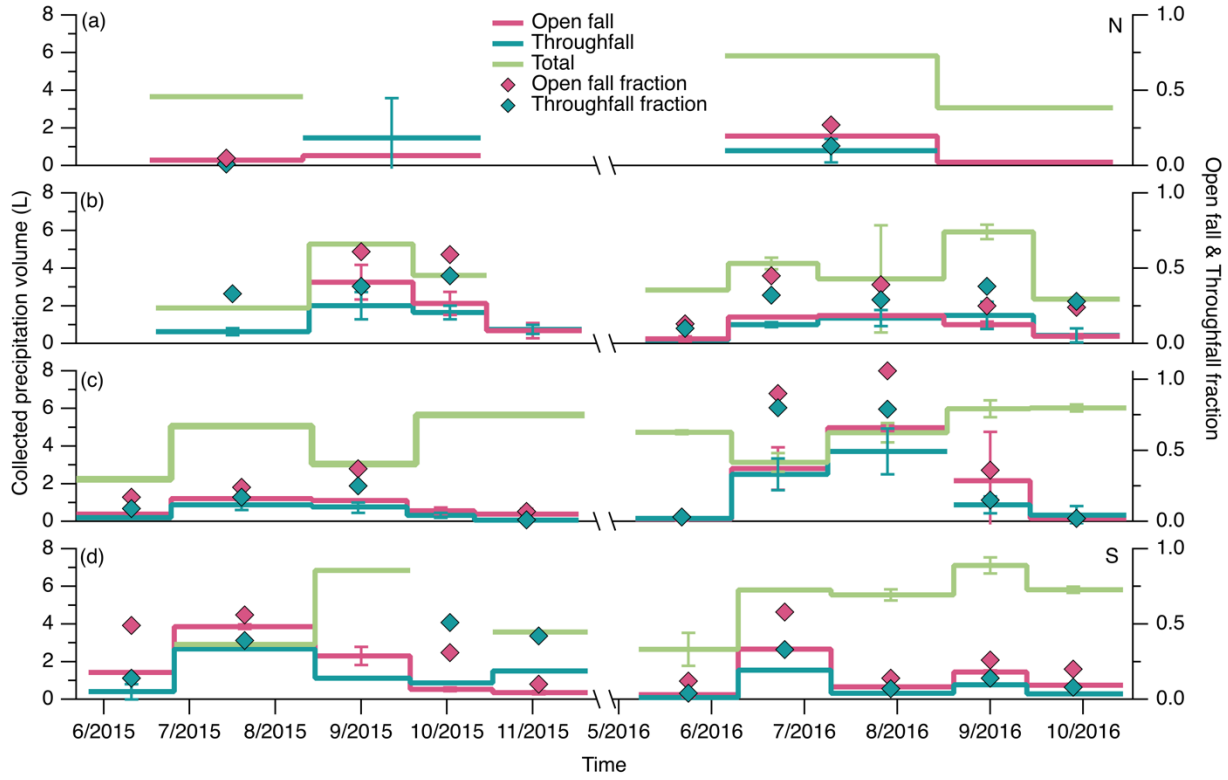

Figure 3-4. Average volumes collected from replicate automated samplers deployed from June 2015 to October 2016 at the NL-BELT field sites (from north (N) to south (S)) **(a)** ER, **(b)** SR, **(c)** PB, and **(d)** GCo. The red trace represents open fall, teal represents through fall, and light green represents total deposition (the sum of conductive and non-conductive precipitation). The total precipitation volumes depicted for PB from July 2015 to November 2015 were collected at the nearby HR site in the same watershed since no total deposition measurements were in place at PB during this period. The missing volume for GCo in 2015 was estimated from the linear relationship determined for ECCC stations and is presented as a broken line. The fraction of precipitation collected as open fall or throughfall, compared to the total deposition (right axis), is represented by diamonds of the corresponding colour. Error bars represent the standard deviation of three measurements from replicate samples. The axis break spans the winter months when the off-grid automated samplers were stored.

It is evident that the volume of precipitation decreased as the latitude increased for OF samples, whereas the opposite relationship was observed in TF samples, although the absolute volumes are more comparable in magnitude. The total deposition volumes collected were as expected; they decreased from south to north in agreement with the expectations from the long-term normals and were comparable to the estimates from the DAYMET model (Table 3-1), where the largest

integrated volume of precipitation was collected at the lowest latitude (GCo) and a lower amount was collected at the highest latitude (ER), with the intermediate sites (HR and PB) having the lowest inputs overall during this observation period. Total annual deposition volumes collected by our deployed samplers from south to north in 2015 were 39.5, 39.4, 31.9, and 17.5 L, while in 2016 they were 51.7, 37.8, 32.8, and 34.2 L. The total deposition volume collected from HR was used for comparison to automated sample volumes collected at PB in 2015, as both sites share the same watershed. This approach had to be taken, as the HR site was initially planned for full experimental use before becoming inaccessible in early 2015. The relative error between the two sites for samples collected in 2016 was 15% (24.6 L in PB and 32.2 L in HR), comparable to the reproducibility we observe for replicates collected within a given site (see below). The total deposition samplers were installed in HR in late 2014, and the automated samplers were then set up at PB. Despite this, there is good agreement between the trends in deposition values predicted by DAYMET and the measured values, although the absolute amounts are systematically lower in all of our observations (Section B.2). Regardless, by following the recommended siting criteria from the NADP and CAPMoN as best as possible, the very strong agreement of our temporal trends at both annual and monthly timescales with both comparators demonstrates the suitability of the total deposition samplers and, therefore, the automated samplers for use in quantifying chemical species of atmospheric interest deposited into the experimental sites.

The wet deposition volumes collected for the snow-free period using the automated precipitation samplers did not follow the trends in total deposition (Figure 3-4) that might be expected (e.g., due to pollutant loading, rainfall quantity/rate, and scavenging processes). For the 2015 collection period from June through October, the summed volumes of OF precipitation from south to north across the NL-BELT were 25.4, 10.9, 20.4, and 2.2 L, while in 2016 they were 17.3,

30.4, 13.5, and 5.1 L. While the total and OF fractions would typically be much closer to unity in more-polluted regions, it would be expected that the differences in these remote NL-BELT field sites would be driven by complex non-linear processes that cannot be easily disentangled. Here we present three reasons as to why the measured OF wet deposition volumes do not follow the total deposition trend across the transect. First, these samplers are designed specifically to collect only conductive precipitation (i.e., containing conductive atmospheric compounds), not total/bulk precipitation. As a result, the OF wet deposition volume collected across the sites is mostly below 50% of the total volume collected, while the TF volumes are similar in magnitude to or lower than the OF volumes (Figure 3-4). The wet deposition fraction collected was variable within and between regions; it was sometimes less than 10% despite the large volumes collected in total, presumably due to the intense atmospheric washout that this region is well-known for. Secondly, the NL-BELT total deposition trend estimated using the ECCC long-term climate normals represents a 30-year period[56], while the automated volume measurements described here represent two years of targeted conductive precipitation collection. The combined summed volumes of targeted conductive wet deposition across the 2015 and 2016 field seasons were 42.7, 41.3, 33.9, and 7.3 L, which somewhat better reflect the expected precipitation trends within the transect (Table 3-1). Lastly, our monthly automated wet deposition sample collection periods occurred from June through November and so are temporally incomplete with respect to the substantial amount of precipitation volume deposited as snow during the winter (Table B-3). The discrepancies between the long-term trends and our shorter-term observations therefore make sense, as they are sensitive to interannual changes in synoptic-scale transport and rainwater solute loadings, as exemplified by the volumes collected in SR in 2015 (Figure 3-4b) and PB in 2016 (Figure 3-4c). Overall, for the automated sampler observations on a per-year basis, there is no consistent trend

between site latitude and the volume collected in either OF or TF. This is unsurprising, as they are dependent on the conditions that drive the rate of atmospheric washout and the presence of conductive solutes.

The automated OF wet deposition volumes collected each year have peak values that range from 1 to 4 L, with an overall variability of 33% for any triplicate of samples across the entire dataset. Across our 33 sample collection periods, our replicate relative standard deviations (RSDs) follow a log-normal distribution where volume reproducibility is typically within 125% and almost always within 315% (Figure B-11). A few outliers with higher variability skew the overall view of volume precision. Out of 33 OF samples collected, 10 have RSDs greater than 40.5%, with two of those 10 having RSDs greater than 100%. Those values greater than 40.5% had no systematic relationship with site or time of year. Wind speeds were considered as a possible source of variability. The prevailing winds over Atlantic Canada are known to be southwesterly in the summer – intensifying during the autumn months – and westerly to northwesterly in the winter.[57-59] Strong wind speeds (i.e., >100 km hr^{-1}) could occur on an event basis during any time of the year and, thus, could contribute to the variability seen at each field site. Wind is known to generate bias in gauge-based precipitation measurements, as unshielded precipitation gauges can catch less than half of the amount caught by a shielded gauge.[60] A more-reproducible windscreen design for obtaining rainfall rates – and, thus, volumes – could be considered in future deployments of our developed samplers, similar to recently reported innovations for smaller rainfall-rate devices.[61] This would, however, increase costs and logistical considerations in deploying the developed devices, which currently operate synonymously to deposition systems employed by government monitoring programs. Our siting approach is consistent with those, which often deploy a single sampler without wind protection. Thus, by employing replicates, we are able to ascertain the

environmental variability. In addition, the collection of replicate samples allows our observations to span a wider physical area, reducing the impact of confounding variables such as wind speed in comparison to a more typical sample size of one for many field collections. Imperfect siting and a lack of shielding is necessary where remote field sampling prevents the setting up of such infrastructure. As a result, the deployment of triplicate samplers provides researchers with a better opportunity to implement quality control, as they can reduce bias in the event of dynamic OF. While the effect of wind is reduced, additional factors can drive variability when the samplers are placed under a forest canopy for TF collection.

To demonstrate the canopy dynamics impacting interception volumes within the sampling sites, the ratio of through fall to open fall (TF/OF) volumes was compared amongst our total pool of 31 samples. This group of samples encompassed the monthly average TF/OF values for each set of triplicate samplers, at all four sites, from 2015 to 2016. These measurements were then split into two separate populations – samples that have a TF/OF of less than 1 (n = 24) and those that have a TF/OF of greater than 1 (n = 7). The samplers were positioned identically between years, and no single sampler was reproducibly found in the second population. In the first population, the fraction collected was 56 ± 21% (ranging from 19 to 88%), likely due to the known processes of canopy and stem interception.[62,63] For example, in two young balsam fir-white birch mixed-forest stands, the amount of precipitation intercepted by the forest canopy in similar snow-free conditions was estimated to be 11 ± 5%.[64] In mature boreal forests, 9 to 55% of rainfall can be intercepted by the canopy.[65] Relevant to the deposition of atmospheric constituents, Pomeroy et al. also reported that up to 70% of intercepted rainfall may evaporate directly from the canopy, which can leave behind non-volatile rainfall solutes.[65] Wet deposition that undergoes stemflow (SF) proceeds down the branches, stems, and/or trunks of a plant, transferring precipitation and nutrients from the

canopy to the soil at the trunk or stem base.[66] These known mechanisms of canopy interception ultimately reduce the amount of precipitation reaching the ground as TF, thus explaining the smaller volumes found in our samplers compared to the OF measured simultaneously. In contrast, the fractions that ranged from 108% to 424%, averaging 186%, demonstrate a different aspect of the highly dynamic nature of canopies, where they can sometimes intercept rainfall like an impermeable surface to act as a funnel, guiding large volumes of precipitation onto the ground or, in this case, into the TF samplers.[67]

3.4.4 Characterizing Chemical Parameters from the NL-BELT

In addition to assessing physical parameters, chemical parameters were also evaluated in this work. Conductivity and pH are measurements commonly made on precipitation samples collected from the field and so incorporating them into our analysis is useful for instrumental validation. Additionally, with increasing recognition of their importance as a proxy for ROC estimation and in biogeochemical carbon budget closure, DOC flux measurements were used to compare against a limited number of prior reports, each using different sampling or data interpretation strategies. These chemical measurements were also made in an underrepresented part of the world in terms of atmospheric deposition sampling and are useful additions to the overarching study of precipitation chemistry.

3.4.4.1 Precipitation pH

The deposition of atmospherically persistent pollutants and biogeochemically relevant species onto the Earth's surface, or even nitrate and sulfate historically, can affect the environmental health of soil, air, and water. The pH range of natural rainwater in equilibrium with atmospheric CO_2 is expected to be between 5.0 to 5.6 and so acid rain is defined by values lower

than this.[68] Traditionally, the extent of acidity depended on the intercepted atmospheric concentrations of nitric acid (HNO_3) and sulfuric acid (H_2SO_4). In any case, monitoring acidity and deposition is especially relevant in remote regions, where major uncertainties and gaps in deposition measurements and global ion concentrations exist.[7,69] A change in pH can modify the chemical states of many pollutants, altering their transport, bioavailability, and solubility.[70] For example, this can increase the exposure and toxicity of metals and nutrients in marine habitats, which can go undetected for longer periods in remote areas.

Most TF samples were observed to have slightly higher pH values than those from OF, which had pH values ranging from 4.14 to 5.71 (Figure 3-5, Table 3-1). The TF precipitation pH, on average, ranged from 4.74 to 5.99, with rare exceptions falling outside of that range (e.g., in July and September 2015 at PB, the pH was 3.69 and 4.26, respectively, and in July 2015 at GCo, the pH was 4.12). Excluding these exceptions, there are no major variations observed spatially between the four sites or temporally between seasons or years (Figure 3-5). The pH values reported at each of the NL-BELT field sites are comparable to recent OF measurements made at CAPMoN sites in Nova Scotia and Newfoundland and Labrador, where the reported pH of precipitation ranged from 4.44 to 5.19.[71] The more-basic TF overall is expected, as it has been found that up to 90% of the hydronium ions in precipitation can be absorbed by leaves while it passes through the canopy.[72] Foliar leaching, the release of ions from leaves, has been commonly reported for base cations such as magnesium, potassium, and calcium, while being minimally observed for other ions such as chloride and sulfate.[73] Mechanisms for foliar leaching include the passive cation exchange of hydronium ions with, for example, cells in the interior of the leaf.[74] Additionally, alkaline dust deposited on the leaves of the canopy can decrease the acidity of TF precipitation.

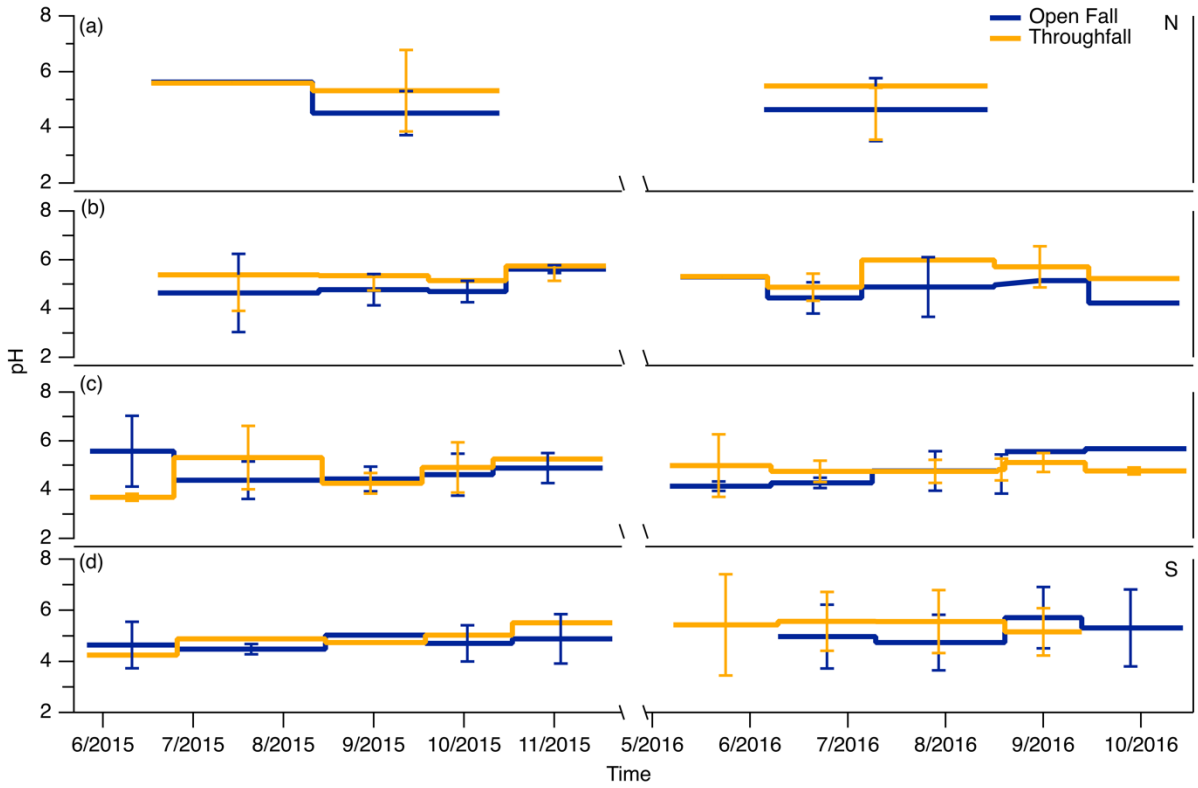

Figure 3-5. Average pH values from replicate samples collected at the NL-BELT field sites (from north (N) to south (S)) **(a)** ER, **(b)** SR, **(c)** PB, and **(d)** GCo from June 2015 to August 2016. Open fall collections are represented using a solid blue trace, whereas the orange trace is the pH of the precipitation collected as throughfall under the balsam fir canopy.

Such dust can accumulate on leaf surfaces as a result of anthropogenic (i.e., industrial processes) or natural (i.e., wind erosion) sources[75], so that precipitation passing through the canopy can interact with it (e.g., calcium carbonate), thus neutralizing acidic species and increasing the TF pH observed in our automated samplers.

The pH of the collected precipitation appears to be similar in both TF and OF as a function of time despite the potential for foliar leaching and dust dissolution in the canopy. The same chemical components may be setting the pH, as these measurements do not vary much seasonally, geographically, or temporally. As pH is a long-studied measurement, its purpose in this work was to validate the sample quality obtained from our described collection approach rather than drive any scientific objective. Nevertheless, while the NL-BELT measurements demonstrate a recovery

compared to rainwater pH in 1980s eastern North America prior to NO_x (nitrogen oxides; NO + NO_2) and SO_2 regulation (pH from 4.1 to 5.0)[76], the present-day pH remains lower than expected for natural rainwater (~5.6).[77] Keeping in mind the successful environmental policies limiting SO_2 and NO_x, which have led to considerable decreases in atmospheric concentrations of H_2SO_4 and HNO_3, a modern view on the trajectory of continental USA cloud water composition and pH has recently been reported.[78] Across the USA and eastern Canada, measurements of anion molar charge equivalents have been lower than those of cations, with a potential explanation being an increase in the presence of weak organic acids, which commonly have pK_a values near to 4[79] – an outcome we have also observed in aerosol sample chemical compositions from Atlantic Canada.[80] With the frequency of acid rain of pH <5 decreasing over the past 20 years, these recently reported measurements depict that the deposition composition is shifting away from a "linear" chemical regime dominated by hydronium and sulfate ions towards a "non-linear" regime designated by low acidity, moderate to high conductivity, potentially weak acid-base buffer systems, and increasing base cation and total organic carbon concentrations.[78] It would seem that the evolving chemical contributors to global rainwater pH remain an open line of investigation.

3.4.4.2 Precipitation Conductivity

In all the OF and TF precipitation samples collected across all four NL-BELT sites, the average measured conductivity values ranged from 21 to 166 μS cm^{-1} and followed no apparent seasonal or temporal trend (Figure 3-6). Additionally, the conductivities of both OF and TF also appear to vary across the field sites – only within the 2016 TF samples does the conductivity appear to increase with decreasing latitude. Yet, with the typical conductivity of surface and drinking

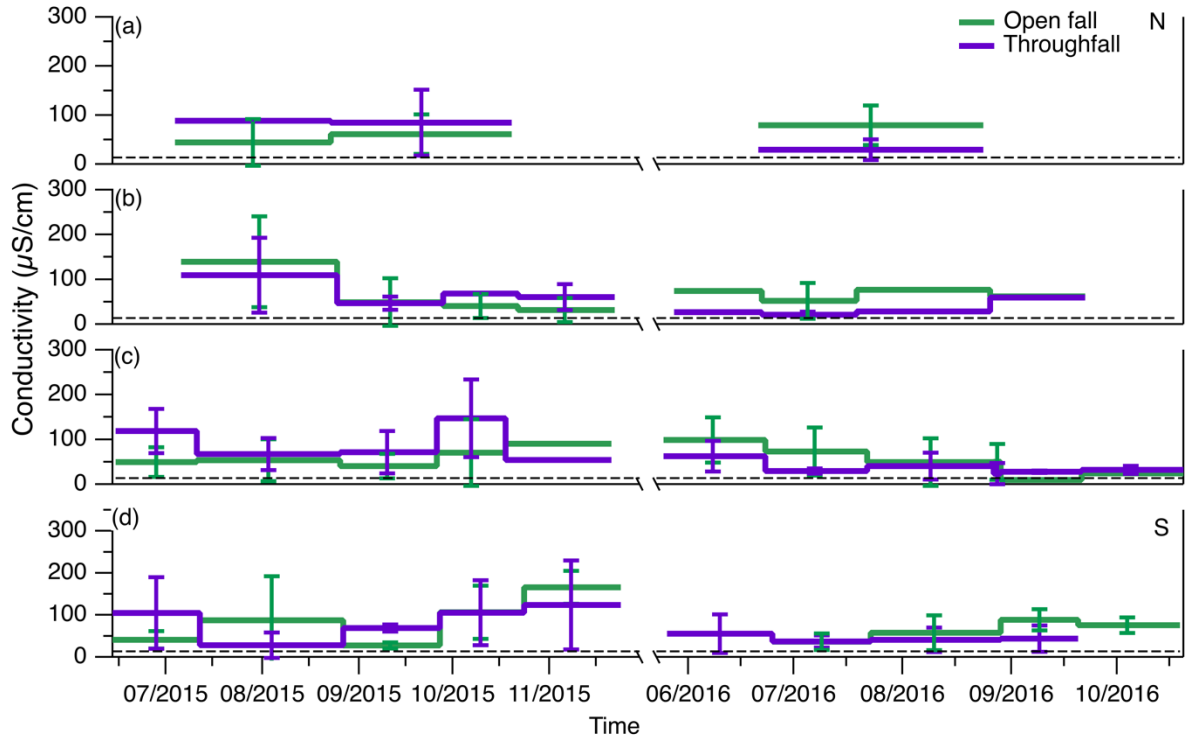

Figure 3-6. Average conductivities measured from replicate automated samplers at the NL-BELT field sites (from north (N) to south (S)) **(a)** ER, **(b)** SR, **(c)** PB, and **(d)** GCo from June 2015 to October 2016. The green trace represents open fall samplers, whereas the purple trace represents throughfall samples. The error bar represents the standard deviation between replicate measurements. The dashed black line represents the upper threshold of conductivity (13.6 µS cm^{-1}), which arises when saturated aqueous $HgCl_2$ is added to microbially sterilize samples. Note that all samples have conductivities equivalent to or higher than 13.6 µS cm^{-1}.

waters[81] being between 1 to 1000 µS cm^{-1} and typically below 200 µS cm^{-1} in stream water measurements within the watersheds of each of the NL-BELT sites, our observations are comparable and fall within the expected range. Our field blanks – encompassing a variety of materials and apparatuses as well as our cleaning procedures – routinely produced conductivities of 9 ± 5 µS cm^{-1}. The conductivity of saturated $HgCl_2$ in water (at 0.1% vol/vol) was 13.6 ± 0.4 µS cm^{-1}, which is also comparable to but statistically higher than our field blanks ($\rho = 0.0015$; unpaired t-test) and less than what was observed for our samples ($\rho < 2 \times 10^{-6}$) for each site considered separately and also across all sites; unpaired t-test). Even with this background correction applied, the conductivity values presented here are expected to be similar to or higher

than what would typically be found in rainwater (4 to 150 μS cm^{-1})[82], as the rain sensor deliberately selects for precipitation containing ionic chemical components with a conductivity greater than 1.0 μS cm^{-1} while excluding pure water during atmospheric washout, which would dilute the dissolved solutes in the wet deposition sample and lower the resulting conductivity values. The overall comparability between our range and those previously reported, where the lower limit is slightly higher in our dataset, demonstrates that the principle of operation of our instrument is robust. It decisively collects precipitation with the property of conductance, indicating the presence of dissolved ionic solutes of interest in relation to atmospheric chemical processes.

3.4.4.3 Wet Deposition of Dissolved Organic Carbon (DOC) at the NL-BELT

The concentration of DOC in OF and TF precipitation across all four sites ranged from 3 to 46 mg L^{-1} and from 5 to 65 mg L^{-1}, with averages of 16 ± 10 mg L^{-1} and 22 ± 12 mg L^{-1}, respectively (Table 3-3). Concentrations are influenced by the volume collected and are not useful when discerning deposition trends and/or mechanisms. The concentrations were converted to elemental fluxes using the volume of precipitation collected, the area of the funnel, and the number of sampling days in each sampling period (Figure 3-7). The total flux for each sample period was summed and reported as an equivalent annual flux in the following units: mg m^{-2} $year^{-1}$. Annual fluxes ranged from 600 to 4200 mg C m^{-2} $year^{-1}$ across the study sites for the snow-free period (Table B-4).

The TF DOC fluxes were enhanced compared to the corresponding OF samples, as precipitation was intercepted by the forest canopy, with fluxes being higher in TF samples by 600, 400, and 400 mg C m^{-2} $year^{-1}$ at GCo, SR, and ER, respectively (Table B-5). The accumulation of water-soluble organics on forest canopies, which increases the DOC detected in TF, could originate

Table 3-3. Concentrations (mg C L^{-1}) and annual fluxes (g C m^{-2} $year^{-1}$) of DOC in precipitation (P), open fall (OF), throughfall (TF), and stemflow (SF) collected at forested sites. Where volumes were not available in the other studies, it was not possible to calculate fluxes. The values reported in the current study are the estimated DOC flux for the sampling period (~ June through October) for each year and therefore represents the lower limit of DOC deposition, as the dataset excludes now.

Site	Type	Mean Concentration (mg C L^{-1})	Annual Flux (g C m^{-2} $year^{-1}$)	References
Grand Codroy, NL, Canada (2015 – 2016)	OF	12.83	1.56	This study
	TF	23.40	2.20	
Pynn's Brooke, NL, Canada (2015 – 2016)	OF	19.98	4.21	
	TF	21.24	2.44	
Salmon River, NL, Canada (2015 – 2016)	OF	16.14	1.33	
	TF	21.00	2.65	
Eagle River, NL, Canada (2015 – 2016)	OF	11.59	0.53	
	TF	28.26	0.86	
Mont St. Hilaire, QC, Canada (1987)	P	2.00	0.49	Dalva and Moore[100]
	TF	12.13	2.05	
	SF	40.10	0.10	
Northern China (2007 – 2008)	P	2.4 to 3.9	1.4 to 2.7	Pan et al.[103]
Coulissenhieb, Northeast Bavaria (1995 – 1997)	P	2.70	-	Michalzik and Moore[104]
	TF	15.20	-	
Hobcaw Barony, South Carolina, USA (2014 – 2015)	P	1.20	-	Chen et al.[105]
	Pine TF	26.00	-	
	Oak TF	38.8	-	
University of Georgia, USA (2015 – 2016)	TF Epiphyte Oak	17	23**	Van Stan et al.[101]
	TF Bare Cedar	20	32**	
	TF Epiphyte Cedar	54	48**	
SMEARII Site, Southern Finland (1998 – 2012)	P	3.24	2.32	Pumpanen et al.[99]
	TF	10.10	4.35	

** Estimated DOC yield for 2016 (g C m^{-2} $year^{-1}$) where sampled storms values (g C $event^{-1}$) were scaled to an annual deposition value using meteorological data and a linear rainfall-DOC yield relationship.

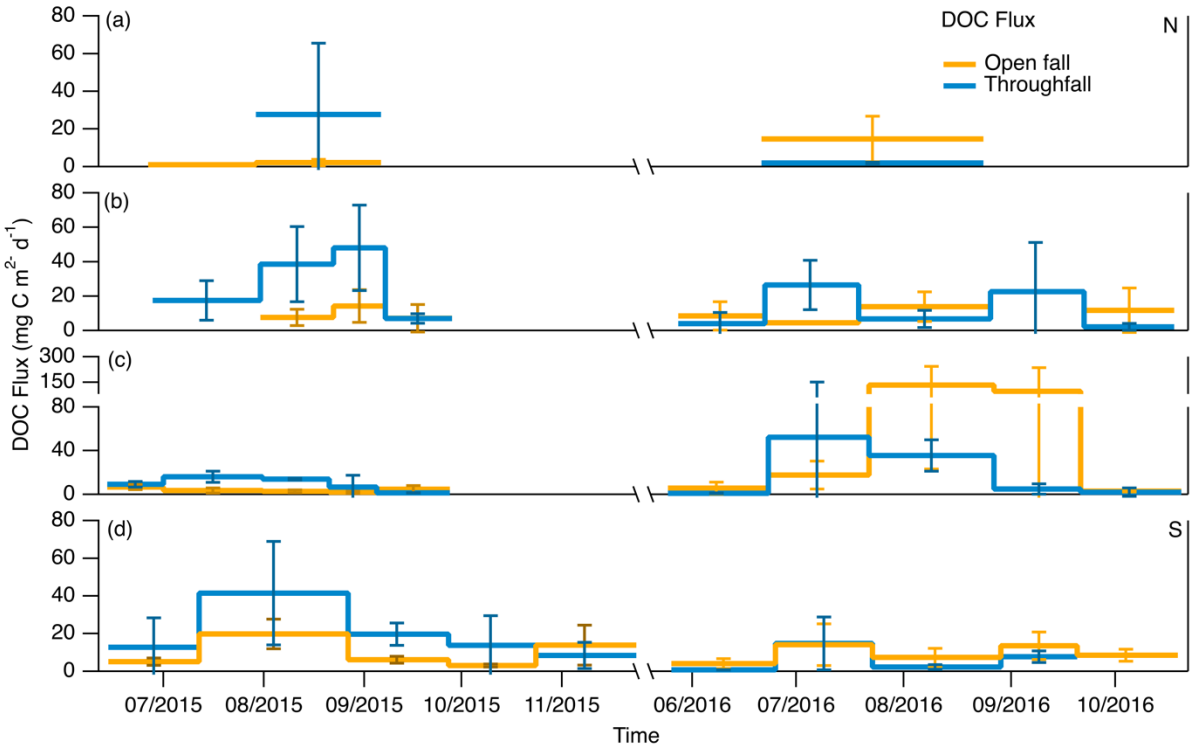

sites (ranging from north (N) to south (S)) **(a)** ER, **(b)** SR, **(c)** PB, and **(d)** GCo from June 2015 to August 2016. The yellow trace represents samplers that were placed in the open without any obstruction, whereas the blue trace represents samplers that were placed under the canopy. Error bars represent the standard deviation of three measurements from three independent samples.

in part from organic carbon-containing compounds that age through oxidation reactions in the atmosphere, which increases their water solubility and propensity for surface interactions. In periods without substantial rain, these oxidized organics deposit effectively onto the high surface area of forest canopies, contributing to the elevated DOC measured in TF. Additionally, non-volatile organics left behind from evaporated precipitation intercepted by the canopy could also contribute. Conversely, other mechanisms within the forest could result in the enhanced DOC in TF. Recently, Cha et al. utilized a mass balance approach to determine whether DOC deposition is driven by canopy leaching (i.e., soluble tree resin, leaf exudates, internal tissues, and microbes) or the dissolution in rainwater of dry deposited gases and fine mode particulate matter (≤ 2.5 μm; $PM_{2.5}$) on plant foliage.[83] It was found that canopy leaching is the major contributor to TF DOC,

accounting for 83% of the throughfall DOC, whereas $PM_{2.5}$ and rainwater only accounted for 3% and 14%, respectively, while dry deposited gases were not considered. This suggests that internal cycling of DOC within the forest could be an important source of DOC at the throughfall-soil interface.[83] It is possible that a similar mechanism may be responsible for the elevated levels of DOC in TF at the NL-BELT sites, but we cannot explicitly distinguish between internal cycling versus external deposition in the current study.

A notable exception was observed at PB, where the DOC fluxes in the open fall sample were enhanced by up to 1800 mg C m^{-2} $year^{-1}$ when compared to the TF in 2016. This may be attributed to a difference in forest type within this NL-BELT region, with black spruce (*Picea mariana)* being present instead of balsam fir.[84] Some studies have suggested that forest type could be a major factor affecting DOC variability.[85,86] Specific differences in canopy height, leaf area index, canopy structure, and the shapes of leaves and needles could drive DOC differences between forest types.[86-88] The elevated levels in the OF samples relative to TF within PB are consistent with the idea of uptake in the canopy, while the enhanced TF at the rest of the sites makes it more difficult to observationally constrain canopy uptake and/or leaching processes in the internal cycling of DOC.

Episodic events, such as polluted air masses from wildfires, could also result in an elevated deposition of DOC. It is estimated that ~116 to 385 Tg C $year^{-1}$ is produced globally due to the incomplete combustion of biomass during landscape fires.[89,90] Several studies have associated enhanced DOC levels with wildfires.[91-94] More recently, Coward et al. measured the DOC in Pacific surface waters along the California coastline and observed a 100% to 400% increase in DOC concentration when compared to pre-wildfire conditions.[90] It is possible that a similar biomass-burning plume that underwent atmospheric washout could be responsible for the

enhancement in the observed DOC at the NL-BELT, which overlies a background more typical of seasonal oxidation of biogenic DOC. This also coincides with the seasonal variability observed in OF samples from the same summer when elevated levels of DOC were measured. For instance, the DOC deposition at PB for August 2016 was 4800 mg C m^{-2}, whereas the total deposition for the same year was 7800 mg C m^{-2} $year^{-1}$. This single period accounts for 62% of the total DOC deposition at this site. This underscores the pivotal role that episodic transport may play in influencing the dynamics of DOC deposition, particularly in a warming future when wildfires are more prevalent.

The deposition trend observed in the current study also highlights the complexity of the various drivers of atmospheric ROC, with more DOC being present in TF versus OF during some months, whereas occasionally the opposite is observed. Generally, we measured similar fluxes in both samples – suggesting that the amount of deposited carbon is comparable. Although the volume of precipitation captured in TF samplers is generally lower when compared to the corresponding OF samplers, the deposition flux of DOC is greater in TF samplers. With the enhanced DOC in TF samples, the values reported here could be an underestimation of the amount of carbon reaching the forest floor during precipitation events due to competing processes within the canopy. One such process is SF, where a fraction of the precipitation intercepted by the forest canopy is funnelled over the bark of the tree surface to the base of the tree stem.[95] Although SF was not measured in the current study, several studies have demonstrated that DOC concentrations are enhanced in SF when compared to the corresponding TF and bulk precipitation samples.[96-98] Additionally, we cannot rule out that the chemical speciation differs between OF, TF, and SF, even if the DOC values are similar, but such insights require more selective instrumentation for chemical analysis (e.g., high-resolution mass spectrometry).

The ability to accurately determine DOC in OF and TF precipitation demonstrates the capability of the automated deposition samplers. To validate our measurements, we compared our observed fluxes to other studies in different forest types. Mean annual DOC fluxes were generally similar to those reported in some other boreal forests (Table 3-3). These include results from stands in Finland that consisted mainly of Scots pine (*Pinus sylvestris L.*; mean OF 2.32; TF 4.35 g C m^{-2} $year^{-1}$)[99] as well as stands in Mont St. Hilaire, QC, Canada (mean OF 0.49; TF 2.05 g C m^{-2} $year^{-1}$)[100], which also consisted of a variety of tree species, such as yellow birch (*Betula allenghanien*), red maple (*Acer rubrum*), and sugar maple (*Acer saccharum*). Conversely, the annual fluxes were orders of magnitude lower than measurements (23 to 48 g C m^{-2} $year^{-1}$) made at the University of Georgia in a forest (with a subtropical climate) consisting mainly of southern live oak (*Quercus virginiana Mill.)* and eastern red cedar (*Juniperus virginiana L.*) and which occasionally hosts dense epiphytes.[101] This highlights the potential variability to expect when measuring DOC in different forest systems, as the annual DOC fluxes vary depending on factors such as climate, tree species composition, and environmental conditions.

These results underscore the pivotal role that off-grid custom-built automated deposition samplers can play in advancing scientific research, particularly in precipitation monitoring and analysis. The automated system enabled long-term continuous sample collection in remote locations, which was previously challenging to achieve due to the need for frequent human intervention and the resources required to regularly access these experimental forest stands. These samplers also allowed us to compare DOC through replicate measurements in TF and OF samples, which sheds light on the potentially different DOC deposition chemistries within the NL-BELT region. The automated system better maintains the integrity of DOC in the samples. This was achieved by following standard procedures for biogeochemical sample preservation (i.e., adding

$HgCl_2$)[102], employing a rigorous cleaning procedure, and using a design that prevents against the intrusion of forest litter, which could result in a positive bias for DOC in the collected precipitation. The use of replicates also results in more robust scientific conclusions and broader applicability of the results, and they can be obtained for a fraction of the cost of a commercial equivalent, highlighting the contribution that these automated systems are capable of when applied to current precipitation monitoring. As a result, these samplers show promise in the quantification of biogeochemical and anthropogenic chemical species of interest. This will be visited in future works drawing from the samples presented in this dataset and others obtained since but are beyond the scope of this paper, which is to demonstrate the performance of this new instrumentation.

3.5. Conclusions and Future Directions

This paper presents a cost-effective automated deposition sampler for the continuous collection of precipitation. An open-source procedure and schematics for building these samplers are provided alongside the rationale for selecting the materials in the current study to target analytes of scientific interest in wet deposition samples. These low-power systems are demonstrated as being capable of continuous off-grid use for sample collection over two years at the NL-BELT experimental sites with monthly or bimonthly replacement of battery power packs, with their on-grid performance also provided for comparison. The resulting systems enhance the accessibility of automated wet deposition samplers to scientists globally, and this work highlights their robust performance in collecting and preserving rainwater conductivity and pH alongside providing measurements of DOC from this understudied region, which build a broader picture of the atmosphere-surface exchange of this biogeochemical pool across the NL-BELT. The comparability and complementariness of our results to well-established and current measurements of interest like DOC demonstrate their efficacy and potential application to the study of processes

such as canopy precipitation interactions through the collection of OF and TF replicates. The capacity to autonomously collect wet deposition in addition to traditional bulk deposition samples can shed light on competing wet and dry deposition processes. Should the on-grid capacity suit scientific objectives, it is anticipated that these samplers could be used year-round when paired with more power-intensive strategies to facilitate solid-to-liquid phase transfer for precipitation detected and collected in the winter.

For the broader deposition-motivated community, the instrument design also allows for easy and cost-effective modification of the number of replicate samplers, the material composition of all the surfaces the aqueous samples interact with, and preservation strategies – depending on the analyte of interest. For example, the lack of organic nitrogen measurements within universally established sampling and measurement procedures serves as a general example of the substantial knowledge gaps that may result when translating limited datasets to the wider global picture. This includes incomplete speciation and quantification across precipitation, aerosol, and gas phases. Monitoring systems that support deposition assessments in the USA (e.g., the NADP) only characterize the inorganic fraction of wet deposition. Additionally, modern emerging issues that require the continuation of existing deposition measurements or the expansion of observation programs revolve around identifying and quantifying compound classes of concern, such as persistent organic pollutants. As reported in the literature, the deposition of these types of pollutants (e.g., polychlorinated biphenyls and polycyclic aromatic hydrocarbons) can be monitored using suitable collectors made of amber-coloured glass or stainless steel[106,107] – modifications which can be applied to the sample design detailed here. The samples collected in this work from this new instrumentation are expected to be used further in several upcoming complementary and novel environmental monitoring studies. Not only will this future work extend

our biogeochemical analysis, but it will also assist in our study of the transport of other anthropogenic pollutants of emerging interest which are beyond the scope of describing this new platform.

3.6. References

1. Pacyna, J. M. Ecological Processes: Atmospheric Deposition, in: Encyclopedia of Ecology, Vol. 1, ed. Jorgensen, S. E.; Fath, B. D. *Elsevier Science.* **2008**, 275–285.

2. Fowler, D. Wet and dry deposition of sulphur and nitrogen compounds from the atmosphere. In *Effects of acid precipitation on terrestrial ecosystems*. Boston, MA: Springer US, **1980**, 9–27.

3. Lovett, G. M.; Kinsman, J. D. Atmospheric pollutant deposition to high-elevation ecosystems. *Atmos. Environ. Part A. Gen. Top*. **1990**, *24*(11), 2767–2786.

4. Farmer, D. K.; Boedicker, E. K.; DeBolt, H. M. Dry deposition of atmospheric aerosols: Approaches, observations, and mechanisms. *Annual review of physical chemistry*, **2021**, *72*(1), 375–397.

5. Lovett, G. M. Atmospheric deposition of nutrients and pollutants in North America: an ecological perspective. *Ecol. Appl.* **1994**, *4*(4), 629–650.

6. Meteorological Service of Canada. 2004 Canadian Acid Deposition Science Assessment, Library and Archives Canada, ISBN 0-662-38754-6, **2005**. Retrieved from: https://publications.gc.ca/collections/Collection/ En4-46-2004E.pdf.

7. Vet, R.; Artz, R. S.; Carou, S.; Shaw, M.; Ro, C. U.; Aas, W.; Baker, A.; Bowersox, V. C.; Dentener, F.; Galy-Lacaux, C.; Hou, A. A global assessment of precipitation chemistry and deposition of sulfur, nitrogen, sea salt, base cations, organic acids, acidity and pH, and phosphorus. *Atmos. Environ.* **2014**, *93*, 3–100.

8. Safieddine, S. A.; Heald, C. L. A global assessment of dissolved organic carbon in precipitation. *Geophys. Res. Lett.* **2017**, *44*(22), 11–672.

9. United States Environmental Protection Agency. Integrated Science Assessment (ISA) for Oxides of Nitrogen, Oxides of Sulfur and Particulate Matter Ecological Criteria (Final Report, 2020). *U.S. Environmental Protection Agency*, Washington, DC, EPA/600/R 20/278, **2020**.

10. Likens, G. E.; Butler, T. J. Atmospheric Acid Deposition, in: The Handbook of Natural Resources, Atmosphere and Climate. Vol. 6, ed. Wang, Y. *CRC Press*, ISBN 9781138339675, **2020**.

11. Grennfelt, P.; Engleryd, A.; Forsius, M.; Hov, Ø.; Rodhe, H.; Cowling, E. Acid rain and air pollution: 50 years of progress in environmental science and policy. *Ambio*, **2020**, *49*(4), 849–864.

12. Stoddard, J. L.; Jeffries, D. S.; Lükewille, A.; Clair, T. A.; Dillon, P. J.; Driscoll, C. T.; Forsius, M.; Johannessen, M.; Kahl, J. S.; Kellogg, J. H.; Kemp, A. Regional trends

in aquatic recovery from acidification in North America and Europe. *Nature*, **1999**, *401*(6753), 575–578.

13. Kuylenstierna, J. C.; Rodhe, H.; Cinderby, S.; Hicks, K. Acidification in developing countries: ecosystem sensitivity and the critical load approach on a global scale. *Ambio*, **2001**, 20–28.

14. Siksna, R. The electrolytical conductivity of precipitation water as an aid to the chemical analysis. *Pure Appl. Geophys.* **1959**, *42*(1), 32–41.

15. Hall, D. J. Precipitation collector for use in the Secondary National Acid Deposition Network, United States Department of Energy, Report No. PB-87-126181/XAB; LR-561(AP)M, **1985**.

16. Lindberg, S. E.; Lovett, G. M.; Richter, D. D.; Johnson, D. W. Atmospheric Deposition and Canopy Interactions of Major Ions in a Forest. *Science.* **1986**, *231*(4734), 141–145, doi:10.1126/science.231.4734.141.

17. Richter, D. D.; Lindberg, S. E. Wet Deposition Estimates from Long-Term Bulk and Event Wet-Only Samples of Incident Precipitation and Throughfall. *J. Environ. Qual.* **1988**, *17*(4), 619–622, doi: 10.2134/jeq1988.00472425001700040017x.

18. Stedman, J. R.; Heyes, C. J.; Irwin, J. G. A comparison of bulk and wet-only precipitation collectors at rural sites in the United Kingdom. *Water Air Soil Pollut.* **1990**, *52*(3), 377–395.

19. Gatz, D. F.; Selman, R. F.; Langs, R. K.; Holtzman, R. B. An automatic sequential rain sampler. *J. Appl. Meteorol. Climatol.* **1971**, *10*(2), 341–344.

20. Reddy, M. M.; Liebermann, T. D.; Jelinski, J. C.; Caine, N. Variation in pH during summer storms near the continental divide in central Colorado, USA. *Arct. Antarct. Alp. Res.* **1985**, *17*(1), 79–88.

21. Vermette, S. J.; Drake, J. J. Simplified wet-only and sequential fraction rain collector. *Atmos. Environ.* **1987**, *21*(3), 715–716.

22. Laquer, F. C. Sequential precipitation samplers: A literature review. *Atmos. Environ. Part A. General Topics.* **1990**, *24*(9), 2289–2297.

23. Germer, S.; Neill, C.; Krusche, A. V.; Neto, S. C. G.; Elsenbeer, H. Seasonal and within-event dynamics of rainfall and throughfall chemistry in an open tropical rainforest in Rondônia, Brazil. *Biogeochemistry.* **2007**, *86*(2), 155–174.

24. Sanei, H.; Outridge, P. M.; Goodarzi, F.; Wang, F.; Armstrong, D.; Warren, K.; Fishback, L. J. A. E. Wet deposition mercury fluxes in the Canadian sub-Arctic and southern Alberta,

measured using an automated precipitation collector adapted to cold regions. *Atmos. Environ.* **2010**, *44*(13), 1672–1681.

25. Canadian Air and Precipitation Monitoring Network: Inspector's reference manual, 1-1–2-14 pp., Cat. No. En56-273/1985E-PDF, **1985**.

26. National Atmospheric Deposition Program. NADP Site Selection and Installation Manual. *Wisconsin State Laboratory of Hygiene*, EHD NADP PO GENOP 002, **2009**. Retrieved from: https://nadp.slh.wisc.edu/wp-content/ uploads/2022/01/NADP-2010_Site_Selection_and_Installation_ Manual_v1.pdf.

27. Casas-Ruiz, J. P.; Bodmer, P.; Bona, K. A.; Butman, D.; Couturier, M.; Emilson, E. J.; Finlay, K.; Genet, H.; Hayes, D.; Karlsson, J.; Paré, D. Integrating terrestrial and aquatic ecosystems to constrain estimates of land-atmosphere carbon exchange. *Nat. Commun.* **2023**, *14*(1), 1571.

28. Jurado, E.; Jaward, F. M.; Lohmann, R.; Jones, K. C.; Simó, R.; Dachs, J. Atmospheric dry deposition of persistent organic pollutants to the Atlantic and inferences for the global oceans. *Environ. Sci. Technol.* **2004**, *38*(21), 5505–5513.

29. Jurado, E.; Jaward, F.; Lohmann, R.; Jones, K. C.; Simó, R.; Dachs, J. Wet deposition of persistent organic pollutants to the global oceans. *Environ. Sci. Technol.* **2005**, *39*(8), 2426–2435.

30. Kroll, J. H.; Donahue, N. M.; Jimenez, J. L.; Kessler, S. H.; Canagaratna, M. R.; Wilson, K. R.; Altieri, K. E.; Mazzoleni, L. R.; Wozniak, A. S.; Bluhm, H.; Mysak, E. R. Carbon oxidation state as a metric for describing the chemistry of atmospheric organic aerosol. *Nat. Chem.* **2011**, *3*(2), 133–139.

31. Saleh, R. From measurements to models: toward accurate representation of brown carbon in climate calculations. *Curr. Pollut. Rep.* **2020**, *6*(2), 90–104.

32. Wang, X.; Gemayel, R.; Baboomian, V. J.; Li, K.; Boreave, A.; Dubois, C.; Tomaz, S.; Perrier, S.; Nizkorodov, S. A.; George, C. Naphthalene-derived secondary organic aerosols interfacial photosensitizing properties. *J Geophys. Res. Lett.* **2021**, *48*(13), e2021GL093465.

33. Washenfelder, R. A.; Azzarello, L.; Ball, K.; Brown, S. S.; Decker, Z. C. J.; Franchin, A.; Fredrickson, C. D.; Hayden, K.; Holmes, C. D.; Middlebrook, A. M.; Palm, B. B. Complexity in the evolution, composition, and spectroscopy of brown carbon in aircraft measurements of wildfire plumes. *J Geophys. Res. Lett.* **2022**, *49*(9), e2022GL098951.

34. George, C. Photosensitization is in the air and impacts the multiphase on oxidation capacity, EGU23, the 25th EGU General Assembly, 23–28 April, Vienna, Austria and Online, **2023**.

35. Avery Jr, G. B.; Willey, J. D.; Kieber, R. J. Carbon isotopic characterization of dissolved organic carbon in rainwater: Terrestrial and marine influences. *Atmos. Environ.* **2006**, *40*(39), 7539–7545.

36. Ramanathan, V.; Carmichael, G. Global and regional climate changes due to black carbon. *Nat. Geosci.* **2008**, *1*(4), 221–227.

37. Heald, C. L.; Kroll, J. H. The fuel of atmospheric chemistry: Toward a complete description of reactive organic carbon. *Sci. Adv.* **2020**, *6*(6), eaay8967.

38. Iavorivska, L.; Boyer, E. W.; DeWalle, D. R. Atmospheric deposition of organic carbon via precipitation. *Atmos. Environ.* **2016**, *146*, 153–163.

39. Kroll, J. H.; Donahue, N. M.; Jimenez, J. L.; Kessler, S. H.; Canagaratna, M. R.; Wilson, K. R.; Altieri, K. E.; Mazzoleni, L. R.; Wozniak, A. S.; Bluhm, H.; Mysak, E. R. Carbon oxidation state as a metric for describing the chemistry of atmospheric organic aerosol. *Nat. Chem.* **2011**, *3*(2), 133–139.

40. Heald, C. L.; de Gouw, J. D.; Goldstein, A. H.; Guenther, A. B.; Hayes, P. L.; Hu, W.; Isaacman-VanWertz, G.; Jimenez, J. L.; Keutsch, F. N.; Koss, A. R.; Misztal, P. K. Contrasting reactive organic carbon observations in the southeast United States (SOAS) and southern California (CalNex). *Environ. Sci. Technol.* **2020**, *54*(23), 14923–14935.

41. Barber, V. P.; Kroll, J. H. Chemistry of functionalized reactive organic intermediates in the earth's atmosphere: impact, challenges, and progress. *J. Phys. Chem. A.* **2021**, *125*(48), 10264–10279.

42. VandenBoer, T. C.: AIM-IC: Applications to Nitrous Acid (HONO) in the Ambient Atmosphere and Precipitation Monitoring. Masters of Science, *University of Toronto*, **2009**.

43. Colussi, A. A.; Persaud, D.; Lao, M.; Place, B. K.; Hems, R. F.; Ziegler, S. E.; Edwards, K. A.; Young, C. J.; VandenBoer, T. C. Cost Effective Off-Grid Automatic Precipitation Samplers for Pollutant and Biogeochemical Atmospheric Deposition. *Atmos. Meas. Tech.* **2024**, *17,* 3697–3718. https://doi.org/10.5194/amt-17-3697-2024.

44. Ziegler, S. E.; Benner, R.; Billings, S. A.; Edwards, K. A.; Philben, M.; Zhu, X.; Laganière, J. Climate warming can accelerate carbon fluxes without changing soil carbon stocks. *Front. Earth Sci.* **2017**, *5*, 2.

45. Environment and Climate Change Canada. Canadian Climate Normals, 1981 to 2010. **2023**. Retrieved from: https://climate.weather.gc.ca/climate_normals/.

46. Thornton, M. M.; Shrestha, R.; Wei, Y.; Thornton, P. E.; Kao, S. C.; Wilson, B. E. Daymet: Monthly Climate Summaries on a 1-km Grid for North America, Version 4 R1, https://doi.org/10.3334/ORNLDAAC/2131, **2022**.

47. Kirkwood, D. S. Stability of solutions of nutrient salts during storage. *Mar. Chem.* **1992**, *38*(3–4), 151–164.

48. Kattner, G. Storage of dissolved inorganic nutrients in seawater: poisoning with mercuric chloride. *Mar. Chem.* **1999**, *67*(1–2), 61–66.

49. Galloway, J. N.; Likens, G. E. The collection of precipitation for chemical analysis. *Tellus*, **1978**, *30*(1), 71–82.

50. Peden, M. E.; Bachman, S. R.; Brennan, C. J.; Demir, B.; James, K. O.; Kaiser, B. W.; Lockard, J. M.; Rothery, J. E.; Sauer, J.; Skowron, L. M.; Slater, M. J. Methods for collection and analysis of precipitation. *ISWS Contract Report CR 381*, **1986**.

51. Dossett, S. R.; Bowersox, V. C. National Trends Network Site Operation Manual, Illinois State Water Survey, 2-1–2-2, **1999**. Retrieved from: https://www.arlis.org/docs/vol1/123915417/opman.pdf.

52. Wetherbee, G. A.; Shaw, M. J.; Latysh, N. E.; Lehmann, C. M.; Rothert, J. E. Comparison of precipitation chemistry measurements obtained by the Canadian Air and Precipitation Monitoring Network and National Atmospheric Deposition Program for the period 1995–2004. *Environ. Monit. Assess.* **2010**, *164*(1), 111–132.

53. Laurent, B.; Losno, R.; Chevaillier, S.; Vincent, J.; Roullet, P.; Bon Nguyen, E.; Ouboulmane, N.; Triquet, S.; Fornier, M.; Raimbault, P.; Bergametti, G. An automatic collector to monitor insoluble atmospheric deposition: application for mineral dust deposition. *Atmos. Meas. Tech.* **2015**, *8*(7), 2801–2811.

54. Brahney, J.; Wetherbee, G.; Sexstone, G. A.; Youngbull, C.; Strong, P.; Heindel, R. C.; A new sampler for the collection and retrieval of dry dust deposition. *Aeolian Research*, **2020**, *45*, 100600.

55. Audoux, T.; Laurent, B.; Desboeufs, K.; Noyalet, G.; Maisonneuve, F.; Lauret, O.; Chevaillier, S. Intra-event evolution of elemental and ionic concentrations in wet deposition in an urban environment. *Atmos. Chem. Phys.* **2023**, *23*(20), 13485–13503.

56. Bowering, K. L.; Edwards, K. A.; Wiersma, Y. F.; Billings, S. A.; Warren, J.; Skinner, A.; Ziegler, S. E. Dissolved organic carbon mobilization across a climate transect of mesic boreal forests is explained by air temperature and snowpack duration. *Ecosystems.* **2023**, *26*(1), 55–71.

57. Bowyer, P. J. (ed.). Where the Wind Blows: A Guide to Marine Weather in Atlantic Canada. *Breakwater Books Ltd*. St John's, Newfoundland, ISBN 1-55081-119-3, **1995**.

58. Jacob, D. J. Introduction to Atmospheric Chemistry. *Princeton University Press*, Princeton, New Jersey, **1999**.

59. Randall, D. An Introduction to the Global Circulation of the Atmosphere. *Princeton University Press*, Princeton, New Jersey. ISBN 9780691148960, **2015**.

60. Colli, M.; Lanza, L. G.; Rasmussen, R.; Thériault, J. M. The collection efficiency of shielded and unshielded precipitation gauges. Part II: Modeling particle trajectories. *Journal of Hydrometeorology*, **2016**, *17*(1), 245–255.

61. Kochendorfer, J.; Meyers, T. P.; Hall, M. E.; Landolt, S. D.; Diamond, H. J. A new reference-quality precipitation gauge wind shield. *Atmos. Meas. Tech.* **2023***, 16*, 5647–5657.

62. Eaton, J. S.; Likens, G. E.; Bormann, F. H. Throughfall and stemflow chemistry in a northern hardwood forest. *J. Ecol.* **1973**, 495–508.

63. Howard, M.; Hathaway, J. M.; Tirpak, R. A.; Lisenbee, W. A.; Sims, S. Quantifying urban tree canopy interception in the southeastern United States. *Urban Forestry & Urban Greening*, **2022**, *77*, 127741.

64. Hadiwijaya, B.; Isabelle, P. E.; Nadeau, D. F.; Pepin, S. Observations of canopy storage capacity and wet canopy evaporation in a humid boreal forest. *Hydrol. Process.* **2021**, *35*(2), e14021.

65. Pomeroy, J. W.; Granger, R.; Pietroniro, A.; Elliott, J.; Toth, B.; Hedstrom, N. September. Classification of the boreal forest for hydrological processes. In *Proceedings of the ninth international boreal forest research association conference, **1998**,* 49–59.

66. Ciruzzi, D. M.; Loheide, S. P. Monitoring tree sway as an indicator of interception dynamics before, during, and following a storm. *Geophys. Res. Lett.* **2021**, *48*(20), e2021GL094980.

67. Metzger, J. C.; Schumacher, J.; Lange, M.; Hildebrandt, A. Neighbourhood and stand structure affect stemflow generation in a heterogeneous deciduous temperate forest. *Hydrol. Earth Syst. Sci.* **2019**, *23*(11), 4433–4452.

68. Han, G.; Song, Z.; Tang, Y.; Wu, Q.; Wang, Z. Ca and Sr isotope compositions of rainwater from Guiyang city, Southwest China: Implication for the sources of atmospheric aerosols and their seasonal variations. *Atmos. Environ.* **2019**, *214*, 116854.

69. Escarré, A.; Carratalá, A.; Àvila, A.; Bellot, J.; Piñol, J.; Milán, M. Precipitation chemistry and air pollution. In *Ecology of Mediterranean evergreen oak forests.* Berlin, Heidelberg: *Springer Berlin Heidelberg*. **1999***,* 195–208.

70. Guinotte, J. M.; Fabry, V. J. Ocean acidification and its potential effects on marine ecosystems. *Ann. N.Y. Acad. Sci.* **2008**, *1134*(1), 320–342.

71. Houle, D.; Augustin, F.; Couture, S. Rapid improvement of lake acid–base status in Atlantic Canada following steep decline in precipitation acidity. *Can. J. Fish. Aquat. Sci.* **2022**, *79*(12), 2126–2137.

72. Cappellato, R.; Peters, N. E.; Ragsdale, H. L. Acidic atmospheric deposition and canopy interactions of adjacent deciduous and coniferous forests in the Georgia Piedmont. *Can. J. For. Res.* **1993**, *23*(6), 1114–1124.

73. Carlson, J.; Gough, W. A.; Karagatzides, J. D.; Tsuji, L. J. Canopy interception of acid deposition in southern Ontario. *Can. Field-Nat.* **2003**, *117*(4), 523–530.

74. Burkhardt, J.; Drechsel, P. The synergism between SO2 oxidation and manganese leaching on spruce needles—a chamber experiment. *Environ. Pollut.* **1997**, *95*(1), 1–11.

75. Csavina, J.; Field, J.; Taylor, M. P.; Gao, S.; Landázuri, A.; Betterton, E. A.; Sáez, A. E. A review on the importance of metals and metalloids in atmospheric dust and aerosol from mining operations. *Science of the Total Environment.* **2012**, *433*, 58–73.

76. Barrie, L. A.; Hales, J. M.; The spatial distributions of precipitation acidity and major ion wet deposition in North America during 1980. *Tellus B: Chemical and Physical Meteorology*, **1984**, *36*(5), 333–355.

77. Boyd, C. E. Carbon dioxide, pH, and alkalinity. In *Water quality: an introduction. Cham: Springer International Publishing*. **2019**, 177–203.

78. Lawrence, C. E.; Casson, P.; Brandt, R.; Schwab, J. J.; Dukett, J. E.; Snyder, P.; Yerger, E.; Kelting, D.; VandenBoer, T. C.; Lance, S. Long-term monitoring of cloud water chemistry at Whiteface Mountain: the emergence of a new chemical regime. *Atmos. Chem. Phys.* **2023**, *23*(2), 1619–1639.

79. Feng, J.; Vet, R.; Cole, A.; Zhang, L.; Cheng, I.; O'Brien, J.; Macdonald, A. M. Inorganic chemical components in precipitation in the eastern US and Eastern Canada during 1989–2016: Temporal and regional trends of wet concentration and wet deposition from the NADP and CAPMoN measurements. *Atmos. Environ.* **2021**, *254*, 118367.

80. Di Lorenzo, R. A.; Place, B. K.; VandenBoer, T. C.; Young, C. J. Composition of size-resolved aged boreal fire aerosols: brown carbon, biomass burning tracers, and reduced nitrogen. *ACS Earth and Space Chemistry*, **2018**, *2*(3), 278–285.

81. Lin, W. C.; Brondum, K.; Monroe, C. W.; Burns, M. A. Multifunctional water sensors for pH, ORP, and conductivity using only microfabricated platinum electrodes. *Sensors.* **2017**, *17*(7), 1655.

82. Beverland, I. J.; Heal, M. R.; Crowther, J. M.; Srinivas, M. S. N. Real-time measurement and interpretation of the conductivity and pH of precipitation samples. *Water, Air, and Soil Pollution*, **1997**, *98*(3), 325–344.

83. Cha, J. Y.; Lee, S. C.; Lee, E. J.; Lee, K.; Lee, H.; Kim, H. S.; Ahn, J.; Oh, N. H.; Canopy leaching rather than desorption of PM2. 5 from leaves is the dominant source of throughfall dissolved organic carbon in forest. *Geophys. Res. Lett.* **2023**, *50*(17), e2023GL103731.

84. Bowering, K. L.; Edwards, K. A.; Ziegler, S. E. Seasonal controls override forest harvesting effects on the composition of dissolved organic matter mobilized from boreal forest soil organic horizons. *Biogeosciences.* **2023**, *20*(11), 2189–2206.

85. Arisci, S.; Rogora, M.; Marchetto, A.; Dichiaro, F. The role of forest type in the variability of DOC in atmospheric deposition at forest plots in Italy. *Environ. Monit. Assess*. **2012**, *184*(6), 3415–3425.

86. Sleutel, S.; Vandenbruwane, J.; De Schrijver, A.; Wuyts, K.; Moeskops, B.; Verheyen, K.; De Neve, S. Patterns of dissolved organic carbon and nitrogen fluxes in deciduous and coniferous forests under historic high nitrogen deposition. *Biogeosciences*, **2009**, *6*(12), 2743–2758.

87. Smith, W. H. Air Pollution and Forests: Interactions Between Air Contaminants and Forest Ecosystems, 1st Edn., *Springer*, New York, New York. **1981**.

88. Erisman, J. W.; Draaijers, G. Deposition to forests in Europe: most important factors influencing dry deposition and models used for generalisation. *Environ. Pollut.* **2003**, *124*(3), 379–388.

89. Santín, C.; Doerr, S. H.; Kane, E. S.; Masiello, C. A.; Ohlson, M.; de la Rosa, J. M.; Preston, C. M.; Dittmar, T. Towards a global assessment of pyrogenic carbon from vegetation fires. *Glob. Chang. Biol.* **2016**, *22*(1), 76–91.

90. Coward, E. K.; Seech, K.; Carter, M. L.; Flick, R. E.; Grassian, V. H. Of sea and smoke: Evidence of marine dissolved organic matter deposition from 2020 western United States wildfires. *Environ. Sci. Technol. Lett.* **2022**, *9*(10), 869–876.

91. Gao, S.; Hegg, D. A.; Hobbs, P. V.; Kirchstetter, T. W.; Magi, B. I.; Sadilek, M. Water-soluble organic components in aerosols associated with savanna fires in southern Africa: Identification, evolution, and distribution. *J Geophys. Res. Atmos.* **2003**, *108*(D13), 8491.

92. Moore, T. R. Dissolved organic carbon in a northern boreal landscape. *Glob. Biogeochem. Cy.* **2003**, *17*(4), 1109.

93. Wonaschütz, A.; Hersey, S. P.; Sorooshian, A.; Craven, J. S.; Metcalf, A. R.; Flagan, R. C.; Seinfeld, J. H. Impact of a large wildfire on water-soluble organic aerosol in a major urban area: the 2009 Station Fire in Los Angeles County. *Atmos. Chem. Phys.* **2011**, *11*(16), 8257–8270.

94. Myers-Pigg, A. N.; Louchouarn, P.; Amon, R. M.; Prokushkin, A.; Pierce, K.; Rubtsov, A. Labile pyrogenic dissolved organic carbon in major Siberian Arctic rivers: Implications for wildfire-stream metabolic linkages. *Geophys. Res. Lett.* **2015**, *42*(2), 377–385.

95. Oka, A.; Takahashi, J.; Endoh, Y.; Seino, T. Bark effects on stemflow chemistry in a Japanese temperate forest I. The role of bark surface morphology. *Frontiers in Forests and Global Change*, **2021**, *4*, 654375.

96. Stubbins, A.; Silva, L. M.; Dittmar, T.; Van Stan, J. T. Molecular and optical properties of tree-derived dissolved organic matter in throughfall and stemflow from live oaks and eastern red cedar. *Front. Earth Sci.* **2017**, *5*, 22.

97. Van Stan, J. T.; Stubbins, A. Tree-DOM: Dissolved organic matter in throughfall and stemflow. *Limnol. Oceanogr. Lett.* **2018**, *3*(3), 199–214.

98. Ryan, K. A.; Adler, T.; Chalmers, A.; Perdrial, J.; Shanley, J. B.; Stubbins, A. Event scale relationships of DOC and TDN fluxes in throughfall and stemflow diverge from stream exports in a forested catchment. *J Geophys. Res. Biogeosci.* **2021**, *126*(7), e2021JG006281.

99. Pumpanen, J.; Lindén, A.; Miettinen, H.; Kolari, P.; Ilvesniemi, H.; Mammarella, I.; Hari, P.; Nikinmaa, E.; Heinonsalo, J.; Bäck, J.; Ojala, A. Precipitation and net ecosystem exchange are the most important drivers of DOC flux in upland boreal catchments. *J Geophys. Res. Biogeosciences.* **2014**, *119*(9), 1861–1878.

100. Dalva, M.; Moore, T. R. Sources and sinks of dissolved organic carbon in a forested swamp catchment. *Biogeochemistry*, **1991**, *15*(1), 1–19.

101. Van Stan, J. T.; Wagner, S.; Guillemette, F.; Whitetree, A.; Lewis, J.; Silva, L.; Stubbins, A. Temporal dynamics in the concentration, flux, and optical properties of tree-derived dissolved organic matter in an epiphyte-laden oak-cedar forest. *J Geophys. Res. Biogeosciences.* **2017**, *122*(11), 2982–2997.

102. Argentino, C.; Kalenitchenko, D.; Lindgren, M.; Panieri, G. HgCl2 addition to pore water samples from cold seeps can affect the geochemistry of dissolved inorganic carbon ([DIC], δ13CDIC). *Mar. Chem.* **2023**, *251*, 104236.

103. Pan, Y.; Wang, Y.; Xin, J.; Tang, G.; Song, T.; Wang, Y.; Li, X.; Wu, F. Study on dissolved organic carbon in precipitation in Northern China. *Atmos. Environ.* **2010**, *44*(19), 2350–2357.

104. Michalzik, B.; Matzner, E. Dynamics of dissolved organic nitrogen and carbon in a Central European Norway spruce ecosystem. *Eur. J. Soil Sci.* **1999**, *50*(4), 579–590.

105. Chen, H.; Tsai, K. P.; Su, Q.; Chow, A. T.; Wang, J. J. Throughfall dissolved organic matter as a terrestrial disinfection byproduct precursor. *ACS Earth and Space Chemistry*, **2019**, *3*(8), 1603–1613.

106. Fingler, S.; Tkalčević, B.; Fröbe, Z.; Drevenkar, V. Analysis of polychlorinated biphenyls, organochlorine pesticides and chlorophenols in rain and snow. *Analyst*, **1994**, *119*(6), 1135–1140.

107. Amodio, M.; Catino, S.; Dambruoso, P. R.; De Gennaro, G.; Di Gilio, A.; Giungato, P.; Laiola, E.; Marzocca, A.; Mazzone, A.; Sardaro, A.; Tutino, M. Atmospheric Deposition: Sampling Procedures, Analytical Methods, and Main Recent Findings from the Scientific Literature. *Adv. Meteorol*. **2014**, *2014*(1), 161730.

Appendix B: Supporting Information for Chapter 3

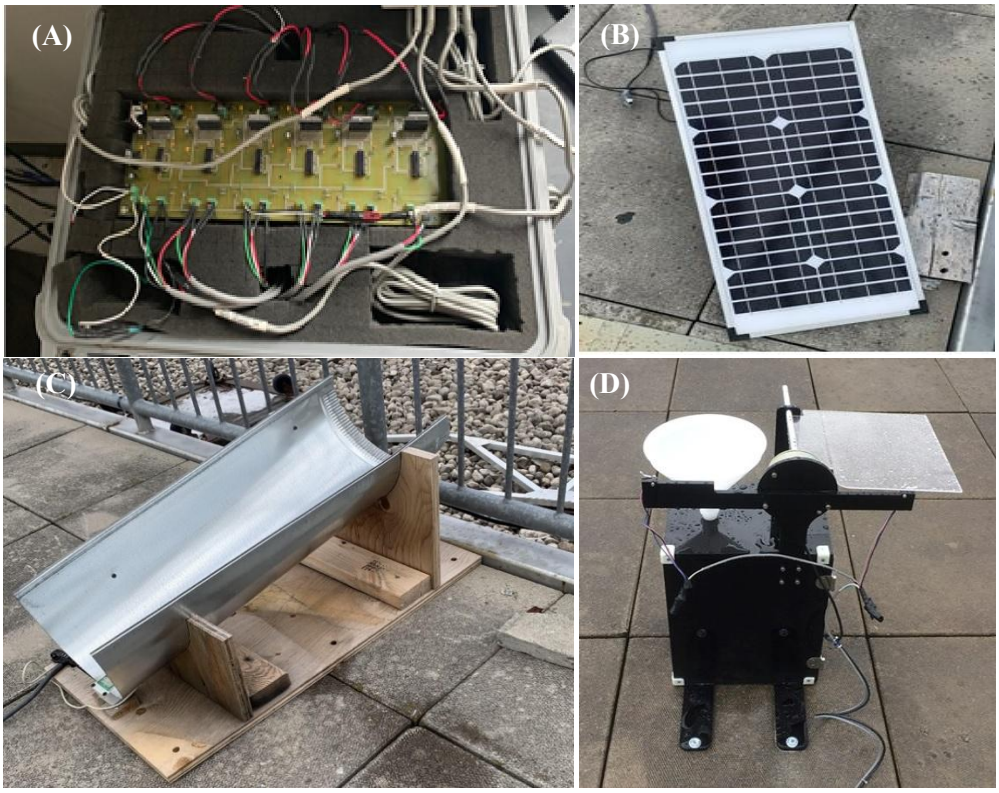

Figure B-1. Automated precipitation array stationed at the Air Quality Research Station, York University, Toronto, ON, consisting of: **(A)** weather-proofed control board, **(B)** 40 W solar panel, **(C)** rain sensor and enhanced sensitivity chute, and **(D)** an automated collection unit fixed to concrete with lag sleeves and bolts during a rain event.

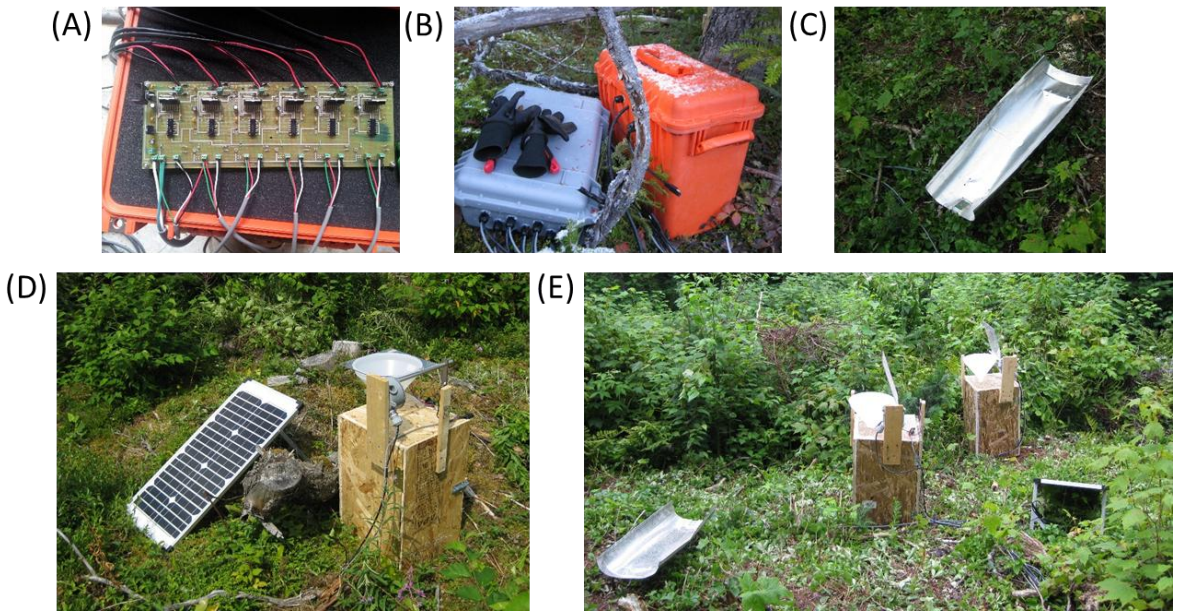

Figure B-2. Automated precipitation samplers deployed at NL-BELT. The **(A)** weatherproof control board was powered by **(B)** an off-grid AGM battery. The **(C)** sensor chute modulated the opening of the samplers for precipitation collection with **(D)** a 40 W solar panel to recharge the power package between **(E)** precipitation events when the lids open to collect wet deposition.

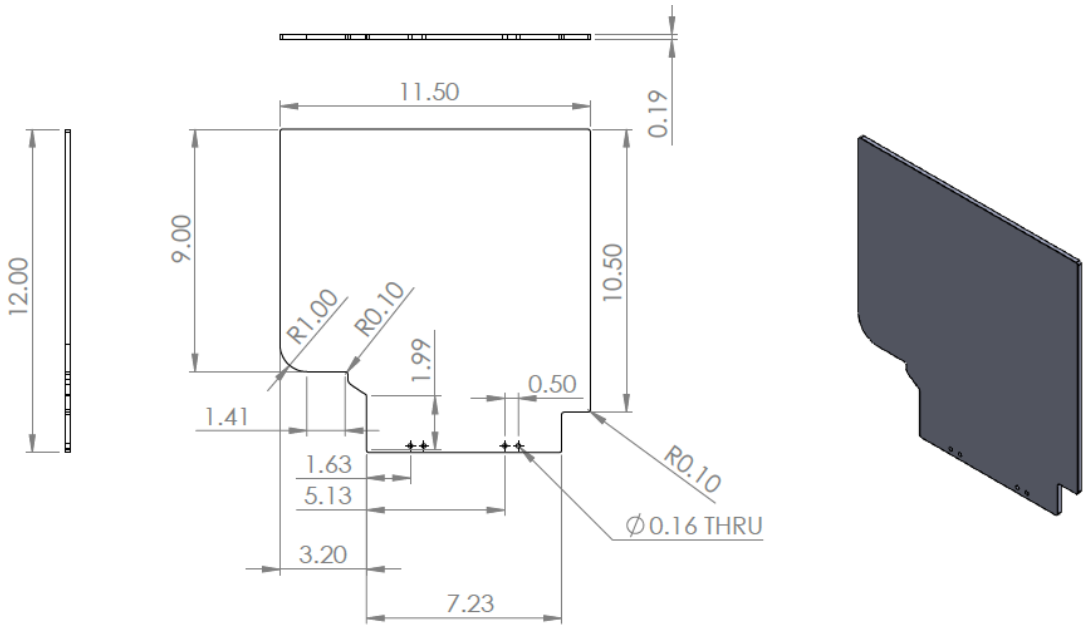

Figure B-3. Dimensions (in inches; where 1 inch is equivalent to 2.54 cm) for automated collection unit lid, with mounting holes on the bottom edge to secure it to the aluminum lid rod.

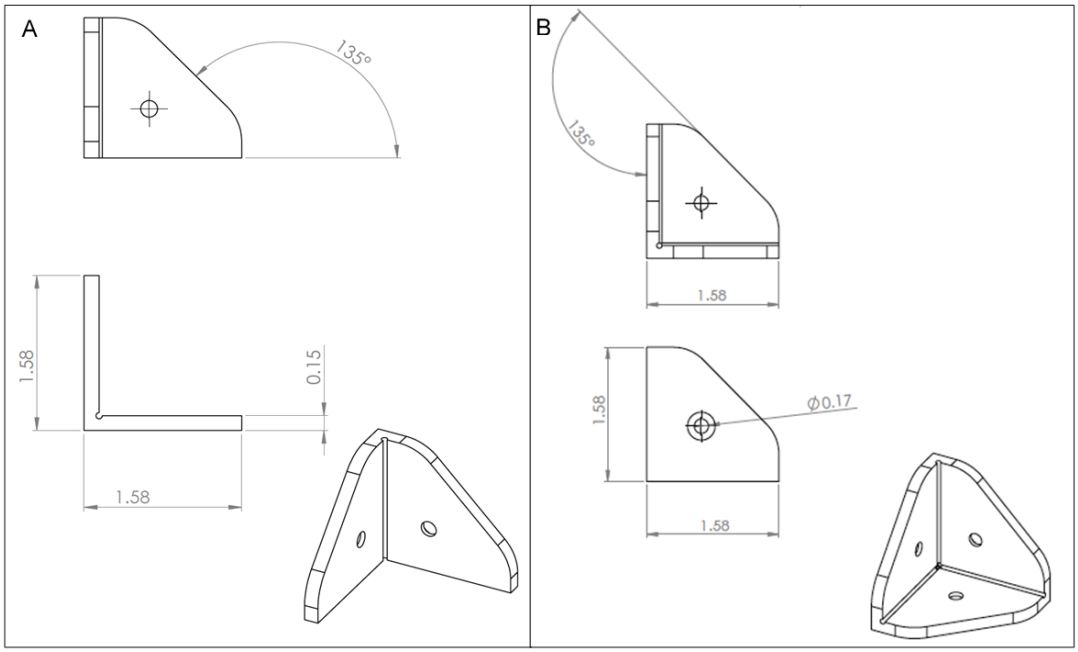

Figure B-4. Dimensions (in mm) of 3D printed corner options: **(A)** double corner to affix panels adjoining the door and **(B)** multi corner used to secure three panels throughout the remainder of the collection unit.

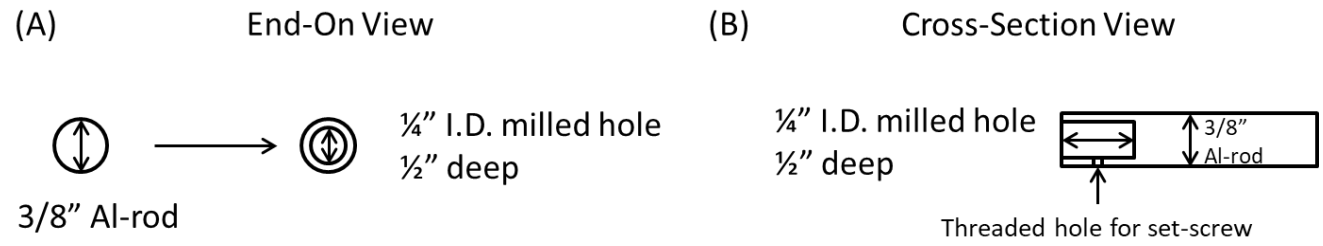

Figure B-5. Aluminum rod milling schematics showing **(A)** end-on view for motor drive shaft and **(B)** cross-section for situating the setscrew to hold the rod to the drive shaft of the motor. All dimensions are in inches where 1 inch is equivalent to 2.54 cm.

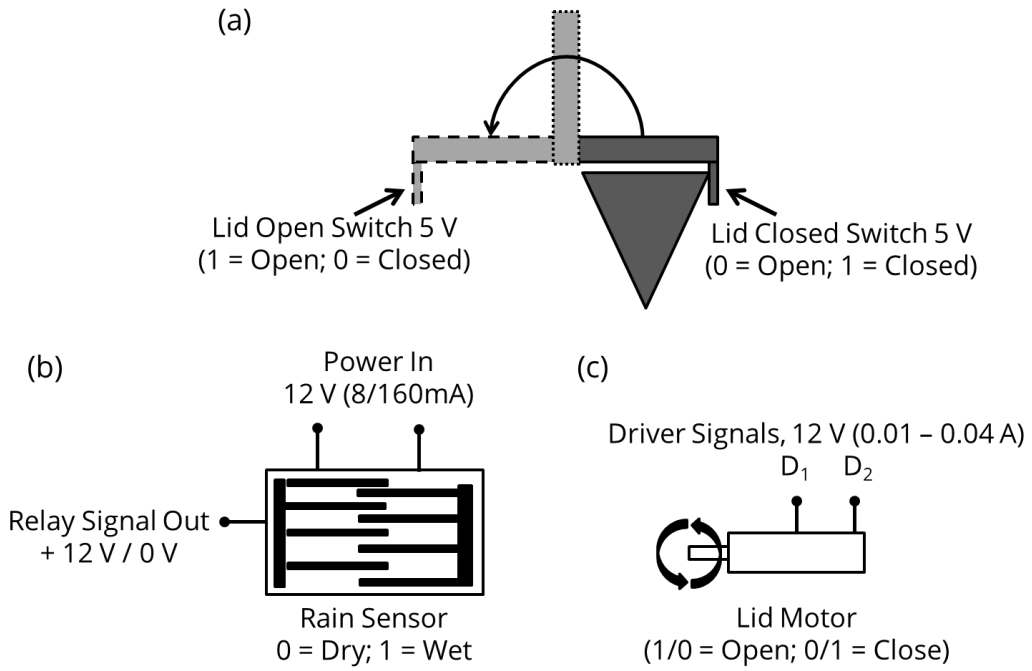

Figure B-6. Voltage and logic states of the **(a)** lid switches, **(b)** precipitation sensor, and **(c)** lid motor used to drive digital decision making on custom control boards.

(a)

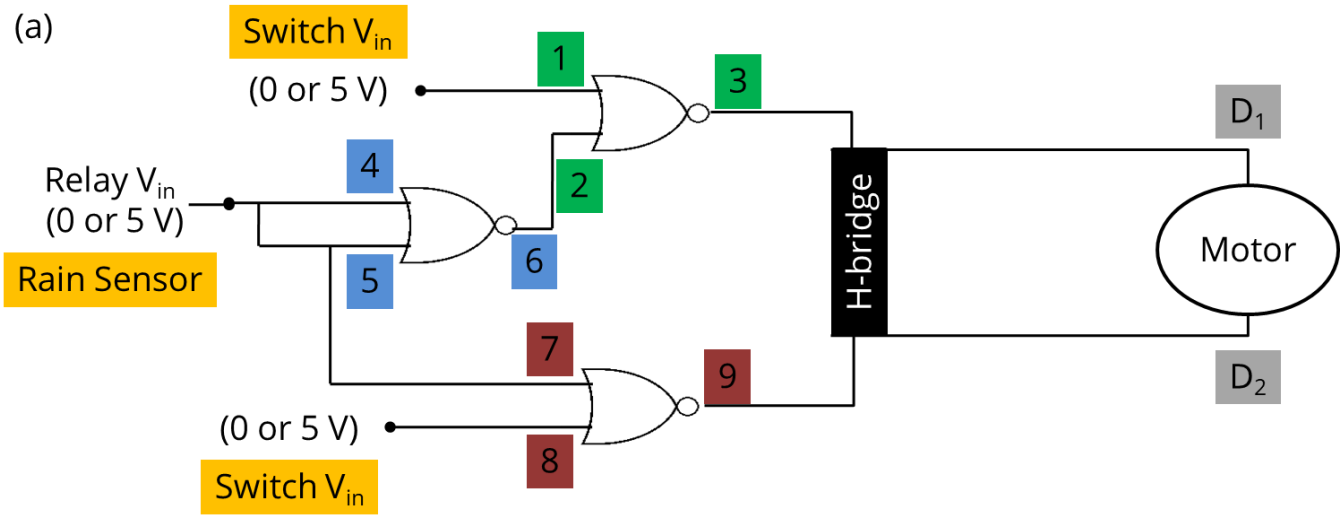

(b)

Switch	Switch	Rain	1	2	3	4	5	6	7	8	9	D1	D2
1	1	1	X	X	X	X	X	X	X	X	X	X	X
1	1	0	X	X	X	X	X	X	X	X	X	X	X
1	0	1	1	0	0	1	1	0	1	0	0	0	0
1	0	0	1	1	0	0	0	1	0	0	1	0	1
0	1	1	0	0	1	1	1	0	1	1	0	1	0
0	1	0	0	1	0	0	0	1	0	1	0	0	0
0	0	1	0	0	1	1	1	0	1	0	0	1	0
0	0	0	0	1	0	0	0	1	0	0	1	0	1

Figure B-7. (a) Input layout for digital logic control of precipitation sampler using three NOR gates to operate a H-bridge motor driver and **(b)** corresponding truth table to input and output logic states for switches and rain sensor (yellow), first NOR gate (green), second NOR gate (blue), and third NOR gate (red) to control 12 VDC from the motor driver to the motor terminals (D_1 and D_2).

B.1 Measuring Conductivity Threshold of Kemo Electronic Rain Sensor

A simple procedure determined the conductivity threshold of the 12 VDC Kemo Electronic rain sensor. A 1000 uS cm^{-1} stock standard was prepared by dissolving 0.225 g of NaCl in 500 mL Milli-Q water, ensuring thorough mixing for homogeneity. A series of conductivity standards were then prepared by diluting the stock standard with Milli-Q to different levels near the suspected threshold of the sensor (0.75, 0.8, 0.9, 1.0, 2.0, 3.0, 4.0, and 5.0 uS cm^{-1}). Prior to this testing, the rain sensor was flushed with copious amount of Milli-Q to remove any conductive substance from the surface of the sensor – this was also repeated in between trials. The result from testing with these solutions determined that the conductivity threshold for the relay is 1.0 uS cm^{-1}, as the rain sensor was observed to be only partially activated at 0.9 uS cm^{-1} and the result was not consistent.

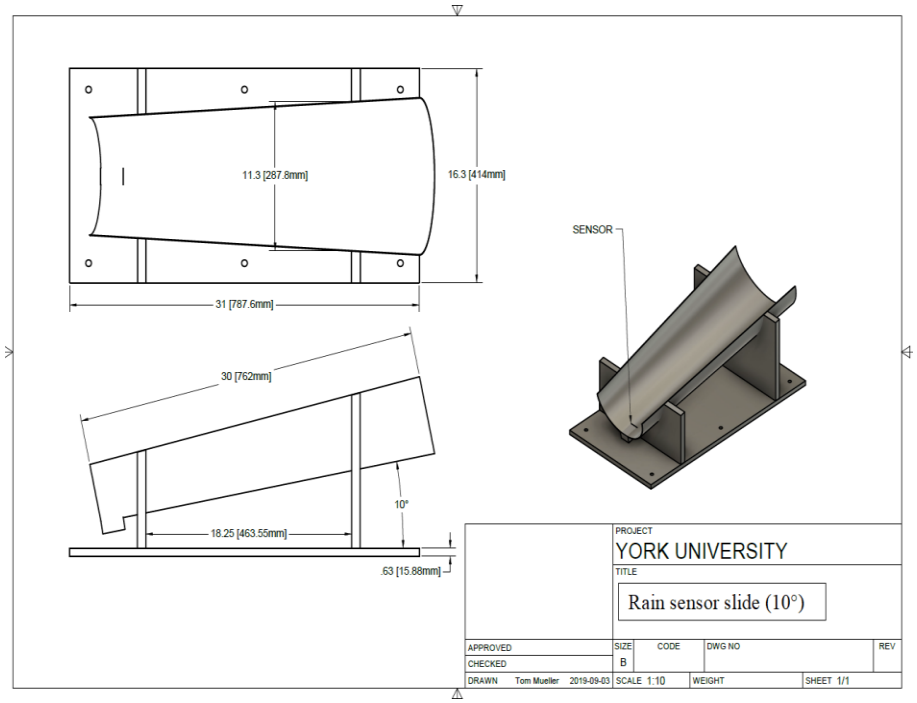

Figure B-8. Design and dimensions (in mm) of the mounting chute for the rain sensor. The chute slope is fixed at an optimized angle of 10°, that maintains water on the surface of the sensor throughout a rain event but allows excess water to flow over the sensor when necessary. We also tested 15° and 20° through manual observation but found that rainwater would flow over the sensor too rapidly – limiting or even preventing detection of wet deposition events.

(a)

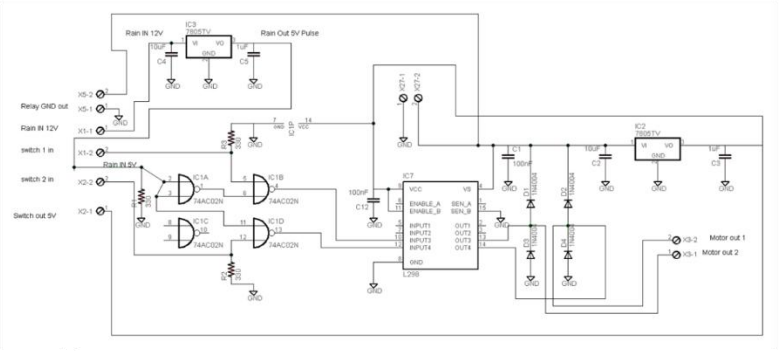

(b)

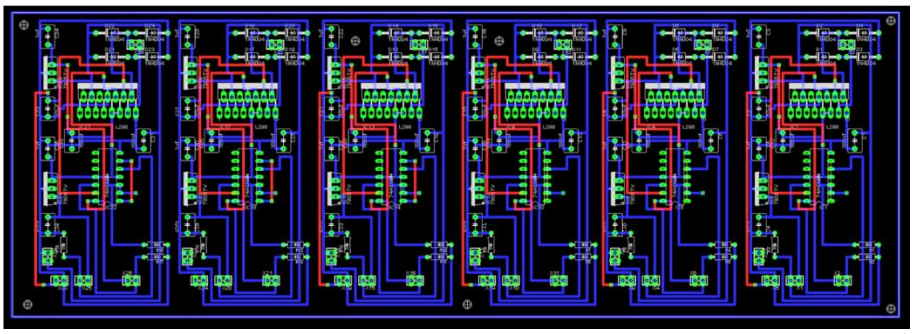

Figure B-9. Technical schematics for all printed circuit board components required to control **(a)** one precipitation collector with all components and connections to chips indicated and **(b)** a complete six-unit array composed of replicate layouts.

Table B-1. List of required components, part numbers, and quantities required to assemble a single printed circuit board.

Component	Part Identification	Description	Quantity	Unit Price (CAD)
Integrated Circuit 1 (IC1)	74AC02N = SN7402n	Four channels, two input NOR gate	1	3.52
Integrated Circuit 7 (IC7)	L298N	Dual Full Bridge Driver	1	7.41
Integrated Circuit 3 (IC2), Integrated Circuit 2 (IC3)	7805TV = MC7805CT-BP	5V regulator, TO220	2	0.67
Dioide 1, Diode 2, Diode 3, Diode 4	1N4004	Diode	4	0.14
Resistor 1, Resistor 2, Resistor 3	10k	Resistor, %1, 1/4W	3	0.21
Capacitor 1, Capacitor 12	100nF cap	Capacitor, 0.1Uf / 50 V	2	0.35
Capacitor 3, Capacitor 5	1Uf cap	Capacitor, 1Uf, 50 V	2	0.84
Capacitor 2, Capacitor 4	10Uf	Capacitor, %10, 10Uf, 50 V	2	1.84

Table B-2. List of specific components, manufacturers, and specifications required to construct precipitation collection arrays. Note that 1 inch is equivalent to 2.54 cm.

Components	Description	Selection Rationale
Collection Units		
Boxes	**Material:** 3/8" Acrylic or Plywood **Dimensions:** (33.78 W x 33.78 L x 42.94 H) cm See Figure 3-2 for more details	Acrylic and plywood were chosen for their low cost and durability against a variety of environmental conditions. Both materials are opaque to minimize light intrusion.
Collection Container	**Material:** High Density Polyethylene **Brand:** Bel-Art Products **Dimensions:** (19 H x 26 W x 36 H) cm; Volume: 10 L	Large volume collection of precipitation and resistance of material to environmental degradation. Quantitatively transfers analytes such as inorganic ions and DOC.
Funnel	**Material:** High Density Polyethylene **Brand:** Dynalon **Dimensions:** 9.4" W x 8.68" H; 20 cm diameter	Guides conductive precipitation into the collection container. Material is matched to maintain quantitative analyte transfer.
Sampler Lids	**Materials:** Lexan **Brand:** Kraloy, Carlon® Lamson & Sessions **Dimensions:** See Figure B-3 for more details Voltage: 12 V	Prevents foreign material entering the collection container when closed. Lexan was chosen due to its high flexibility and impact resistance. Acrylic was determined to be too fragile and not suitable for environmental conditions with elevated winds.
Geared Box DC Motor	**Brand:** Tsiny Motor Industrial Co. Ltd. TS-32GZ370-1650 **Operating voltage range:** 6-24 VDC **Nominal voltage:** 12 VDC **Speed:** 2 - 8 revolutions per minute	The worm gear motor is connected to the aluminum rod and sampler lids to open and close them when conductive precipitation is detected by the rain sensor.
Lid Rod	**Material:** Aluminum **Outer diameter:** 3/8" **Inner diameter:** 1/4" **Depth:** 1/2" deep	The aluminum rod is attached to the motor and facilitates the opening and closing of the Lexan lids. The rod is attached to the motor by an 8/32" threaded 1/4" set screw.
Lid Limit Switches	**Brand:** Omron Electronics **Part Number, P/N:** D2FW-G271(D) **Max. Current:** 1 A	Snap action switches are used to detect the open and closed position of the motorized sampler lids. Weatherproofing keeps them watertight.
Funnel Mesh	**Material:** HDPE **Brand:** McMaster-Carr **P/N:** 9265T49	When the automated sampler is in the open position, these cone shaped filters prevent debris from entering the collection jug.
Lag Shields, Lag Bolts, and Washers	**Lag Shield Dimensions:** 3/8" x 1-3/4" (requires masonry drill bit: 5/8") **Lag Bolt and Washer Dimensions:** 1/2"	These are utilized to secure precipitation collectors to concrete. This prevents unit tipping during storms or from animal interactions. Tent pegs or rebar may be alternatively used to secure the samplers into soils.

Table B-2 (cont'd). List of specific components, manufacturers, and specifications required to construct precipitation collection arrays. Note that 1 inch is equivalent to 2.54 cm.

Components	Description	Selection Rationale
Power System		
Solar Panel	**Brand:** Coleman 40 W Folding Panel **Output Voltage**: 17.1 V, 2.3 A **Dimensions:** (79 L x 35.1 W x 1.8 H) cm	The solar panel recharges the off-grid battery. This can be repositioned to optimize sunlight exposure and maximize recharging capabilities.
Solar Charge Controller	**Brand:** Coleman **Load Charge:** 8.5 A **Cut-out:** 14.2 A **Cut-in:** 13 V	The ability of the solar panel to deliver charge to the battery or stop when it is fully charged is regulated. The controller prevents the battery from overcharging.
103 Ah Off-grid Battery	**Brand:** Motomaster Nautilus Ultra XD Group 31 High Performance AGM Deep Cycle Battery (103 Ah) **Voltage:** 12 V **Dimensions:** (33 L x 18 W x 25 H) cm	The 99.99% lead AGM (absorbed glass mat) was used for long lasting power and reliability for field testing without a solar panel.
76 Ah Off-grid Battery	**Brand:** Motomaster Nautilus Ultra XD Group 24 High Performance AGM Deep Cycle Battery (76 Ah) **Voltage:** 12 V **Dimensions:** (27.6 L x 17.1 W x 22.2 H) cm	The 99.99% lead AGM with 76 Ah battery was used for field testing while being charged with a solar panel for long periods.
Transformer	**Brand:** TDK Lambda Americas **Voltage:** 115 VAC to 12 VDC	The transformer replaces an off-grid battery and converts 115 VAC to 12 VDC. This can be used when sampling in locations with grid power available.
Rain Detection		
Heated Precipitation Sensor	**Brand:** Kemo Electronic M152 **Voltage:** 12 V **Dimensions:** (6.5 x 4.5 x 3.6) cm	A waterproof conductive sensor that becomes activated and switches on a relay when in contact with conductive rain or snow. The sensor relay triggers the control board so that the sampler lids rotate open. The operating temperature range provided by the manufacturer is -10 to +55°C.
Sensor Chute	**Dimensions:** (see Figure B-8)	Increases surface area of precipitation sensor to activate the relay. Delays lid closing by providing more conductive ions to the sensor surface when atmospheric wash out may occur.

Table B-2 (cont'd). List of specific components, manufacturers, and specifications required to construct precipitation collection arrays. Note that 1 inch is equivalent to 2.54 cm.

Components	Description	Selection Rationale
Digital Control Board		
Control Boards	See Figure B-9 for more details.	Controls communication between the motors, power supply, and rain sensor (12 VDC), as well as the two limit switches (5 VDC).
Control Board Protective Case	**Brand:** Pelican ™ 1450 Case **Material of body:** polypropylene **Exterior Dimensions:** (41.8 L x 33 W x 17.3 D) cm **Interior Dimensions:** (37.2 L x 26 W x 15.5 D) cm **Weight with foam** (polyurethane): 2.9 kg	The 1450 case contains custom foam for cable accommodations with automatic pressure equalization valve to balance interior pressure. It is watertight, crushproof, and dustproof with double throw latches and a rubber handle.
Reusable Hydrosorbent Silica Gel Beads	**Brand:** Pelican Case Desiccant **Canister Dimensions:** (1.3 L x 5.1 W x 10.2 H) cm **Mass:** 40 g	The silica gel beads absorb moisture to prevent water damage to the control board; when clear, must reactivate in an oven for 3 hrs at 300°F.
Miscellaneous		
Data logger	**Brand:** ONSET® HOBO 4-channel analog data logger **Part/N**: UX120-006M **Program:** HOBOware	To collect and offload data from the control board using one of four channels. This work: CH1 – battery voltage, CH2 – motor driver voltage, CH3 – rain sensor voltage, CH4 – limit switch voltage.
Cable Connectors	**Brand:** Bulgin (400 or 4000 Series Buccaneer) IP68 Sealed Electrical Circular Cable Connectors PXP4010/03P/3540 and PSP4011/03S/3540 PSP4010/08P/3540 and PSP4011/08S/3540 SA3349, SA3350, SA3348, SA3347 **Materials:** Polyamide UL94-V0 body, gold contacts **Cable acceptance:** 3 mm - 7 mm **Contact insertion:** crimp or solder	Waterproof and dustproof cable connectors provide electrical connections from the control board to the battery, solar panel, and sampler motors and switches. Different numbers of contacts represent different cable requirements within the system (2- or 3-contact = battery and solar panel cables, 6- or 8-contact = rain samplers).
Extension Cables	Any commercial outdoor-rated extension cord	To increase distance from VAC power source to sampling location.

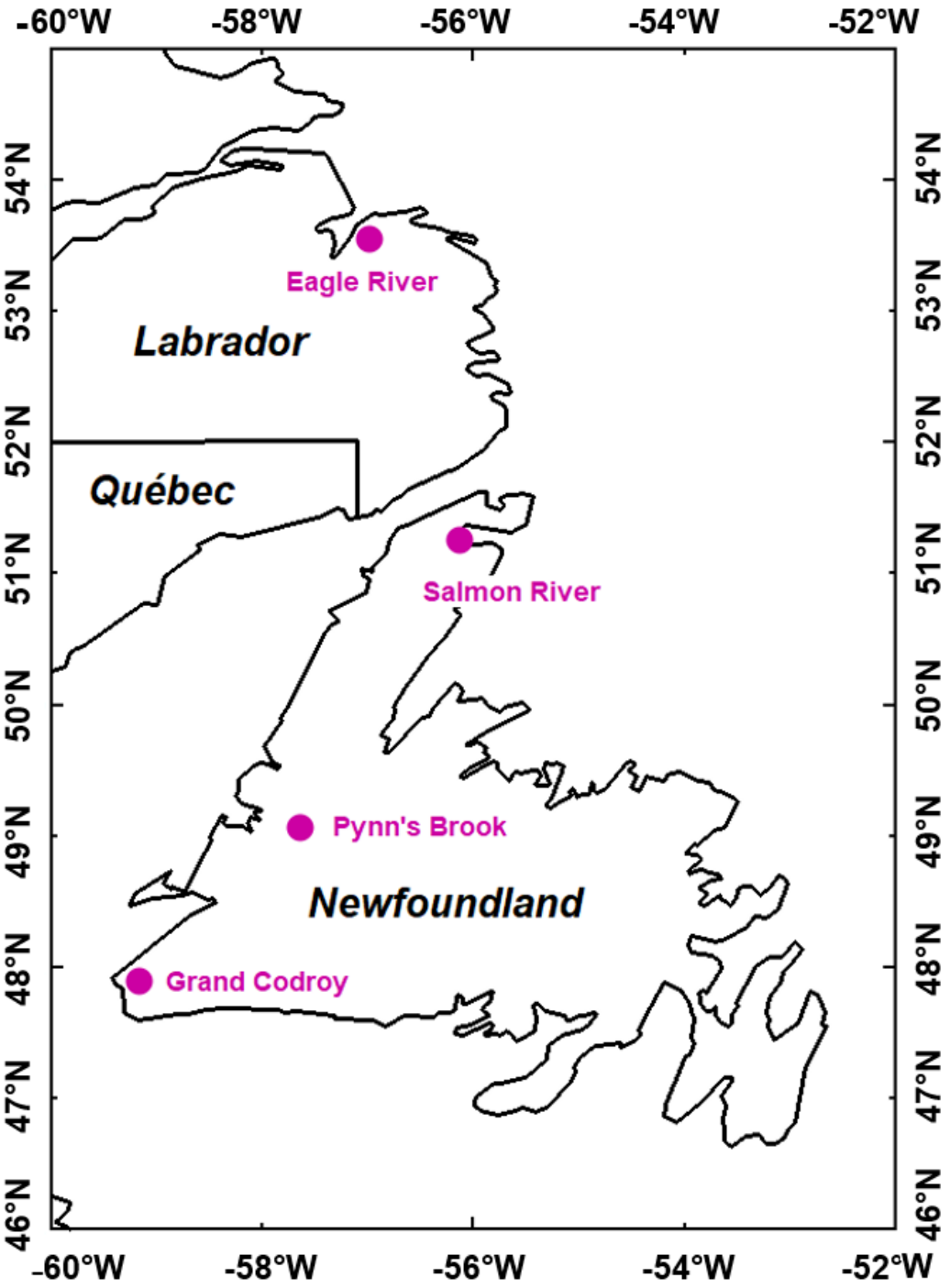

Figure B-10. Map of the NL-BELT highlighting the four watershed regions where sampling occurred: Grand Codroy (GCo), Pynn's Brook (PB), Salmon River (SR), and Eagle River (ER).

B.2 Deposition comparison: this work, DAYMET, and ECCC

Sufficiently continuous measurements from ECCC stations near each site are challenging to obtain for the 2015-16 period. When available with greater than 80% coverage, the ECCC datasets both agree and disagree with our observations in GCo and SR, respectively, suggesting that there is substantial deposition volume heterogeneity at the scale of ~10 km in this region. In SR, the disagreement with our measurements is identical to the DAYMET model which uses ECCC observations as input data, while at GCo the ECCC measurements are identical to ours (Table S3). Further, the discrepancy in the PB or ER average annual precipitation volume between ECCC and those of this work and DAYMET are not possible to integrate due to the large quantity of data missing from the ECCC monitoring station (35.22% in ER and 39.65% in HR/PB; Table B-3). The DAYMET observations are representative of a larger spatial scale, where our discrete samplers could be subject to heterogeneity in deposition (e.g., orographic precipitation, driven by topography like steep slopes) or impacted by meteorological conditions not captured by the model (e.g., undercatch driven by local winds). The temporally resolved volume comparisons at sampling interval timescales better-demonstrates comparability, despite the systematic differences. The month-to-month relationships between DAYMET and our observations, as well as between ECCC and our observations, all show strong correlations with linear regressions having R^2 values, from north to south, of 0.72, 0.99, 0.99, and 0.86, and N/A, 0.94, N/A, and 0.93, respectively (Table B-3). The discrepancy between DAYMET, ECCC, and our observations for total deposition were highest in the most northerly site, where the experimental site was located on a steep slope, with only 43% of the predicted volume collected. At all of the sample collection sites on the island of Newfoundland, a consistent difference was observed with 65 ± 4 % of the estimated volume collected, except at GCo where our measurements and those from ECCC are identical and starkly

contrasting to DAYMET. Overall, parsing these comparisons is difficult and demonstrates that there may be up to 55% additional uncertainty in deposited species, should given measurements of a species be scaled for a watershed like ER by concentration in total deposition samples. We propose, that by isolating only the deposited analytes and using analyte fluxes instead of concentrations in precipitation samples, that uncertainty issues in representing volumes, improves overall deposition budget certainties.

Table B-3. Collected precipitation volumes from NL-BELT in bulk deposition samplers for rainwater were deployed for one to two months, while snow was collected as an integrated sample throughout the winter because sites were not accessible. The Environment and Climate Change Canada (ECCC) precipitation data was obtained for identical sampling intervals. The DAYMET model for North America (1 km x 1 km resolution) for precipitation was obtained for the identical sampling intervals, which utilizes interpolated and extrapolated data from daily weather observations to predict inputs at the NL-BELT locations. Linear regression results for slope (m) and correlation coefficient (R^2) between observations and DAYMET (*italics*), and observations and ECCC (where possible; underlined), were calculated. For sampling periods where a measurement was compromised or not collected for a given interval in this work, these are reported as with '-' and an estimated volume from the regression relationship with ECCC is reported in parentheses when used to replace compromised samples.

	Grand Codroy			**Pynn's Brook/ Humber River**		
Date (mmm-yy)	**This Work (L)**	**DAYMET (L)**	**ECCC (L)**	**This Work (L)**	**DAYMET (L)**	**ECCC (L)**
Jun-15	22.68	40.98	23.80[b]	23.44	36.94	11.47[b]
Jul-15	2.92	3.38	2.06	2.24	2.93	1.04[b]
Aug-15	6.86	8.08	7.20	5.06	6.86	-
Sep-15	(5.17)[a]	2.93	5.17	3.05	4.70	-
Oct-15	1.71	4.31	4.44	-	-	-
Nov-15	3.57	5.92	4.92	5.66	8.61	-
May-16	26.00	28.15	25.38	15.62	24.18	11.22[b]
Jun-16	1.83	4.21	3.79	4.25	4.51	2.79
Jul-16	5.81	3.96	6.10	3.13	3.80	3.19
Aug-16	5.19	4.10	3.98	4.67	6.14	4.23
Sep-16	7.79	5.17	4.06	4.97	4.04	-
Oct-16	5.10	6.69	5.30	5.15	5.84	3.47[b]
m, R^2	0.62, *0.859*; 1.02, 0.934			0.60, *0.990,* -, -		
	Salmon River			**Eagle River**		
Date (mmm-yy)	**This Work (L)**	**DAYMET (L)**	**ECCC (L)**	**This Work (L)**	**DAYMET (L)**	**ECCC (L)**
Jun-15	-	-	-	-	-	
Jul-15	21.12	31.13	30.94	13.85	40.92	15.09[b]
Aug-15	1.89	4.71	9.52	3.66	6.96	2.64[c]
Sep-15	5.29	6.62	6.44	-	-	-
Oct-15	3.62	5.20	6.18	-	-	-
Nov-15	-	-	-	-	-	-
May-16	16.19	22.73	25.33	-	-	-
Jun-16	2.39	3.11	3.05[a]	22.94	45.68	22.70[b]
Jul-16	3.68	3.26	-	-	-	-
Aug-16	3.60	5.18	3.89[a]	5.82	10.79	6.94[b]
Sep-16	4.95	5.95	6.69	-	-	-
Oct-16	2.00	2.82	2.58	5.42	8.32	4.39[b]
m, R^2	0.68, *0.987*; 0.67, 0.941			0.43, *0.719,* -, -		

[a]Sample compromised by wildlife-sampler interaction.

[b]These values result from periods where <80% of the observation days report collected data. Partial volumes from the available data are presented.

[c]These values result from periods where <50% of the observation days report collected data. Partial volumes from the available data are presented.

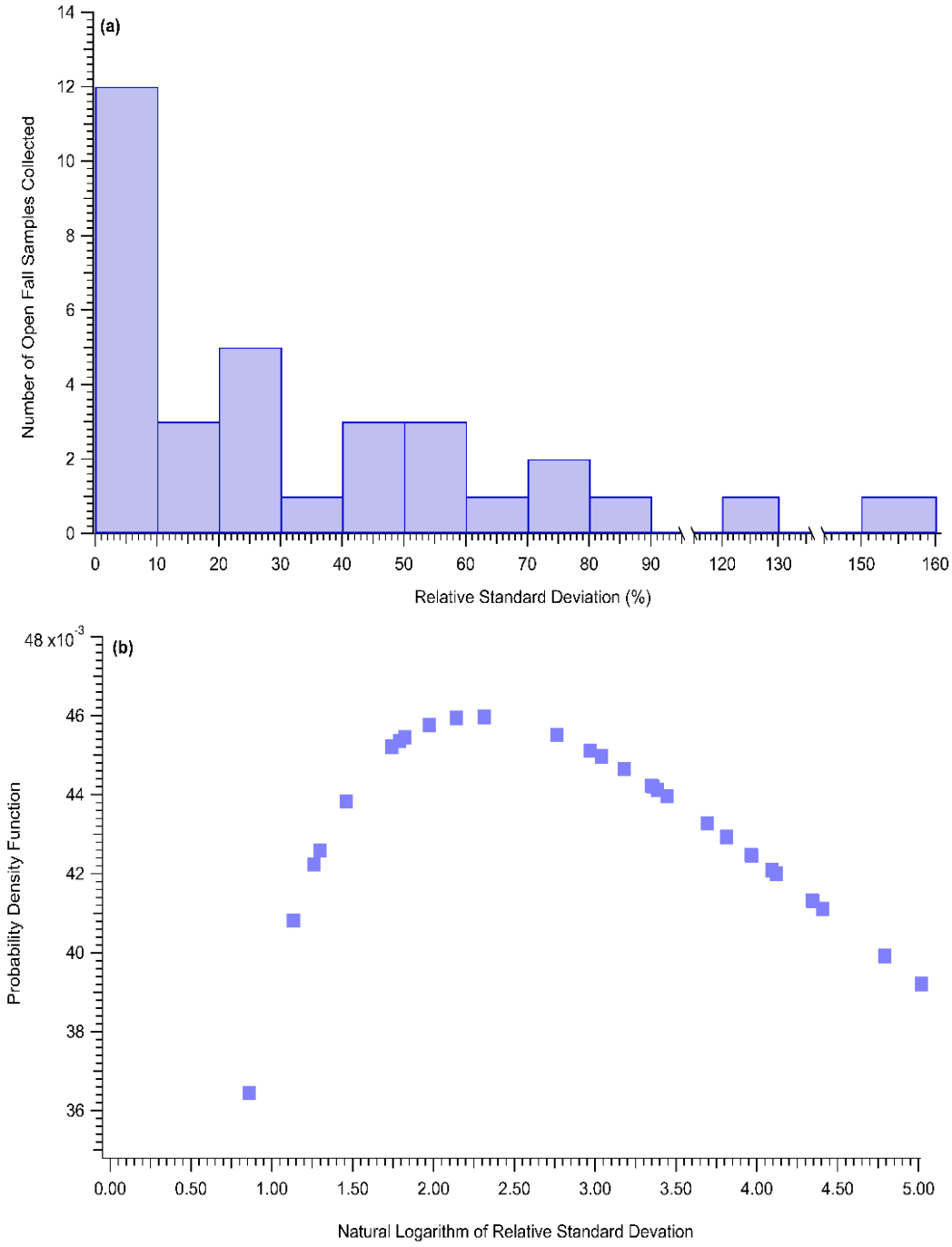

Figure B-11. Thirty-three sets of triplicate open fall samples were collected across the NL-BELT between 2015 and 2016. **(a)** The replicate relative standard deviations (RSDs) appear to follow a log-normal distribution where reproducibility is typically within ± 12.5% and almost always within ± 31.5%. **(b)** A variable 'x' is said to have a lognormal distribution if y = ln(x) is normally distributed. The RSDs were treated as variable 'x' and then log-transformed, resulting in a mean (μ) and standard deviation (σ) of 2.81 and 1.41, respectively. The probability density function for the log-normal, plotted against these log-transformed values, is defined by the two parameters μ and σ, where x > 0. As a result, one of the 33 RSD values was excluded from this plot as it became a negative value after being log-transformed.

Table B-4. Sum of DOC fluxes (mg C m^{-2} $year^{-1}$) in wet deposition samples for 2015 and 2016 at GCo, PB, SR, and ER. The average DOC flux error (mg C m^{-2} $year^{-1}$) propagated by summing the errors across the sampling sites to obtain the annual values.

		OF	TF
Site	**Year**	**Deposition Flux (mg C m^{-2} $year^{-1}$)**	
GCo	2015	1800 (± 800)	3700 (± 2400)
	2016	1400 (± 800)	700 (± 700)
PB	2015	600 (± 300)	1800 (± 600)
	2016	7800 (± 7700)	3000 (± 3600)
SR	2015	2000 (± 900)	3500 (± 2000)
	2016	4000 (± 1700)	1700 (± 1500)
ER	2015	100 (± 100)	1600 (± 2200)
	2016	1000 (± 800)	100 (± 30)

Table B-5. Average DOC flux (mg C m^{-2} $year^{-1}$) for 2015 to 2016 at GCo, PB, SR, and ER. The difference between calculated fluxes in TF and OF samples are also included.

	OF	TF	TF – OF
Site	**Flux (mg C m^{-2} $year^{-1}$)**		
GCo	1600	2200	600
PB	4200	2400	-1800
SR	3000	2600	400
ER	500	900	400

Chapter 4

Quantifying Ultrashort- and Short-chain Perfluorocarboxylic Acids in Endangered Canadian Whale Habitats

4.1 Abstract

Accurate atmospheric measurements of ultrashort- and short-chain perfluorocarboxylic acids (PFCAs) are essential for quantifying their deposition to aquatic environments, yet such measurements remain scarce due to methodological challenges. Here, we develop and validate an artifact-minimized method for collected gas-phase perfluoropropionic acid (PFPrA; C3 PFCA) using sodium carbonate-coated annular diffusion denuders. Laboratory experiments demonstrated a capture efficiency of 99.83 ± 0.03% under dry conditions, providing a robust foundation for atmospheric measurements. Using this validated approach, we conducted year-long active air sampling alongside wet and total deposition collection at two field sites within regions home to endangered Canadian whale populations: Tadoussac, Québec (St. Lawrence Estuary belugas) and Saturna Island, British Columbia (Southern Resident killer whales). Ion chromatography-mass spectrometry was used to quantify C2 to C6 PFCAs in both gas-phase and deposition samples. Trifluoroacetic acid (TFA; C2 PFCA) and PFPrA were the most frequently detected and abundant PFCAs within the gas-phase and deposition samples at both sites. A method intercomparison with concurrently deployed passive air samplers showed similar seasonal trends for TFA. Dry deposition fluxes, derived from wet and total deposition measurements, revealed site-specific contrasts, with wet deposition dominating at Tadoussac and a greater dry deposition contribution to total deposition at Saturna Island. These measurements provide atmospheric data that could be used to estimate PFCA inputs to coastal waters, further evaluate wet versus dry deposition pathways, inform atmospheric fate and transport models/PFAS exposure assessment frameworks, and establish baseline PFCA levels in whale habitats. Ultimately, our results indicate that atmospheric deposition represents a non-negligible source of ultrashort-chain PFCAs to marine environments.

4.2 Introduction

Per- and polyfluoroalkyl substances (PFAS) are a class of synthetic compounds in which carbon-hydrogen bonds are partially or completely replaced with carbon-fluorine bonds. Due to the strength of the carbon-fluorine bond, PFAS have ideal commercial and industrial properties including chemical inertness, hydrophobicity, and low surface tension.[1] These properties have led to the widespread use of PFAS in products such as cosmetics, non-stick cookware, and textiles, resulting in environmental emissions from manufacturing, wastewater treatment, landfills, etc.[2,3] As their terminal acid degradation products are very resistant to environmental and metabolic degradation[4], these PFAS persist and accumulate globally, with some potentially bioaccumulating in wildlife and humans and exhibiting toxicity in organs such as the liver, kidneys, and lungs.[5,6] Long-chain perfluoroalkyl acids (PFAAs; C7 to C20) are of particular concern due to their demonstrated biomagnification within aquatic food webs, posing risks to apex predators like seals, polar bears, and whales.[7,8]

In response to these concerns, regulatory measures and phase-outs within North America and Europe have targeted the production and use of long-chain PFAS, such as perfluorooctanoic acid (PFOA) and perfluorooctane sulfonic acid, with the aim of reducing environmental and human exposure.[9-12] Industrial manufacturers have since replaced them with ultrashort- (C2 to C3) and short-chain (C4 to C6) homologues, maintaining that their reduced bioaccumulation potential lessens adverse impacts on mammals.[13] Among these replacements, trifluoroacetic acid (TFA), an ultrashort-chain perfluoroalkyl carboxylic acid (PFCA), is environmentally persistent, highly mobile in surface water and groundwater (pK_a = 0.23), and forms a terminal residue from the degradation of numerous parent PFAS compounds.[14,15] Although less bioaccumulative than their long-chain counterparts, greater quantities of ultrashort- and short-chain PFAS are required to

manufacture the same amount of consumer product – thereby leading to increasing emissions.[16] Consequently, researchers have called for ultrashort- and short-chain PFAAs to warrant a level of concern comparable to that of long-chain PFAAs – particularly with respect to their environmental fate and long-term impacts.[4]

Despite their increasing environmental relevance, atmospheric measurements of ultrashort-chain PFCAs, including TFA and the C3 PFCA, perfluoropropionic acid (PFPrA), remain sparse. Most previous atmospheric PFCA studies have focused on ≥C4 homologues and have relied on indirect approaches such as deposition sampling[17,18] and/or direct approaches such as gas and particle collection.[19,20] Both wet[21,22] and total deposition (wet + dry)[19,20,23] sampling has been used to measure PFAS, yet very few studies have made distinguished measurements between wet and dry deposition.[21,24,25] Wet deposition involves the removal of particles and gases from the atmosphere via precipitation[26], while dry deposition directly transfers them to the Earth's surface via diffusion, impaction, and gravitational settling.[27] This distinction is critical because dry deposition can represent a substantial – yet poorly constrained – pathway for deposition to the Earth's surface. Accurately quantifying dry deposition requires reliable measurements of atmospheric PFCA concentrations and their partitioning between gas and particle phases; however, current understanding of gas-particle partitioning is limited by the availability of reliable measurements and partitioning properties, leading to uncertainty in deposition velocities and scavenging efficiencies.[28] To date, only three prior studies have quantified deposition fluxes of TFA and PFPrA[19,20,24], highlighting a significant gap in our understanding of their atmospheric transport and deposition.

Atmospheric measurements of PFCAs are therefore essential for constraining their environmental fate and deposition to the surface. However, the measurement of ultrashort- and

short-chain PFCAs presents methodological challenges. Direct atmospheric sampling has traditionally relied on offline techniques like passive and active air sampling to collect gas- and particle-phase PFAAs. Passive air samplers (PASs), often using polyurethane foam disks (PUF), or nylon-based sample methods for the chemically selective collection of atmospheric acids (i.e., PFCAs)[29], are convenient for long-term spatial monitoring without power requirements.[30] However, their uptake of ultrashort-chain PFCAs can be influenced by uncertainties in sampling rates and by particulate matter depositing on the samplers.[31] As a result, high- and medium-volume active air samplers (AASs) have become the preferred method of sampling due to their advantageous ability to separately, yet simultaneously, capture particulate and gas-phase PFCAs. A main drawback of this method is the occurrence of blow-on and blow-off sampling artifacts that bias phase partitioning.[2,32-34] These challenges are of particular concern for ultrashort-chain PFCAs, which are more volatile and present at higher atmospheric abundances than their longer-chain homologues. Some studies have followed long-established protocols for sampling atmospheric semi-volatile acids and bases (e.g. ammonia and nitric acid, HNO_3) that minimize these artifacts by using annular diffusion denuders and filter packs. For example, annular denuder coatings have been modified to target neutral PFAS by first collecting the gas-phase on polystyrene-divinylbenzene resins (i.e., XAD), followed by a filter to collect particles – preventing adsorption of PFCAs onto quartz or glass fiber filters as in high-volume samplers.[2,33,35] Denuders have also not been comprehensively validated for C2 and C3 PFCAs, yet they currently represent the most robust approach for artifact-minimized collection of gaseous PFCAs.

An emerging online technique for measuring gas-phase PFCAs – iodide-adduct chemical ionization mass spectrometry – has recently demonstrated in situ, high time-resolution measurements of ultrashort- and short-chain PFCAs.[36] This method is well suited for resolving

short-term variability but currently remains analytically challenging at low ambient concentrations. Analytical limitations further complicate ultrashort- and short-chain PFCA measurements as gas chromatography mass spectrometry (GC-MS) requires derivatization[37,38] whereas liquid chromatography mass spectrometry (LC-MS) can experience ion suppression at trace levels.[39] As a result, only a few studies have measured particle and gas-phase TFA[18,38,40] and gas-phase PFPrA.[38] Ion chromatography has been previously applied to separate and analyze ultrashort-chain PFCAs such as TFA[29,41-43] and, more recently, coupled with mass spectrometry (IC-MS) for haloacetic acid[44,45] and PFCA[42] analysis because PFAS are ionic under most environmental conditions and pH ranges[46], such that IC-MS offers a promising approach for PFCA separation and analysis with good selectivity and sensitivity.[47,48] Improving the reliability of PFCA measurements is therefore essential for accurately characterizing their atmospheric occurrence, transport, and deposition.

The 2018 Whales Initiative was developed under Canada's 2016 Ocean Protection Plan, which committed to the preservation, restoration, and protection of vulnerable Canadian marine ecosystems and marine mammals. This five-year, collaborative initiative sought to inform decisions and actions aimed to support the recovery of endangered Canadian whales by addressing the main risks threatening these populations, such as increasing understanding on the sources and impacts of their exposure to contaminants.[49] Our work supports the goals of the Whales Initiative by investigating the role of the atmosphere as a source of C2 to C6 PFCAs in regions inhabited by the St. Lawrence Estuary belugas (SLEBs) and the Southern Resident killer whales (SRKWs). Specifically, this work addressed key gaps within the literature by: i) quantitatively determining the sampling efficiency of sodium carbonate (Na_2CO_3) coated annular denuders for PFPrA, as previous studies have reported only on other PFCAs or halogenated acids; ii) providing artifact-

minimized, gas-phase C2 to C6 PFCA measurements; iii) comparing concurrent active air samples to long-term passive air samples to assess method performance; and iv) collecting total and wet deposition, using our custom-built samplers[50], to distinguish and constrain wet, dry, and total deposition fluxes. Ultimately, these measurements contribute to an ongoing improvement in our understanding of PFAS atmospheric transport and deposition to inform multimedia models, as well as assessments of contaminant exposure risks to marine mammals.

4.3 Methodology

4.3.1 Chemicals and Materials

Sodium carbonate (No. 223530, >99.5%) and glycerol (No. G-5516, >99%) were obtained from Sigma-Aldrich (St. Louis, MO, USA). Methanol (MeOH) of both high-performance liquid chromatography (HPLC) and Optima LC-MS grades were obtained from Fisher Chemical (Pittsburgh, PA, USA). Sodium salts of TFA (>98%) and PFPrA (>99%) were obtained from Sigma-Aldrich (St. Louis, MO, USA). The sodium salts of perfluorobutanoic acid (PFBA, C4 PFCA; >98%), perfluoropentanoic acid (PFPeA, C5 PFCA; purity not reported), and perfluorohexanoic acid (PFHxA, C6 PFCA; >98%) were obtained from Synquest Laboratories Inc (Alachua, FL, USA). Stock solutions of the PFCA sodium salts were prepared for IC-MS analysis in ultrapure Milli-Q water (18.2 MΩ·cm at 25°C, Direct 8; EMD Millipore) at 1000 μg mL^{-1}, which were then diluted to working stock concentrations. From these working stock concentrations, the following calibration standards were prepared: 0.00, 0.05, 1.00, 0.25, 0.50, 1.00, 2.50, and 5.00 μg L^{-1}. Mass-labelled $^{13}C_2$-TFA was purchased from Toronto Research Chemicals Inc (Toronto, ON, Canada) while $^{13}C_4$-PFBA, $^{13}C_{3,4,5}$-PFPeA, and $^{13}C_{1,2}$ PFHxA were individually obtained from Wellington Laboratories (MPFBA, M3PFPeA, and MPFHxA; Guelph,

ON, Canada) and dissolved in HPLC grade MeOH before being combined into one 10 μg L^{-1} Milli-Q water solution for use as an internal standard (IS) for IC-MS analysis.

4.3.2 Active Air Sampling

Active air sampling was conducted using an annular denuder system (ADS), following the United States Environmental Protection Agency Compendium Method IO-4.2, consisting of: i) a cyclone inlet, ii) annular denuders, and iii) filter packs.[51] A medium-volume sampler (MVS) was deployed at each field site and collected gas- and particle-phase samples. Each MVS drew an ambient air sample through a cyclone to fractionate the airborne particles to a specified cut-off diameter of the inlet at 2.5 μm ($PM_{2.5}$), or through a total suspended particulate inlet with a nominal cutoff at 10 μm (PM_{10}; Figure C-1). Each MVS contained four PM_{10} and four $PM_{2.5}$ channels. The PM_{10} channels were connected only to 47 mm dual-stage filter packs (URG-2000-30FG; URG Corp., Chapel Hill, NC, USA), while the $PM_{2.5}$ channels incorporated annular denuders (URG-2000-30X150-3CSS; URG Corp., Chapel Hill, NC, USA) upstream of identical filter packs. The singular PM_{10} inlet sampled at ~32 L min^{-1}, split evenly among four ports while the two $PM_{2.5}$ inlets drew ~16 L min^{-1}, meaning that each sample was collected from a flow of ~8 L min^{-1} per channel. As per the manufacturer guidelines, sampling at Hovington Farm, QC was paused during the winter due to temperatures below -20°C being reached. Sampling at Saturna Island, BC was continuous due to the milder climatology.

4.3.2.1 Coating Performance for Annular Denuders

Primary gas-phase standards of PFPrA were generated via acid displacement using potassium perfluoropropionate (K-PFPrA) and hydrochloric acid (HCl), with nitrogen gas (N_2) as the carrier gas (EQ 1), following our previous work.[52]

$$HCl_{(g)} + KC_2F_5C(O)O_{(s)} \rightarrow KCl_{(s)} + C_2F_5C(O)OH_{(g)} \qquad \textbf{(EQ 1)}$$

Housed inside of a custom-built permeation oven was a 6 M HCl permeation tube and salt bed (Lao et al., 2020).[53] This permeation tube was connected to a salt bed containing 0.5 g of K-PFPrA in 1/2" PFA (perfluoroalkoxy) tubing (8 cm long) filled with short pieces of 1/8" PFA tubing to increase the surface area available for acid displacement. The gaseous PFPrA produced was directed either to an annular denuder (three channels, 28 x 150 mm, URG Corp., Chapel Hill, NC, USA) with its outflow directed to an impinger filled with Milli-Q water, or to just the impinger alone (Figure C-2). Denuder scrubbing efficiency could be determined by difference between the two configurations. Three replicate experiments delivering gaseous PFPrA were carried out for 24 hours at room temperature (~298 K) and in dry air (0% relative humidity) as a worst-case scenario for collection. The bubbler solution or denuder extract were recovered quantitatively and stored in a fridge until analysis using ion chromatography coupled to conductivity detection (IC-CD; Section C.1, Table C-1).

4.3.3 Deposition Samplers

Deposition sampling using wet and total deposition collection units was conducted at Tadoussac from October 14, 2021, to October 12, 2022, and at Saturna Island from December 15, 2021, to December 3, 2022. One total deposition sampler and three automated wet deposition samplers were deployed at each site. The design, validation, and operating principles of these custom-built deposition samplers are detailed elsewhere.[50] At Tadoussac, wet deposition sampling was paused between December 15, 2021, and June 8, 2022, due to freezing conditions. Total deposition continued where we deployed a new heated funnel and these sampled throughout the winter and spring, melting solid precipitation. In July 2022, one wet deposition sampler was

converted to a total deposition sampler. We made a similar change in the sampling design at Saturna Island in January 2022, resulting in two wet and two total deposition samplers at each site.

4.3.4 Field Sampling

Over the course of one year, we collected air and deposition samples at two Canadian field sites within the watersheds connected to endangered whale populations. The first field site was located at Hovington Farm in Tadoussac, Québec (48°08'34.000" N, 69°41'03.000" W) – situated ~750 m from the St. Lawrence River (Figure C-3). Deposition, active air, and passive air[29] sampling occurred simultaneously. With a recent study having identified a suite of 54 PFAS within the livers of endangered SLEBs[54], this location is relevant for quantifying ultrashort- and short-chain PFCAs fluxes into the watersheds that connect to their habitat. The second field site was located at the Meteorological Service of Canada's Air and Precipitation Monitoring Network (CAPMoN) site on Saturna Island, British Columbia (48°46'30.080" N, 123°07'41.080" W) – approximately 1 km from the Salish Sea (Figure C-4) but situated to intercept air from the remote North Pacific Ocean rather than mainland British Columbia. As CAPMoN sites make up a system of rural background stations designed to establish spatial patterns and long-term trends in pollutants linked to air and precipitation chemistry, they are sited to ensure regionally representative measurements.[55,56] Deposition, active air, and passive air samples[29] were collected concurrently. A recent study has reported PFAS, amongst other persistent organic pollutants (POPs), within the skeletal muscle and liver of SRKWs[57], such that this remote sampling location could prove informative for long-range and/or background atmospheric determinations.

4.3.5 Sample Preparation

4.3.5.1 Wet and Total Deposition Sampling

For sample collection, four 10 L high-density polyethylene (HDPE) jerricans (Bel-Art, part number, P/N, 11215-314; VWR, Mississauga, ON, Canada) per site were pre-cleaned by rinsing five times with 400 mL Milli-Q water and once with 100 mL HPLC grade MeOH. A travelling field blank (one per site) consisting of 1 L Milli-Q water in a pre-cleaned 1 L HDPE container (Nalgene; VWR, Mississauga, ON, Canada) remained capped for the entirety of the sampling period and was included to assess potential contamination caused from transport. All 1 L HDPE containers used for blanks and sample storage were pre-cleaned with five rinses of 80 mL Milli-Q water followed by one rinse of 18 mL HPLC grade MeOH. After each sampling period, deposition volumes were measured at York University (Toronto, ON) using a 1 L polypropylene graduated cylinder. Volumes of 1 to 2 L from each sample were kept for analysis and archiving, with any remainder discarded. Deposition samples and field blanks were stored at room temperature until IC-MS analysis.

4.3.5.2 Annular Denuder System: Active Air Sampling

The annular denuders consist of three concentric etched glass channels to provide maximum surface area for application of a reactive coating and subsequent gas-phase sample collection. Denuders were rinsed five times with Milli-Q water and once with 5 mL HPLC grade MeOH, dried for 20 mins under a dry flow of N_2 at ~2.5 L min^{-1}, then coated with 15 mL of a denuder coating solution (20 g L^{-1} Na_2CO_3 and 1.0 g L^{-1} glycerol in 1:1 (v/v) DIW:Optima grade MeOH). After being measured in a precleaned graduated cylinder (rinsed six times with Milli-Q water), the coating was applied by pouring the solution into the denuder with one end capped,

followed by capping the entire device, then carefully tipping and rotating the denuder around all axes to obtain an even coating prior to decanting excess solution. The coated denuder was then dried a second time under dry N_2 for 20 mins. For the collection of particles, one pre-baked (650°C, 1 hr) 47 mm quartz fibre filter (Pallflex® Tissuquartz™, 7204, Pall Corporation; Port Washington, NY, USA) was placed in each PM_{10} and $PM_{2.5}$ filter pack. To assess potential contamination, field blanks consisting of one coated denuder and one filter pack per site were transported and left undisturbed during each sampling period. After each deployment, denuders and blanks were extracted at York University with two 5 mL aliquots of Milli-Q water. Prior to denuder extraction, 15 mL conical Falcon® tubes were rinsed six times with Milli-Q water. To extract the annular denuder, a 5 mL aliquot of Milli-Q water was pipetted into the denuder with one end capped, after which the device was fully capped. The denuder was then carefully inverted and rotated along all axes several times. The extract was poured into a precleaned 15 mL conical Falcon® tube and the procedure was repeated for a second aliquot. The pooled extracts were stored at 4°C until analysis. Quartz filters were stored intact and refrigerated but are part of a future investigation. This study focuses solely on the analysis of gas-phase PFCAs.

4.3.5.3 Ion Chromatography Mass Spectrometry (IC-MS): Quantitative Determinations

To analyze the collected field samples for C2 to C6 PFCAs, we used our developed IC-MS method (Section C.2, Table C-2).[29,42,43] Each 1 mL polypropylene IC-MS vial (P/N 5182-0567; Agilent Technologies Canada, Mississauga, ON, Canada) contained 700 µL of the sample and 100 uL of the IS mixture, combined by vortex for ~30 s. Depending on the total volume collected during each sampling period, anywhere from 5 to 15 mL of wet and total deposition samples were filtered using a 13 mm diameter, 0.22 µm pore size polytetrafluoroethylene filter (Avantor, Cat.

No. 76479-010; VWR International LLC, Mississauga, ON, Canada). Following the filtering process, deposition samples required no additional cleanup prior to preparation with IS, whereas the denuders extracts were diluted threefold to reduce matrix effects from the coating solution and minimize potential analytical interferences prior to IS addition. Blanks were prepared for both deposition and denuder samples: deposition blanks were aliquots of 1 L of Milli-Q water, and denuder blanks were aliquots of Milli-Q water extract obtained from dried coated denuders. In both cases, the blanks were prepared in the laboratory and shipped to the field sites without exposure to ambient air, serving as both method and travelling field blanks to monitor potential contamination during transport and handling. The IC-MS instrument blank was an untreated aliquot of Milli-Q water.

4.3.6 Data Analysis

All data processing and analyses were performed following quality assurance procedures described below to convert measured deposition concentrations into fluxes, gas-phase concentrations into mixing ratios, and to enable comparison across sampling methods and sites. The instrument limit of detection (LOD) and limit of quantification (LOQ) were defined at signal to noise ratios of three and ten, respectively, determined from the slope of the signal to noise ratio plotted against the concentration of the calibration standards inclusive of an instrument blank. The method LODs from travelling annular denuder and deposition field blanks were found to be indistinguishable from the instrument LODs and LOQs; thus, we do not distinguish between these two measures of LOD and LOQ. The various analyte LODs do not exceed 0.128 μg L^{-1} (Table C-3). Those replicates with levels above the LOD and LOQ (>LOQ), in-between the LOD and LOQ (<LOQ), and below the LOD (<LOD) are characterized as quantitative, semi-quantitative, and not

detected, respectively. Measurements below the LOD were assigned a value equal to one-half of the respective LOD, providing a conservative lower-bound estimate and enabling consistent treatments of non-detectable values across sample types.

Measured PFCA concentrations in wet and total deposition samples (μg L^{-1}) were converted to annual deposition fluxes (μg m^{-2} $year^{-1}$) using the volume of deposition collected (L), the known area of the sampler funnel (0.038013 m^2), and the duration of each sampling interval (days). Fluxes for individual sampling periods were annualized and averaged to obtain site-specific annual wet and total deposition fluxes. Dry deposition fluxes were calculated by subtracting the measured wet deposition flux from the corresponding total deposition flux for each analyte and sampling period. Details of flux calculations and uncertainty propagation are provided in Section C.3. For gas-phase samples collected using annular diffusion denuders, analyte concentrations measured in extraction solutions were first converted to total moles of PFCA per sample. These values were then normalized by the total volume of air sampled to obtain atmospheric mass concentrations (pg m^{-3}). Atmospheric mixing ratios reported in parts-per-quadrillion by volume (10^{-15} mol mol^{-1}, ppqv) were then calculated using the ideal gas law, assuming standard pressure and using the average ambient temperature for each sampling period and the molecular weight of each analyte. Mixing ratios from replicate denuders within a sampling period were averaged, with replicates below the LOD treated as described above to estimate lower-bound mixing ratios.

For both deposition and gas-phase measurements, uncertainties associated with replicate samples where $n \geq 3$ were calculated as standard deviations. For sampling periods where $n = 2$, the uncertainty is expressed as the relative difference between the two replicates and where $n = 1$, an instrument-based uncertainty derived from calibration data was used as a proxy. Propagation of uncertainty was applied for addition and subtraction operations when calculating annual average

fluxes and dry deposition fluxes, following standard error propagation approaches (Section C.3). To allow for comparison between the AAS results and the concurrently deployed PASs, weighted average atmospheric mixing ratios were calculated to account for differences in sampling duration. Each active air sampling interval was weighted by its duration relative to the total sampling period at each site. Uncertainties associated with the weighted averages were calculated using propagation of uncertainty for addition and further details can be found in Section C.4.

4.4 Results and Discussion

4.4.1 Sampling of Gas-phase PFPrA Using Na_2CO_3-coated Annular Denuders

Annular denuders are used for routine quantitative collection of strong atmospheric acids by monitoring programs like those of CAPMoN and the National Atmospheric Deposition Program. Their acid-selective sampling chemistry makes them appealing for the quantitative collection of PFCAs, which are strong acids akin to HNO_3 and HCl, for which CO_3-coated annular denuders are analytically validated.[51] Sampling efficiency of PFPrA by the Na_2CO_3-coated denuder was quantitatively determined by passing a known quantity of 18 parts-per-million-by-volume (ppmv; 10^{-6} mol mol^{-1}) of PFPrA in zero air through a denuder or directly to a bubbler to collect the gas-phase amounts quantitatively. Denuder capture efficiency was calculated using EQ 2.

$$1 - \left(\frac{C_{denuder}}{C_{no\ denuder}}\right) \times 100\% \qquad \textbf{(EQ 2)}$$

Where $C_{denuder}$ is the concentration of the PFPrA samples with the denuder attached and $C_{no\ denuder}$ is the concentration with no denuder attached. If $C_{denuder}$ was below the IC detection limits, the LOD for the method was used when calculating the capture efficiency. Sampling efficiency of

PFPrA by a triplicate set of Na_2CO_3-coated annular denuder experiments was calculated to be 99.83 ± 0.03%. This indicates that they are extremely efficient at sampling and removing gaseous PFPrA from a flow of air that the denuder is rated for.

While this work is the first to report on the sampling efficiency of PFPrA using annular denuders, its efficient collection is consistent with previous demonstrations of quantitative TFA capture using similar denuder-based approaches[29,40] and can be readily inferred for other short-chain PFCAs, which exhibit similarly strong acid behaviour under environmental conditions.[58-60] More broadly, carbonate-coated denuders are well established for the quantitative retention of strong acids, with extensive supporting literature spanning several decades.[51] Sampling efficiencies for the target haloacetic acids were determined using a denuder-based test system with a cyclone inlet and controlled introduction of analytes via acetone spiking. Test compounds (~500 ng per analyte) were introduced into a glass inlet and drawn through the system for one hour, with each denuder section analyzed individually by GC-MS/MS following derivatization to ethyl esters. Sampling efficiency was calculated from triplicate experiments by comparing denuder recoveries to direct spiked aqueous standards.[40]

Compared to this experimental approach, several methodological refinements in the present work improve accuracy and reduce the quantity of materials needed. One is the delivery method of PFCAs into the denuders. Permeation ovens are a stable and reliable way to introduce gas-phase compounds to experimental setups, free of interferences caused by the presence of a solvent.[53] On a molecular level, the permeation device is more representative of collecting a real atmospheric sample as opposed to introducing a large pulse of gas-phase TFA into a denuder. The latter could result in the over-saturation of active surface sites, thereby causing breakthroughs if exceeding the sampling capabilities of the denuder. The use of a glass elbow to introduce TFA

samples into denuders may have also led to a decrease in sampling efficiency due to the known action of glass adsorbing gas-phase acids.[61,62] Another study reported the sampling efficiency of C4 to C17 PFCAs onto annular denuders coated with ground XAD-4, with sampling efficiencies ranging from 99.64% to 99.99%.[2] Denuder performance for gas-phase PFCAs was evaluated using calculated diffusion coefficients and breakthrough experiments utilizing denuders operated in series. Vapour-phase breakthrough and gas-particle partitioning were compared between denuder and high-volume AASs to assess sampling efficiency and artifacts. These experiments demonstrated that the denuder-based measurements minimize gas-to-particle sampling artifacts that can lead to overestimation of PFCA aerosol fractions in conventional filter-based samplers. While the denuder performance and calculated sampling efficiencies reported by Ahrens et al. are comparable to those observed here for PFPrA, differences in gas-phase PFCA generation methods should be considered when comparing results across studies.[2] Nevertheless, these findings provide a relevant gauge for evaluating PFPrA collection in the present work.

4.4.2 PFAS Deposition Measurements in Rural and Remote Field Sites

4.4.2.1 Wet and Total Deposition Fluxes

At the Tadoussac sampling site, ultrashort- and short-chain PFCAs were quantified in wet (n = 15) and total deposition samples (n = 13). In the wet deposition samples, the quantitative detection frequencies of TFA and PFPrA were 40% and 93%, respectively, with PFBA, PFPeA, and PFHxA each being detected in only 7% of the samples (Table C-4). Within the total deposition, the quantitative detection frequencies for TFA and PFPrA were 46% and 77%, respectively, while PFBA, PFPeA, and PFHxA were below LOD for all samples analyzed (Figure C-5). The C4 to C6 PFCAs were predominantly below detection limits – consistent with the previously reported

inverse relationship between chain length and atmospheric concentrations[19,63] – and are therefore not discussed further. In wet deposition, the concentrations of TFA and PFPrA range from <LOD to 0.797 μg L^{-1} and <LOD to 0.327 μg L^{-1}, respectively. In total deposition, the concentrations of TFA and PFPrA range from 0.162 μg L^{-1} to 0.650 μg L^{-1} and <LOD to 1.84 μg L^{-1}, respectively (Table C-5).

The same C2 to C6 PFCAs were analyzed in wet (n = 23) and total (n = 21) deposition collected from Saturna Island. All targeted analytes except for PFHxA were detected in at least one wet deposition sample whereas in the total deposition samples, PFBA and PFHxA were below the LOD in all samples. In these wet deposition samples, the quantitative detection frequencies of TFA and PFPrA were ~43% and 65%, respectively, with PFBA and PFPeA being detected in ~9% and 4% of the samples, respectively (Table C-4). Within the total deposition, the quantitative detection frequencies for TFA and PFPrA were ~43% and 33%, respectively, while PFBA and PFHxA were again below LOD for all samples analyzed (Figure C-6) and – along with PFPeA which was only detected in two samples – will not be discussed in detail moving forward. In wet deposition, the concentrations of TFA and PFPrA in solution range from <LOD to 2.09 μg L^{-1} and <LOD to 1.95 μg L^{-1}, respectively. In total deposition, the concentrations of TFA and PFPrA range from <LOD to 1.62 μg L^{-1} and <LOD to 2.57 μg L^{-1}, respectively. At both sampling sites, TFA was observed to have the highest concentrations in both wet deposition and total deposition followed by PFPrA (Table C-6).

Concentrations are influenced by the volume collected and are thus not well suited for discerning atmospheric mechanisms or deposition trends. Precipitation concentrations alone do not account for variability in precipitation amount, event duration, or the length of the sampling period, all of which influence total deposited mass; consequently, identical concentration values

can correspond to substantially different deposition loads depending on rainfall depth and frequency.[24,64,65] Thus, the concentrations reported here were converted to fluxes as described in Sections 2.6 and C.3. The measured replicate wet and total deposition fluxes for each individual sampling period were averaged and reported as an equivalent annual flux with units of μg m^{-2} $year^{-1}$. In our flux estimates, any below LOD measurement was treated here using a replacement value of half of that analyte's LOD to estimate the annual flux. The calculated TFA and PFPrA wet deposition fluxes normalized to an annual timescale at Tadoussac ranged from 30.21 to 628.66 μg m^{-2} $year^{-1}$ and 43.01 to 285.73 μg m^{-2} $year^{-1}$, respectively. In total deposition, TFA and PFPrA fluxes ranged from 38.71 to 807.21 μg m^{-2} $year^{-1}$ and 40.98 to 525.20 μg m^{-2} $year^{-1}$, respectively (Table C-7) and are consistent with the mass balance design of this sampling approach.[50] At Saturna Island, wet deposition fluxes for TFA and PFPrA ranged from 16.67 to 59.11 μg m^{-2} $year^{-1}$ and 6.97 to 85.31 μg m^{-2} $year^{-1}$, respectively. In total deposition, the TFA and PFPrA fluxes ranged from 45.43 to 245.80 μg m^{-2} $year^{-1}$ and 8.60 to 592.67 μg m^{-2} $year^{-1}$, respectively (Table C-8). In general, at both sampling sites, the total deposition fluxes were greater than the wet deposition fluxes for both TFA and PFPrA (Figure 4-1). A tabulated comparison of our TFA and PFPrA total deposition findings to selected literature is included in Table C-9. Fluxes were broadly comparable to those reported in mid-latitude regions and did not exhibit a consistent increase with latitude. While latitude can influence atmospheric processes through gradients in temperature, solar irradiance, and associated photochemical activity, as well as differences in transport pathways and source regions, such effects were not reflected in the observed deposition fluxes.[25] Instead, higher values were more frequently associated with regions influenced by anthropogenic sources, suggesting that emissions and regional activity may be more important drivers than latitude alone at these sampling sites.[23-25,64,66-73]

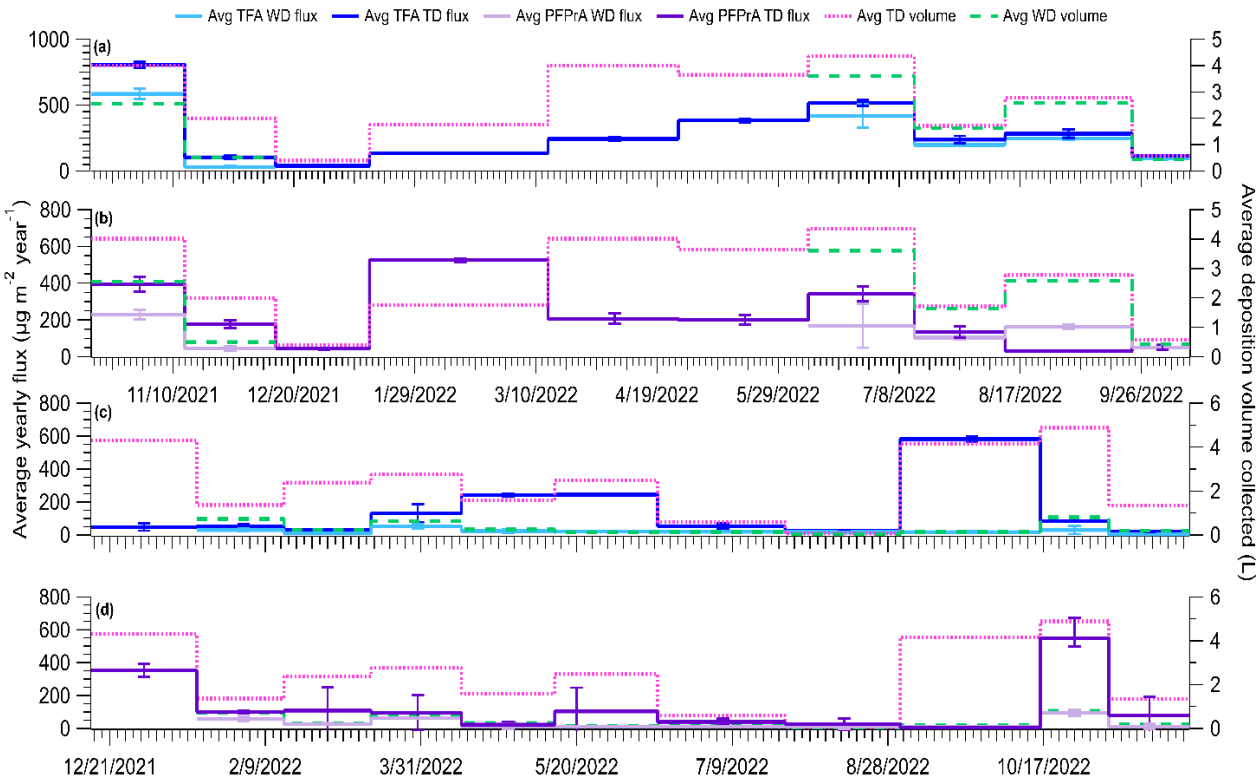

Figure 4-1. The average wet and total deposition fluxes (µg m^{-2} $year^{-1}$) of TFA and PFPrA at the Tadoussac and Saturna Island field sites. Panels **(a)** and **(b)** correspond to Tadoussac, while **(c)** and **(d)** correspond to Saturna Island. Panels **(a)** and **(c)** show TFA wet deposition fluxes (light blue) and total deposition fluxes (dark blue) plotted on the left y-axis. Panels **(b)** and **(d)** show PFPrA wet deposition fluxes (light purple) and total deposition fluxes (dark purple), also on the left y-axis. In all panels, dashed lines referenced to the right y-axis represent the average wet deposition volume (green) and average total deposition volume (pink) collected during each sampling period (x-axis). The error bars are the associated uncertainties as reported in Tables C-7 and C-8.

At the Tadoussac site, we observed both higher TFA fluxes and aqueous concentrations during the summer months compared to the shouldering seasons. This summertime enhancement is consistent with other studies reporting observed seasonal variations in TFA fluxes linked to increased atmospheric oxidation of PFCA precursors under higher concentrations of photochemically generated oxidants.[71] For example, national rainwater monitoring in Germany reported higher summer TFA fluxes and correlations with oxidant production[71] and multi-year measurements in Toronto, ON showed total and wet deposition fluxes peaking during the summer months, consistent with enhanced precursor oxidation under warmer conditions.[24] Regional studies

done in Switzerland, combining surface water and precipitation measurements with atmospheric modelling, similarly assign a substantial amount of TFA deposition to the degradation of volatile fluorinated precursors while noting that models tend to underpredict summertime deposition, suggesting complex seasonal processes that vary with source inputs and local meteorology.[73]

In contrast, no consistent seasonal trend was observed for PFPrA at either site and an obvious seasonal trend was not observed for TFA at the Saturna Island field site. Based on previous measurements, it might be expected for there to be higher levels of PFCAs in samples collected during the summertime months at this site. However, drought-like conditions were observed at Saturna Island from June through August during the sampling year and corresponded to the lowest volumes of deposition collected and fluxes in this study. The lack of a clear seasonal trend at Saturna Island likely reflects the influence of decreased precipitation and highlights the importance of gas-phase precursor oxidation, long-range atmospheric transport, and regional meteorology in this remote coastal environment. Similar observations have been reported in remote regions, where, for example, widespread PFAS contamination in remote Arctic surface snow has been shown to result from the long-range atmospheric transport, and subsequent degradation, of volatile precursors – even in areas far from local emission sources.[74] Consistent with this interpretation, ice core records from remote glaciers also have exhibited PFAS deposition driven by long-range emissions and transport rather than local sources or precipitation alone.[75,76] Together, these findings support that Saturna Island's PFAS deposition is most likely influenced by regional-to-long-range transport, with local meteorology and precipitation events exerting stronger control on observed deposition fluxes than seasonal photochemical production alone.

4.4.2.2 Dry Deposition Fluxes

A limited number of studies have evaluated the individual contributions of wet and dry deposition to the total deposition of PFAS[21,24,25,77], despite their fundamental importance in controlling atmospheric lifetime and fate. Wet deposition represents an episodic yet highly efficient removal pathway during precipitation events, whereas dry deposition occurs continuously in the absence of rain. In this study, we collected total and wet deposition from both field sites and calculated dry deposition fluxes by subtracting the two (Table 4-1, Table C-10). Based on quality-assured measurements and model estimates, a global assessment of atmospheric deposition has shown the varying relative contributions of wet and dry deposition based on precipitation frequency and distance from emission sources.[78] In locations which experience frequent rainfall and moderate- to high-emissions, wet deposition tends to dominate atmospheric removal, whereas dry deposition becomes more important in remote, low-emission, or coastal regions experiencing infrequent precipitation. These general patterns help contextualize our PFCA observations during the year-long sampling periods. As shown in Figure 4-2a, wet deposition contributed more to total TFA and PFPrA deposition at Tadoussac. While classified as rural, this sampling site is downwind of major urban centers including Québec City, Trois Rivières, and Montreal, which likely contribute measurable PFAS to the atmosphere via wastewater treatment, industrial activities, and other localized sources.[79,80] This proximity, combined with regular precipitation, supports our observations of wet deposition dominating atmospheric PFCA removal at Tadoussac during the sampling period. In contrast, at the drier, coastal Saturna Island site, dry deposition contributed more substantially to total atmospheric TFA and PFPrA removal (Figure 4-2b). While remote, this site can be influenced by regional emissions from industrialized areas of mainland British Columbia, Washington, and Oregon, as well as long-range transport of volatile PFAS precursors

Table 4-1. Comparison of measured wet deposition (WD) to calculated dry deposition (DD) fluxes at each field site for TFA and PFPrA. Dry deposition was calculated by subtracting WD from total deposition (TD). Values <LOQ are **bolded**, values <LOD are *italicized* and reported as half the analyte's LOD, and all remaining values (>LOQ) are shown in regular font. Due to technical issues with the deposition sampler motor arms deployed during December 15, 2021, to January 18, 2022, at Saturna Island, this sampling period was excluded from the dataset. In instances where WD ≫ TD, entries with "--" indicate a sampling interval where TD and WD were not statistically different from each other, and the resulting DD flux was not significantly different from zero. Details on the calculation of uncertainty for WD and DD fluxes are provided in Section C.3. Note that the reported uncertainties reflect observed sample-to-sample variation in deposition samples[25,50] and therefore represent natural environmental heterogeneity rather than analytical error.

	Avg. Volume (L)		**TFA (μg m^{-2} year^{-1})**		**PFPrA (μg m^{-2} year^{-1})**	
Tadoussac, QC	WD	TD	WD	DD	WD	DD
Oct 14 - Nov 14/21	2.55	4.01	585.09 (± 37.87)	222.12 (± 44.47)	228.79 (± 26.10)	165.43 (± 47.77)
Nov 14 - Dec 14/21	0.50	2.00	**30.55** (± 0.48)	72.89 (± 14.19)	44.24 (± 12.57)	133.95 (± 24.15)
June 8 - July 13/22	3.60	4.35	**418.69** (± 91.64)	97.92 (± 94.34)	*168.75* (± 119.56)	173.42 (± 125.60)
July 13 - Aug 12/22	1.63	1.71	**197.42** (± 2.15)	40.13 (± 29.11)	103.97 (± 16.17)	31.49 (± 47.08)
Aug 12 - Sept 23/22	2.58	2.78	246.16 (± 11.94)	36.45 (± 36.31)	162.66 (± 18.93)	--
Sept 23 - Oct 12/22	0.44	0.58	96.33 (± 10.05)	17.33 (± 10.05)	50.50 (± 5.42)	0.09 (± 19.96)
Saturna Island, BC	WD	TD	WD	DD	WD	DD
Jan 18 - Feb 15/22	0.73	1.36	28.84 (± 8.34)	23.17 (± 16.73)	55.95 (± 14.48)	43.49 (± 16.01)
Feb 15 - Mar 15/22	0.24	2.38	8.38 (± 0.67)	47.21 (± 14.37)	26.06 (± 5.58)	81.94 (± 142.60)
Mar 15 - April 13/22	0.64	2.76	52.57 (± 13.08)	77.93 (± 57.10)	62.93 (± 4.14)	32.15 (± 108.36)
April 13 - May 13/22	0.25	1.58	22.85 (± 10.53)	217.60 (± 14.17)	12.43 (± 17.46)	26.47 (± 23.88)
May 13 - June 15/22	0.13	2.48	20.10 (± 0.68)	224.53 (± 2.43)	9.98 (± 1.17)	93.38 (± 144.61)
June 15 – July 26/22	0.13	0.58	18.56 (± 0.42)	34.64 (± 15.56)	10.36 (± 2.00)	29.93 (± 21.66)
July 26 - Sept 1/22	0.04	0.06	17.83 (± 2.31)	6.30 (± 3.17)	11.71 (± 17.13)	14.26 (± 38.75)
Sept 1 - Oct 16/22	0.13	4.16	16.53 (± 7.17)	565.57 (± 18.13)	8.16 (± 2.37)	0.00*
Oct 16 - Nov 7/22	0.80	4.88	28.90 (± 24.46)	68.63 (± 96.04)	95.05 (± 19.49)	453.49 (± 90.40)
Nov 7 - Dec 3/22	0.19	1.35	2.69 (± 0.15)	17.38 (± 11.86)	11.54 (± 17.18)	67.79 (± 115.12)

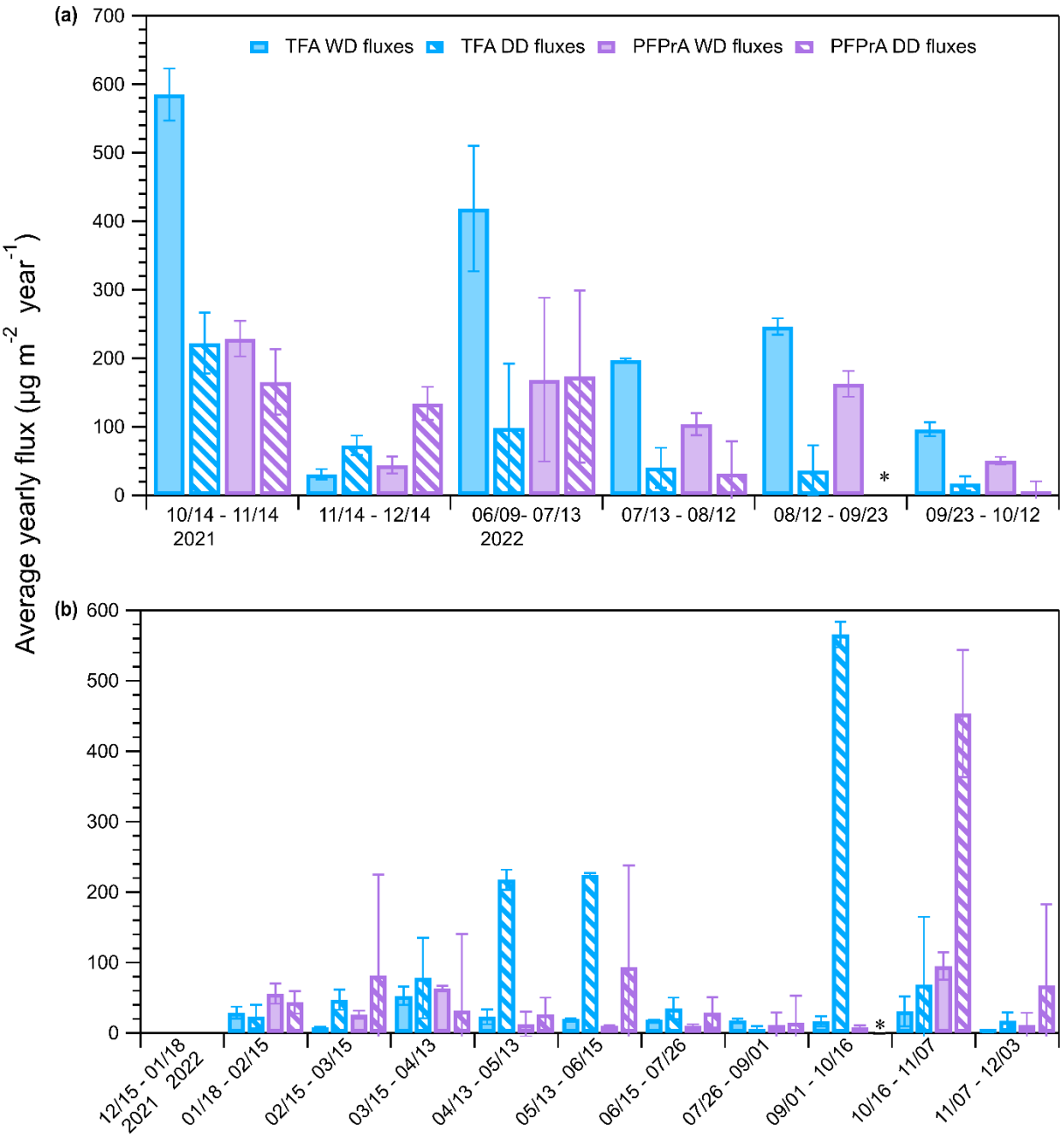

Figure 4-2. Comparison of measured wet (solid bar) and calculated dry (striped bar) deposition fluxes (ug m^{-2} $year^{-1}$) for both TFA (blue) and PFPrA (purple) at **(a)** Tadoussac and **(b)** Saturna Island. Asterisked (*) values indicate that total deposition and wet deposition were not statistically different from each other, and the resulting dry deposition flux was not significantly different from zero and is reported as such. Due to technical issues with the deposition sampler motor arms deployed during December 15, 2021, to January 18, 2022, at Saturna Island, this sampling period was excluded from the dataset. The error bars are the associated uncertainties as described in Section C.3. Note that the reported uncertainties reflect observed sample-to-sample variation in deposition samples[25,50] and therefore represent natural environmental heterogeneity rather than analytical error.

and contributions from sea spray aerosols and trans-Pacific air masses.[81-85] Overall, the relative importance of wet versus dry deposition at remote sites is influenced largely by precipitation frequency and the presence of atmospheric precursors, rather than proximity to emission sources alone.

Event-based PFAS measurements from previous studies provide further quantitative context for our findings. In a 2021 study conducted ~110 km from a fluorochemical manufacturer, wet deposition fluxes (ng m^{-2} $event^{-1}$) were calculated as the product of PFAS concentrations in rainwater and precipitation volume, while dry deposition fluxes (ng m^{-2} day^{-1}) were derived by subtracting the collected wet deposition from total deposition.[21] Measured fluxes showed that wet deposition removed PFAS from the atmosphere one to three orders of magnitude more efficiently than dry deposition, highlighting rainfall as the dominant atmospheric removal mechanism in this non-remote, source-proximal region. As expected, the amount of dry deposition depends not only on the atmospheric abundance of PFAS within the given region but also on the length of the rain-free periods it experiences. Our Tadoussac observations align with these findings, where precipitation intensity and frequency increased wet deposition relative to dry deposition.

At the coastal Saturna Island site, dry deposition was the dominant removal pathway for atmospheric PFAS during the sampling period, consistent with expectations for remote regions with limited precipitation. This finding is supported by measurements made within the Newfoundland and Labrador Boreal Ecosystem Latitudinal Transect, where dry deposition predominated for PFBA, PFOA, and perfluorononanoic acid – each an atmospherically formed PFCA – at remote sites[25], as well as by a modelling study which showed dry deposition to dominate farther from emission sources.[75] Observations for PFCAs with known volatile precursors suggest that even in low-emission regions, gas-phase precursors can undergo long-range transport and

contribute to dry deposition. Accordingly, PFAS follow the same general deposition trends as more commonly studied atmospheric pollutants such as nitrogen, with precipitation frequency primarily governing the relative importance of wet versus dry deposition. However, the presence of long-lived volatile precursors can maintain gas-phase reservoirs and enhance the role of dry deposition in remote, coastal, and low-precipitation environments.[77]

A three-dimensional global modelling study further supports the role of precipitation in governing atmospheric PFCA removal. In assessing both TFA formation and deposition, dry deposition fluxes were predicted to be, on average, only about 20% of wet fluxes across all regions.[86] Higher TFA rainwater concentrations in tropical and near-source regions reflected a combination of local precursor emissions, efficient atmospheric oxidation under higher sunlight/temperature, and frequent precipitation. This is consistent with the summertime flux enhancements observed at Tadoussac, where both precursor availability and regularly occurring precipitation contributed to efficient PFCA removal via wet deposition. Conversely, at Saturna Island, lower precipitation and more distant precursor sources result in lower seasonal fluxes, highlighting the role of regional transport and dry deposition in controlling atmospheric PFCA removal in remote coastal environments. Overall, these findings demonstrate that the relative importance of wet versus dry deposition is governed primarily by precipitation frequency. Where precipitation is frequent, wet deposition dominates PFCA removal, while in remote coastal regions with an increased number of dry periods, dry deposition acts continuously and can become the leading atmospheric removal pathway.

4.4.3 Gas-phase PFAS Measurements in Rural and Remote Field Sites

4.4.3.1 Active Air Sampling

During months when temperatures remained above -20°C in Tadoussac, an ADS was utilized to collect gas-phase PFCAs (n = 22). All five target analytes were quantitatively detected in at least one denuded air extract (Tables C-4 and C-11). The quantitative (>LOQ) detection frequencies of TFA and PFPrA were both 100%, with PFBA and PFHxA each being detected in only 5% of samples and PFPeA in 9% of samples (Figure C-5). In contrast to the temperature sampling limitations imposed at Tadoussac, daily temperatures remained above -20°C on Saturna Island and gas-phase denuder samples (n = 43) were collected for the entirety of the year-long sampling period. All target analytes were quantitatively detected in at least one denuded air extract while PFHxA remained below the LOD in every replicate (Tables C-4 and C-12). The quantitative (>LOQ) detection frequencies of TFA, PFPrA, PFBA, and PFPeA were 100%, 88%, 61%, and 14%, respectively (Figure C-6). As TFA and PFPrA have the highest detection frequencies, they will be the focus of this analysis for direct comparison to the Tadoussac observations.

At both sites, TFA was found to have the highest atmospheric abundance throughout the active air sampling period; however, PFPrA average mixing ratios exceeded TFA during two discrete sampling intervals: i) June 9 to July 13, 2022 (Tadoussac) and ii) January 18 to February 15, 2022 (Saturna Island). Environmental measurements of atmospheric pollutants, including gas-phase PFCA levels, are frequently positively skewed due to episodic emission events and transport variability.[87] As a result, such data are often well described by lognormal distributions and log-transformation is commonly applied in atmospheric chemistry to stabilize variance and improve adherence to normality assumptions.[87] Normality was assessed for both raw and log-transformed average mixing ratios of TFA and PFPrA at both field sites using the Shapiro-Wilk test. In the raw

data, a single high-concentration sampling interval for TFA at Saturna Island (May 13 to June 15, 2022) contributed to deviation from normality, consistent with episodic atmospheric variability. Following log-transformation, all four datasets (TFA and PFPrA at both sites) satisfied normality assumptions (Shapiro-Wilk, $p > 0.05$ in all cases). Statistical t-tests were then performed on the log-transformed values for the two discrete sampling intervals in which PFPrA exceeded TFA and no statistically significant differences were observed at either Tadoussac ($p = 0.26$) or Saturna Island ($p = 0.40$).

The TFA and PFPrA atmospheric mixing ratios at the Tadoussac site ranged from 11 to 109 ppqv and 6 to 157 ppqv, respectively (Table C-13). In the samples collected from Saturna Island, their mixing ratios ranged 14 to 304 ppqv and 0.4 to 64 ppqv, respectively (Table C-14). Here we present a tabulated comparison of selected atmospheric gas-phase measurements to the average range of concentrations found in this study and others (Table 4-2). At both Tadoussac and Saturna Island, TFA levels were generally lower than reported from Guelph, ON in 2000 and Toronto, ON in 2010[33,40], reflecting both spatial variability and the effects of established PFAS guidelines and regulatory controls implemented in Canada over the past two decades.[88,89] Overall, the average mixing ratios determined in this study at both field sites are on the same order of magnitude and are thus comparable to other studies characterizing the abundance of these PFCAs in North America (Table 4-2). The same seasonal trend for TFA was noted in the active air samples at both Tadoussac and Saturna Island (Figure 4-3) with higher mixing ratios occurring during the summer months, as was measured in the deposition samples. This is consistent with the relationship expected between atmospheric abundance and the magnitude of deposition fluxes.

In addition to overall atmospheric mixing ratios, seasonal variability was observed for TFA and PFPrA at both sites, consistent with precursor oxidation rather than changes in gas-particle

Table 4-2. Comparison of selected atmospheric gas-phase concentrations (pg m^{-3}) to average range of concentrations found in this study and others (-- indicates a compound was not measured). The sampling method for each study included here utilized an AAS, annular denuder, and filter (either quartz or glass). The asterisk (*) indicates a value which is reported as the sum of the gas-phase and particle-phase. Replicate values below the LOD in this study were substituted with half of that analyte's LOD when computing averages. Mean values that include sub-LOD replicates are *italicized* and the number of replicates below LOD are in parentheses.

		Gas-phase concentration (pg m^{-3})					
Location	**Date**	**TFA**	**PFPrA**	**PFBA**	**PFPeA**	**PFHxA**	**Reference**
Guelph, ON, Canada	Jan – Dec 2000	760*	--	--	--	--	Martin et al.[40]
Toronto, ON, Canada	Nov – Dec 2010	--	--	14.0	2.96	0.70	Ahrens et al.[33]
Beijing, China	April – Oct 2012	2593	--	--	--	--	Xia et al.[90]
Beijing, China	May 2012 – April 2013	1580	--	--	--	--	Wu et al.[18]
Beijing, China	June – Nov 2013	--	--	4.66	163	1.39	Wu et al.[63]
Lake Chaohu, China	Sept 2013 – Sept 2015	--	--	12.61	4.00	3.33	Liu et al.[91]
Beijing, China	April 2013 – April 2014	1396	--	--	--	--	Zhang et al.[92]
	April 2014 – April 2015	1617	--	--	--	--	
	April 2015 – April 2016	1058	--	--	--	--	
Tadoussac, QC, Canada	Oct 2021 – Oct 2022	76 – 495	55 – 863	*7 – 17* (21)	*6 – 29* (20)	*3 – 9* (21)	This study
Saturna Island, BC, Canada	Dec 2021 – Dec 22	132 – 1220	*45 – 286* (8)	*8 – 78* (17)	*4 – 17* (36)	*3 – 6* (43)	

partitioning. At Tadoussac, PFPrA exhibited higher atmospheric mixing ratios during the warmer sampling periods, with a noticeable increase during the June 9 to July 13, 2022, sampling period followed by a gradual decline later in the summer. This observation is consistent with enhanced summertime oxidation and increased formation of ultrashort- and short-chain PFCAs from volatile PFAS precursors under increased photochemical activity. For example, HFO-1234yf is a commonly used hydrofluoroolefin refrigerant in automobile air conditioners and has been shown to degrade into TFA.[93] Contrastingly, no obvious seasonal trend was observed for PFPrA at

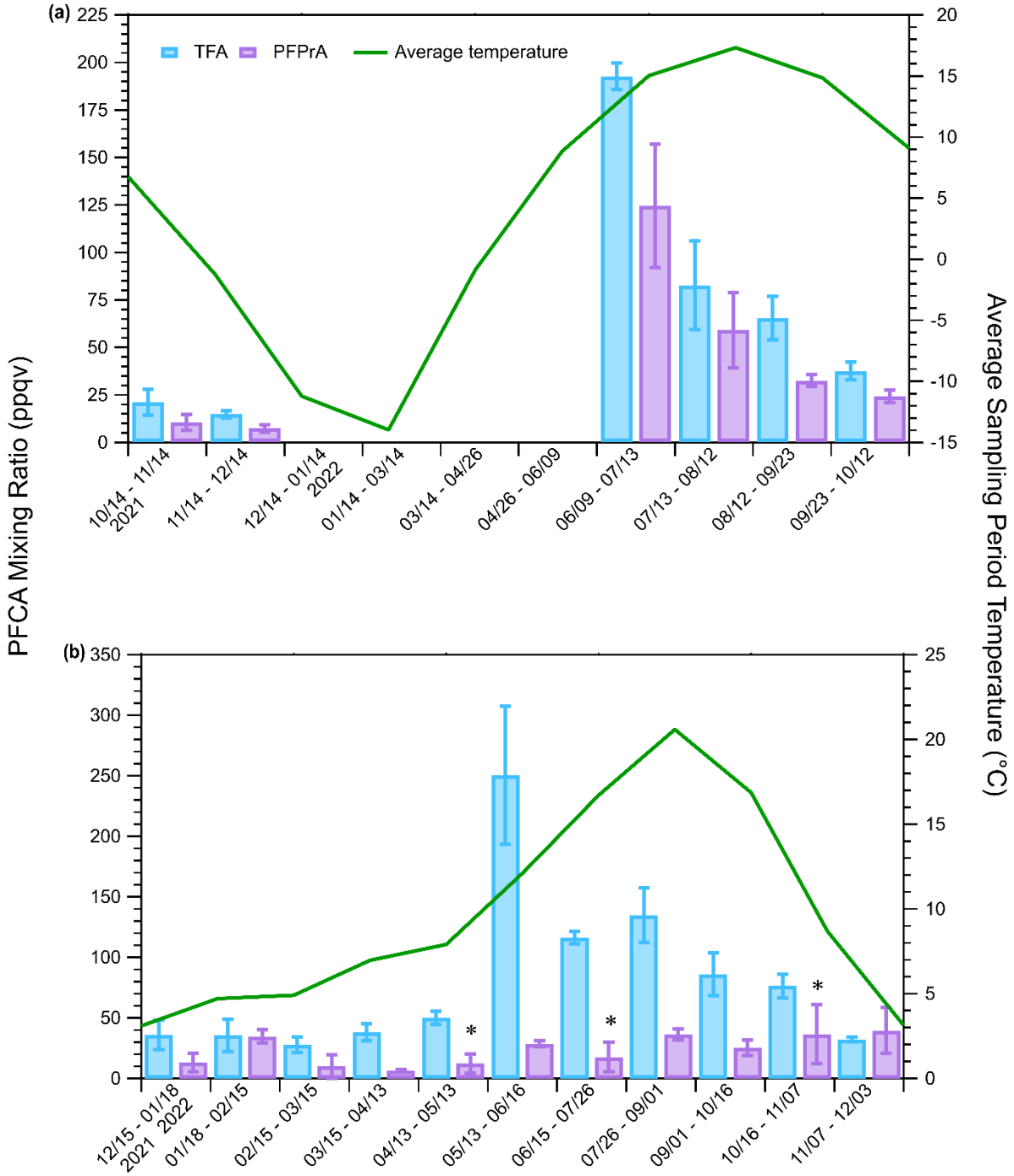

Figure 4-3. The average atmospheric mixes ratios (left y-axis, ppqv) for TFA (blue) and PFPrA (purple) at **(a)** Tadoussac and **(b)** Saturna Island. The green trace indicates the average temperature during each sampling interval (°C, right y-axis). The asterisks (*) indicate a sampling interval in which one of the denuder replicates sampled were <LOD and reported as half of that analyte's LOD to determine the overall average mixing ratio. The error bars are the associated uncertainties as described in Tables C-13 and C-14.

Saturna Island, where mixing ratios were generally lower and more variable, suggesting a reduced influence of regional precursor sources. These observations suggest that seasonal trends in ultrashort- and short-chain PFCAs are driven primarily by variations in precursor emissions and atmospheric oxidation processes rather than by gas-particle partitioning, as a modelling study has previously indicated that ≤C4 PFCAs exist predominantly in the gas-phase.[28] The differences between the measurements at both field sites suggest that local and regional precursor sources and atmospheric chemical processes can strongly affect the levels and temporal variability of C2 to C6 PFCA mixing ratios.

A closer look at PFPrA reveals site-specific differences and the potential factors driving them. The evident summertime enhancement at Tadoussac and the absence of one at Saturna Island highlights the limited understanding of PFPrA's fate in the atmosphere as well as the lack of time-resolved measurements for this compound. The episodic nature of increased PFPrA levels at Tadoussac suggests that both precursor oxidation and regional source influences may contribute to its atmospheric abundance. Notably, concurrently deployed PASs did not show a clear seasonal trend for PFPrA at either Tadoussac or Saturna Island but instead revealed a consistent spatial distribution. The highest PFPrA mixing ratios were found in urban Toronto, followed by rural Tadoussac, and then the lowest levels were reported at remote Saturna Island.[29] This suggests that gas-phase PFPrA may be site-dependent and influenced by precursor availability and proximity to nearby source emissions rather than by photochemical production alone. Given the differing temporal resolution of active and passive sampling approaches, comparing these datasets provides an opportunity to evaluate whether the observed PFPrA trends reflect short-term variability or longer-term seasonal trends. This motivates a direct comparison between active and passive air sampling approaches which we explore in the following section.

4.4.3.2 Intercomparison of Active and Passive Air Sampling Methods

Given the differing temporal resolution and collection principles of active and passive air sampling approaches, a method intercomparison is needed to assess how well each method captured the gas-phase PFCAs. Here we compare the AAS data described in Section 4.4.3.1 with concurrent passive air sampling results[29] to evaluate potential biases and methodological differences. At Saturna Island, there was only one passive air sampling period which lasted the entire sampling year; whereas at Tadoussac, there were three periods but only one that overlapped with the active air sampling reported in this study. To enable a direct comparison, the active air sampling period overlapping with those of passive air sampling were reported in Table 4-3 as weighted averages based on the number of days in each individual active air sampling interval (Figure 4-4). Notably, the active and passive air sampling periods at Saturna Island differed by only two days over the full year: December 15, 2021, to December 3, 2022, for active sampling, and December 14, 2021, to December 4, 2022, for passive sampling. This represents a negligible fraction (< 1%) of the sampling duration and so for comparison, the weighted average of the active air sampling data was used to align with the passive sampling interval. Ultimately, this approach accounts for differences in sampling duration and ensures each period contributes proportionally to the annual mean, allowing the active sampling data to reflect the same integrated timescale as the year-long passive air sampling measurements.

The previously reported PAS data[29] used in this intercomparison was generated using nylon-based chemisorption samplers, which differ fundamentally from equilibrium partitioning PASs (e.g., PUF- or XAD-based samplers) commonly applied in atmospheric POP monitoring.[94] In contrast to equilibrium-driven uptake, these samplers rely on irreversible chemisorption of gaseous acidic species onto a reactive nylon surface – where uptake can occur at terminal amino

Table 4-3. Comparison of average PFCA mixing ratios (ppqv) derived from PAS data[29] and AAS data. To directly compare the overlapping gas-phase measurements, the AAS results are reported as weighted averages based on the number of days in each sampling interval (Section C.4). Replicate values below the LOD in this active air study were substituted with half of that analyte's LOD when computing averages (Tables C-13 and C-14), likewise was done for the passive air samples. Mean values that include sub-LOD replicates are *italicized*.

		Average Atmospheric Mixing Ratio (ppqv)				
Tadoussac		**TFA**	**PFPrA**	**PFBA**	**PFPeA**	**PFHxA**
PAS	June 9 – Oct 12/22	42.46 (± 2.12)	3.89 (± 0.37)	3.03 (± 0.45)	2.24 (± 0.63)	*0.15* (± 0.00)
AAS (this study)	June 9 – Oct 12/22	76 (± 7)	63 (± 10)	*1.8* (± 2.2)	*1.3* (± 0.2)	*0.4* (± 0.8)
Saturna Island		**TFA**	**PFPrA**	**PFBA**	**PFPeA**	**PFHxA**
PAS	Dec 14/21 – Dec 4/22	10.98 (± 1.84)	*0.04* (± 0.00)	1.01 (± 0.05)	0.19 (± 0.09)	*0.04* (± 0.01)
AAS (this study)	Dec 15/21 – Dec 3/22	84 (± 11)	*25* (± 4)	*4* (± 1)	*0.7* (± 1.2)	*0.4* (± 0.8)

groups – enabling selective retention of PFCAs and reducing volatility-dependent sampling bias, particularly for highly mobile species such as TFA and PFPrA.[29] The sampling rate for TFA using nylon-based PASs was previously determined by controlled atmospheric chamber experiments, in which PASs were exposed to known amounts of TFA independently quantified using Na_2CO_3-coated annular denuders. A linear relationship between accumulated TFA mass on the nylon filters and time-weighted gas-phase concentrations were observed and the sampling rate was derived from the slope of this regression. This yielded a calibrated value of 113 ± 12 ng m^{-3} • hour per ng collected on the filter (R^2 = 0.81) and no evidence of sampler saturation over the tested exposure range.[29]

In the passive air samples, all target analytes were detected above the reported LODs, with their abundance decreasing with i) increasing chain length and ii) from rural to remote sampling sites.[29] When plotting the data presented in Table 4-3, active air samples against passive air samples

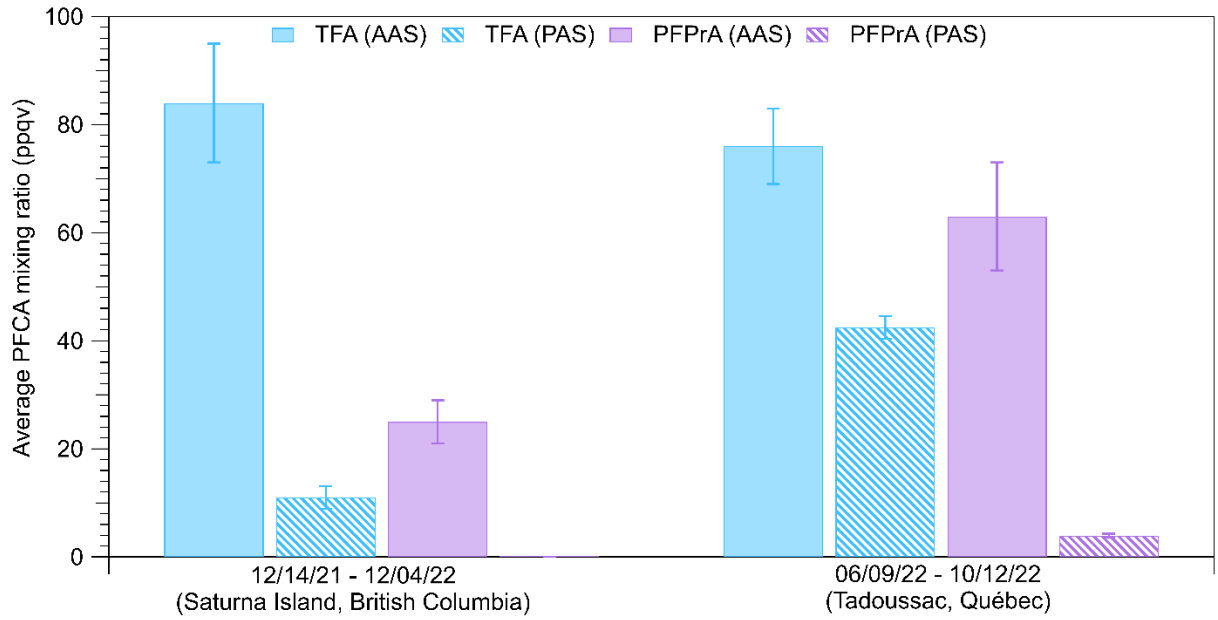

Figure 4-4. Comparison of average atmospheric mixing ratios of TFA (blue) and PFPrA (purple) measured in weighted active air samples (solid bars) and concurrently collected passive air samples (striped bars) at the Tadoussac and Saturna Island field sites. The error bars on the active air sampling data are the associated uncertainties as described in Tables C-11 and C-12, while those for the passive air sampling data can be found in the study by Vanhauwaert et al.[29]

(Figure C-7), PFBA, PFPeA, and PFHxA cluster near zero possibly due to the analytical challenges associated with measuring short-chain PFCAs or their low atmospheric concentrations.[19,63] In contrast, TFA and PFPrA are more scattered (though consistently above the 1:1 line), which may reflect their higher atmospheric abundances and/or episodic or site-specific variability more effectively captured by the denuders than the PASs. Overall, PFCA atmospheric mixing ratios were higher in the active denuder extracts than in the concurrent passive samples. To better understand the differences between active and passive measurements, it is important to consider the underlying mechanisms of gas-phase PFAS collection. Atmospheric PFAS sampling approaches differ not only in temporal resolution and air volume sampled[17], but also in the fundamental way by which these gas-phase compounds are collected. Traditional partitioning-based passive approaches, which use sorbents like PUF and XAD, were originally developed for semi-volatile POPs and rely

on equilibrium uptake of lower volatility species.[94] As a result, these samplers can display volatility-dependent biases where recoveries tend to decrease for more volatile PFAS and losses may occur during both sampling and sample preparation steps.[2,95]

Contrastingly, chemisorption-based approaches – such as those described here and in Vanhauwaert et al.[29] – use chemically selective surfaces to actively bind target analytes, reducing volatility-related losses and minimizing the influence of changes in sampling rate. Despite the advantages of using chemisorption-based passive air sampling, active air sampling with chemically selective coated annular denuders can still yield higher PFCA concentrations. This is because ADS sampling combines larger volumes of sampled air with reactive coatings or adsorptive surfaces – chosen for the volatility and chemical properties of target analytes.[38,92] This implies that they could potentially collect both terminal PFCAs and volatile precursors or reactive intermediates. Additionally, the instantaneous collection and minimal reliance on equilibrium-based partitioning in active methods may capture short-term/episodic spikes in concentration or site-specific variability that even chemisorption PASs could partially miss. Together with differences in sampled air volume and the instantaneous versus time-integrated nature of compound collection, these mechanistic differences help explain why active air sampling often yields higher PFCA concentrations than passive air sampling and why the relative bias can vary across compounds and sites.

To further evaluate potential systematic differences, the ratio of active to passive air sampling measurements were calculated from the data in Table 4-3 for each PFCA at both sites. Ratios greater than one indicate higher concentrations measured in the denuder extracts, while ratios below one indicates higher levels in the passive samples. At Tadoussac, TFA and PFBA had atmospheric mixing ratios close to unity (1.78, and 1.16, respectively), while PFHxA had a slightly

higher ratio of 3.13, suggesting mostly comparable collection efficiencies. Contrastingly, PFPrA had a substantially higher mixing ratio (~16), reflecting potential episodic events captured by the AASs and not by the PASs. Showing a ratio slightly below unity (~0.59), PFPeA observations were consistent with low-level variability or chemical differences between the samplers. At Saturna Island, all analytes had ratios above unity (TFA ~7.66; PFPrA ~583.75; PFBA ~4.16; PFPeA ~3.84; PFHxA ~8.75), indicating higher levels captured by active air sampling at this remote site. This likely reflects a combination of episodic long-range transport events and the ability of denuders to capture both terminal acids and volatile precursors. Overall, these comparisons suggest that differences between active and passive samplers can be both systematic and chemistry dependent.

Systematic differences can be influenced by the differing sampled air volume and temporal resolution, whereas chemistry-dependent differences reflect the sensitivity of the collection mechanisms – with denuders potentially capturing species that PASs do not efficiently collect. With ≤C4 PFCAs believed to exist predominantly in the gas-phase[28], denuder-based active sampling may collect and hydrolyze acid halides, resulting in higher concentrations of the corresponding carboxylic acids while passive samplers are unlikely to do so. D'Ambro et al.[77] note that the hydrolysis of acyl fluorides to their respective carboxylic acids has been measured in air and incorporated into atmospheric models[86,96-98], indicating that emitted acid fluorides may transform into acids during long-range transport. Although this process cannot be definitively confirmed with the available data, it provides a plausible explanation for higher levels observed in denuder extracts relative to passive samplers and represents a rarely considered factor in gas-phase PFAS sampling.

Overall, in comparing these two gas-phase sampling methods, active denuder sampling

consistently reported higher mixing ratios for TFA and PFPrA relative to passive nylon samplers, while differences for PFBA, PFPeA, and PFHxA were less consistent. To reconcile the differences between these methods, future PFAS sampling could deploy both sampling approaches concurrently across multiple sites and sampling intervals, enabling direct comparison under identical atmospheric conditions. Calculating analyte- and site-specific active/passive air sampling ratios, combined with targeted calibration to determine uptake efficiencies of passive samplers, could help quantify systematic biases and volatility-dependent limitations. Additionally, distinguishing between terminal acids and volatile precursors and intermediates, alongside consideration of meteorological data, could elucidate whether observed differences arise from sample chemistry, temporal resolution, or episodic atmospheric events. Together, these complementary approaches provide a more complete understanding of atmospheric PFCA distributions and can guide future monitoring of ultrashort- and short-chain PFCAs.

4.4.4 Atmospheric PFAS as a Potential Exposure Pathway in Whale Habitats

This study establishes that ultrashort- and short-chain PFCAs are present in both the gas phase and in wet and dry deposition within regions inhabited by endangered SLEBs and SRKWs. These findings indicate that the atmosphere acts as an active and recurring source of PFCA inputs to these estuarine and coastal ecosystems. Within the context of the Whales Initiative, which aims to reduce contaminant exposure and improve monitoring of stressors affecting endangered whale populations[99], these results contribute to the identification and quantification of a previously under-characterized PFCA exposure pathway to the whales. While PFAS contamination in marine mammals has been documented[100-102], the atmospheric contribution to this burden has remained poorly constrained, particularly for ultrashort-chain homologues such as TFA and PFPrA.

The deposition fluxes reported here indicate that both wet and dry deposition can deliver measurable PFCA inputs to surface waters. In this study, deposition concentrations ranged from below instrument detection limits up to 797 ng L^{-1} (TFA) and 327 ng L^{-1} (PFPrA) in wet deposition and, showing comparable or higher values, reaching up to 650 ng L^{-1} (TFA) and 1840 ng L^{-1} (PFPrA) in total deposition at Tadoussac. For context, in the St. Lawrence River watershed, a large-scale monitoring study of 447 water samples reported the mean concentration of Σ77PFAS to be approximately 12 ng L^{-1} (dominated by perfluorooctanesulfonic acid – PFOS, PFBA, and PFOA), with higher values (100 to 3600 ng L^{-1}) occurring near localized source regions such as airports and industrial sites.[103] In comparison, PFAS concentrations in deposition measured in this study frequently reach the low μg L^{-1} range, indicating that atmospheric inputs represent a chemically concentrated but episodic source of PFCA input to surface waters. In contrast, precipitation datasets from the broader Great Lakes Basin – used here as the closest well-characterized atmospheric proxy for the St. Lawrence – report PFAS concentrations (C4 to C12 PFCAs and PFOS) typically in the range of ~0.1 to several ng L^{-1}, occasionally reaching a maximum of 14 ng L^{-1} depending on compound class, location, and sampling year.[104] These datasets show declining trends for legacy compounds such as PFOS and PFOA, alongside an increasing relative contribution of short-chain PFAS, consistent with shifts in global production.[104]

Additionally, deposition concentrations ranged from below detection limits up to 2090 ng L^{-1} (TFA) and 1950 ng L^{-1} (PFPrA) in wet deposition and up to 1620 ng L^{-1} (TFA) and 2570 ng L^{-1} (PFPrA) in total deposition at Saturna Island. In the Pacific Northwest, surface water surveys from British Columbia and the Salish Sea region (including the Strait of Georgia and Puget Sound as a connected transboundary system) have reported total PFAS concentrations ranging from approximately 1.5 to 41 ng L^{-1}, with perfluoroheptanoic acid (C7 PFCA), PFOA, and PFOS

commonly detected.[105] These systems are influenced by urban runoff, wastewater discharge, and atmospheric deposition, and are often evaluated jointly with Puget Sound due to strong hydrological connectivity across the Salish Sea marine network.[106] Although direct rainwater PFAS measurements for the Strait of Georgia and Salish Sea are limited in the peer-reviewed literature, available regional studies and monitoring programs suggest that atmospheric deposition is a relevant but still incompletely quantified input pathway in this transboundary ecosystem. To our knowledge, comparable long-term rainwater datasets are not available for the Salish Sea region which highlights a key spatial and monitoring gap in coastal western North America. Taken together, these comparisons indicate that deposition-phase PFAS concentrations measured in this study are several orders of magnitude higher than concentrations typically observed in bulk precipitation datasets and receiving waters. This reinforces the role of atmospheric deposition as a concentrated input mechanism to terrestrial and aquatic ecosystems.

The deposition fluxes reported here therefore represent a direct, measurable atmospheric input to surfaces within whale habitats. Across both study sites, ultrashort-chain PFCAs dominated deposition profiles, consistent with their high atmospheric mobility – suggesting that the atmospheric input signal to these ecosystems is currently skewed toward highly mobile short-chain homologues rather than legacy long-chain PFAS. However, translating these fluxes into direct exposure estimates for whales requires further work linking atmospheric deposition to seawater concentrations, trophic transfer, and dietary intake. At present, inhalation exposure in air-breathing marine mammals remains poorly quantified and is likely underrepresented in current exposure assessments. However, theoretical frameworks for marine air-breathing organisms suggest that respiratory exchange can contribute to uptake of semi-volatile and volatile organic contaminants, particularly where gas-phase exposure occurs continuously (e.g., at the air-sea interface).[107] In

such systems, uptake and elimination are governed not only by lipid-water partitioning but also by air-blood partitioning and respiratory exchange dynamics.[107] This is relevant in the context of PFAS, as several short-chain PFCAs and their volatile precursors exhibit persistent gas-phase presence and atmospheric transport potential, providing a plausible route for inhalation exposure at the air-sea interface.[108] Nevertheless, at present, atmospheric deposition represents the most directly quantifiable atmospheric exposure pathway to aquatic systems[109] while inhalation exposure via the gas phase remains highly uncertain and is not currently supported by quantitative exposure or uptake data in marine mammals.[110]

Similarly, while atmospheric deposition provides a plausible input pathway to prey species via surface water contamination[111], insufficient information currently exists to quantify its contribution relative to other sources of PFAS exposure in marine food webs such as sediment interactions and trophic transfer efficiency.[112] Therefore, the findings of this study should be interpreted as a foundational step toward integrating atmospheric PFAS measurements into broader contaminant exposure frameworks for marine mammals, rather than as a complete exposure assessment. Within the context of the Whales Initiative, these results directly support the program's objectives of enhanced monitoring of contaminants in both air and water and provide quantitative constraints on atmospheric PFCA inputs to coastal ecosystems. More specifically, this study demonstrates variability in deposition and gas-phase measurements made across rural and remote systems and highlights the importance of precursor-driven formation and meteorological controls on atmospheric loading. However, linking these atmospheric inputs to biological uptake and health outcomes in whales remains a longer-term objective requiring integrated atmospheric and toxicological investigation. Collectively, these findings establish a quantitative basis for atmospheric PFCA deposition in sensitive marine ecosystems and provide a quantified

atmospheric input term relevant to the Whales Initiative, while downstream exposure pathways to whales via diet and inhalation cannot be quantitatively inferred from the present data.

4.5 Conclusions

In this study, we presented a new method to quantify the capture efficiency of PFPrA using Na_2CO_3-coated annular denuders and IC-CD. The capture efficiency for PFPrA was calculated to be 99.83 ± 0.03%, indicating that this PFCA is efficiently scrubbed from air. Vapour pressures of PFCAs have been found to decrease with increasing chain length while the pK_a for both long- and short-chain PFCAs vary only slightly from one another (0.5 to 0.9).[58-60] This indicates that it should be possible to sample long-chain PFCAs with equal or greater efficiency as compared to ultrashort-chain PFCAs such as PFPrA. This efficient sampling demonstrates that annular denuders represent a superior approach to sampling gas-phase PFCAs in the atmosphere as compared to commonly used methods that collect particles prior to the gas-phase and have been shown to be biased for strong atmospheric acids[113], including PFCAs.[33,114]

A potential methodological limitation is the inability to introduce internal standards during sampling. For deposition samples, the large volumes collected (often >1 to 2 L) would require impractically large quantities of isotopically labelled standards to achieve detectable signals, in contrast to the small aliquots (e.g., 700 µL) used during instrumental analysis. For denuder-based air sampling, the addition of internal standards during collection is similarly not feasible. However, this is not expected to significantly impact data quality, as quantitative capture and recovery of strong acid anions using carbonate-coated denuders has been well established in the literature[29,40] and is supported here by the high PFPrA collection efficiency.

Nevertheless, using these validated denuders alongside custom-built deposition samplers,

we quantified atmospheric mixing ratios and deposition fluxes of C2 to C6 PFCAs in samples collected from rural (Tadoussac) and remote (Saturna Island) field sites within endangered Canadian whale habitats. Across both gas-phase and deposition samples, TFA and PFPrA were consistently the most abundant and frequently detected compounds. Seasonal variations were evident for TFA at Tadoussac, with higher mixing ratios and deposition fluxes during the summer months, corresponding to enhanced photochemical oxidation of volatile precursors. In contrast, Saturna Island exhibited less pronounced seasonal trends which reflects lower precipitation and limited local and regional precursor inputs. At Tadoussac, PFPrA displayed episodic summertime peaks, highlighting the influence of local and regional precursor emissions, while no clear seasonal trend was observed at Saturna Island. These findings emphasize the importance of temporal resolution in capturing short-term variability, particularly for ultrashort-chain PFCAs.

This study also distinguished the contributions of wet and dry deposition to total atmospheric PFCA removal. At Tadoussac, wet deposition dominated atmospheric removal due to frequent precipitation and proximity to urban and industrial sources. Contrastingly, at the remote Saturna Island site, dry deposition contributed more substantially, consistent with the long-range transport of PFAS precursors and infrequent precipitation. These findings align with global modelling studies and support the broader understanding that precipitation frequency primarily governs the relative importance of wet versus dry deposition. An inter-method comparison of active versus passive air sampling revealed systematic and chemistry-dependent differences. Active air sampling utilizing denuders consistently captured higher levels of TFA and PFPrA, likely due to the combined collection of terminal acids and reactive precursors. Traditional PASs can underrepresent highly volatile species, while chemisorption PASs collects smaller air volumes via diffusion and may miss short-term or episodic atmospheric events. These differences highlight

the complementary value of active sampling for time-resolved and chemically comprehensive measurements.

Overall, this work demonstrates that ultrashort- and short-chain PFCAs are present in both rural and remote atmospheric environments, with site-specific influences of precursor emissions, photochemistry, and meteorology shaping their temporal and spatial distributions. The validated denuder methodology provides a robust tool for monitoring PFPrA and related compounds in sensitive habitats, enabling more accurate assessments of PFAS fate, transport, and potential exposure risks to endangered whale populations. By combining deposition measurements with gas-phase sampling, this work advances understanding of PFCA sources, atmospheric processes, and removal pathways, informing future monitoring strategies and environmental management efforts in vulnerable aquatic ecosystems.

4.6 References

1. Glüge, J.; Scheringer, M.; Cousins, I. T.; DeWitt, J. C.; Goldenman, G.; Herzke, D.; Lohmann, R.; Ng, C. A.; Trier, X.; Wang, Z. An overview of the uses of per-and polyfluoroalkyl substances (PFAS). *Environ. Sci.: Process. Impacts.* **2020**, *22*(12), 2345–2373.

2. Ahrens, L.; Shoeib, M.; Harner, T.; Lane, D.; Reiner, E. J. Comparison of Annular Diffusion Denuder and High Volume Air Samplers for Measuring Per- and Polyfluoroalkyl Substances in the Atmosphere. *Anal. Chem.* **2011**, *83*(24), 9622–9628.

3. Tian, Y.; Yao, Y.; Chang, S.; Zhao, Z.; Zhao, Y.; Yuan, X.; Wu, F.; Sun, H. Occurrence and phase distribution of neutral and ionizable per-and polyfluoroalkyl substances (PFASs) in the atmosphere and plant leaves around landfills: a case study in Tianjin, China. *Environ. Sci. Technol.* **2018**, *52*(3), 1301–1310.

4. Cousins, I. T.; DeWitt, J. C.; Glüge, J.; Goldenman, G.; Herzke, D.; Lohmann, R.; Ng, C. A.; Scheringer, M.; Wang, Z. The high persistence of PFAS is sufficient for their management as a chemical class. *Environ. Sci.: Process. Impacts.* **2020**, *22*(12), 2307–2312.

5. Pérez, F.; Nadal, M.; Navarro-Ortega, A.; Fàbrega, F.; Domingo, J. L.; Barceló, D.; Farré, M. Accumulation of perfluoroalkyl substances in human tissues. *Environ. Int.* **2013**, *59*, 354–362.

6. Valdersnes, S.; Nilsen, B. M.; Breivik, J. F.; Borge, A.; Maage, A. Geographical trends of PFAS in cod livers along the Norwegian coast. *PloS one*, **2017**, *12*(5), e0177947.

7. Tomy, G. T.; Budakowski, W.; Halldorson, T.; Helm, P. A.; Stern, G. A.; Friesen, K.; Pepper, K.; Tittlemier, S. A.; Fisk, A. T. Fluorinated organic compounds in an eastern Arctic marine food web. *Environ. Sci. Technol.* **2004**, *38*(24), 6475–6481.

8. Butt, C. M.; Berger, U.; Bossi, R.; Tomy, G. T. Levels and trends of poly-and perfluorinated compounds in the arctic environment. *Sci. Total Environ.* **2010**, *408*(15), 2936–2965.

9. United Nations Environment Programme. Governments Unite to Step-Up Reduction on Global DDT Reliance and Add Nine New Chemicals under International Treaty. **2009**.

10. Vierke, L.; Staude, C.; Biegel-Engler, A.; Drost, W.; Schulte, C. Perfluorooctanoic acid (PFOA)—main concerns and regulatory developments in Europe from an environmental point of view. *Environ. Sci. Eur.* **2012**, *24*(1), 16.

11. Longpré, D.; Lorusso, L.; Levicki, C.; Carrier, R.; Cureton, P. PFOS, PFOA, LC-PFCAS, and certain other PFAS: A focus on Canadian guidelines and guidance for contaminated sites management. *Environ. Technol. Innov.* **2020**, *18*, 100752.

12. Zhang, W.; Liang, Y. The wide presence of fluorinated compounds in common chemical products and the environment: A review. *Environmental Science and Pollution Research*, **2023**, *30*(50), 108393–108410.

13. Yeung, L. W.; Dassuncao, C.; Mabury, S.; Sunderland, E. M.; Zhang, X.; Lohmann, R. Vertical profiles, sources, and transport of PFASs in the Arctic Ocean. *Environ. Sci. Technol.* **2017**, *51*(12), 6735–6744.

14. Solomon, K. R.; Velders, G. J.; Wilson, S. R.; Madronich, S.; Longstreth, J.; Aucamp, P. J.; Bornman, J. F. Sources, fates, toxicity, and risks of trifluoroacetic acid and its salts: Relevance to substances regulated under the Montreal and Kyoto Protocols. *J. Toxicol. Environ. Health, Part B.* **2016**, *19*(7), 289–304.

15. Sun, M.; Cui, J. N.; Guo, J.; Zhai, Z.; Zuo, P.; Zhang, J. Fluorochemicals biodegradation as a potential source of trifluoroacetic acid (TFA) to the environment. *Chemosphere*, **2020**, *254*, 126894.

16. Brendel, S.; Fetter, É.; Staude, C.; Vierke, L.; Biegel-Engler, A. Short-chain perfluoroalkyl acids: environmental concerns and a regulatory strategy under REACH. *Environ. Sci. Eur.* **2018**, *30*(1), 9.

17. Vierke, L.; Ahrens, L.; Shoeib, M.; Reiner, E. J.; Guo, R.; Palm, W.; Ebinghaus, R.; Harner, T. Air concentrations and particle–gas partitioning of polyfluoroalkyl compounds at a wastewater treatment plant. *Environ. Chem.* **2011**, *8*(4), 363. https://doi.org/10.1071/en10133.

18. Wu, J.; Martin, J. W.; Zhai, Z.; Lu, K.; Li, L.; Fang, X.; Jin, H.; Hu, J.; Zhang, J. Airborne trifluoroacetic acid and its fraction from the degradation of HFC-134a in Beijing, China. *Environ. Sci. Technol.* **2014**, *48*(7), 3675–3681.

19. Scott, B.; Spencer, C.; Mabury, S. A.; & Muir, D. C. Poly and perfluorinated carboxylates in North American precipitation. *Environ. Sci. Technol.* **2006**, *40*(23), 7167–7174. https://doi.org/10.1021/es061403n .

20. Pike, K. A.; Edmiston, P. L.; Morrison, J. J.; Faust, J. A. Correlation analysis of perfluoroalkyl substances in regional US precipitation events. *Water Res.* **2021**, *190*, 116685.

21. Shimizu, M. S.; Mott, R.; Potter, A.; Zhou, J.; Baumann, K.; Surratt, J. D.; Turpin, B.; Avery, G. B.; Harfmann, J.; Kieber, R. J.; Mead, R. N. Atmospheric deposition and annual flux of legacy perfluoroalkyl substances and replacement perfluoroalkyl ether carboxylic acids in Wilmington, NC, USA. *Environ. Sci. Technol. Lett.* **2021**, *8*(5), 366–372.

22. Wang, S.; Lin, X.; Li, Q.; Li, Y.; Yamazaki, E.; Yamashita, N.; Wang, X. Particle size distribution, wet deposition and scavenging effect of per-and polyfluoroalkyl

substances (PFASs) in the atmosphere from a subtropical city of China. *Sci. Total Environ.* **2022**, *823*, 153528.

23. Kwok, K. Y.; Taniyasu, S.; Yeung, L. W. Y.; Murphy, M. B.; Lam, P. K. S.; Horii, Y.; Kannan, K.; Petrick, G.; Sinha, R. K.; Yamashita, N. Flux of perfluorinated chemicals through wet deposition in Japan, the United States, and several other countries. *Environ. Sci. Technol.* **2010**, *44*(18), 7043−7049.

24. Persaud, D.; Joudan, S.; VandenBoer, T. C.; Young, C. J. Atmospheric removal of trifluoroacetic acid by dry and wet deposition: a multiyear analysis in Toronto. *Environ. Sci. Technol. Lett*. **2026**, *13*(2), 261–267. doi: 10.1021/acs.estlett.5c01100.

25. Persaud, D.; VandenBoer, T. C.; Place, B. K.; Edwards, K. A.; Ziegler, S. E.; Spencer, C.; De Silva, A. O.; Young, C. J. The Occurrence of Legacy Perfluoroalkyl Substances (PFAS) Deposited along a Latitudinal Transect in Newfoundland and Labrador, Canada. **2026**. *Just submitted*.

26. Grantz, D. A.; Garner, J. H. B.; Johnson, D. W. Ecological effects of particulate matter. *Environ. Int.* **2003**, *29*(2–3), 213–239.

27. Lovett, G. M.; Kinsman, J. D. Atmospheric pollutant deposition to high-elevation ecosystems. *Atmos. Environ. Part A Gen. Top.* **1990**, *24*(11), 2767−2786.

28. Tao, Y.; VandenBoer, T. C.; Ye, R.; Young, C. J. Exploring controls on perfluorocarboxylic acid (PFCA) gas–particle partitioning using a model with observational constraints. *Environ. Sci.: Process. Impacts.* **2023**, *25*(2), 264–276.

29. Vanhauwaert, E.; Carmichael, L.; Nistorescu, I.; Crilley, L. R.; Shunthirasingham, C.; Hung, H.; Young, C. J.; VandenBoer, T. C. Selective ultra-trace atmospheric passive sampling of gaseous perfluoroalkyl carboxylic acids. *Environ. Sci.: Process. Impacts.* **2025**, *27*(9), 2785–2797.

30. Shoeib, M.; Harner, T.; Lee, S. C.; Lane, D.; Zhu, J. Sorbent impregnated Polyurethane Foam Disk for Passive Air Sampling of Volatile Fluorinated Chemicals. *Anal. Chem.* **2008**, *80*(3), 675–682.

31. Bytnerowicz, A.; Sanz, M.; Arbaugh, M.; Padgett, P.; Jones, D.; Davila, A. Passive Sampler for Monitoring Ambient Nitric Acid (HNO3) and Nitrous Acid (HNO3) Concentrations. *Atmos. Environ.* **2005**, *39*(14), 2655–2660. https://doi.org/10.1016/j.atmosenv.2005.01.018.

32. Galarneau, E.; Bidleman, T. F. Modelling the temperature-induced blow-off and blow-on artefacts in filter-sorbent measurements of semivolatile substances. *Atmos. Environ.* **2006**, *40*(23), 4258−4268.

33. Ahrens, L.; Harner, T.; Shoeib, M.; Lane, D. A.; Murphy, J. G. Improved characterization of gas-particle partitioning for per- and polyfluoroalkyl substances in the atmosphere using annular diffusion denuder samplers. *Environ. Sci. Technol.* **2012**, *46*(13), 7199−7206.

34. Young, C. J.; VandenBoer, T. C. Separations and Selectivity for Measurements of Atmospheric PFAS, *Sep. Sci.* **2023**, *2*, 12–15.

35. Lane, D. A.; Johnson, N. D.; Barton, S. C.; Thomas, G. H. S.; Schroeder, W. H. Development and evaluation of a novel gas and particle sampler for semivolatile chlorinated organic compounds in ambient air. *Environ. Sci. Technol.* **1988**, *22*(28), 941−947.

36. Young, C. J.; Joudan, S.; Tao, Y.; Wentzell, J. J.; Liggio, J. High time resolution ambient observations of gas-phase perfluoroalkyl carboxylic acids: implications for atmospheric sources. *Environ. Sci. Technol. Lett.* **2024**, *11*(12), 1348–1354.

37. Al Amin, M.; Sobhani, Z.; Liu, Y.; Dharmaraja, R.; Chadalavada, S.; Naidu, R.; Chalker, J. M.; Fang, C. Recent advances in the analysis of per-and polyfluoroalkyl substances (PFAS) - A review. *Environ. Technol. Innov.* **2020**, *19*, 100879.

38. Ye, R.; Di Lorenzo, R. A.; Clouthier, J. T.; Young, C. J.; VandenBoer, T. C. A rapid derivatization for quantitation of perfluorinated carboxylic acids from aqueous matrices by gas chromatography–mass spectrometry. *Anal. Chem.* **2023**, *95*(19), 7648–7655.

39. Stróżyńska, M.; Schuhen, K. Extraction and derivatization for perfluorocarboxylic acids in liquid and solid matrices: A review. *Anal. Sci. Adv.* **2021**, *2*(7-8), 343–353.

40. Martin, J. W.; Madbury, S. A.; Wong, C. S.; Noventa, F.; Solomon, K. R.; Alaee, M.; Muir, D. C. Airborne Haloacetic acids. *Environ. Sci. Technol.* **2003**, *37*(13), 2889–2897.

41. Barron, L.; Paull, B. Simultaneous determination of trace oxyhalides and haloacetic acids using suppressed ion chromatography-electrospray mass spectrometry. *Talanta*, **2006**, *69*(3), 621–630.

42. Cloutheir, J.; VandenBoer, T. C.; Young, C. J. Direct-inject suppressed ion chromatography-mass spectrometry method with online preconcentration for short- and ultrashort-chain perfluoroakyl carboxylic acids in fresh water. *Anal. Methods.* **2026**, *in press*, https://doi.org/10.1039/D5AY02105G

43. Joudan, S.; Liggio, J.; Wentzell, J.; Clouthier, J.; Seoh, NY.; Edwards, P.; VandenBoer, T. C.; Young, C. J. Continuous measurements of atmospheric monochloroacetic acid: Evidence of photochemical formation. *ChemRxiv*. **2025,** doi:10.26434/chemrxiv-2025-1z3jw. *This content is a preprint and has not been peer-reviewed.*

44. Wu, S.; Anumol, T.; Gandhi, J.; Snyder, S. A. Analysis of haloacetic acids, bromate, and dalapon in natural waters by ion chromatography–tandem mass spectrometry. *J. Chromatogr. A. 1487*, **2017**, 100–107.

45. Zhang, X.; Saini, C.; Pohl, C.; Liu, Y. Fast determination of nine haloacetic acids, bromate and dalapon in drinking water samples using ion chromatography–electrospray tandem mass spectrometry. *J. Chromatogr. A.* **2020**, *1621*, 461052.

46. Thackray, C. P.; Selin, N. E.; Young, C. J. A global atmospheric chemistry model for the fate and transport of PFCAs and their precursors. *Environ. Sci.: Process. Impacts.* **2020**, *22*(2), 285–293. https://doi.org/10.1039/c9em00326f.

47. Idjaton, B. I.; Togola, A.; Ghestem, J. P.; Kastler, L.; Bristeau, S.; Ronteltap, M.; Colombano, S.; Devau, N.; Lions, J.; van Hulle-busch, E. D. Determination of Organic Fluorinated Compounds Content in Complex Samples Through Combustion Ion Chromatography Methods: A Way to Define a "Total Per- and Polyfluoroalkyl Substances (PFAS)" Parameter?. *Sci. Total Environ.* **2024,** *932,* 172589. doi: 10.1016/j.scitotenv.2024.172589.

48. Skedung, L.; Savvidou, E.; Schellenberger, S.; Reimann, A.; Cousins, I. T.; Benskin, J. P. Identification and Quantification of Fluorinated Polymers in Consumer Products by Combustion Ion Chromatography and Pyrolysis-Gas Chromatography-Mass Spectrometry. *Environ. Sci.: Process. Impacts.* **2024,** *26*(1), 82–93. doi: 10.1039/D3EM00438D.

49. Fisheries and Oceans Canada. Research to support the protection of whales in Canadian waters. *Government of Canada*, Fisheries and Oceans Canada, Communications Branch. **2022**. Retrieved from: https://www.dfo-mpo.gc.ca/species-especes/mammals-mammiferes/whales-baleines/research-recherche-eng.html.

50. Colussi, A. A.; Persaud, D.; Lao, M.; Place, B. K.; Hems, R. F.; Ziegler, S. E.; Edwards, K. A.; Young, C. J.; VandenBoer, T. C. Cost-effective off-grid automatic precipitation samplers for pollutant and biogeochemical atmospheric deposition. *Atmos. Meas. Tech.* **2024**, *17*(12), 3697–3718.

51. Winberry Jr., W. T.; Ellestad, T.; Stevens, B. Compendium of Methods for the Determination of Inorganic Compounds in Ambient Air: Method IO-4.2, Determination of Reactive Acidic and Basic Gases and Strong Acidity of Atmospheric Fine Particles (<2.5µm) in Ambient Air. Center for Environmental Research Information Office of Research and Development, United States Environmental Protection Agency. **1999**. Retrieved from: https://www.epa.gov/sites/default/files/2019-11/documents/mthd-4-2.pdf.

52. Macinnis, J. J.; VandenBoer, T. C.; Young, C. J. Development of a gas phase source for perfluoroalkyl acids to examine atmospheric sampling methods. Analyst, **2016**, *141*(12), 3765−3775.

53. Lao, M.; Crilley, L. R.; Furlani, T. C.; Bourgeois, I.; Neuman, J. A.; Rollins, A. W.; Veres P. R.; Washenfelder, R. A.; Womack, C. C.; Young, C. J.; VandenBoer, T. C. A portable, robust, and tunable calibration source for gas-phase nitrous acid (HONO). *Atmos. Meas. Tech.* **2020**, *13*(11), 5837−5890.

54. Barrett, H.; Du, X.; Houde, M.; Lair, S.; Verreault, J.; Peng, H. Suspect and nontarget screening revealed class-specific temporal trends (2000–2017) of poly-and perfluoroalkyl substances in St. Lawrence Beluga Whales. *Environ. Sci. Technol.* **2021**, *55*(3), 1659–1671.

55. Olsen, A. R.; Voldner, E. C.; Bigelow, D. S.; Chan, W. H.; Clark, T. L.; Lusis, M. A.; Misra, P. K.; Vet, R. J. Unified wet deposition data summaries for North America: data summary procedures and results for 1980–1986. *Atmos. Environ. Part A. Gen. Top.* **1990**, *24*(3), 661–672.

56. Vingarzan, R.; Thomson, B. Temporal variation in daily concentrations of ozone and acid-related substances at Saturna Island, British Columbia. *J. Air Waste Manage. Assoc.* **2004**, *54*(4), 459–472.

57. Lee, K.; Alava, J. J.; Cottrell, P.; Cottrell, L.; Grace, R.; Zysk, I.; Raverty, S. Emerging contaminants and new POPs (PFAS and HBCDD) in endangered Southern Resident and Bigg's (Transient) killer whales (Orcinus orca): In utero maternal transfer and pollution management implications. *Environ. Sci. Technol.* **2022**, *57*(1), 360−374.

58. Moroi, Y.; Yano, H.; Shibata, O.; Yonemitsu, T. Determination of Acidity Constants of Perfluoroalkanoic Acids. *Bull. Chem. Soc. Jpn.* **2001**, *74*(4), 667–672.

59. Goss, K. U. The pKa values of PFOA and other highly fluorinated carboxylic acids. *Environ. Sci. Technol.* **2008**, *42*(2), 456–458.

60. Wang, Z.; MacLeod, M.; Cousins, I. T.; Scheringer, M.; Hungerbühler, K. Using COSMOtherm to predict physicochemical properties of poly-and perfluorinated alkyl substances (PFASs). *Environ. Chem.* **2011**, *8*(4), 389–398.

61. Lath, S.; Knight, E. M.; Navarro, D. A.; Kookana, R. S.; McLaughlin, M. J. Sorption of PFOA onto different laboratory materials: Filter membranes and centrifuge tubes. *Chemosphere.* **2019**, *222*, 671−678.

62. Furlani, T. C.; Ye, R.; Stewart, J.; Crilley, L. R.; Edwards P. M.; Kahan, T. F. Development and validation of a new in-situ technique to measure total gaseous chlorine in air. *Atmos. Meas. Tech.* **2022**, *16*(1), 181–193.

63. Wu, J.; Jin, H.; Li, L.; Zhai, Z.; Martin, J. W.; Hu, J.; Peng, L.; Wu, P. Atmospheric perfluoroalkyl acid occurrence and isomer profiles in Beijing, China. *Environ. Pollut.* **2019**, *255*, 113129.

64. Berg, M.; Müller, S. R.; Mühlemann, J.; Wiedmer, A.; Schwarzenbach, R. P. Concentrations and mass fluxes of chloroacetic acids and trifluoroacetic acid in rain and natural waters in Switzerland. *Environ. Sci. Technol*. **2000**, *34*(13), 2675–2683.

65. Wang, Q.; Wang, X.; Ding, X. Rainwater trifluoroacetic acid (TFA) in Guangzhou, South China: Levels, wet deposition fluxes and source implication. *Sci. Total. Environ.* **2014**, *468*, 272–279.

66. Scott, B. F.; MacTavish, D.; Spencer, C.; Strachan, W. M.; Muir, D. C. Haloacetic acids in Canadian lake waters and precipitation. *Environ. Sci. Technol.* **2000**, *34*(20), 4266–4272.

67. Scott, B. F.; Spencer, C.; Martin, J. W.; Barra, R.; Bootsma, H. A.; Jones, K. C.; Johnston, A. E.; Muir, D. C. G. Comparison of haloacetic acids in the environment of the northern and southern hemispheres. *Environ. Sci. Technol.* **2005**, *39*(22), 8664–8670.

68. Dreyer, A.; Matthias, V.; Weinberg, I.; Ebinghaus, R. Wet deposition of poly-and perfluorinated compounds in Northern Germany. *Environ. Pollut.* **2010**, *158*(5), 1221–1227.

69. Wang, Q.; Wang, X.; Ding, X. Rainwater trifluoroacetic acid (TFA) in Guangzhou, South China: Levels, wet deposition fluxes and source implication. *Sci. Total Environ.* **2014**, *468*, 272–279.

70. Chen, H.; Zhang, L.; Li, M.; Yao, Y.; Zhao, Z.; Munoz, G.; Sun, H. Per-and polyfluoroalkyl substances (PFASs) in precipitation from mainland China: Contributions of unknown precursors and short-chain (C2C3) perfluoroalkyl carboxylic acids. *Water Res.* **2019**, *153*, 169–177.

71. Freeling, F.; Behringer, D.; Heydel, F.; Scheurer, M.; Ternes, T. A.; Nödler, K. Trifluoroacetate in precipitation: deriving a benchmark data set. *Environ. Sci. Technol.* **2020**, *54*(18), 11210–11219.

72. Pfotenhauer, D.; Sellers, E.; Olson, M.; Praedel, K.; Shafer, M. PFAS concentrations and deposition in precipitation: An intensive 5-month study at National Atmospheric Deposition Program–National trends sites (NADP-NTN) across Wisconsin, USA. *Atmos. Environ.* **2022**, *291*, 119368.

73. Henne, S.; Storck, F. R.; Wöhrnschimmel, H.; Leuenberger, M.; Vollmer, M. K.; Reimann, S. Trifluoroacetate (TFA) in precipitation and surface waters in Switzerland: trends, source attribution, and budget. *Atmos. Chem. Phys.* **2025**, *25*(23), 18157–18186.

74. Hartz, W. F.; Björnsdotter, M. K.; Yeung, L.W.; Humby, J. D.; Eckhardt, S.; Evangeliou, N.; Ericson Jogsten, I.; Karrman, A.; Kallenborn, R. Sources and seasonal variations of per-and polyfluoroalkyl substances (PFAS) in surface snow in the arctic. *Environ. Sci. Technol.* **2024**, *58*(49), 21817–21828.

75. Pickard, H. M.; Criscitiello, A. S.; Spencer, C.; Sharp, M. J.; Muir, D. C.; De Silva, A. O.; Young, C. J. Continuous non-marine inputs of per-and polyfluoroalkyl substances to the High Arctic: a multi-decadal temporal record. *Atmos. Chem. Phys.* **2018**, *18*(7), 5045–5058.

76. Hartz, W. F.; Björnsdotter, M. K.; Yeung, L. W.; Hodson, A.; Thomas, E. R.; Humby, J. D.; Day, C.; Jogsten, I. E.; Kärrman, A.; Kallenborn, R. Levels and distribution profiles of Per-and Polyfluoroalkyl Substances (PFAS) in a high Arctic Svalbard ice core. *Sci. Total Environ.* **2023**, *871*, 161830.

77. D'Ambro, E. L.; Pye, H. O.; Bash, J. O.; Bowyer, J.; Allen, C.; Efstathiou, C.; Gilliam, R. C.; Reynolds, L.; Talgo, K.; Murphy, B. N. Characterizing the air emissions, transport, and deposition of per-and polyfluoroalkyl substances from a fluoropolymer manufacturing facility. *Environ. Sci. Technol.* **2021**, *55*(2), 862–870.

78. Vet, R.; Artz, R. S.; Carou, S.; Shaw, M.; Ro, C. U.; Aas, W.; Baker, A.; Bowersox, V. C.; Dentener, F.; Galy-Lacaux, C.; Hou, A. A global assessment of precipitation chemistry and deposition of sulfur, nitrogen, sea salt, base cations, organic acids, acidity and pH, and phosphorus. *Atmos. Environ.* **2014**, *93*, 3–100.

79. Gewurtz, S. B.; Auyeung, A. S.; De Silva, A. O.; Teslic, S.; Smyth, S. A. Per-and polyfluoroalkyl substances (PFAS) in Canadian municipal wastewater and biosolids: Recent patterns and time trends 2009 to 2021. *Sci. Total Environ.* **2024**, *912*, 168638.

80. Department of National Defence. Statement from the minister of national defence on pfas at CFB Bagotville. *Government of Canada*. **2023**. Retrieved from: https://www.canada.ca/en/department-national-defence/news/2023/07/statement-from-the-minister-of-national-defence-on-pfas-at-cfb-bagotville.html

81. Piekarz, A. M.; Primbs, T.; Field, J. A.; Barofsky, D. F.; Simonich, S. Semivolatile fluorinated organic compounds in Asian and western US air masses. *Environ. Sci. Technol.* **2007**, *41*(24), 8248–8255.

82. Primbs, T.; Simonich, S.; Schmedding, D.; Wilson, G.; Jaffe, D.; Takami, A.; Kato, S.; Hatakeyama, S.; Kajii, Y. Atmospheric outflow of anthropogenic semivolatile organic compounds from East Asia in spring 2004. *Environ. Sci. Technol.* **2007**, *41*(10), 3551–3558.

83. Primbs, T.; Piekarz, A.; Wilson, G.; Schmedding, D.; Higginbotham, C.; Field, J.; Simonich, S. Influence of Asian and western US urban areas and fires on the atmospheric transport of PAHs, PCBs, and FTOHs in the western US. *Environ. Sci. Technol.* **2008**, *42*(17), 6385.

84. Sha, B.; Johansson, J. H.; Tunved, P.; Bohlin-Nizzetto, P.; Cousins, I. T.; Salter, M. E. Sea spray aerosol (SSA) as a source of perfluoroalkyl acids (PFAAs) to the atmosphere: field evidence from long-term air monitoring. *Environ. Sci. Technol.* **2021**, *56*(1), 228–238.

85. Environmental Working Group. PFAS Contamination in the U.S. [ArcGIS]. **2022**. Retrieved from: https://www.ewg.org/interactive-maps/pfas_contamination/map/.

86. Kotamarthi, V. R.; Rodriguez, J. M.; Ko, M. K. W.; Tromp, T. K.; Sze, N. D.; Prather, M. J. Trifluoroacetic acid from degradation of HCFCs and HFCs: A three-dimensional modeling study. *J. Geophys. Res. Atmos.* **1998**, *103*(D5), 5747−5758.

87. Ott, W. R. A physical explanation of the lognormality of pollutant concentrations. *J. Air Waste Manage.* **1990**, *40*(10), 1378−1383.

88. Environment and Climate Change Canada. Risk Management Approach for Per- and Polyfluoroalkyl Substances (PFAS), Excluding Fluoropolymers. *Government of Canada*, **2025**. Retrieved from: https://www.canada.ca/en/environment-climate-change/services/evaluating-existing-substances/risk-management-approach-per-polyfluoroalkyl-substances.html.

89. Environment and Climate Change Canada. State of Per- and Polyfluoroalkyl Substances (PFAS) Report. *Government of Canada*, **2025**. Retrieved from: https://www.canada.ca/en/environment-climate-change/services/evaluating-existing-substances/state-per-polyfluoroalkyl-substances-report.html.

90. Xia, H. U.; Jing, W. U.; Zi-Han, Z. H. A. I. Determination of gaseous and particulate trifluoroacetic acid in atmosphere environmental samples by gas chromatography-mass spectrometry. *Chin. J. Anal. Chem.* **2013**, *41*(8), 1140–1145.

91. Liu, W.; He, W.; Wu, J.; Wu, W.; Xu, F. Distribution, partitioning and inhalation exposure of perfluoroalkyl acids (PFAAs) in urban and rural air near Lake Chaohu, China. *Environ. Pollut.* **2018**, *243*, 143−151.

92. Zhang, B.; Zhai, Z.; Zhang, J. Distribution of trifluoroacetic acid in gas and particulate phases in Beijing from 2013 to 2016. *Sci. Total Environ.* **2018**, *634*, 471–477.

93. Luecken, D. J.; Waterland, R. L.; Papasavva, S.; Taddonio, K. N.; Hutzell, W. T.; Rugh, J. P.; Andersen, S. O. Ozone and TFA impacts in North America from degradation of 2, 3, 3, 3-tetrafluoropropene (HFO-1234yf), a potential greenhouse gas replacement. *Environ. Sci. Technol.* **2010**, *44*(1), 343−348.

94. Martin, J. W.; Muir, D. C. G.; Moody, C. A.; Ellis, D. A.; Kwan, W.; Solomon, K. R.; Mabury, S. A. Collection of Airborne Fluorinated Organics and Analysis by Gas Chromatography/Chemical Ionization Mass Spectrometry. *Anal. Chem.* **2002**, *74*(3), 584–590.

95. Jahnke, A.; Ahrens, L.; Ebinghaus, R.; Berger, U.; Barber, J. L.; Temme, C. An Improved Method for the Analysis of Volatile Polyfluorinated Alkyl Substances in Environmental Air Samples. *Anal Bioanal. Chem.* **2007,** *387*(3), 965–975. https://doi.org/10.1007/s00216-006-1008-y.

96. Kazil, J.; McKeen, S.; Kim, S. W.; Ahmadov, R.; Grell, G. A.; Talukdar, R. K.; Ravishankara, A. R. Deposition and rainwater concentrations of trifluoroacetic acid in the United States from the use of HFO-1234yf. *J. Geophys. Res.* **2014**, *119*(24), 14059−14079.

97. Thackray, C. P.; Selin, N. E. Uncertainty and variability in atmospheric formation of PFCAs from fluorotelomer precursors. *Atmos. Chem. Phys.* **2017**, *17*(7), 4585–4597.

98. Wang, Z.; Wang, Y.; Li, J.; Henne, S.; Zhang, B.; Hu, J.; Zhang, J. Impacts of the degradation of 2, 3, 3, 3-tetrafluoropropene into trifluoroacetic acid from its application in automobile air conditioners in China, the United States, and Europe. *Environ. Sci. Technol.* **2018**, *52(*5), 2819–2826.

99. Transport Canada. Whales Initiative: Protecting The Southern Resident Killer Whale - Transport Canada. **2018.** Retrieved from https://www.tc.gc.ca/en/initiatives/oceans-protection-plan/whales-initiative-protecting-southern-resident-killer-whale.html.

100. Van de Vijver, K. I.; Hoff, P.; Das, K.; Brasseur, S.; Van Dongen, W.; Esmans, E.; Reijnders, P.; Blust, R.; De Coen, W. Tissue distribution of perfluorinated chemicals in harbor seals (Phoca vitulina) from the Dutch Wadden Sea. *Environ. Sci. Technol.* **2005**, *39*(18), 6978–6984.

101. Savoca, M. S.; Robuck, A. R.; Cashman, M. A.; Cantwell, M. G.; Agvent, L. C.; Wiley, D. N.; Rice, R.; Todd, S.; Hunter, N. E.; Robbins, J.; Goldbogen, J. A. Whale baleen to monitor per-and polyfluoroalkyl substances (PFAS) in marine environments. *Environ. Sci. Technol. Lett.* **2024**, *11*(8), 862–870.

102. Khalid, N. K.; Aker, A.; Lair, S.; Sauvé, S. Presence of per-and poly-fluoroalkyl substances (PFAS) in brain samples of marine mammals from the St. Lawrence Estuary and Gulf, Canada. *Environ. Sci. Adv.* **2025**, *4*(10), 1599–1611.

103. Teymoorian, T.; Munoz, G.; Duy, S. V.; Vaudreuil, M. A.; Liu, M.; Liu, J.; Sauvé, S. A province-wide mapping of per-and polyfluoroalkyl substances (PFAS) in surface waters of the St. Lawrence River watershed, Québec, Canada. *Sci. Total Environ.* **2025**, *1000*, 180429.

104. Gewurtz, S. B.; Bradley, L. E.; Backus, S.; Dove, A.; McGoldrick, D.; Hung, H. Dryfhout-Clark, H. Perfluoroalkyl acids in Great Lakes precipitation and surface water (2006–2018) indicate response to phase-outs, regulatory action, and variability in fate and transport processes. *Environ. Sci. Technol.* **2019**, *53*(15), 8543–8552.

105. Dinglasan-Panlilio, M. J.; Prakash, S. S.; Baker, J. E. Perfluorinated compounds in the surface waters of puget sound, Washington and Clayoquot and barkley sounds, British Columbia. *Mar. Pollut. Bull.* **2014**, *78*(1–2), pp.173–180.

106. Wong, C.; Rylko, M. Health of the Salish Sea as measured using transboundary ecosystem indicators. *Aquat. Ecosyst. Health Manag.* **2014**, *17*(4), 463–471.

107. Kelly, B. C.; Ikonomou, M. G.; Blair, J. D.; Morin, A. E.; Gobas, F. A. Food web specific biomagnification of persistent organic pollutants. *Science*, **2007**, *317*(5835), 236–239.

108. Sha, B.; Johansson, J. H.; Salter, M. E.; Blichner, S. M.; Cousins, I. T. Constraining global transport of perfluoroalkyl acids on sea spray aerosol using field measurements. *Sci. Adv.* **2024**, *10*(14), eadl1026.

109. De Silva, A. O.; Armitage, J. M.; Bruton, T. A.; Dassuncao, C.; Heiger-Bernays, W.; Hu, X. C.; Kärrman, A.; Kelly, B.; Ng, C.; Robuck, A.; Sun, M. PFAS exposure pathways for humans and wildlife: a synthesis of current knowledge and key gaps in understanding. *Environ. Toxicol. Chem.* **2021**, *40*(3), 631–657.

110. Lachmuth, C. L.; Barrett-Lennard, L. G.; Steyn, D. Q.; Milsom, W. K. Estimation of southern resident killer whale exposure to exhaust emissions from whale-watching vessels and potential adverse health effects and toxicity thresholds. *Mar. Pollut. Bull.* **2011**, *62*(4), 792–805.

111. Simcik, M. F.; Dorweiler, K. J. Ratio of perfluorochemical concentrations as a tracer of atmospheric deposition to surface waters. *Environmental science & technology*, **2005**, *39*(22), 8678–8683.

112. Shaffer, K. W.; Ye, X.; Lee, C. S.; Shipley, O. N.; McDonough, C. A.; Venkatesan, A. K.; Gobler, C. J. Accumulation and trophic transfer of per-and polyfluoroalkyl substances (PFAS) in estuarine organisms determined via stable isotopes. *Sci. Total Environ.* **2025**, *967*, 178742.

113. Nie, W.; Wang, T.; Gao, X.; Pathak, R. K.; Wang, X.; Gao, R.; Zhang, Q.; Yang, L.; Wang, W. Comparison among filter-based, impactor-based and continuous techniques for measuring atmospheric fine sulfate and nitrate. *Atmos. Environ.* **2010**, *44*(35), 4396–4403.

114. Arp, H. P. H.; Goss, K. U. Irreversible sorption of trace concentrations of perfluorocarboxylic acids to fiber filters used for air sampling. *Atmos. Environ.* **2008**, *42*(28), 6869-6872.

Appendix C: Supporting Information for Chapter 4

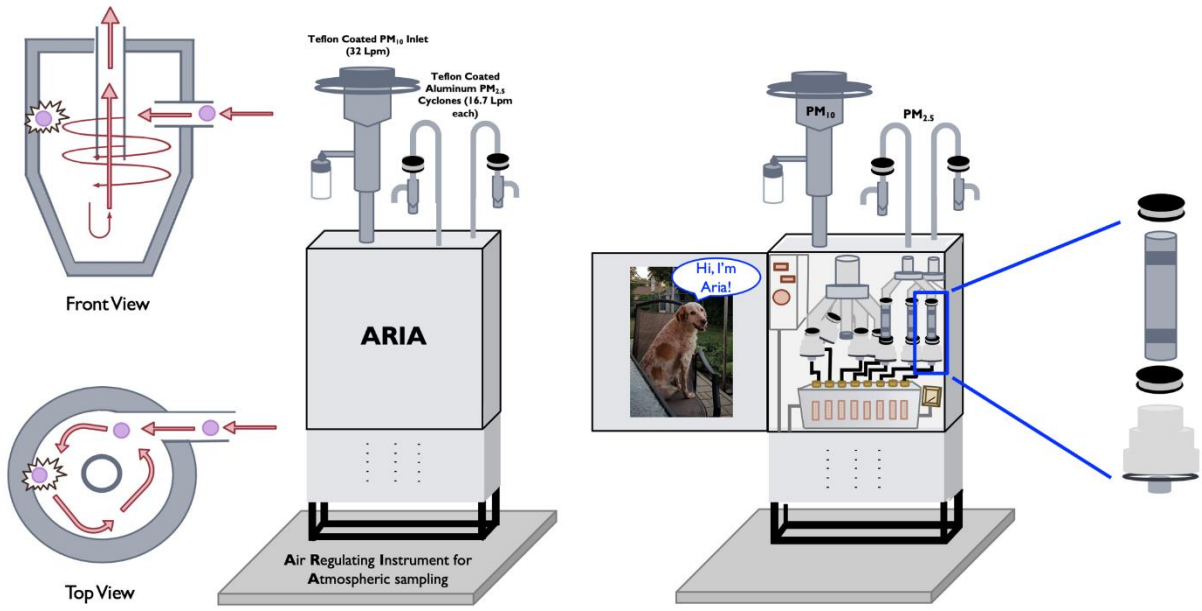

Figure C-1. Schematic of a medium volume sampler (MVS), nicknamed the "ARIA" (Air Regulating Instrument for Atmospheric sampling), used for active air sampling of gas- and particle-phase PFCAs. The MVS includes two inlets with particle cut-off diameters of 2.5 μm ($PM_{2.5}$) and 10 μm (PM_{10}), annular diffusion denuders for gas-phase collection, and filter packs for particle collection.

C.1 Sampling Efficiency of PFPrA

The denuders used were pre-cleaned and coated as described in the main text. Collection efficiency samples consisted of bubbler solutions obtained with the denuder installed between the PFPrA gas source and bubbler (Line 1, Figure C-2). Blanks were collected by running dry N_2 through the setup and into the bubbler – bypassing the permeation oven (Line 2, Figure C-2). Mass balance was obtained by extraction and experiments conducted in triplicate to assess reproducibility. Aliquots of the bubbler samples were diluted by a factor of ten to prevent overloading of the IC column for the PFPrA obtained directly from the permeation oven.

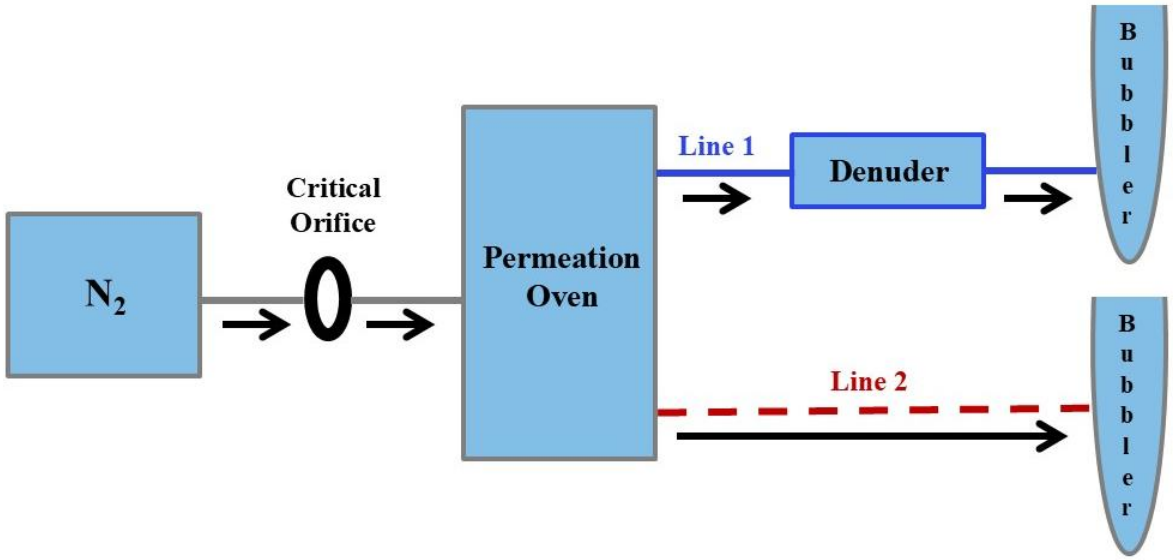

Figure C-2. Schematic of denuder PFPrA efficiency experiments. Lines 1 and 2 were not interchangeable (only one line was running at a time). Line 1 (blue, solid) served as the denuder-equipped configuration, in which PFPrA was removed prior to collection in the bubbler. Line 2 (red, dashed) served as the control configuration, representing the baseline PFPrA concentration entering the bubbler in the absence of denuder scrubbing. The solid black arrow indicates the direction of flow through the system.

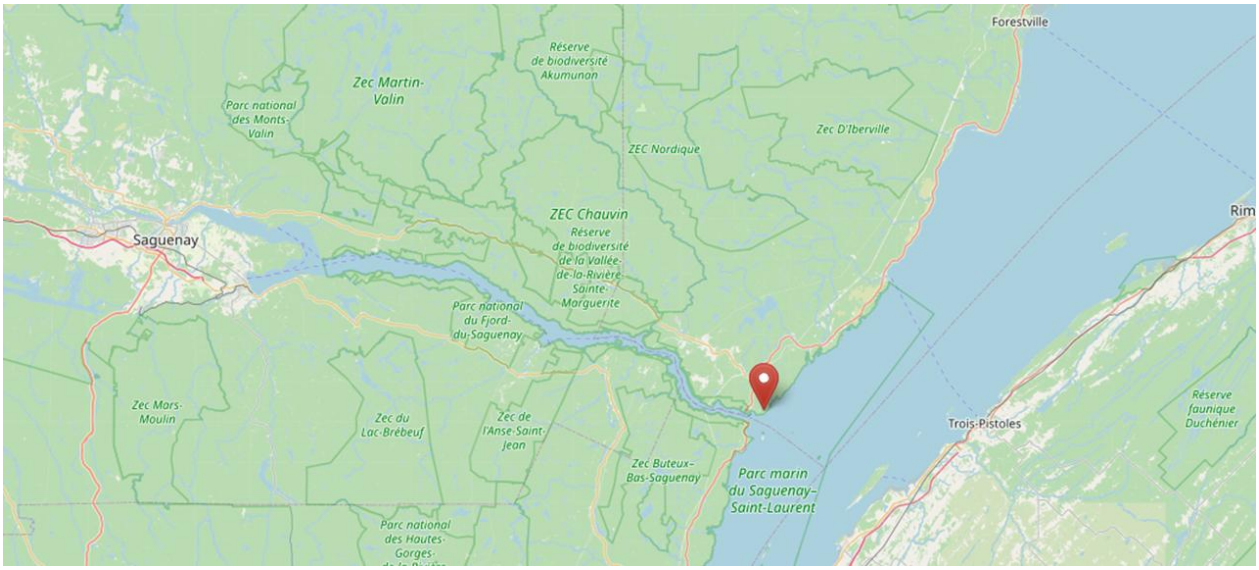

Figure C-3. Map depicting the approximate location of the field site at Hovington Farm in Tadoussac, Québec (48°08'34.000" N, 69°41'03.000" W).

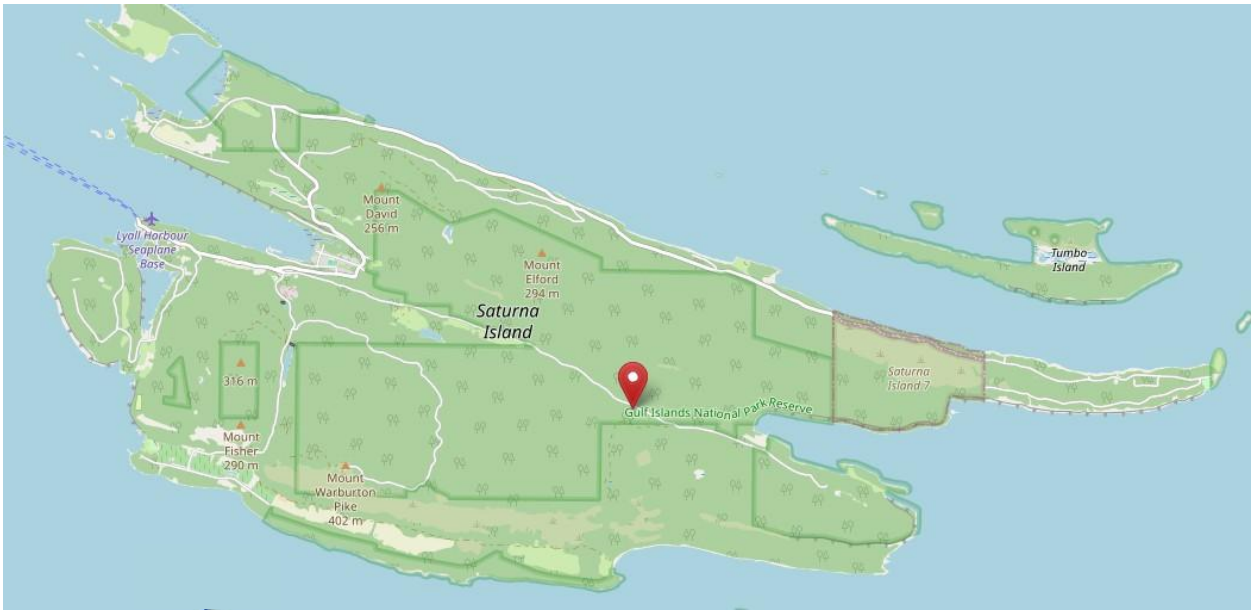

Figure C-4. Map depicting the approximate location of Meteorological Service of Canada's Air and Precipitation Monitoring Site on Saturna Island, British Columbia (48°47'02.067" N, 123°02'41.082" W).

C.2 Analytical Determinations

C.2.1 Sampling Efficiency of PFPrA: Ion Chromatography with Conductivity Detection (IC-CD)

Ion chromatography with conductivity detection (IC-CD) was used to determine the sampling efficiency of PFPrA. The IC system consisted of a Thermo Scientific™ Dionex™ ICS-6000 equipped with a quaternary pump and a a Thermo Scientific™ AS-AP autosampler. Standards were prepared by dissolving K-PFPrA in Milli-Q water and generating a series of dilutions (0.50, 1.00, 5.00, and 10.0 mg L^{-1}). The autosampler injected 300 µL of each bubbler sample or standard onto a concentrator column (5 x 23 mm, TAC-ULP1). Separation was performed on a Thermo Scientific™ Dionex™ IonPac™ AS23 analytical column (4 x 250 mm) fitted with a Thermo Scientific™ Dionex™ IonPac™ AG23 guard column (4 x 50 mm) at a flow rate of 1.0 mL min^{-1}. The eluent was sodium hydroxide (NaOH) prepared at a concentration of 100 mM and delivered using the ICS-6000 quaternary pump. A multi-step gradient program was used and the total runtime for each separation was 30 mins. (Table C-1). Prior to conductivity detection, analytes were suppressed using a Thermo Scientific™ Dionex™ ADRS 600 suppressor (4 mm). Chromatographic peak areas were integrated using Chromeleon software and data analysis was conducted using Microsoft Excel and Igor Pro (Wavemetrics, version 9).

Table C-1. This IC-CD gradient scheme, with Milli-Q water (A) and 100 mM sodium hydroxide (B), was used and, at a flow rate of 1.00 mL min^{-1}, each separation lasted 30 mins.

Time (mins)	A (%)	B%	Gradient Description
0 to 10	99	1	Held
10 to 18	98	2	Linear increase in B
18 to 28	80	20	Linear increase in B
28 to 30	99	1	Step change and re-equilibration

C.2.2 Deposition and Gas-phase Analysis: Ion Chromatography Mass Spectrometry (IC-MS)

The IC-MS system utilized in this work was composed of a Thermo Scientific™ Dionex™ ICS-6000 (outfitted with dual pump and dual column and detector compartments) and a single quadrupole ISQ™ EC MS analyzer. The autosampler used a 5 mL syringe to inject 250 µL of the sample onto a 250 µL anion loop. A gradient separation was completed on a Thermo Scientific™ Dionex™ IonPac™ AS24 analytical column (2 × 250 mm, 7 µm particle size, 55% DVB, alkanol quaternary ammonium exchanger), fitted with a Thermo Scientific™ Dionex™ IonPac™ AG24 guard column (2 × 50mm, 11 µm particle size). A 2 mm Thermo Scientific™ Dionex™ ADRS 600 Dynamically Regenerated Suppressor was operated in external water mode. A gradient scheme using Milli-Q water (A) and 100 mM NaOH (B) was used, with a flow rate of 0.35 mL min^{-1} and a column temperature of 30°C, resulting in separations lasting 31 mins each (Table C-2). Following suppression, the IC effluent was mixed with Optima grade MeOH and introduced into the MS via electrospray ionization operated in negative ion mode. The ion transfer tube temperature was set to 250°C and the vaporizer temperature was maintained at 450°C. Target analytes were detected and quantified using selected ion monitoring. The Chromeleon 7 Chromatography Data System software was used to integrate the peaks for each chromatogram, and the data was analyzed using Microsoft Excel and Igor Pro (Wavemetrics, version 8.04).

Table C-2. This IC-MS gradient scheme, with Milli-Q water (A) and 100 mM NaOH (B), was used and, at a flow rate of 0.35 mL min^{-1}, each separation lasted 31 mins.

Time (mins)	A (%)	B%	Gradient Description
0 to 7	90	10	Held
7 to 10	73	27	Linear increase in B
10 to 16.5	68	32	Linear increase in B
16.5 to 20	50	50	Linear increase in B
20 to 22	40	60	Linear increase in B
22 to 29	40	60	Held
29 to 31	90	10	Step change and re-equilibration

Table C-3. The limit of detection (LOD, 3/m) and limit of quantification (LOQ, 10/m) in solution (µg L^{-1}) for each PFCA and sample type.

	Saturna Island: Deposition		Tadoussac: Deposition		Tadoussac + Saturna Island: Denuders	
PFCA	**LOQ (µg L^{-1})**	**LOD (µg L^{-1})**	**LOQ (µg L^{-1})**	**LOD (µg L^{-1})**	**LOQ (µg L^{-1})**	**LOD (µg L^{-1})**
TFA	0.262	0.079	0.428	0.128	0.223	0.067
PFPrA	0.270	0.081	0.140	0.042	0.157	0.047
PFBA	0.245	0.073	0.240	0.072	0.166	0.050
PFPeA	0.140	0.042	0.088	0.026	0.100	0.030
PFHxA	0.216	0.065	0.081	0.024	0.113	0.034

Table C-4. The approximate detection frequencies of C2 to C6 PFCAs in deposition and active air samples at both field sites.

Detection Frequencies (%) in Active Air Samples						
	Tadoussac, Québec (n = 22)			Saturna Island, British Columbia (n = 43)		
PFCA	**>LOQ**	**<LOQ, >LOD**	**<LOD**	**>LOQ**	**<LOQ, >LOD**	**<LOD**
TFA	100.0	0.0	0.0	100.0	0.0	0.0
PFPrA	100.0	0.0	0.0	88.4	0.0	11.6
PFBA	4.5	0.0	95.5	60.5	0.0	39.5
PFPeA	9.1	0.0	90.9	14.0	2.3	83.7
PFHxA	4.5	0.0	95.5	0.0	0.0	100.0
Detection Frequencies (%) in Tadoussac, Québec Deposition Samples						
	Wet Deposition (n = 15)			Total Deposition (n = 13)		
PFCA	**>LOQ**	**<LOQ, >LOD**	**<LOD**	**>LOQ**	**<LOQ, >LOD**	**<LOD**
TFA	40.0	53.3	6.7	46.2	53.8	0.0
PFPrA	93.3	0.0	6.7	76.9	7.7	15.4
PFBA	6.7	0.0	93.3	0.0	0.0	100.0
PFPeA	6.7	0.0	93.3	0.0	0.0	100.0
PFHxA	6.7	0.0	93.3	0.0	0.0	100.0
Detection Frequencies (%) in Saturna Island, British Columbia Deposition Samples						
	Wet Deposition (n = 23)			Total Deposition (n = 21)		
PFCA	**>LOQ**	**<LOQ, >LOD**	**<LOD**	**>LOQ**	**<LOQ, >LOD**	**<LOD**
TFA	43.5	34.8	21.7	42.9	23.8	33.3
PFPrA	65.2	17.4	17.4	33.3	38.1	28.6
PFBA	8.7	0.0	91.3	0.0	0.0	100.0
PFPeA	4.3	0.0	95.7	0.0	9.5	90.5
PFHxA	0.0	0.0	100.0	0.0	0.0	100.0

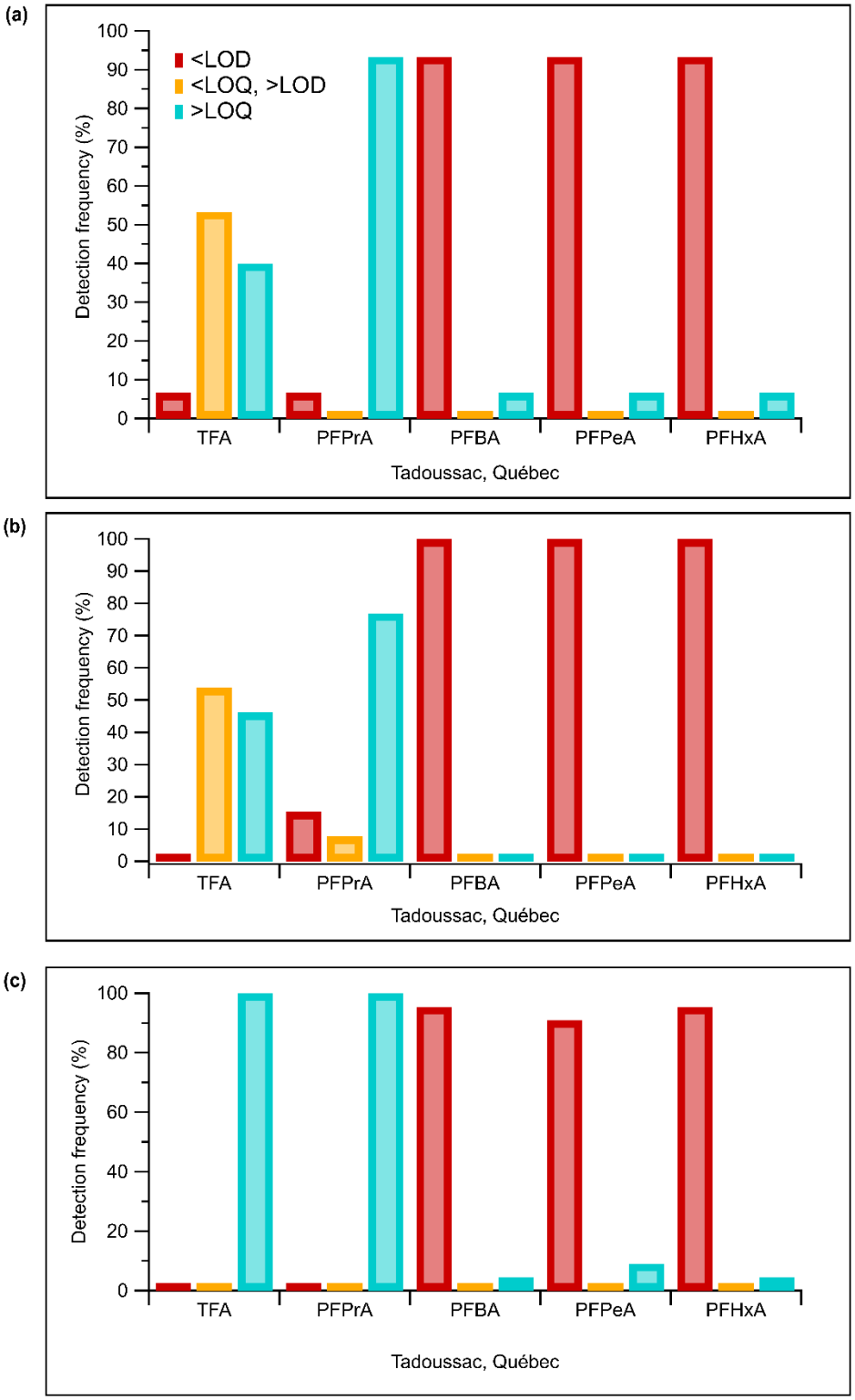

Figure C-5. The not detected (red), semi-quantitative (orange), and quantitative (aqua) detection frequencies of C2 to C6 PFCAs in the **(a)** wet deposition (n = 15), **(b)** total deposition (n = 13), and **(c)** active air (n = 22) samples collected at the Tadoussac, Québec field site.

Table C-5. Summary of PFCA concentrations (µg L^{-1}) in deposition samples collected at the Tadoussac field site: "WD" and "TD" representing wet deposition and total deposition, respectively. Values <LOD are identified in blue, values <LOQ are in red, and values >LOQ are in black.

		Concentration in solution (µg L^{-1})				
Sampling Period	**Denuder**	**TFA**	**PFPrA**	**PFBA**	**PFPeA**	**PFHxA**
Oct 14 – Nov 14, 2021	Travelling field blank	0.586	0.119	<0.072	<0.026	<0.024
	1 (WD)	0.729	0.283	<0.072	<0.026	<0.024
	2 (WD)	0.701	0.260	<0.072	<0.026	<0.024
	3 (WD)	0.797	0.327	<0.072	<0.026	<0.024
	4 (TD)	0.650	0.317	<0.072	<0.026	<0.024
Nov 14 – Dec 14, 2021	Travelling field blank	<0.128	0.099	0.567	0.998	1.052
	1 (WD)	<0.128	0.278	<0.072	<0.026	<0.024
	2 (WD)	0.193	0.284	<0.072	<0.026	<0.024
	3 (WD)	0.189	0.269	<0.072	<0.026	<0.024
	4 (TD)	0.162	0.278	<0.072	<0.026	<0.024
Dec 14, 2021 – June 9, 2022	Travelling field blank	<0.128	<0.042	<0.072	<0.026	<0.024
Dec 14, 2021 – Jan 14, 2022	4 (TD)	0.316	0.356	<0.072	<0.026	<0.024
Jan 14 – Mar 14, 2022	4 (TD)	0.468	1.839	<0.072	<0.026	<0.024
March 14 – April 26, 2022	4 (TD)	0.278	0.236	<0.072	<0.026	<0.024
April 26 – June 9, 2022	4 (TD)	0.470	0.246	<0.072	<0.026	<0.024
June 9 – July 13, 2022	Travelling field blank	<0.128	<0.042	<0.072	<0.026	<0.024
	1 (WD)	0.362	0.195	<0.072	<0.026	<0.024
	2 (WD)	0.448	<0.042	<0.072	<0.026	<0.024
	3 (WD)	0.451	0.256	<0.072	<0.026	<0.024
	4 (TD)	0.433	0.286	<0.072	<0.026	<0.024
July 13 – Aug 12, 2022	Travelling field blank	<0.128	<0.042	<0.072	<0.026	<0.024
	1 (TD)	0.461	0.288	<0.072	<0.026	<0.024
	4 (TD)	0.408	0.207	<0.072	<0.026	<0.024
	2 (WD)	0.383	0.187	1.112	0.952	0.891
	3 (WD)	0.374	0.211	<0.072	<0.026	<0.024
Aug 12 – Sept 23, 2022	Travelling field blank	<0.128	<0.042	<0.072	<0.026	<0.024
	1 (TD)	0.478	<0.042	<0.072	<0.026	<0.024
	4 (TD)	0.413	<0.042	<0.072	<0.026	<0.024
	2 (WD)	0.410	0.262	<0.072	<0.026	<0.024
	3 (WD)	0.424	0.290	<0.072	<0.026	<0.024
Sept 23 – Oct 12, 2022	Travelling field blank (rep. 1)	<0.128	<0.042	<0.072	<0.026	<0.024
	Travelling field blank (rep. 2)	<0.128	<0.042	<0.072	<0.026	<0.024
	Travelling field blank (rep. 3)	<0.128	<0.042	<0.072	<0.026	<0.024
	1 (TD)	0.387	0.205	<0.072	<0.026	<0.024
	4 (TD)	0.388	0.140	<0.072	<0.026	<0.024
	2 (WD)	0.456	0.215	<0.072	<0.026	<0.024
	3 (WD)	0.420	0.245	<0.072	<0.026	<0.024

Table C-6. Summary of PFCA concentrations (µg L^{-1}) in deposition samples collected at the Saturna Island field site: "WD" and "TD" representing wet deposition and total deposition, respectively. Values <LOD are identified in blue, values <LOQ are in red, and values >LOQ are in black.

		Concentration in solution (µg L^{-1})				
Sampling Period	**Denuder**	**TFA**	**PFPrA**	**PFBA**	**PFPeA**	**PFHxA**
Dec 15, 2021 – Jan 18, 2022	Travelling field blank	<0.079	<0.081	<0.073	<0.042	<0.065
	5 (WD)	0.243	0.555	<0.073	<0.042	<0.065
	6 (WD)	<0.079	0.272	<0.073	<0.042	<0.065
	7 (WD)	<0.079	0.242	<0.073	<0.042	<0.065
	8 (TD)	<0.079	0.289	<0.073	<0.042	<0.065
Jan 18 – Feb 15, 2022	Travelling field blank	<0.079	<0.081	<0.073	<0.042	<0.065
	5 (WD)	0.132	0.261	<0.073	<0.042	<0.065
	6 (WD)	0.106	0.202	<0.073	<0.042	<0.065
	7 (TD)	0.121	0.210	<0.073	0.125	<0.065
	8 (TD)	0.101	0.217	<0.073	<0.042	<0.065
Feb 15 – March 15, 2022	Travelling field blank	<0.079	<0.081	<0.073	<0.042	<0.065
	5 (WD)	0.094	0.336	<0.073	<0.042	<0.065
	6 (WD)	0.110	0.295	<0.073	<0.042	<0.065
	7 (TD)	<0.079	<0.081	<0.073	<0.042	<0.065
	8 (TD)	<0.079	0.222	<0.073	<0.042	<0.065
March 15 – April 13, 2022	Travelling field blank	<0.079	<0.081	<0.073	<0.042	<0.065
	5 (WD)	0.224	0.296	<0.073	<0.042	<0.065
	6 (WD)	0.275	0.302	<0.073	<0.042	<0.065
	7 (TD)	0.172	<0.081	<0.073	<0.042	<0.065
	8 (TD)	0.114	0.165	<0.073	<0.042	<0.065
April 13 – May 13, 2022	Travelling field blank	<0.079	<0.081	<0.073	<0.042	<0.065
	5 (WD)	0.234	0.281	<0.073	<0.042	<0.065
	6 (WD)	0.338	<0.081	<0.073	<0.042	<0.065
	7 (TD)	0.475	<0.081	<0.073	<0.042	<0.065
	8 (TD)	0.317	<0.081	<0.073	<0.042	<0.065
May 13 – June 15, 2022	Travelling field blank	<0.079	0.82	<0.073	<0.042	<0.065
	5 (WD)	0.553	0.275	<0.073	<0.042	<0.065
	6 (WD)	0.299	<0.081	<0.073	<0.042	<0.065
	7 (TD)	0.331	0.237	<0.073	<0.042	<0.065
	8 (TD)	0.349	<0.081	<0.073	<0.042	<0.065
June 15 – July 26, 2022	Travelling field blank	0.155	0.207	<0.073	<0.042	<0.065
	5 (WD)	0.681	0.348	<0.073	<0.042	<0.065
	6 (WD)	0.534	0.323	0.270	<0.042	<0.065
	7 (TD)	0.423	0.350	<0.073	<0.042	<0.065
	8 (TD)	0.356	0.226	<0.073	<0.042	<0.065
July 26 – Sept 1, 2022	Travelling field blank	<0.079	<0.081	<0.073	<0.042	<0.065
	5 (WD)	2.090	0.347	0.282	2.813	<0.065
	6 (WD)	1.606	1.953	<0.073	<0.042	<0.065
	7 (TD)	1.619	0.552	<0.073	<0.042	<0.065
	8 (TD)	1.366	2.570	<0.073	0.095	<0.065

Table C-6 (cont'd). Summary of PFCA concentrations (µg L^{-1}) in deposition samples collected at the Saturna Island field site: "WD" and "TD" representing wet deposition and total deposition, respectively. Values <LOD are identified in blue, values <LOQ are in red, and values >LOQ are in black.

		Concentration in solution (µg L^{-1})				
Sampling Period	**Denuder**	**TFA**	**PFPrA**	**PFBA**	**PFPeA**	**PFHxA**
Sept 1 – Oct 16, 2022	Travelling field blank (rep. 1)	<0.079	0.296	<0.073	<0.042	<0.065
	Travelling field blank (rep. 2)	<0.079	0.275	<0.073	<0.042	<0.065
	Travelling field blank (rep. 3)	<0.079	0.339	<0.073	<0.042	<0.065
	5 (WD)	0.650	0.302	<0.073	<0.042	<0.065
	6 (WD)	0.519	0.279	<0.073	<0.042	<0.065
	7 (TD)	0.656	0.167	<0.073	<0.042	<0.065
	8 (TD)	0.138	0.278	<0.073	<0.042	<0.065
Oct 16 – Nov 7, 2022	Travelling field blank	<0.079	<0.081	<0.073	<0.042	<0.065
	5 (WD)	0.150	0.310	<0.073	<0.042	<0.065
	6 (WD)	<0.079	0.248	<0.073	<0.042	<0.065
	7 (TD)	<0.079	0.237	<0.073	<0.042	<0.065
	8 (TD)	<0.079	0.277	<0.073	<0.042	<0.065
Nov 7 – Dec 3, 2022	Travelling field blank	<0.079	<0.081	<0.073	<0.042	<0.065
	5 (WD)	<0.079	<0.081	<0.073	<0.042	<0.065
	6 (WD)	<0.079	0.287	<0.073	<0.042	<0.065
	7 (TD)	<0.079	<0.081	<0.073	<0.042	<0.065
	8 (TD)	<0.079	0.278	<0.073	<0.042	<0.065

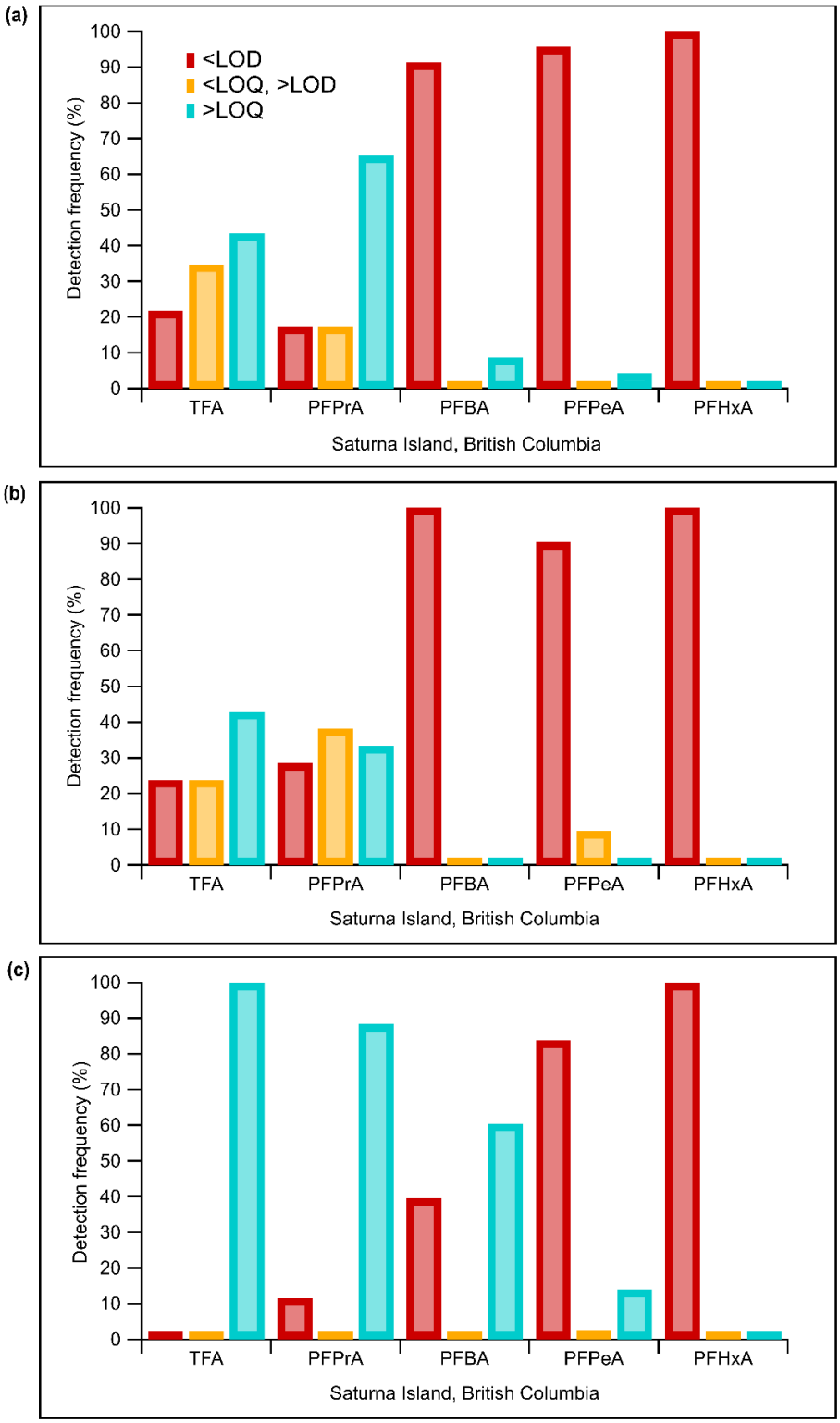

Figure C-6. The not detected (red), semi-quantitative (orange), and quantitative (aqua) detection detection frequencies of C2 to C6 PFCAs in the **(a)** wet deposition (n = 23), **(b)** total deposition (n = 21), and **(c)** active air (n = 43) samples collected at the Saturna Island, British Columbia field site.

Table C-7. Annual fluxes of deposition collected at the Tadoussac field site: "WD" and "TD" representing wet deposition and total deposition, respectively. Values marked with an asterisk (*) are those values removed from the overall reported average due to instrumentation issues (e.g., malfunctioning motor arms). Values >LOQ are identified in black, <LOQ are in red, and values <LOD are in blue and are here reported as half of that analyte's LOD. For sampling periods where n = 2, 3, or 4, the mean values are reported. The associated uncertainties are reported as followed for sampling periods where: i) n = 3 or 4, the standard deviation of the mean is reported; ii) n = 2, the uncertainty is expressed as the relative difference between the two samples, converted to absolute units using the mean, and iii) n = 1, uncertainties were derived by propagating the 65% confidence interval errors from the calibration curves before being transformed using the same flux calculation applied to the sample. Entries with "--" for uncertainty indicate that, although minor variability existed on a mass basis due to differences in sampled deposition volume, replicate PFCA levels were identical after conversion and rounding to one decimal place to avoid false precision, resulting in a calculated uncertainty of zero. Note that the reported uncertainties reflect observed sample-to-sample variation in deposition samples[1,2] and therefore represent natural environmental heterogeneity rather than analytical error.

		Yearly Flux (± Uncertainties, µg m^{-2} $year^{-1}$)				
Sampling Period	**Sampler #**	**TFA**	**PFPrA**	**PFBA**	**PFPeA**	**PFHxA**
Oct 14 – Nov 14, 2021	1 (WD)	566.54	220.34	48.10	40.54	30.41
	2 (WD)	560.06	207.96	49.44	41.67	31.26
	3 (WD)	628.66	258.06	48.77	41.10	30.83
	4 (TD)	807.21 (± 23.31)	394.21 (± 40.01)	76.84 (± 27.76)	64.77 (± 0.00)	48.58 (± 17.29)
	Average **(WD, n = 3)**	585.09 (± 37.87)	228.79 (± 26.10)	48.77 (± 0.67)	41.10 (± 0.57)	30.83 (± 0.42)
Nov 14 – Dec 14, 2021	1 (WD)	41.17*	88.96*	19.80*	16.69*	12.52*
	2 (WD)	30.89	45.47	9.90	8.34	6.26
	3 (WD)	30.21	43.01	9.90	8.34	6.26
	4 (TD)	103.44 (± 12.01)	178.19 (± 20.62)	39.60 (± 14.31)	33.38 (± 12.25)	25.04 (± 8.91)
	Average **(WD, n = 2)**	30.55 (± 0.48)	44.24 (± 12.57)	9.90 (± 0.00)	8.34 (± 0.00)	6.26 (± 0.00)
Dec 14, 2021 – Jan 14, 2022	4 (TD)	38.71 (± 2.30)	43.60 (± 3.94)	7.57 (± 2.73)	6.38 (± 2.34)	4.79 (± 1.70)
Jan 14 – Mar 14, 2022	4 (TD)	133.53 (± 5.36)	525.20 (± 9.20)	17.67 (± 6.38)	14.89 (± 5.47)	11.17 (± 3.98)
Mar 14 – April 26, 2022	4 (TD)	243.44 (± 16.42)	206.56 (± 28.19)	54.14 (± 19.56)	45.63 (± 16.75)	34.23 (± 12.18)
April 26 – June 9, 2022	4 (TD)	382.99 (± 15.29)	200.59 (± 26.26)	50.43 (± 18.22)	42.50 (± 25.60)	31.88 (± 11.35)
June 9 – July 13, 2022	1 (WD)	322.09	173.73	55.06	46.41	34.81
	2 (WD)	429.59	46.77	59.27	49.95	37.47
	3 (WD)	504.40	285.72	69.15	58.28	43.71
	4 (TD)	516.62 (± 22.41)	342.16 (± 38.48)	73.90 (± 26.70)	62.29 (± 22.86)	46.72 (± 16.63)
	Average **(WD, n = 3)**	418.69 (± 91.64)	168.75 (± 119.56)	61.16 (± 7.23)	51.55 (± 6.09)	38.66 (± 4.57)

Table C-7 (cont'd). Annual fluxes of deposition collected at the Tadoussac field site: "WD" and "TD" representing wet deposition and total deposition, respectively. Values marked with an asterisk (*) are those values removed from the overall reported average due to instrumentation issues (e.g., malfunctioning motor arms). Values >LOQ are identified in black, <LOQ are in red, and values <LOD are in blue and are here reported as half of that analyte's LOD. For sampling periods where n = 2, 3, or 4, the mean values are reported. The associated uncertainties are reported as followed for sampling periods where: i) n = 3 or 4, the standard deviation of the mean is reported; ii) n = 2, the uncertainty is expressed as the relative difference between the two samples, converted to absolute units using the mean, and iii) n = 1, uncertainties were derived by propagating the 65% confidence interval errors from the calibration curves before being transformed using the same flux calculation applied to the sample. Entries with "--" for uncertainty indicate that, although minor variability existed on a mass basis due to differences in sampled deposition volume, replicate PFCA levels were identical after conversion and rounding to one decimal place to avoid false precision, resulting in a calculated uncertainty of zero. Note that the reported uncertainties reflect observed sample-to-sample variation in deposition samples[1,2] and therefore represent natural environmental heterogeneity rather than analytical error.

		Yearly Flux (± Uncertainties, µg m^{-2} $year^{-1}$)				
Sampling Period	**Sampler #**	**TFA**	**PFPrA**	**PFBA**	**PFPeA**	**PFHxA**
July 13 – Aug 12, 2022	1 (TD)	252.07	157.57	33.86	28.54	21.41
	4 (TD)	223.04	113.35	33.86	28.54	21.41
	2 (WD)	196.35	95.88	569.29	487.48	456.42
	3 (WD)	198.50	112.05	32.87	27.70	20.78
	Average **(WD, n = 2)**	197.42 (± 2.15)	103.97 (± 16.17)	301.08 (± 536.42)	257.59 (± 459.78)	238.60 (± 435.64)
	Average **(TD, n = 2)**	237.56 (± 29.03)	135.46 (± 44.22)	33.86 (± --)	28.54 (± --)	21.41 (± --)
Aug 12 – Sept 23, 2022	1 (TD)	299.76	30.64	38.83	32.72	24.54
	4 (TD)	265.46	31.37	39.75	33.50	25.13
	2 (WD)	240.19	153.20	36.21	30.52	22.89
	3 (WD)	252.13	172.13	36.78	30.99	23.25
	Average **(WD, n = 2)**	246.16 (± 11.94)	162.66 (± 18.93)	36.49 (± 0.57)	30.76 (± 0.48)	23.07 (± 0.36)
	Average **(TD, n = 2)**	282.61 (± 34.29)	31.00 (± 0.18)	39.29 (± 19.21)	33.11 (± 0.77)	24.84 (± 0.58)
Sept 23 – Oct 12, 2022	1 (TD)	113.57	60.20	18.13	15.28	11.46
	4 (TD)	113.75	40.98	18.13	15.28	11.46
	2 (WD)	101.35	47.79	13.76	11.59	8.70
	3 (WD)	91.30	53.21	13.44	11.33	8.50
	Average **(WD, n = 2)**	96.33 (± 10.05)	50.50 (± 5.42)	13.60 (± 0.31)	11.46 (± 0.26)	8.60 (± 0.20)
	Average **(TD, n = 2)**	113.66 (± 0.18)	50.59 (± 19.21)	18.13 (± 0.00)	15.28 (± 0.00)	11.46 (± 0.00)

Table C-8. Annual fluxes of deposition collected at the Saturna Island field site: "WD" and "TD" representing wet deposition and total deposition, respectively. Values marked with an asterisk (*) are those values removed from the overall reported average due to instrumentation issues (e.g., malfunctioning motor arms). Values >LOQ are identified in black, <LOQ are in red, and values <LOD are in blue and are here reported as half of that analyte's LOD. For sampling periods where n = 2, 3, or 4, the mean values are reported. The associated uncertainties are reported as followed - for sampling periods where: i) n = 3 or 4, the standard deviation of the mean is reported; ii) n = 2, the uncertainty is expressed as the relative difference between the two samples, converted to absolute units using the mean, and iii) n = 1, uncertainties were derived by propagating the 65% confidence interval errors from the calibration curves before being transformed using the same flux calculation applied to the sample. Note that the reported uncertainties reflect observed sample-to-sample variation in deposition samples[1,2] and therefore represent natural environmental heterogeneity rather than analytical error.

		Yearly Flux (± Uncertainties, µg m^{-2} year^{-1})				
Sampling Period	**Sampler #**	**TFA**	**PFPrA**	**PFBA**	**PFPeA**	**PFHxA**
Dec 15, 2021 – Jan 18, 2022	5 (WD)	140.88*	321.30*	59.14*	51.39*	45.76*
	6 (WD)	29.74*	205.48*	77.17*	67.06*	59.71*
	7 (WD)	27.57*	169.69*	71.55*	62.17*	55.36*
	8 (TD)	47.92 (± 22.84)	352.29 (± 39.21)	124.34 (± 27.20)	108.05 (± 23.30)	96.20 (± 16.94)
Jan 18 – Feb 15, 2022	5 (WD)	24.67	48.71	19.09	16.59	14.77
	6 (WD)	33.01	63.19	31.88	27.70	24.66
	7 (TD)	59.26	102.86	50.10	61.53	38.76
	8 (TD)	44.76	96.02	45.19	39.27	34.96
	Avg **(WD, n = 2)**	28.84 (± 8.34)	55.95 (± 14.48)	25.49 (± 12.79)	22.15 (± 11.11)	19.72 (± 9.89)
	Avg **(TD, n = 2)**	52.01 (± 14.50)	99.44 (± 6.84)	47.64 (± 4.90)	50.40 (± 22.26)	36.86 (± 3.79)
Feb 15 – Mar 15, 2022	5 (WD)	8.04	28.85	8.76	7.61	6.78
	6 (WD)	8.71	23.27	8.06	7.00	6.23
	7 (TD)	32.54	36.76	84.43	73.36	65.32
	8 (TD)	31.73	179.24	82.32	71.54	63.69
	Avg **(WD, n = 2)**	8.38 (± 0.67)	26.06 (± 5.58)	8.41 (± 0.70)	7.31 (± 0.61)	6.50 (± 0.54)
	Avg **(TD, n = 2)**	32.13 (± 0.81)	108.00 (± 142.49)	83.38 (± 2.10)	72.45 (± 1.83)	64.51 (± 1.63)
Mar 15 – April 13, 2022	5 (WD)	46.03	60.86	20.97	18.22	16.22
	6 (WD)	59.11	65.00	21.99	19.10	17.01
	7 (TD)	158.29	40.94	94.03	81.71	72.75
	8 (TD)	102.71	149.22	92.34	80.24	71.44
	Avg **(WD, n = 2)**	52.57 (± 13.08)	62.93 (± 4.14)	21.48 (± 1.01)	18.66 (± 0.88)	16.62 (± 0.79)
	Avg **(TD, n = 2)**	130.50 (± 55.59)	95.08 (± 109.28)	93.18 (± 1.69)	80.97 (± 1.47)	72.10 (± 1.31)
April 13 – May 13, 2022	5 (WD)	17.59	21.16	7.68	6.68	5.94
	6 (WD)	28.12	3.70	8.50	7.39	6.58
	7 (TD)	240.45 (± 9.49)	22.49 (± 16.29)	51.66 (± 11.30)	44.89 (± 9.68)	39.97
	8 (TD)	23.37*	3.27*	7.52*	6.53*	5.82*
	Avg **(WD, n = 2)**	22.85 (± 10.53)	12.43 (± 17.46)	8.09 (± 0.82)	7.03 (± 0.71)	6.26 (± 0.63)
May 13 – June 15, 2022	5 (WD)	20.10 (± 0.68)	9.98 (± 1.17)	0.93 (± 0.20)	3.23 (± 0.70)	2.87 (± 0.51)
	6 (WD)	65.04*	9.68*	22.23*	19.32*	17.20*
	7 (TD)	245.80	175.66	75.80	65.86	58.64
	8 (TD)	243.46	31.06	71.34	61.99	55.19
	Avg **(TD, n = 2)**	244.63 (± 2.34)	103.36 (± 144.61)	73.57 (± 4.46)	63.93 (± 3.87)	56.92 (± 3.45)

Table C-8 (cont'd). Annual fluxes of deposition collected at the Saturna Island field site: "WD" and "TD" representing wet deposition and total deposition, respectively. Values marked with an asterisk (*) are those values removed from the overall reported average due to instrumentation issues (e.g., malfunctioning motor arms). Values >LOQ are identified in black, <LOQ are in red, and values <LOD are in blue and are here reported as half of that analyte's LOD. For sampling periods where n = 2, 3, or 4, the mean values are reported. The associated uncertainties are reported as followed - for sampling periods where: i) n = 3 or 4, the standard deviation of the mean is reported; ii) n = 2, the uncertainty is expressed as the relative difference between the two samples, converted to absolute units using the mean, and iii) n = 1, uncertainties were derived by propagating the 65% confidence interval errors from the calibration curves before being transformed using the same flux calculation applied to the sample. Note that the reported uncertainties reflect observed sample-to-sample variation in deposition samples[1,2] and therefore represent natural environmental heterogeneity rather than analytical error.

		Yearly Flux (± Uncertainties, µg m^{-2} $year^{-1}$)				
Sampling Period	**Sampler #**	**TFA**	**PFPrA**	**PFBA**	**PFPeA**	**PFHxA**
June 15 – July 26, 2022	5 (WD)	18.35	9.37	2.75	2.39	2.13
	6 (WD)	18.77	11.36	9.50	3.12	2.78
	7 (TD)	60.98	50.37	14.71	12.79	11.38
	8 (TD)	45.43	28.81	13.04	11.33	10.09
	Average **(WD, n = 2)**	18.56 (± 0.42)	10.36 (± 2.00)	6.12 (± 6.75)	2.75 (± 0.73)	2.45 (± 0.65)
	Average **(TD, n = 2)**	53.20 (± 15.56)	39.59 (± 21.57)	13.88 (± 1.67)	12.06 (± 1.46)	10.74 (± 1.30)
July 26 – Sept 1, 2022	5 (WD)	18.98	3.15	2.56	25.55	0.72
	6 (WD)	16.67	20.28	1.06	0.92	0.82
	7 (TD)	25.22	8.60	1.59	1.38	1.23
	8 (TD)	23.05	43.35	1.72	0.40	1.33
	Avg **(WD, n = 2)**	17.83 (± 2.31)	11.71 (± 17.13)	1.81 (± 1.50)	13.23 (± 24.63)	0.77 (± 0.10)
	Avg **(TD, n = 2)**	24.13 (± 2.17)	25.98 (± 34.75)	1.66 (± 0.13)	0.89 (± 0.98)	1.28 (± 0.10)
Sept 1 – Oct 16, 2022	5 (WD)	20.12	9.34	3.16	2.75	2.45
	6 (WD)	12.94	6.97	2.55	2.22	1.97
	7 (TD)	582.11 (± 16.65)	5.62 (± 1.09)	3.44 (± 0.75)	2.99 (± 0.65)	2.66 (± 0.47)
	8 (TD)	3.54*	7.11*	2.62*	2.27*	2.02*
	Avg **(WD, n = 2)**	16.53 (± 7.17)	8.16 (± 2.37)	2.86 (± 0.61)	2.48 (± 0.53)	2.21 (± 0.47)
Oct 16 – Nov 7, 2022	5 (WD)	41.13	85.31	28.09	24.41	21.73
	6 (WD)	16.67	104.80	43.25	37.58	33.46
	7 (TD)	83.68	504.40	217.13	188.68	167.99
	8 (TD)	84.11	592.67	218.25	189.65	168.86
	Avg **(WD, n = 2)**	28.90 (± 24.46)	95.05 (± 19.49)	35.67 (± 15.16)	30.99 (± 13.17)	27.60 (± 11.73)
	Avg **(TD, n = 2)**	83.90 (± 0.43)	548.54 (± 88.27)	217.69 (± 1.11)	189.16 (± 0.97)	168.43 (± 0.86)
Nov 7 – Dec 3, 2022	5 (WD)	2.62	2.96	6.79	5.90	5.25
	6 (WD)	2.76	20.13	7.17	6.23	5.55
	7 (TD)	19.85	22.42	51.50	44.75	39.84
	8 (TD)	19.27	136.25	49.99	43.44	38.67
	Avg **(WD, n = 2)**	2.69 (± 0.15)	11.54 (± 17.18)	6.98 (± 0.38)	6.06 (± 0.33)	5.40 (± 0.29)
	Avg **(TD, n = 2)**	19.56 (± 0.58)	79.33 (± 113.83)	50.74 (± 1.51)	44.09 (±1.31)	39.26 (± 1.17)

Table C-9. Comparison of selected total (bulk) deposition literature fluxes (ranges and/or averages; μg m^{-2} $year^{-1}$) to total deposition fluxes found in this study (-- = not measured, LOD = limit of detection, LOQ = limit of quantification).

Location	Date	TFA	PFPrA	PFBA	PFPeA	PFHxA	Reference
Switzerland (total country input)	1996 – 1997	230	--	--	--	--	Berg et al.[3]
Canada (various locations)	1997	44 – 304	--	--	--	--	Scott et al.[4]
Senga Bay, Malawi	1999	73	--	--	--	--	Scott et al.[5]
Concepcion, Chile		33 – 263	--	--	--	--	
Canada (various locations)		62 – 631	--	--	--	--	
Tsukuba, Japan	2006 – 2008	--	4.53 – 10.51	1.28 – 2.03	0.67 – 0.69	0.659 – 1.59	Kwok et al.[6]
Kawaguchi, Japan		--	6.15 – 8.38	1.42 – 1.66	0.80 – 0.82	1.020 – 1.35	
Slingerlands, NY, USA	2006 – 2007	--	3.81	<LOQ	0.21	0.83	
Albany, NY, USA		--	9.02	<LOQ	0.85	1.05	
Barsbuttel, Germany	2007 – 2008	--	--	<LOD – 3.91	--	<LOD – 2.7	Dreyer et al.[7]
Guangzhou, China	2007 – 2008	229	--	--	--	--	Wang et al.[8]
Grand Codroy, NL, Canada	2014 – 2016	--	--	<LOD – 5.48	<LOD – 0.60	<LOD – 0.56	Persaud et al.[2]
Humber River, NL, Canada		--	--	1.31 – 8.91	<LOD – 0.38	<LOD – 1.98	
Salmon River, NL, Canada		--	--	<LOD – 4.51	<LOD – 0.33	<LOD – 1.41	
Eagle River, NL, Canada		--	--	<LOD – 2.19	<LOD – 0.06	<LOD – 0.34	
Mainland China		438 – 5840	0.73 – 98.6	2.19 – 270	2.19 – 146	0.91 – 80.3	Chen et al.[9]
Germany (various locations)	2018 – 2019	91.4-401	--	--	--	--	Freeling et al.[10]
Toronto, ON, Canada	2018 – 2024	66 -1558	--	--	--	--	Persaud et al.[11]

Table C-9 (cont'd). Comparison of selected total (bulk) deposition literature fluxes (ranges and/or averages; μg m^{-2} $year^{-1}$) to total deposition fluxes found in this study (-- = not measured, LOD = limit of detection, LOQ = limit of quantification).

Location	Date	TFA	PFPrA	PFBA	PFPeA	PFHxA	Reference
UW Arboretum, WI, USA	2020	--	--	--	--	0.09 – 1.56	Pfotenhauer et al.[12]
Brule River, WI, USA		--	--	--	--	<LOD – 1.41	
Potawatomi, WI, USA		--	--	--	--	<LOD – 0.97	
Baraboo, WI, USA		--	--	--	--	<LOD – 1.19	
Perkinstown, WI, USA		--	--	--	--	<LOD – 1.20	
Trout Lake, WI, USA		--	--	--	--	0.05 – 1.01	
Spooner, WI, USA		--	--	--	--	<LOD – 1.39	
Marinette, USA		--	--	--	--	<LOD – 2.84	
Tadoussac, QC, Canada	2021 – 2022	38.71 – 807.21	40.98 – 394.21	38.71 – 807.21	40.98 – 394.21	<LOD	This study
Saturna Island, BC, Canada		12.46 – 582.10	5.62 – 548.54	12.46 – 582.10	5.62 – 548.54	<LOD	
Locarno, Switzerland	2021 – 2023	1280	--	1280	--	--	Henne et al.[13]
Jungfraujoch, Switzerland		310	--	310	--	--	
Grächen St. Niklaus, Switzerland		410	--	410	--	--	

Table C-10. Comparison of measured wet deposition (WD) to calculated dry deposition (DD) fluxes at each field site for PFBA, PFPeA, and PFHxA. Dry deposition was calculated by subtracting WD from total deposition (TD). Values containing replicates >LOQ are identified in black, <LOQ are in red, and <LOD are in blue and were reported as half of that analyte's LOD. Due to technical issues with the motor arms deployed during December 15, 2021, to January 18, 2022, at Saturna Island, this sampling period was excluded from the dataset. In instances where WD ≫ TD, asterisked (*) values indicate that TD and WD were not statistically different from each other, and therefore a distinct DD flux could not be resolved. Details on the calculation of uncertainty for WD and DD values are provided in Section C.3. Note that the reported uncertainties in WD reflect observed sample-to-sample variation in deposition samples[1,2] and therefore represent natural environmental heterogeneity rather than analytical error.

	Avg. Volume (L)		**PFBA (µg m^{-2} year^{-1})**		**PFPeA (µg m^{-2} year^{-1})**		**PFHxA (µg m^{-2} year^{-1})**	
Tadoussac, QC	WD	TD	WD	DD	WD	DD	WD	DD
Oct 14 – Nov 14/21	2.55	4.01	48.77 (± 0.67)	28.07 (± 27.77)	41.10 (± 0.57)	23.66 (± 23.78)	30.83 (± 0.42)	17.75 (± 17.29)
Nov 14 – Dec 14/21	0.50	2.00	9.90 (± 0.00)	29.70 (± 14.31)	8.34 (± 0.00)	25.03 (± 12.25)	6.26 (± 0.00)	18.78 (± 8.91)
June 9 – July 13/22	3.60	4.35	61.16 (± 7.23)	12.74 (± 27.66)	51.55 (± 6.09)	10.74 (± 23.66)	38.66 (± 4.57)	8.05 (± 17.24)
July 13 – Aug 12/22	1.63	1.71	301.08 (± 536.42)	0.00*	257.59 (± 459.78)	0.00*	238.60 (± 435.64)	0.00*
Aug 12 – Sept 23/22	2.58	2.78	36.49 (± 0.57)	2.79 (± 19.22)	30.76 (± 0.48)	2.35 (± 0.91)	23.07 (± 0.36)	1.77 (± 0.68)
Sept 23 – Oct 12/22	0.44	0.58	13.60 (± 0.31)	4.53 (± 0.31)	11.46 (± 0.26)	3.82 (± 0.26)	8.60 (± 0.20)	2.87 (± 0.20)
Saturna Island, BC	WD	TD	WD	DD	WD	DD	WD	DD
Jan 18 – Feb 15/22	0.73	1.36	25.49 (± 12.79)	22.16 (± 13.69)	22.15 (± 11.11)	28.25 (± 24.88)	19.72 (± 9.89)	17.14 (± 10.60)
Feb 15 – Mar 15/22	0.24	2.38	8.41 (± 0.70)	74.97 (± 2.22)	7.31 (± 0.61)	65.14 (± 1.93)	6.50 (± 0.54)	58.00 (± 1.71)
Mar 15 – April 13/22	0.64	2.76	21.48 (± 1.01)	71.71 (± 1.97)	18.66 (± 0.88)	62.31 (± 1.71)	16.62 (± 0.79)	55.48 (± 1.53)
April 13 – May 13/22	0.25	1.58	8.09 (± 0.82)	6.26 (± 0.63)	7.03 (± 0.71)	37.86 (± 9.71)	6.26 (± 0.63)	33.71 (± 7.07)
May 13 – June 15/22	0.13	2.48	73.57 (± 4.46)	43.57 (± 11.33)	63.93 (± 3.87)	60.70 (± 3.94)	56.92 (± 3.45)	8.28 (± 1.45)
June 15 – July 26/22	0.13	0.58	6.12 (± 6.75)	7.75 (± 6.95)	2.75 (± 0.73)	9.30 (± 1.63)	10.74 (± 1.30)	10.74 (± 1.30)
July 26 – Sept 1/22	0.04	0.06	1.81 (± 1.50)	0.00*	13.23 (± 24.63)	0.00*	0.77 (± 0.10)	0.51 (± 0.15)
Sept 1 – Oct 16/22	0.13	4.16	2.86 (± 0.61)	0.59 (± 0.97)	2.48 (± 0.53)	0.51 (± 0.84)	2.21 (± 0.47)	0.46 (± 0.67)
Oct 16 – Nov 7/22	0.80	4.88	35.67 (± 15.16)	72.64 (± 4.46)	30.99 (± 13.17)	158.17 (± 13.21)	27.60 (± 11.73)	140.83 (± 11.76)
Nov 7 – Dec 3/22	0.19	1.35	6.98 (± 0.38)	43.76 (± 1.56)	6.06 (± 0.33)	38.03 (± 1.35)	5.40 (± 0.29)	33.86 (± 1.20)

C.3 Wet, Dry, and Total Deposition Fluxes

The average yearly wet and total deposition fluxes for the five target analytes were determined for the samples collected at both Tadoussac and Saturna Island. The concentration of PFCAs in precipitation is affected by volume and is therefore not a reliable indicator for assessing trends in atmospheric deposition to the surface. To incorporate the effect of volume, deposition fluxes (μg m^{-2} $year^{-1}$) were calculated for each analyte using EQ C1.

$$\text{Deposition Flux} = = \left[\frac{\text{Analyte Concentration}\left(\frac{\mu g}{L}\right) \text{ x Volume of Sample (L)}}{\text{Area of Static Sampler (m}^2\text{) x Sampling Duration (days)}}\left(\frac{365 \text{ days}}{1 \text{ year}}\right)\right] \quad \textbf{(EQ C1)}$$

With the area of the static sampler funnel being 0.038013 m^2, deposition fluxes were annualized and averaged to ensure consistency across different sampling periods and to enable direct comparison of atmospheric deposition trends across both sites.

Four collection jugs were placed at each site where a minimum of n =1 and a maximum of n = 3 was collected for either wet or total deposition. When n = 3, the errors associated with that sampling period mean corresponded to the respective standard deviation. The following equations were used to estimate uncertainty when n = 2, where 'n_1' and 'n_2' represent the two total or the two wet deposition average yearly fluxes within the given sampling period (EQ C2).

$$\text{Relative Standard Difference (\%)} = \left(\frac{n_1 - n_2}{\left(\frac{n_1 + n_2}{2}\right)}\right)(100\%) \qquad \textbf{(EQ C2a)}$$

$$\text{Error}_{(n=2)} = \left(\frac{\text{Relative Standard Difference \%}}{100\%}\right)(\text{Yearly Average Flux}) \qquad \textbf{(EQ C2b)}$$

Due to the number of samples in this study, their analyses were grouped into three separate batches (BC deposition, QC deposition, and BC + QC gas-phase) with their own calibration data.

To determine the uncertainty associated with a n = 1 sampling period, the instrument error was used as a proxy and so each set of calibration data was fit to 65% confidence interval where values for the slope (± error), y-intercept, and R^2 were obtained. An average of the three slopes (μg L^{-1}) were determined and then propagation of uncertainty for addition was used to calculate the uncertainty of this averaged value (μg L^{-1}) for each analyte (EQ C3). This error was then transformed into the correct flux units (μg m^{-2} $year^{-1}$) using EQ C4.

$$S_y = \sqrt{(slope\ error_{batch\ 1})^2 + (slope\ error_{batch\ 2})^2 + (slope\ error_{batch\ 3})^2} \quad \textbf{(EQ C3)}$$

$$\text{Error}_{(n=2)} = \left[\frac{\text{Slope Error } \left(\frac{\mu g}{L}\right) \text{ x Volume of Sample (L)}}{\text{Area of Static Sampler } (m^2) \text{ x Sampling Duration (days)}} \left(365 \frac{\text{days}}{\text{year}}\right)\right] \quad \textbf{(EQ C4)}$$

The average yearly dry deposition fluxes were then estimated by subtracting the measured average wet deposition from the measured average total deposition fluxes. The propagation of uncertainty for subtraction, the same as EQ C3, was used to calculate the uncertainty of this calculated value by using the determined errors for average yearly wet and total deposition fluxes.

Table C-11. Concentration (µg L^{-1}) of 3x diluted denuded air samples and travelling field blanks, in 250 µL injection volume, collected at the Tadoussac field site. (To determine the concentration of the original, undiluted 10 mL extract, the 3x diluted concentration was: i) multiplied by the 250 uL injection volume, ii) divided by a dilution factor of 15.15, and iii) further divided by a second dilution factor of 0.125.) Values <LOD are identified in blue, values <LOQ are in red, and values >LOQ are in black.

		Concentration in solution (µg L^{-1})				
Sampling Period	**Denuder**	**TFA**	**PFPrA**	**PFBA**	**PFPeA**	**PFHxA**
Oct 14 – Nov 14, 2021	Field blank	0.506	<0.047	<0.050	<0.030	<0.034
	1	1.274	1.007	<0.050	<0.030	<0.034
	2	1.450	1.337	<0.050	<0.030	<0.034
	3	1.466	0.481	<0.050	<0.030	<0.034
	4	1.660	0.813	<0.050	<0.030	<0.034
Nov 14 – Dec 14, 2021	Field blank	0.204	0.079	<0.050	<0.030	<0.034
	1	0.908	0.790	<0.050	<0.030	<0.034
	2	0.972	0.597	<0.050	<0.030	<0.034
	3	0.766	0.592	<0.050	<0.030	<0.034
	4	0.798	0.482	<0.050	<0.030	<0.034
June 9 – July 13, 2022	Field blank	0.580	<0.047	<0.050	<0.030	<0.034
	1	5.750	8.772	<0.050	<0.030	<0.034
	2	6.511	14.209	<0.050	<0.030	0.322
	3	6.873	13.380	<0.050	<0.030	<0.034
	4	6.848	8.872	<0.050	<0.030	<0.034
July 13 – Aug 12, 2022	Field blank	0.391	0.471	<0.050	<0.030	<0.034
	1	5.312	6.316	<0.050	<0.030	<0.034
	2	4.283	3.593	<0.050	<0.030	<0.034
	3	2.834	3.076	<0.050	<0.030	<0.034
	4	5.872	5.808	<0.050	<0.030	<0.034
Aug 12 – Sept 23, 2022	Field blank	0.397	0.095	<0.050	<0.030	<0.034
	1	-	-	-	-	-
	2	5.433	3.745	<0.050	0.531	<0.034
	3	4.664	3.491	<0.050	0.394	<0.034
	4	-	-	-	-	-
Sept 23 – Oct 12, 2022	Field blank (rep. 1)	0.702	0.294	<0.050	<0.030	<0.034
	Field blank (rep. 2)	0.715	0.290	<0.050	<0.030	<0.034
	Field blank (rep. 3)	0.697	0.278	<0.050	<0.030	<0.034
	1	1.203	1.256	<0.050	<0.030	<0.034
	2	1.534	1.417	<0.050	<0.030	<0.034
	3	1.337	1.040	4.382	<0.030	<0.034
	4	1.281	1.233	<0.050	<0.030	<0.034

Table C-12. Concentration (µg L^{-1}) of 3x diluted denuded air samples and travelling field blanks, in 250 µL injection volume, collected at the Saturna Island field site. (To determine the concentration of the original, undiluted 10 mL extract, the 3x diluted concentration was: i) multiplied by the 250 uL injection volume, ii) divided by a dilution factor of 15.15, and iii) further divided by a second dilution factor of 0.125.) Values <LOD are identified in blue, values <LOQ are in red, and values >LOQ are in black.

		Concentration in solution (µg L^{-1})				
Sampling Period	**Denuder**	**TFA**	**PFPrA**	**PFBA**	**PFPeA**	**PFHxA**
Dec 15, 2021 – Jan 18, 2022	Field blank	0.614	0.100	<0.050	<0.030	<0.034
	1	0.950	0.259	<0.050	<0.030	<0.034
	2	1.242	1.877	<0.050	<0.030	<0.034
	3	2.764	1.724	<0.050	<0.030	<0.034
	4	2.045	1.244	<0.050	<0.030	<0.034
Jan 18 – Feb 15, 2022	Field blank	0.505	<0.047	<0.050	<0.030	<0.034
	1	2.291	3.018	<0.050	0.113	<0.034
	2	2.401	2.979	<0.050	0.126	<0.034
	3	1.119	2.153	<0.050	0.099	<0.034
	4	14.953	2.531	<0.050	<0.030	<0.034
Feb 15 – Mar 15, 2022	Field blank	0.473	<0.047	<0.050	<0.030	<0.034
	1	1.756	<0.047	0.564	<0.030	<0.034
	2	1.329	<0.047	0.520	<0.030	<0.034
	3	1.067	1.317	0.427	<0.030	<0.034
	4	1.565	1.271	0.389	<0.030	<0.034
Mar 15 – April 13, 2022	Field blank	0.737	<0.047	<0.050	<0.030	<0.034
	1	1.667	0.500	0.257	<0.030	<0.034
	2	-	-	-	-	<0.034
	3	2.454	0.436	0.373	<0.030	<0.034
	4	1.971	0.506	0.279	<0.030	<0.034
April 13 – May 13, 2022	Field blank (rep. 1)	0.468	0.070	<0.050	<0.030	<0.034
	Field blank (rep. 2)	0.429	0.078	<0.050	<0.030	<0.034
	Field blank (rep. 3)	0.413	0.060	<0.050	<0.030	<0.034
	1	2.831	<0.047	0.476	<0.030	<0.034
	2	2.848	1.194	0.525	<0.030	<0.034
	3	3.028	1.353	0.689	<0.030	<0.034
	4	2.156	1.159	0.445	<0.030	<0.034
May 13 – June 15, 2022	Field blank	0.502	<0.047	<0.050	<0.030	<0.034
	1	14.207	2.355	<0.050	<0.030	<0.034
	2	9.811	2.131	<0.050	<0.030	<0.034
	3	18.928	2.845	<0.050	<0.030	<0.034
	4	14.902	2.144	<0.050	<0.030	<0.034
June 15 – July 26, 2022	Travelling field blank	0.893	0.086	<0.050	<0.030	<0.034
	1	9.046	2.506	1.044	<0.030	<0.034
	2	8.380	<0.047	1.093	<0.030	<0.034
	3	9.098	3.012	1.167	<0.030	<0.034
	4	7.724	2.033	0.751	<0.030	<0.034

Table C-12 (cont'd). Concentration (µg L^{-1}) of 3x diluted denuded air samples and travelling field blanks, in 250 µL injection volume, collected at the Saturna Island field site. (To determine the concentration of the original, undiluted 10 mL extract, the 3x diluted concentration was: i) multiplied by the 250 uL injection volume, ii) divided by a dilution factor of 15.15, and iii) further divided by a second dilution factor of 0.125.) Values <LOD are identified in blue, values <LOQ are in red, and values >LOQ are in black.

		Concentration in solution (µg L^{-1})				
Sampling Period	**Denuder**	**TFA**	**PFPrA**	**PFBA**	**PFPeA**	**PFHxA**
July 26 – Sept 1, 2022	Travelling field blank	0.765	0.311	<0.050	<0.030	<0.034
	1	9.338	3.224	<0.050	0.153	<0.034
	2	7.838	4.247	<0.050	0.380	<0.034
	3	8.214	3.440	<0.050	0.184	<0.034
	4	11.164	3.333	<0.050	0.308	<0.034
Sept 1 – Oct 16, 2022	Travelling field blank	0.616	0.732	<0.050	<0.030	<0.034
	1	7.039	2.897	0.819	<0.030	<0.034
	2	5.185	2.049	0.942	<0.030	<0.034
	3	8.464	3.783	1.538	<0.030	<0.034
	4	7.974	3.405	0.931	<0.030	<0.034
Oct 16 – Nov 7, 2022	Travelling field blank (rep. 1)	2.140	<0.047	<0.050	0.119	<0.034
	Travelling field blank (rep. 2)	2.126	<0.047	<0.050	0.133	<0.034
	Travelling field blank (rep. 3)	2.103	<0.047	<0.050	0.134	<0.034
	1	3.317	3.050	0.584	<0.030	<0.034
	2	2.885	3.175	0.868	<0.030	<0.034
	3	3.710	2.505	1.077	<0.030	<0.034
	4	2.819	<0.047	<0.050	<0.030	<0.034
Nov 7 – Dec 3, 2022	Travelling field blank	0.714	<0.047	<0.050	0.081	<0.034
	1	1.598	2.394	0.659	<0.030	<0.034
	2	1.575	1.386	0.830	<0.030	<0.034
	3	1.725	4.602	0.441	<0.030	<0.034
	4	1.527	3.042	0.555	<0.030	<0.034

Table C-13. Concentration (pg m^{-3}) and mixing ratios (ppqv) of denuded air samples collected at the Tadoussac field site. Values >LOQ are identified in black, values <LOQ are in red, and values <LOD are identified in blue and are here reported as half of that analyte's LOD. For sampling periods where n = 2, 3, or 4, the mean values are reported. The associated uncertainties are reported as followed - for sampling periods where: i) n = 4, the standard deviation of the mean is recorded and ii) n = 2, the uncertainty is expressed as the relative difference between the two samples, converted to absolute units using the mean. *Italicized* values were identified as statistical outliers at the 95% confidence interval according to Grubb's test ($G_{calc} > G_{critical}$) and were not included in the reported averages and associated uncertainties. Entries with "--" for uncertainty indicate that, although minor variability existed on a mass basis due to differences in sampled air volume, replicate PFCA levels were identical after conversion and rounding to one decimal place to avoid false precision, resulting in a calculated uncertainty of zero.

		TFA		**PFPrA**		**PFBA**		**PFPeA**		**PFHxA**	
	Denuder	**pg m^{-3}**	**ppqv**	**pg m^{-3}**	**ppqv**	**pg m^{-3}**	**ppqv**	**pg m^{-3}**	**ppqv**	**pg m^{-3}**	**ppqv**
Oct 14 – Nov 14, 2021	1	106	21	84	12	10.0	1.1	6.8	0.6	4.8	0.4
	2	119	11	109	15	9.8	1.1	6.7	0.6	4.7	0.4
	3	121	24	40	6	9.9	1.1	6.8	0.6	4.8	0.4
	4	135	27	66	9	9.8	1.1	6.7	0.6	4.7	0.3
	Avg (**n = 4**)	120	21	75	10	9.9	1.1	6.8	0.6	4.8	0.4
	Uncertainty	12	7	30	4	0.1	--	0.1	--	0.1	--
Nov 14 – Dec 14, 2021	1	85	17	74	10	11.3	1.2	7.7	0.7	5.4	0.4
	2	83	16	51	7	10.3	1.1	7.1	0.6	5.0	0.4
	3	67	13	52	7	10.6	1.1	7.2	0.6	5.1	0.4
	4	67	13	41	6	10.1	1.1	6.9	0.6	4.9	0.4
	Avg (**n = 4**)	76	15	55	7	10.6	1.1	7.2	0.6	5.1	0.4
	Uncertainty	10	2	14	2	0.5	0.1	0.3	--	0.2	--
June 9 – July 13, 2022	1	449	93	684	99	9.4	1.0	6.4	0.6	4.5	0.3
	2	499	104	1088	157	9.2	1.0	6.3	0.6	*24.6*	*1.9*
	3	526	109	1024	148	9.2	1.0	6.3	0.6	4.4	0.3
	4	505	105	655	95	8.9	1.0	6.1	0.5	4.3	0.3
	Avg (**n = 4**)	495	193	863	125	9.2	1.0	6.3	0.6	4.4	0.3
	Uncertainty	33	7	225	32	0.2	--	0.1	--	0.1	--
July 13 – Aug 12 2022	1	466	97	554	81	10.5	1.2	7.2	0.7	5.1	0.4
	2	378	79	317	46	10.6	1.2	7.3	0.7	5.1	0.4
	3	246	51	267	39	10.4	1.2	7.1	0.6	5.0	0.4
	4	494	103	488	71	10.1	1.1	6.9	0.6	4.9	0.4
	Avg (**n = 4**)	396	83	406	59	10.4	1.2	7.1	0.6	5.0	0.4
	Uncertainty	112	23	137	20	0.2	--	0.2	--	0.1	--
Aug 12 – Sept 23, 2022	2	345	71	238	34	7.6	0.8	33.7	3.0	3.7	0.3
	3	289	60	216	31	7.4	0.8	24.4	2.2	3.6	0.3
	Avg (**n = 2**)	317	65	227	33	7.5	0.8	29.1	2.6	3.6	0.3
	Uncertainty	56	12	22	3	0.2	--	9.3	0.8	0.1	--
Sept 23 – Oct 12, 2022	1	168	34	175	25	16.8	1.8	11.5	1.0	8.1	0.6
	2	217	44	200	28	17.0	1.8	11.6	1.0	8.2	0.6
	3	184	37	143	20	*604.4*	*65.4*	11.3	1.0	8.0	0.6
	4	171	35	165	23	16.1	1.7	11.0	1.0	7.7	0.6
	Avg (**n = 4**)	185	38	172	24	16.6	1.8	11.4	1.0	8.0	0.6
	Uncertainty	22	5	24	3	0.5	0.1	0.3	--	0.2	--

Table C-14. Concentration (pg m^{-3}) and mixing ratios (ppqv) of denuded air samples collected at the Saturna Island field site. Values >LOQ are identified in black, values <LOQ are in red, and values <LOD are identified in blue and are here reported as half of that analyte's LOD. The average mean values are reported with their associated standard deviations (n = 3 or 4). Those uncertainties *Italicized* values were identified as statistical outliers at the 95% confidence interval according to Grubb's test ($G_{calc} > G_{critical}$) and were not included in the reported averages and associated uncertainties. Entries with "--" for uncertainty indicate that, although minor variability existed on a mass basis due to differences in sampled air volume, replicate PFCA levels were identical after conversion and rounding to one decimal place to avoid false precision, resulting in a calculated uncertainty of zero.

		TFA		PFPrA		PFBA		PFPeA		PFHxA	
	Denuder	**pg m^{-3}**	**ppqv**	**pg m^{-3}**	**ppqv**	**pg m^{-3}**	**ppqv**	**pg m^{-3}**	**ppqv**	**pg m^{-3}**	**ppqv**
Dec 15, 2021 – Jan 18, 2022	1	71	14	19	3	9.0	0.9	6.1	0.5	4.3	0.3
	2	93	18	140	19	9.0	0.9	6.1	0.5	4.3	0.3
	3	206	41	129	18	9.0	0.9	6.1	0.5	4.3	0.3
	4	157	31	96	13	9.2	1.0	6.3	0.5	4.4	0.3
	Avg (**n = 4**)	132	36	96	13	9.0	1.0	6.2	0.5	4.3	0.3
	Uncertainty	62	12	54	7	0.1	--	0.1	--	0.1	--
Jan 18 – Feb 15, 2022	1	208	42	1	38	10.9	1.2	10.2	0.9	5.2	0.4
	2	224	45	1	39	11.2	1.2	11.8	1.0	5.4	0.4
	3	101	20	1	27	10.9	1.2	9.0	0.8	5.2	0.4
	4	*1490*	*298*	1	35	12.0	1.3	8.2	0.7	5.8	0.4
	Avg (**n = 4**)	178	36	250	35	11.2	1.2	9.8	0.9	5.4	0.4
	Uncertainty	67	13	38	5	0.5	0.1	1.6	0.1	0.3	--
Feb 15 – Mar 15, 2022	1	159	32	3	0.5	51.0	5.4	7.4	0.6	5.2	0.4
	2	135	27	4	0.5	52.7	5.6	8.3	0.7	5.9	0.4
	3	96	19	119	17	38.6	4.1	7.4	0.6	5.2	0.4
	4	164	33	133	18.55	40.8	4.4	8.6	0.7	6.1	0.4
	Avg (**n = 4**)	139	28	65	9	45.8	4.8	8.0	0.7	5.6	0.4
	Uncertainty	31	6	71	10	7.1	0.8	0.6	0.1	0.4	--
Mar 15 – April 13, 2022	1	148	30	44	6	22.3	2.4	7.3	0.6	5.1	0.4
	3	213	43	38	5	32.3	3.5	7.1	0.6	5.0	0.4
	4	206	42	53	7	29.2	3.1	8.6	0.8	6.0	0.4
	Avg (**n = 4**)	189	38	45	6	27.9	3.0	7.7	0.7	5.4	0.4
	Uncertainty	36	7	8	1	5.2	0.6	0.8	0.1	0.6	--
Apri13 – May 13, 2022	1	242	49	*3*	*0*	40.7	4.4	7.0	0.6	4.9	0.4
	2	281	57	118	17	51.9	5.6	8.1	0.7	5.7	0.4
	3	253	51	113	16	57.5	6.2	6.9	0.6	4.8	0.4
	4	216	44	116	16	44.5	4.8	8.2	0.7	5.8	0.4
	Avg (**n = 4**)	248	50	116	16	48.7	5.2	7.6	0.7	5.3	0.4
	Uncertainty	27	5	3	--	7.5	0.8	0.7	0.1	0.5	--
May 13 – June 15, 2022	1	1106	227	183	26	9.4	1.0	6.4	0.6	4.5	0.3
	2	882	181	192	27	10.8	1.2	7.4	0.7	5.2	0.4
	3	1483	304	223	32	9.4	1.0	6.4	0.6	4.5	0.3
	4	1409	289	203	29	11.4	1.2	7.8	0.7	5.5	0.4
	Avg (**n = 4**)	1220	250	200	29	10.2	1.1	7.0	0.6	4.9	0.4
	Uncertainty	278	57	17	2	1.0	0.1	0.7	0.1	0.5	--

Table C-14 (cont'd). Concentration (pg m^{-3}) and mixing ratios (ppqv) of denuded air samples collected at the Saturna Island field site. Values >LOQ are identified in black, values <LOQ are in red, and values <LOD are identified in blue and are here reported as half of that analyte's LOD. The average mean values are reported with their associated standard deviations (n = 3 or 4). *Italicized* values were identified as statistical outliers at the 95% confidence interval according to Grubb's test ($G_{calc} > G_{critical}$) and were not included in the reported averages and associated uncertainties. Entries with "--" for uncertainty indicate that, although minor variability existed on a mass basis due to differences in sampled air volume, replicate PFCA levels were identical after conversion and rounding to one decimal place to avoid false precision, resulting in a calculated uncertainty of zero.

		TFA		PFPrA		PFBA		PFPeA		PFHxA	
	Denuder	**pg m^{-3}**	**ppqv**	**pg m^{-3}**	**ppqv**	**pg m^{-3}**	**ppqv**	**pg m^{-3}**	**ppqv**	**pg m^{-3}**	**ppqv**
June 15 – July 26, 2022	1	567	118	157	23	65.4	7.3	5.1	0.5	3.6	0.3
	2	566	118	*2*	*0*	73.9	8.2	5.6	0.5	3.9	0.3
	3	577	120	191	28	74.0	8.2	5.2	0.5	3.7	0.3
	4	522	109	137	20	50.8	5.6	5.6	0.5	3.9	0.3
	Avg (**n = 4**)	558	116	162	23	66.0	7.3	5.4	0.5	3.8	0.3
	Uncertainty	24	5	27	4	10.9	1.2	0.2	--	0.2	--
July 26 – Sept 1, 2022	1	647	137	223	33	8.3	0.9	10.6	1.0	4.0	0.3
	2	543	115	294	43	8.3	0.9	26.3	2.4	4.0	0.3
	3	580	123	243	36	8.5	1.0	13.0	1.2	4.1	0.3
	4	783	166	234	34	8.4	1.0	21.6	2.0	4.1	0.3
	Avg (**n = 4**)	638	135	249	37	8.4	0.9	17.9	1.6	4.0	0.3
	Uncertainty	106	22	31	5	0.1	--	7.3	0.7	--	--
Sept 1 – Oct 16, 2022	1	402	84	166	24	46.8	5.2	4.7	0.4	3.3	0.3
	2	296	62	117	17	53.9	6.0	4.7	0.4	3.3	0.3
	3	490	102	219	32	89.0	9.9	4.8	0.4	3.3	0.3
	4	461	96	197	29	53.9	6.0	4.8	0.4	3.3	0.3
	Avg (**n = 4**)	413	86	175	25	60.9	6.8	4.7	0.4	3.3	0.3
	Uncertainty	86	18	44	6	19.0	2.1	--	--	--	--
Oct 16 – Nov 7, 2022	1	387	78	356	50	68.1	7.4	9.6	0.8	6.7	0.5
	2	343	70	377	53	103.1	11.1	9.8	0.9	6.9	0.5
	3	441	89	298	42	127.9	13.8	9.8	0.9	6.9	0.5
	4	337	68	*4*	*1*	14.4	1.6	9.8	0.9	6.9	0.5
	Avg (**n = 4**)	377	76	344	48	78.4	8.5	9.7	0.9	6.8	0.5
	Uncertainty	48	10	41	6	49.2	5.3	0.1	--	0.1	--
Nov 7 – Dec 3, 2022	1	158	31	237	33	65.1	6.9	8.1	0.7	5.7	0.4
	2	161	32	141	20	84.6	9.0	8.4	0.7	5.9	0.4
	3	175	35	466	64	44.7	4.7	8.3	0.7	5.9	0.4
	4	153	30	304	42	55.5	5.9	8.2	0.7	5.8	0.4
	Avg (**n = 4**)	161	32	287	40	62.4	6.6	8.3	0.7	5.8	0.4
	Uncertainty	9	2	137	19	17.0	1.8	0.1	--	0.1	--

C.4 Gas-phase PFAS Sampling

C.4.1 Calculating Atmospheric Mixing Ratios

To compare directly to what has been reported in the literature, these diluted concentrations were converted to both mass concentrations in air (pg m^{-3}) and atmospheric mixing ratios (ppqv). The concentration (in solution) of the diluted sample was used to determine the amount (moles) of each PFCA within the original undiluted extract. The amount of PFCA was then divided by the original extract volume (10 mL) and using the total volume of air sampled by the MVSs, the concentration in air was determined. Next, both the number density of air (calculated using the average temperature of each sampling period and assuming standard pressure) and the molar PFCA concentration were determined, each expressed in units of mol m^{-3}. The atmospheric PFCA mixing ratios for the replicates in each individual sampling period were calculated, averaged, and reported with their respective uncertainties.

C.4.2 Comparing Active and Passive Air Sampling

Four annular denuders were initially deployed at each site, where a minimum of N = 3 and a maximum of N = 4 samples were collected during the given sampling period and used to determine the average atmospheric mixing ratio of each PFCA. For sampling periods with N = 3 or N = 4, the associated errors corresponded to the standard deviation. To better compare this data to the concurrent PAS measurements, a weighted average ($x_{weighted}$, ppqv) was determined (EQ C5). For the Tadoussac and Saturna Island data, n = 4 and n = 11 sampling intervals were accounted for, respectively, within the total weighted averages for each analyte. Here $x_{measured}$ is the average mixing ratio (ppqv) for a given sampling interval (t_i, days) and t_{total} is the duration of the entire sampling period being considered (days). The propagation of uncertainty for addition (EQ C6) was used to calculate the standard error of the weighted total (EQ C7). For the Tadoussac and Saturna

Island data, N = 14 and N = 42 sampling intervals were accounted for within the standard error, respectively.

$$x_{weighted} = \left(\sum_i^n \left(x_{measured} \times \frac{t_i}{t_{total}}\right)\right) \qquad \textbf{(EQ C5)}$$

$$S_y = \sqrt{\left(stdev_{period\ 1}\right)^2 + \left(stdev_{period\ 2}\right)^2 + \left(stdev_{period\ 3}\right)^2 \ldots} \qquad \textbf{(EQ C6)}$$

$$\text{Standard Error} = \frac{S_y}{\sqrt{N}} \qquad \textbf{(EQ C7)}$$

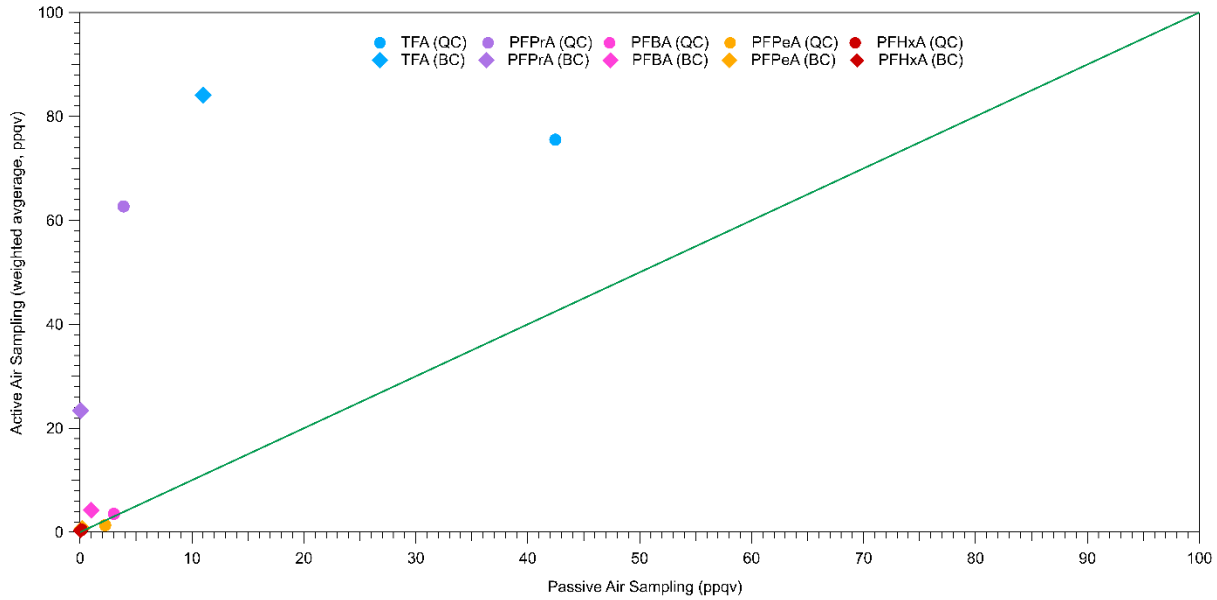

Figure C-7. Comparison of atmospheric mixing ratios of C2 to C6 PFCAs in active (denuder) and passive air samples collected at the Tadoussac (QC) and Saturna Island (BC) field sites. The atmospheric mixing ratios from active samples (weighted, ppqv) are plotted against corresponding passive measurements (ppqv). The green 1:1 line indicates equal agreement between the two sampling approaches.

C.5 References

1. Colussi, A. A.; Persaud, D.; Lao, M.; Place, B. K.; Hems, R. F.; Ziegler, S. E.; Edwards, K. A.; Young, C. J.; VandenBoer, T. C. Cost-effective off-grid automatic precipitation samplers for pollutant and biogeochemical atmospheric deposition. *Atmos. Meas. Tech.* **2024**, *17*(12), 3697–3718.

2. Persaud, D.; VandenBoer, T. C.; Place, B. K.; Edwards, K. A.; Ziegler, S. E.; Spencer, C.; De Silva, A. O.; Young, C. J. The Occurrence of Legacy Perfluoroalkyl Substances (PFAS) Deposited along a Latitudinal Transect in Newfoundland and Labrador, Canada. **2026**. *Just submitted*.

3. Berg, M.; Müller, S. R.; Mühlemann, J.; Wiedmer, A.; Schwarzenbach, R. P. Concentrations and mass fluxes of chloroacetic acids and trifluoroacetic acid in rain and natural waters in Switzerland. *Environ. Sci. Technol.* **2000**, *34*(13), 2675–2683.

4. Scott, B. F.; MacTavish, D.; Spencer, C.; Strachan, W. M.; Muir, D. C. Haloacetic acids in Canadian lake waters and precipitation. *Environ. Sci. Technol.* **2000**, *34*(20), 4266–4272.

5. Scott, B. F.; Spencer, C.; Martin, J. W.; Barra, R.; Bootsma, H. A.; Jones, K. C.; Johnston, A. E.; Muir, D. C. G. Comparison of haloacetic acids in the environment of the northern and southern hemispheres. *Environ. Sci. Technol.* **2005**, *39*(22), 8664–8670.

6. Kwok, K. Y.; Taniyasu, S.; Yeung, L. W. Y.; Murphy, M. B.; Lam, P. K. S.; Horii, Y.; Kannan, K.; Petrick, G.; Sinha, R. K.; Yamashita, N. Flux of perfluorinated chemicals through wet deposition in Japan, the United States, and several other countries. *Environ. Sci. Technol.* **2010**, *44*(18), 7043−7049.

7. Dreyer, A.; Matthias, V.; Weinberg, I.; Ebinghaus, R. Wet deposition of poly-and perfluorinated compounds in Northern Germany. *Environ. Pollut.* **2010**, *158*(5), 1221–1227.

8. Wang, Q.; Wang, X.; Ding, X. Rainwater trifluoroacetic acid (TFA) in Guangzhou, South China: Levels, wet deposition fluxes and source implication. *Sci. Total Environ.* **2014**, *468*, 272–279.

9. Chen, H.; Zhang, L.; Li, M.; Yao, Y.; Zhao, Z.; Munoz, G.; Sun, H. Per-and polyfluoroalkyl substances (PFASs) in precipitation from mainland China: Contributions of unknown precursors and short-chain (C2C3) perfluoroalkyl carboxylic acids. *Water Res.* **2019**, *153*, 169–177.

10. Freeling, F.; Behringer, D.; Heydel, F.; Scheurer, M.; Ternes, T. A.; Nödler, K. Trifluoroacetate in precipitation: deriving a benchmark data set. *Environ. Sci. Technol.* **2020**, *54*(18), 11210–11219.

11. Persaud, D.; Joudan, S.; VandenBoer, T. C.; Young, C. J. Atmospheric removal of trifluoroacetic acid by dry and wet deposition: a multiyear analysis in Toronto. *Environ. Sci. Technol. Lett*. **2026**, *13*(2), 261–267. doi: 10.1021/acs.estlett.5c01100.

12. Pfotenhauer, D.; Sellers, E.; Olson, M.; Praedel, K.; Shafer, M. PFAS concentrations and deposition in precipitation: An intensive 5-month study at National Atmospheric Deposition Program–National trends sites (NADP-NTN) across Wisconsin, USA. *Atmos. Environ.* **2022**, *291*, 119368.

13. Henne, S.; Storck, F. R.; Wöhrnschimmel, H.; Leuenberger, M.; Vollmer, M. K.; Reimann, S. Trifluoroacetate (TFA) in precipitation and surface waters in Switzerland: trends, source attribution, and budget. *Atmos. Chem. Phys.* **2025**, *25*(23), 18157–18186.

Chapter 5

Conclusions and Future Directions

5.1 Conclusions

This dissertation developed and applied new laboratory and field-based approaches to improve the measurement and understanding of the atmospheric oxidation and deposition of per- and polyfluoroalkyl substances (PFAS). By integrating chamber experiments, method development, and field observations, this work provides mechanistic and quantitative insights on the formation, transport, and environmental input of PFAS, with a particular focus on ultrashort- and short-chain perfluorocarboxylic acids (PFCAs).

In Chapter 2, an oxidation flow reactor (OFR) was coupled to proton-transfer-reaction time-of-flight mass spectrometry (PTR-ToF-MS) to investigate, for the first time, the hydroxyl (OH)-initiated oxidation of a PFAS precursor – the 4:2 fluorotelomer alcohol (FTOH). This approach enabled real-time detection of oxidation products under low-NO_x ($NO + NO_2$) conditions and at atmospherically relevant relative humidities (RHs). The determined pseudo-first-order rate constants were $(1.0 \pm 0.1) \times 10^{-12}$ (22% RH), $(7.4 \pm 0.8) \times 10^{-13}$ (44% RH), and $(7.2 \pm 0.8) \times 10^{-13}$ cm^3 $molecules^{-1}$ s^{-1} (60% RH), indicating a decrease in observed reaction rates with increasing RH. These results provide initial experimental constraints on the role of water vapour in PFAS oxidation chemistry and demonstrate the capability of OFR-PTR-ToF-MS to resolve early-stage transformation pathways of volatile PFAS within a laboratory setting.

Chapter 3 introduced a cost-effective, automated precipitation sampler capable of off-grid operation for long-term wet deposition measurements. These samplers were successfully deployed during the growing seasons of 2015 and 2016 at four remote sites within the Newfoundland and Labrador Boreal Ecosystem Latitudinal Transect. Field measurements showed pH values ranging from 4.14 to 5.71, conductivities from 21 to 166 μS cm^{-1}, and dissolved organic carbon fluxes spanning 600 to 4200 mg C m^{-2} $year^{-1}$, consistent with previously reported values, supporting the

reliability of the sampling approach. Laboratory and field validation of these samplers further demonstrated reliable performance in collecting and preserving sample integrity. The ability to selectively collect conductive precipitation and operate off-grid represents a practical advancement for expanding deposition monitoring into remote environments. As a result, the utility of this automated sampler has already been demonstrated through its application in recent PFAS deposition measurements, further highlighting its value for generating reliable atmospheric data in both urban[1] and remote[2] environments.

In Chapter 4, we present the first quantitative validation of sodium carbonate (Na_2CO_3)-coated annular denuders for capturing gas-phase perfluoropropionic acid (PFPrA). With a measured capture efficiency of 99.83 ± 0.03%, this represents a highly reliable, artifact-minimized method for gas-phase PFPrA sampling, consistent with the quantitative collection reported for other strong atmospheric acids. The annular denuders were then deployed in the field with active air samplers, alongside the automated deposition samplers introduced in Chapter 3. Field measurements made at rural (Tadoussac, Québec) and remote (Saturna Island, British Columbia) sites within regions home to endangered Canadian whale populations demonstrated the widespread presence of ultrashort-chain and short-chain PFCAs in both the gas phase and deposition. Across both sites, trifluoroacetic acid (TFA) and PFPrA dominated, indicating that atmospheric PFAS inputs are currently skewed toward highly mobile ultrashort-chain species. Gas-phase mixing ratios of 11 to 304 (TFA) and 0.4 to 157 (PFPrA) parts-per-quadrillion-by-volume were measured at both sites. Corresponding wet and total deposition fluxes ranged from 16.67 to 807.21 (TFA) and 6.97 to 592.67 (PFPrA) $\mu g\ m^{-2}\ year^{-1}$, with generally higher values at Tadoussac compared to Saturna Island. Site-specific differences in wet versus dry deposition fluxes further highlighted the influence of precipitation patterns and regional transport. Intercomparison with concurrently made

passive air sampler measurements[3] showed that active denuder sampling consistently measured higher PFCA concentrations, reflecting its ability to sample episodic events and potentially capture reactive precursor species.

Collectively, these findings demonstrate measurable atmospheric inputs of PFAS to remote and sensitive ecosystems. The combination of validated gas-phase and deposition measurements provides a framework for quantifying these inputs and assessing their spatial and temporal variability. Overall, this dissertation makes three primary contributions: i) it establishes OFR-PTR-ToF-MS as a viable laboratory method for real-time investigation of PFAS oxidation under atmospherically relevant conditions; ii) it develops and validates an adaptable, cost-effective, and off-grid precipitation sampler for long-term wet deposition measurements; and iii) it demonstrates that Na_2CO_3-coated denuder-based sampling, validated here for PFPrA enables quantitative, artifact-minimized field measurements of ultrashort-chain gas phase PFCAs. By linking laboratory oxidation experiments with field-based measurements of atmospheric deposition, this work strengthens the ability to measure atmospheric PFAS inputs to surface environments. These approaches provide a foundation for improving atmospheric PFAS monitoring, informing environmental models, and supporting future exposure assessments in vulnerable ecosystems.

5.2 Future Directions

5.2.1 Atmospheric PFAS as a Priority Environmental Issue in Canada

Atmospheric PFAS are widespread environmental contaminants and have become increasingly prevalent in Canadian ecosystems due to their persistence, potential for long-range atmospheric transport, and accumulation in remote environments.[4] Ultrashort- and short-chain PFCAs, such as TFA and PFPrA, are now frequently detected in precipitation and air masses far

from known emission sources[5,6], indicating that atmospheric transport is a key pathway delivering PFAS and their precursors to remote environments. Monitoring these fluorinated compounds is particularly important within Canada, where atmospheric deposition contributes to the contamination of watersheds supporting drinking water resources, fisheries, and ecologically sensitive ecosystems.[7,8] Remote regions such as the Arctic, sub-Arctic, and Atlantic coastal zones are especially vulnerable due to limited local emissions but efficient input of long-lived atmospheric contaminants.[9] The presence of PFAS in these regions therefore reflects hemispheric-scale transport combined with continuous atmospheric formation from precursor compounds.[10] Consequently, atmospheric PFAS deposition should be treated as a priority within Canadian environmental monitoring strategies focused on long-term exposure and environmental accumulation. This is a perspective that aligns with Canada's evolving approach to PFAS management as there has been recent movement toward class-based regulatory assessment under the Canadian Environmental Protection Act for all PFAS excluding fluoropolymers.[11] This reflects growing recognition that these substances should be addressed as a chemically related group rather than as individual compounds and highlights the need for improved atmospheric data to support risk assessment and policy development.[11] Addressing this need requires robust measurement approaches capable of resolving both atmospheric transformation processes and deposition pathways, as developed and applied in this dissertation.

5.2.2 Development of Laboratory Platforms for Investigating PFAS Oxidation

Future work should continue advancing laboratory approaches for resolving atmospheric PFAS oxidation, particularly through the utilization of enhanced analytical detection. The OFR-PTR-ToF-MS framework developed in this dissertation enables real-time observation of PFAS

oxidation under atmospherically relevant RHs; however, its capabilities could be extended through complementary techniques. For example, coupling an OFR to iodide-adduct chemical ionization mass spectrometry (I-CIMS) represents a key opportunity to improve sensitivity and extend detection toward lower-volatility and more functionalized oxidation products.[12,13] While PTR-ToF-MS provides robust real-time measurements, I-CIMS offers greater chemical selectivity and has been successfully applied to a range of PFAS, including FTOHs[14,15,] TFA[16,17], and additional compounds such as perfluorobutanoic acid, perfluorohexanoic acid, perfluorooctanoic acid (PFOA), and perfluorooctane sulfonic acid (PFOS).[15] This broader analytical coverage would enable more complete characterization of oxidation pathways.

In contrast to fluorinated alcohols, non-fluorinated alcohols such as n-butanol[18] and 1-pentanol[19] react relatively rapidly with OH radicals and have reported rate constants – in the presence and absence of NO_x – of $(8.86 \pm 0.85) \times 10^{-12}$ cm^3 $molecule^{-1}$ s^{-1} and $(1.11 \pm 0.11) \times 10^{-11}$ cm^3 $molecule^{-1}$ s^{-1}, respectively, at room temperature under dry conditions. In both cases, oxidation occurs primarily via hydrogen abstraction at the α-carbon adjacent to the alcohol group, forming alkyl radicals that react with molecular oxygen to yield aldehydes (e.g., butyraldehyde, pentanal) and smaller fragmentation products. By comparison, the measured rate constants in Chapter 2 for the reaction of OH radicals with 4:2 FTOH under low-NO_x conditions, $(1.0 \pm 0.1) \times 10^{-12}$ (22% RH), $(7.4 \pm 0.8) \times 10^{-13}$ (44% RH), and $(7.2 \pm 0.8) \times 10^{-13}$ cm^3 $molecule^{-1}$ s^{-1} (60% RH), show a decrease between 22% and 44% RH, with little further change at higher RH. The lower rate constants observed for 4:2 FTOH relative to non-fluorinated alcohols are consistent with established structure-reactivity relationships for polyfluorinated compounds, in which electron-withdrawing fluorine substituents reduce OH radical reactivity by suppressing hydrogen abstraction.[20] In contrast, non-fluorinated alcohols exhibit higher reactivity toward OH radicals

due to weaker C-H bond dissociation energies and the formation of more stabilized alkyl radicals.[21] While hydrogen abstraction at the carbon adjacent to the alcohol group remains the dominant pathway for both FTOHs and non-fluorinated alcohols[10,22,23], fluorination alters radical stability and reaction pathways, favouring, ultimately, the formation of PFCAs[10,22], rather than the less persistent oxidation products typical of hydrocarbon oxidation.

The apparent variation in measured rate constants with increasing RH further suggests that water vapour may influence observed oxidation kinetics, although a definitive mechanistic interpretation cannot be made and contributions from system artifacts cannot be ruled out. While non-fluorinated alcohols can exhibit water-assisted rate enhancements through weak complex formation and transition-state stabilization[24], the apparent decrease in observed rate constants for the 4:2 FTOH suggests that water vapour may influence FTOH oxidation in a system-specific manner that is not yet resolved within the current experimental framework. From 22% to 44% RH, the rate constant decreases by approximately 26%, corresponding to an increase in the inferred atmospheric lifetime by a factor of ~1.35. Based on estimated FTOH atmospheric lifetimes of lifetimes of ~10 to 20 days[25], this suggests an extended lifetime of approximately ~13 to 27 days under more humid conditions. While the mechanism remains uncertain, this extended persistence increases the potential for long-range atmospheric transport prior to oxidation, enhancing the spatial redistribution of PFAS precursors before conversion to persistent terminal products. Overall, these findings reinforce the importance of directly constraining their atmospheric chemistry. Together, these laboratory developments form part of a broader measurement framework that must be complemented by coordinated field-based observations to fully resolve atmospheric PFAS formation, transformation, and deposition processes.

5.2.3 Advancing Field-Based PFAS Measurements

A key future direction is the expansion of integrated field-based strategies for atmospheric PFAS, including the wet deposition samplers and gas-phase annular denuder systems utilized in this work. These provide a complementary approach for quantifying atmospheric inputs across a range of environments.

5.2.3.1 Expansion of Deposition Monitoring Networks

Future work should expand deployment of automated precipitation samplers across broader spatial and temporal scales to capture variability in PFAS wet deposition under differing environmental and emission conditions. Coordinated measurements across urban, rural, and remote[2] environments would improve separation of local sources from long-range transport and strengthen regional deposition estimates. The selective collection of conductive precipitation improves separation of true atmospheric deposition from non-atmospheric contamination compared with bulk sampling, improving flux interpretability and inter-site comparability. Even in non-remote environments, such as rooftop sampling campaigns[1], this separation enhances interpretation of atmospheric inputs and improves quantification of deposition fluxes.

Further development could also focus on adaptation for cold-climate operation. Heated collection systems (i.e., utilizing heated collection funnels) would enable year-round sampling in snow-dominated environments, extending measurements into northern Canada, including Arctic and sub-Arctic regions where PFAS deposition remains poorly constrained. These regions are particularly important due to their sensitivity to long-range atmospheric transport and their role as early indicators of global-scale contamination. Ultimately, long-term deposition monitoring using

these samplers could also provide reference data to evaluate changes in atmospheric PFAS levels in response to evolving regulations and industrial practices.

5.2.3.2 Deposition Sampling: Spike and Recovery Experiments

Future work could include controlled laboratory-based spike and recovery experiments to further evaluate potential biases associated with sample collection and handling. This could be achieved by preparing artificial rainwater matrices representative of field conditions (i.e., deionized water in a pH range similar to rainwater) and spiking known concentrations of target ultrashort- and short-chain PFCAs prior to processing through the full sampling workflow, including collection containers, storage, and analytical transfer steps. Such experiments would enable quantification of potential losses due to adsorption to container walls, storage stability, and handling procedures[26], and would provide additional validation of recovery efficiencies under controlled conditions. This approach would complement field measurements and strengthen confidence in the quantitative interpretation of deposition fluxes.

5.2.3.3 Integration of Complementary Gas-phase and Deposition Measurements

The application of Na_2CO_3-coated denuders should also be extended beyond PFPrA to a broader suite of ultrashort-chain PFCAs. The high collection efficiency demonstrated here (99.83 ± 0.03%) indicates strong suitability for gas-phase PFAAs. Future work could also include intercomparisons between active and passive sampling approaches to confirm performance consistency, alongside concurrent deployment with deposition samplers. Deploying gas-phase and deposition samplers across urban, coastal, rural, and remote environments would assist in improving our spatial and temporal understanding of gas-phase concentrations, partitioning

behaviour, and the relative contributions of wet versus dry deposition. Combining denuder sampling with concurrent precursor measurements (e.g., ambient CIMS measurements) could also improve source identification and help link precursor oxidation to observed terminal acid concentrations. Together, the integration of gas-phase measurements with deposition sampling provides a framework for more complete characterization of atmospheric PFAS inputs, enabling simultaneous evaluation of precursor transport, transformation, and deposition pathways.

5.2.4 Persistence, Atmospheric Lifetimes, and Long-term Environmental Risks

A key conceptual direction for future work is the integration of chemical persistence into environmental risk frameworks for PFAS. Increasing detection of persistent compounds (i.e., TFA) reflects a system in which continuous atmospheric formation and extreme persistence lead to effectively irreversible accumulation in environmental compartments.[27] Unlike many conventional contaminants, PFAS such as TFA do not follow exposure-limited behaviour, where concentrations rise and fall with changing emissions. Instead, their persistence means that environmental concentrations can continue to increase even under stable or reduced emissions scenarios, due to ongoing formation from precursor compounds and their resistance to degradation.[28] Persistence therefore determines how long these compounds remain in the environment and how widely they are distributed, directly influencing exposure levels and the likelihood of contact with ecological and human systems, rather than simply being a property of the chemical itself.[29]

This has important implications for environmental protection and risk assessment. For highly persistent substances, long-term exposure can occur due to environmental persistence and bioaccumulation, with the potential for adverse health effects to manifest only after extended periods of environmental accumulation and organism exposure, particularly given current

uncertainties in toxicological understanding.[30] Accordingly, regulatory limits for persistent environmental contaminants have repeatedly been lowered as new toxicological information becomes available. This pattern is particularly evident for PFAS where, for example, drinking water guideline values for PFOA have decreased dramatically in West Virginia over time, from 150 μg L^{-1} in 2002[31] to 0.004 μg L^{-1} in 2025[32]. These repeated reductions in regulatory limits highlight a key limitation of conventional risk assessment frameworks for highly persistent chemicals, where environmental accumulation and delayed recognition of health outcomes can outpace regulatory response.[29] In this context, persistence determines whether a chemical remains in the environment long enough for its full exposure and toxicity potential to be realised, even if those effects are not immediately observable.

This perspective is consistent with arguments in the literature that identify persistence as a central driver of long-term environmental risk for continuously emitted chemicals.[29,33] The concern is not only the presence of individual compounds, but the sustained and accumulative nature of exposure that arises when degradation is effectively absent. For PFAS, this is particularly relevant given their global distribution and the ongoing formation of terminal products such as TFA from a wide range of precursors.[25,34] The continued increase in global TFA concentrations illustrates this dynamic, where environmental burdens accumulate over time and are effectively irreversible on environmental timescales. This creates a situation in which future ecological or human health impacts may only be recognised after long-term exposure has already occurred, at which point mitigation options are limited and technically challenging.[33] Future research should therefore focus on improving long-term observational datasets and developing modelling frameworks that explicitly account for continuous atmospheric production and accumulation across environmental matrices. Within this context, the integrated methodological framework

developed in this dissertation – linking laboratory oxidation studies with field-based measurements of gas-phase species and deposition fluxes – provides a foundation for constraining how current emissions translate into future environmental burdens. This is critical for assessing whether accumulation trajectories may eventually approach levels of ecological concern, even in the absence of acute toxicity levels in present-day measurements.

5.3 References

1. Persaud, D.; Joudan, S.; VandenBoer, T. C.; Young, C. J. Atmospheric removal of trifluoroacetic acid by dry and wet deposition: a multiyear analysis in Toronto. *Environ. Sci. Technol. Lett*. **2026**, *13*(2), 261–267. doi: 10.1021/acs.estlett.5c01100.

2. Persaud, D.; VandenBoer, T. C.; Place, B. K.; Edwards, K. A.; Ziegler, S. E.; Spencer, C.; De Silva, A. O.; Young, C. J. The Occurrence of Legacy Perfluoroalkyl Substances (PFAS) Deposited along a Latitudinal Transect in Newfoundland and Labrador, Canada. **2026**. *Just submitted*.

3. Vanhauwaert, E.; Carmichael, L.; Nistorescu, I.; Crilley, L. R.; Shunthirasingham, C.; Hung, H.; Young, C. J.; VandenBoer, T. C. Selective ultra-trace atmospheric passive sampling of gaseous perfluoroalkyl carboxylic acids. *Environ. Sci.: Process. Impacts.* **2025**, *27*(9), 2785–2797.

4. Faust, J. A. PFAS on atmospheric aerosol particles: a review. *Environ. Sci.: Process. Impacts.* **2023**, *25*(2), 133–150.

5. Wallington, T. J.; Hurley, M. D.; Xia, J.; Wuebbles, D. J.; Sillman, S.; Ito, A.; Penner, J. E.; Ellis, D. A.; Martin, J.; Mabury, S. A.; Nielsen, O. J.; Sulbaek Andersen, M. P. Formation of C7F15COOH (PFOA) and Other Perfluorocarboxylic Acids during the Atmospheric Oxidation of 8:2 Fluorotelomer Alcohol. *Environ. Sci. Technol.* **2006**, *40*(3), 924–930. https://doi.org/10.1021/es051858x.

6. Pickard, H. M.; Criscitiello, A. S.; Spencer, C.; Sharp, M. J.; Muir, D. C. G.; De Silva, A. O.; Young, C. J. Continuous Non-Marine Inputs of Per- and Polyfluoroalkyl Substances to the High Arctic: A Multi-Decadal Temporal Record. *Atmos. Chem. Phys*. **2018**, *18*(7), 5045–5058.

7. Alsadik, A.; Akintunde, O. O.; Habibi, H. R.; Achari, G. PFAS in water environments: recent progress and challenges in monitoring, toxicity, treatment technologies, and post-treatment toxicity. *Environ. Syst. Res.* **2025**, *14*(1), 18.

8. Ceballos, I. M.; Terro, H.; Barbeau, B.; McQuaid, N.; Sauvé, S.; Dorner, S. Characterization of Per-and Polyfluoroalkyl Substances in Drinking Water Sources in the Greater Montreal Area, Quebec, Canada. *ACS ES&T Water*. **2025**, *5*(9), 5509–5522.

9. Garcia-Barrios, J.; Drysdale, M.; Ratelle, M.; Gaudreau, É.; LeBlanc, A.; Gamberg, M.; Laird, B. D. Biomarkers of poly-and perfluoroalkyl substances (PFAS) in Sub-Arctic and Arctic communities in Canada. *Int. J. Hyg. Environ. Health.* **2021**, *235*, 113754.

10. Ellis, D. A.; Martin, J. W.; De Silva, A. O.; Mabury, S. A.; Hurley, M. D.; Sulbaek Andersen, M. P.; Wallington, T. J. Degradation of Fluorotelomer Alcohols: A Likely Atmospheric Source of Perfluorinated Carboxylic Acids. *Environ. Sci. Technol.* **2004**, *38*(12), 3316–3321. https://doi.org/10.1021/es049860w.

11. Environment and Climate Change Canada & Health Canada. Risk management approach for per- and polyfluoroalkyl substances (PFAS), excluding fluoropolymers. **2025**. Retrieved from: https://www.canada.ca/en/environment-climate-change/services/evaluating-existing-substances/risk-management-approach-per-polyfluoroalkyl-substances.html.

12. Zaytsev, A.; Breitenlechner, M.; Koss, A. R.; Lim, C. Y.; Rowe, J. C.; Kroll, J. H.; Keutsch, F. N. Using collision-induced dissociation to constrain sensitivity of ammonia chemical ionization mass spectrometry (NH 4+ CIMS) to oxygenated volatile organic compounds. *Atmos. Meas. Tech.* **2019**, *12*(3),1861–1870.

13. Song, M.; He, S.; Li, X.; Liu, Y.; Lou, S.; Lu, S.; Zeng, L.; Zhang, Y. Optimizing the iodide-adduct chemical ionization mass spectrometry (CIMS) quantitative method for toluene oxidation intermediates: experimental insights into functional-group differences. *Atmos. Meas. Tech.* **2024**, *17*(17), 5113–5127.

14. Riedel, T. P.; Lang, J. R.; Strynar, M. J.; Lindstrom, A. B.; Offenberg, J. H. Gas-Phase Detection of Fluorotelomer Alcohols and Other Oxygenated Per- and Polyfluoroalkyl Substances by Chemical Ionization Mass Spectrometry. *Environ. Sci. Technol. Lett.* **2019**, *6*(5), 289–293. https://doi.org/10.1021/acs.estlett.9b00196.

15. Bowers, B. B.; Thornton, J. A.; Sullivan, R. C. Evaluation of Iodide Chemical Ionization Mass Spectrometry for Gas and Aerosol-Phase per- and Polyfluoroalkyl Substances (PFAS) Analysis. *Environ. Sci.: Process. Impacts.* **2023**, *25*(2), 277–287. https://doi.org/10.1039/D2EM00275B.

16. Mattila, J. M.; Offenberg, J. H. Measuring Short-Chain per- and Polyfluoroalkyl Substances in Central New Jersey Air Using Chemical Ionization Mass Spectrometry. *J. Air Waste Manag. Assoc.* **2024**, *74*(8), 531–539. https://doi.org/10.1080/10962247.2024.2366491.

17. Young, C. J.; Joudan, S.; Tao, Y.; Wentzell, J. J.; Liggio, J. High time resolution ambient observations of gas-phase perfluoroalkyl carboxylic acids: implications for atmospheric sources. *Environ. Sci. Technol. Lett.* **2024**, *11*(12), 1348−1354.

18. Hurley, M. D.; Wallington, T. J.; Laursen, L.; Javadi, M. S.; Nielsen, O. J.; Yamanaka, T.; Kawasaki, M. Atmospheric Chemistry of n-Butanol: Kinetics, Mechanisms, and Products of Cl Atom and OH Radical Initiated Oxidation in the Presence and Absence of NO x. *J. Phys. Chem. A.* **2009**, *113*(25), 7011−7020.

19. Cavalli, F.; Barnes, I.; Becker, K. H. FT-IR kinetic and product study of the OH radical-initiated oxidation of 1-pentanol. *Environ. Sci. Technol.* **2000**, *34*(19), 4111−4116.

20. Young, C. J.; Hurley, M. D.; Wallington, T. J.; Mabury, S. A. Molecular structure and radiative efficiency of fluorinated ethers: A structure-activity relationship. *J. Geophys. Res. Atmos.* **2008**, *113*, D24301, doi:10.1029/2008JD010178.

21. De Bruycker, R.; Herbinet, O.; Carstensen, H. H.; Battin-Leclerc, F.; Van Geem, K. M. Understanding the reactivity of unsaturated alcohols: Experimental and kinetic modeling study of the pyrolysis and oxidation of 3-methyl-2-butenol and 3-methyl-3-butenol. *Combust. Flame.* **2016**, *171*, 237−251.

22. Ellis, D. A.; Martin, J. W.; Mabury, S. A.; Hurley, M. D.; Sulbaek Andersen, M. P.; Wallington, T. J. Atmospheric lifetime of fluorotelomer alcohols. *Environ. Sci. Technol.* **2003**, *37*(17), 3816−3820.

23. Douroudgari, H.; Zarepour, H.; Vahedpour, M.; Jaberi, M.; Zarepour, M. The atmospheric relevance of primary alcohols and imidogen reactions. *Sci. Rep.* **2023**, *13*(1), 9150.

24. Chao, W.; Jr-Min Lin, J.; Takahashi, K.; Tomas, A.; Yu, L.; Kajii, Y.; Batut, S.; Schoemaecker, C.; Fittschen, C. Water vapor does not catalyze the reaction between methanol and OH radicals. *Angew. Chem. Int. Ed.* **2019**, *58*(15), 5013–5017.

25. Young, C. J.; Mabury, S. A. *Atmospheric Perfluorinated Acid Precursors: Chemistry, Occurrence, and Impacts*. Edited by N. Whitacre, D. M.; Springer New York, New York, **2010**. doi: 10.1007/978-1-4419-6880-6887.

26. Folorunsho, O.; Kizhakkethil, J. P.; Bogush, A.; Kourtchev, I. Effect of short-term sample storage and preparatory conditions on losses of 18 per-and polyfluoroalkyl substances (PFAS) to container materials. *Chemosphere*. **2024**, *363*, 142814.

27. Guidance on Information Requirements and Chemical Safety Assessment, Chapter R11: PBT/vPvB Assessment. European Chemicals Agency: Helsinki, **2023**. Retrieved from: https://echa.europa.eu/ documents/10162/17224/information_requirements_r11_en.pdf/ a8cce23f-a65a-46d2-ac68-92fee1f9e54f.

28. Cousins, I. T.; DeWitt, J. C.; Glüge, J.; Goldenman, G.; Herzke, D.; Lohmann, R.; Ng, C. A.; Scheringer, M.; Wang, Z. The high persistence of PFAS is sufficient for their management as a chemical class. *Environ. Sci. Process. Impacts.* **2020** *22*(12), 2307–2312.

29. Scheringer, M.; Cousins, I. T. Is Persistence a Hazard? *Environ. Sci. Technol.* **2026**, *60*(13), 9718–9720.

30. Pereira, L. C.; de Souza, A. O.; Bernardes, M. F. F.; Pazin, M.; Tasso, M. J.; Pereira, P. H.; Dorta, D. J. A perspective on the potential risks of emerging contaminants to human and environmental health. *Environ. Sci. Pollut. Res.* **2015**, *22*, 13800–13823.

31. Post, G. B. Recent US State and Federal Drinking Water Guidelines for Per- and Polyfluoroalkyl Substances. *Environ. Toxicol. Chem.* **2020**, *40*, 550–563.

32. United States Environmental Protection Agency. Per- and Polyfluoroalkyl Substances (PFAS) - Final PFAS National Primary Drinking Water Regulation, Washington DC. **2025**. Retrieved from: https://www.epa.gov/ sdwa/and-polyfluoroalkyl-substances-pfas.

33. Cousins, I. T.; Ng, C. A.; Wang, Z. Y.; Scheringer, M. Why is high persistence alone a major cause of concern? *Environ. Sci. Process. Impacts*. **2019**, *21*, 781–792.

34. Sulbaek Andersen, M. P.; Wallington, T. J.; Burkholder, J. B.; Madronich, S.; Hanson, M. L.; Van Hoomissen, D.; Solomon, K. R. Yields of perfluorocarboxylic acids from the atmospheric oxidation of Montreal Protocol related gases. *Environmental Science: Atmospheres*. **2026**, doi: 10.1039/D5EA00179J.